



HAL
open science

Stabilized C1-bicubic finite element method for nonlinear MHD modeling of tokamak plasma

Ashish Bhole

► **To cite this version:**

Ashish Bhole. Stabilized C1-bicubic finite element method for nonlinear MHD modeling of tokamak plasma. Mathematics [math]. Université Côte D'Azur, 2021. English. NNT: 2021COAZ4098 . tel-03852251

HAL Id: tel-03852251

<https://hal.science/tel-03852251>

Submitted on 14 Nov 2022

HAL is a multi-disciplinary open access archive for the deposit and dissemination of scientific research documents, whether they are published or not. The documents may come from teaching and research institutions in France or abroad, or from public or private research centers.

L'archive ouverte pluridisciplinaire **HAL**, est destinée au dépôt et à la diffusion de documents scientifiques de niveau recherche, publiés ou non, émanant des établissements d'enseignement et de recherche français ou étrangers, des laboratoires publics ou privés.



Distributed under a Creative Commons Attribution 4.0 International License



HAL
open science

Stabilized C1-bicubic finite element method for nonlinear MHD modeling of tokamak plasma

Ashish Bhole

► **To cite this version:**

Ashish Bhole. Stabilized C1-bicubic finite element method for nonlinear MHD modeling of tokamak plasma. Modeling and Simulation. Université Côte d'Azur, 2021. English. NNT : 2021COAZ4098 . tel-03578187

HAL Id: tel-03578187

<https://tel.archives-ouvertes.fr/tel-03578187>

Submitted on 17 Feb 2022

HAL is a multi-disciplinary open access archive for the deposit and dissemination of scientific research documents, whether they are published or not. The documents may come from teaching and research institutions in France or abroad, or from public or private research centers.

L'archive ouverte pluridisciplinaire **HAL**, est destinée au dépôt et à la diffusion de documents scientifiques de niveau recherche, publiés ou non, émanant des établissements d'enseignement et de recherche français ou étrangers, des laboratoires publics ou privés.



$$\rho \left(\frac{\partial v}{\partial t} + v \cdot \nabla v \right) = -\nabla p + \nabla \cdot T + f$$

$$e^{i\pi} + 1 = 0$$

THÈSE DE DOCTORAT

Méthode d'éléments finis C1
bicubique stabilisée pour la
modélisation MHD non linéaire du
plasma de tokamak

Ashish Bhole

Laboratoire de Mathématiques J. A. Dieudonné (LJAD)

**Présentée en vue de l'obtention
du grade de docteur en
Mathématique
d'Université Côte d'Azur**

Dirigée par : *Boniface Nkonga*

Soutenue le : 17 novembre 2021

Devant le jury, composé de :

Eric Serre, Dr CNRS, M2P2, Aix-Marseille Université
Eric Nardon, Ingénieur-HDR, IFRM, CEA Cadarache
Hervé Guillard, Dr Inria, CASTOR, Inria Sophia Antipolis
Boniface Nkonga, Pr, LJAD/CASTOR, Université Côte d'Azur
Pierre Ramet, MdC, LABRI/Inria, Université de Bordeaux
Stanislas Pamela, Ingénieur-Cherche, CCFE - UKAEA
Dinshaw Balsara, Pr Associé, Uni. of Notre Dame, USA
Praveen Chandrashekar, Chercheur, TIFR-CAM, India

THÈSE DE DOCTORAT

en vue d'obtenir le titre de
Docteur en Sciences
de l'Université Côte d'Azur

Discipline: Mathématiques

présentée et soutenue par

Ashish BHOLE

Méthode d'éléments finis C1-bicubique stabilisée
pour la modélisation MHD non linéaire du plasma
de tokamak

Thèse dirigée par:
Boniface Nkonga

Soutenu le **17 Novembre 2021**

devant le jury composé de :

Eric Serre	Dr CNRS, M2P2, Aix-Marseille Université	Rapporteur
Eric Nardon	Ingénieur-HDR, IFRM, CEA Cadarache	Rapporteur
Hervé Guillard	Dr Inria, CASTOR, Inria Sophia Antipolis	Examineur
Boniface Nkonga	Pr, LJAD/CASTOR, Université Côte d'Azur	Dir. de Thèse
Pierre Ramet	MdC, LABRI/Inria, Université de Bordeaux	Examineur
Stanislas Pamela	Ingénieur-Cherche, CCFE - UKAEA	Examineur
Dinshaw Balsara	Pr Associé, Uni. of Notre Dame, USA	invité
Praveen Chandrashekar	Chercheur, TIFR-CAM, India	invité

Résumé

Le tokamak est l'un des systèmes prometteurs mis au point pour exploiter l'énergie de fusion. Un tokamak est une chambre toroïdale dans laquelle un plasma chaud est confiné magnétiquement. Pour le bon fonctionnement des tokamaks, il est souhaitable que le plasma reste dans une configuration d'équilibre. Les ruptures de confinement, appelées disruptions, sont des événements inévitables et indésirables d'instabilités du plasma survenant dans les tokamaks qui peuvent dégrader les performances d'un tokamak et endommager gravement les parois du tokamak. Afin d'atténuer les effets néfastes des disruptions, une quantité massive de matière est injectée dans le plasma du tokamak. En plus des expériences et observations réalisées sur des tokamaks opérationnels, la compréhension et la maîtrise des stratégies d'injection passent souvent par les simulations numériques. En effet, la dynamique du plasma après l'injection s'accompagne d'interactions complexes que nous pouvons décrire par les équations de la MagnétoHydroDynamique (MHD). Il est donc primordial de développer des méthodes numériques robustes et précises pour obtenir par la simulation numérique une évaluation qualitative et quantitative des processus physiques complexes qui sont en œuvres.

L'objectif principal de cette thèse est de développer des stratégies numériques pour la simulation des instabilités MHD dans les plasmas de tokamaks, en y incluant les ondes acoustiques rapides absentes dans les modèles réduits. Les développements sont effectués dans le cadre des méthodes d'éléments finis (FEM) dans une base décrite par des fonctions de Bézier bi-cubique de régularité $C1$. Les écoulements concernés sont très souvent dominés par la convection, par conséquent il est indispensable de prendre en compte les effets des échelles non résolues dans la formulation éléments finis. En pratique, les échelles non résolues sont pris en compte à la fois par une approche multi-échelle variationnelle et par une technique de capture des chocs. D'autres ingrédients viennent compléter l'approche numérique : le traitement de la singularité des grilles polaires, l'intégration temporelle par une méthode de Gears du second ordre pour des pas de temps variables. Le modèle numérique proposé est validé par rapport aux stratégies basées sur des modèles de MHD réduite. Une attention particulière est accordée aux simulations MHD non linéaires avec injection massive de matière dans le plasma de tokamak. Les équations de la MHD sont ici étendues pour y inclure le transport des neutres et des impuretés dans le plasma ainsi que les termes

de source pour modéliser l'injection massive de matière. Le modèle résultant est utilisé pour simuler l'injection massive de gaz et l'injection de pastilles brisées dans un plasma de type JET. De nombreuses simulations non linéaires sont réalisées et démontrent la capacité, de la stratégie numérique développée, à capturer la dynamique complexe d'instabilités MHD dans lesquels se développent l'étouffement thermique et la stochastisation du champ magnétique.

Mots-clés: Magnétohydrodynamique, instabilités MHD, mitigation des disruptions, MHD complète, méthode des éléments finis, singularités du maillage, méthodes implicites, stabilisation variationnelle multi-échelle, stabilisation par chocs, l'instabilité de kink interne, injection massive de gaz, injection de pastilles éclatées.

Abstract

The tokamak is one of the promising systems developed to harness fusion energy. A tokamak is a toroidal chamber in which a hot plasma is magnetically confined. For tokamaks to function properly, it is desirable that the plasma remain in an equilibrium configuration. Confinement failures, called disruptions, are unavoidable and undesirable events of plasma instabilities occurring in tokamaks that can degrade the performance of a tokamak and severely damage the tokamak walls. In order to mitigate the adverse effects of disruptions, a massive amount of material is injected into the tokamak plasma. In addition to the experiments and observations carried out on operational tokamaks, the understanding and control of injection strategies often requires numerical simulations. Indeed, the dynamics of the plasma after the injection is accompanied by complex interactions that we can describe by the equations of magneto-hydrodynamics (MHD). It is therefore essential to develop robust and accurate numerical methods to perform numerical simulations and obtain a qualitative and quantitative assessment of the complex physical processes.

The main objective of this thesis is to develop numerical strategies for the simulation of MHD instabilities in tokamak plasma. The full MHD model is used for the physical modeling that includes fast magnetosonic waves, which are absent in reduced MHD models. The developments are carried out within the framework of bi-cubic Bézier $C1$ finite element method (FEM). The plasma flows concerned are very often dominated by convection and therefore it is essential to take into account the effects of unresolved scales in the finite element formulation. In practice, the unresolved scales are taken into account both by a variational multiscale approach and by a shock capturing technique. Other ingredients used in the numerical approach include: the treatment of the polar grid singularity, the time integration by a second order Gears method for variable time steps. The proposed numerical model is validated against the reduced MHD model. Particular attention is paid to nonlinear MHD simulations with massive material injection in tokamak plasma. The full MHD equations are then extended to include the transport of neutrals and impurities in the plasma and the source terms to model the massive material injection. The resulting model is used to simulate the massive gas injection and the shattered pellet injection into a JET like plasma. Numerous nonlinear simulations are performed to demonstrate the ability of the developed numerical strategy to capture the complex dynamics of MHD

instabilities in which thermal quench and magnetic field stochastization occur.

Keywords: Magnetohydrodynamics, MHD instabilities, Disruption mitigation, Full MHD, Finite element method, Grid singularities, Implicit methods, Variational multi-scale stabilization, Shock-capturing stabilization, Internal kink modes, Massive gas injection, Shattered pellet injection.

Acknowledgments

I would like to thank my doctoral adviser Boniface Nkonga for giving me the opportunity of working on this subject, directing my doctoral research work and his support on the professional as well as personal level. His precise and clear explanation to my questions and doubts throughout the work is much appreciated. I am thankful to the members of the CASTOR team at INRIA for creating the wonderful working environment. I would like to thank Hervé Guillard for the fruitful academic discussions and his support specially in the pandemic times.

I thank the members of JOREK team on whom I relied for the help on many practical aspects of JOREK. Specially, I am grateful to Stanislas Pamela for his contribution and help in this work. Discussions with him were always enlightening and productive. I am also thankful to Matthias Hoelzl for his extremely precise help and comments on the problems I faced time to time. I am thankful to my past academic advisors Praveen Chandrashekar and T K Senugupta for their support on the academic path I chose.

I am thankful to my teammate and friend, Ali Elarif, for the wonderful time we spend together at INRIA as well as at home. I am thankful to my colleague Montserrat Argente for her help on professional as well as personal level. I am also thankful to Konstanze Beck at UCA welcome center for her help with the administrative procedures at the Prefecture which is very much appreciated.

I thank my family members, teachers and friends for their love, support and encouragement all along.

Contents

1	Introduction	1
1.1	Fusion and plasma confinement	1
1.1.1	Fusion energy	1
1.1.2	Plasma	3
1.1.3	Plasma confinement	4
1.2	Tokamaks and some terminologies	4
1.2.1	Tokamaks	4
1.2.2	Magnetic surfaces and some definitions	7
1.2.3	Limiter and divertor configurations	8
1.3	Disruptions and their mitigation	9
1.3.1	Disruptions	9
1.3.2	Sequence of events during major disruptions	10
1.3.3	Disruptions control	12
1.3.4	Shattered pellet injection	13
1.4	Numerical modeling	15
1.4.1	JOEKE	15
1.5	Organization of the manuscript	16
2	Physical models	18
2.1	Physical models for plasma	20
2.1.1	Kinetic model	20
2.1.2	Multi fluid model	22

2.1.3	Two fluid model	25
2.1.4	Single fluid model	26
2.2	Tokamak modeling	30
2.2.1	Co-ordinate system	30
2.2.2	MHD instabilities	31
2.2.3	Grad-Shafranov Equation	32
2.2.4	Full MHD model with Potential vector formulation	35
2.2.5	Visco-resistive full MHD model with sources	36
2.2.6	Normalization	38
2.2.7	Reduced MHD model	40
2.3	Full MHD: Massive Material Injection	41
2.4	Conclusion	56
3	Numerical methods	57
3.1	Finite element method and stabilization	60
3.1.1	Galerkin finite element method	60
3.1.2	Variable Multi-scale formulation	61
3.2	Finite Element Method for tokamak modeling	63
3.2.1	Mixed Bi-cubic Bézier-spectral FEM	63
■	The finite element in poloidal plane	65
■	Toroidal basis functions:	71
3.2.2	Time stepping and matrix solver	73
3.2.3	Stabilized FEM for full MHD	75
3.3	Time integration method with variable time step	78
3.4	Grid generation	83
3.4.1	Rectangular grids	84
3.4.2	Polar grids	84
3.4.3	Flux-aligned grids	85
3.4.4	Flux-aligned grids with X-points	87

3.4.5	Grid singularities:	89
3.5	Conclusions	97
4	Implementation and validation of full MHD model	99
4.1	Solving Grad-Shafranov equation	100
4.2	Implementation of full MHD model	110
4.3	Linear simulations	115
4.3.1	Resistive internal kink modes	115
4.3.2	Tearing Modes	117
4.3.3	Ballooning modes	120
4.3.4	Ballooning modes in X-point plasma	123
4.4	Nonlinear Simulations	124
4.4.1	Effect of variable time step Gears method	125
4.4.2	Effect of polar grid center treatment	126
4.4.3	Nonlinear runs for internal kink modes	130
4.5	Conclusion	133
5	Nonlinear simulations with Massive Material Injection	134
5.1	Preliminary validations: MGI and SPI	135
5.2	SPI triggered MHD dynamics	149
5.3	Conclusion	183
6	MHD destabilization and thermal quench	184
6.1	Discontinuity capturing criterion	185
6.2	Thermal quench	186
6.2.1	SPI with constant resistivity	186
6.2.2	SPI with realistic resistivity	193
6.3	Conclusion	200
7	Conclusions and perspectives	202

Appendix A	Jacobians required for the implicit method	206
Appendix B	Integrated quantities	216
Bibliography		217

List of Tables

3.1	Bézier basis functions $H_{v,d}$ where $1 \leq v \leq 4$ and $1 \leq d \leq 4$	70
3.2	Summary of new DoFs, scales and basis functions to be applied at the polar grid center. The basis functions $N_{1,2}^e$, $N_{1,4}^e$, $N_{4,2}^e$ and $N_{4,4}^e$ are given by the equations (3.25).	96
4.1	Growth rates (in normalized units) of magnetic energies for internal kink mode obtained by full MHD model on a series of grids. The grid is denoted by $N_\psi \times N_\theta$ where N_ψ and N_θ are the number of points in radial and poloidal direction.	117
4.2	Growth rates (in normalized units) of magnetic energies for tearing modes obtained by full MHD model on a series of grids. The grid is denoted by $N_\psi \times N_\theta$ where N_ψ and N_θ are the number of points in radial and poloidal direction.	119
5.1	A series of grids used for SPI simulation with constant $\eta = 10^{-7}$. Here, n_ψ and n_θ denotes the number of points in radial and azimuthal direction respectively. n denotes the number of toroidal harmonics added in the simulations and N_p denotes the number of equidistant planes in the toroidal direction which needs to chosen for FFT implementation.	156
6.1	SPI simulations with constant $\eta = 10^{-6}$ identified by grid (g) and the shock-capturing stabilization parameter (C) as ‘case g.C’	187
6.2	SPI simulations with temperature dependent resistivity with $\eta_0 = 10^{-8}$ identified by by grid (g) and the shock-capturing stabilization parameter (C) as ‘case g.C’.	194

List of Figures

1.1	(a) Global energy consumption in the year 2001. The sector marked ‘other’ includes geothermal, solar, and wind energy [65]. (b) Specific carbon dioxide emissions (PV: photo voltaics; CCS: carbon capture and storage; LNG: liquefied natural gas) [58]	2
1.2	Fusion reactivity plotted vs ion temperature [85].	3
1.3	(a) A schematic view of a tokamak [65] (b) Toroidal (r, θ, ϕ) and cylindrical (R, Z, ϕ) coordinate systems. The geometric axis of a tokamak is identified by $R_0 = (R_{max} + R_{min})/2$ while the minor radius is identified by $a = (R_{max} - R_{min})/2$	5
1.4	(a) Fusion triple product as a function of the core ion temperature for different tokamaks [80] (b) Experimental data from all the major tokamaks in the international fusion program showing how the confinement time scales with physical parameters [65].	6
1.5	Outline of the development of the fusion power program [65].	7
1.6	Nested magnetic flux surfaces with magnetic lines on them.	8
1.7	Tokamak configurations.	9
1.8	L-mode and H-mode confinement [77].	10
1.9	Phases of disruptions: the thermal quench (TQ) and current quench (CQ)	11
1.10	(a) Illustration for SPI and MGI set ups in ITER. (b) Simple breaker tube with single bend to shatter large pellets in DIII-D (figure from [28])	13
2.1	The coordinate system used for representation of plasma physics equations.	31

3.1	(a) A curved element Ω_e in physical plane Ω_ξ is marked by the vertices $g(v_1), g(v_2), g(v_3)$ and $g(v_4)$. (b) An element τ_e in the parametric plane Ω_ζ formed by the same vertices. (c) The unit reference element $\hat{\tau}$. . .	65
3.2	A Bézier patch shown in 3D space: The left plot represent the control points of the patch highlighted in blue color. The red control points define the grid nodes. The right plot depicts the resulting Bézier surface. The projection of the surface bounded by red curves at the bottom represents a grid cell in (R, Z) plane. The elevation represents the spatial distribution of any physical variable. The figure is taken from [47].	66
3.3	Two neighboring Bézier elements are shown. The figure is taken from [47].	67
3.4	Bézier basis functions associated with vertex 1 of the reference element $\hat{\tau}$. The coordinate $(\hat{s} = 0, \hat{t} = 0)$ corresponds to vertex 1.	68
3.5	Corner between four Bézier patches with G^1 continuity. The figure is taken from [24].	69
3.6	Convergence of time integration methods shown by plotting absolute value of the error computed for a series of time steps Δt . Implicit Euler (IE) shows first order convergence, Crank-Nicholson (CE) and second order back-word difference (BDF2) show second order convergence. Since knowledge of $n - 1$ -th time level is needed for BDF2, at the first time step the simulation maybe started with either IE or CN. Starting a simulation with CN shows advantage as the errors in this case are lower.	82
3.7	Polar grids generated in JOREK. First row shows circular and non-circular polar grids on which Grad-Shafranov equation is solved for poloidal magnetic flux (ψ) . Second row shows grids aligned to the flux surfaces in red color plotted on the top of previous grids.	86

3.8	Flux aligned grid generated in JOREK with one X-point. The magnetic axis and X-point are marked by ξ_a and ξ_x . The red curve in a) denotes the separatrix. The left divertor cuts the last open field line, separatrix and end of private region at ξ_b^l, ξ_x^l and ξ_p^l respectively. Similarly, the right divertor cuts the last open field line, separatrix and end of private region at ξ_r^l, ξ_x^r and ξ_p^r respectively. The separatrix constitutes three curves: the curve that closes on X-point ($\mathcal{S}(\xi_x, \xi_x)$), the curves joining X-point with left ($\mathcal{S}(\xi_x, \xi_x^l)$) and right legs ($\mathcal{S}(\xi_x, \xi_x^r)$). Other strategic curve are: $\mathcal{S}(\xi_b^l, \xi_b^r), \mathcal{S}(\xi_b^l, \xi_x^l), \mathcal{S}(\xi_b^r, \xi_x^r), \mathcal{S}(\xi_x^l, \xi_p^l)$ and $\mathcal{S}(\xi_x^r, \xi_p^r)$	88
3.9	Grid singularities	89
3.10	An element on the polar grid center. A typical situation where the edge of an element on the axis is formed by vertex v_1 and v_4 falls on the polar grid center which in the reference element forms the edge $\hat{s} = 0$.	91
3.11	Basis function plotted at the polar grid center. The third and fourth basis functions are oscillatory in the θ direction and are not continuous at the grid center.	93
3.12	New global basis functions plotted at the polar grid center. The first basis function is unchanged. The second and fourth basis functions are linear combinations of original basis functions. The third basis function is not to be used as the DoF associate it with 0.	96
3.13	Error in the grid representation at the polar grid center. Errors in $\frac{\partial \xi}{\partial \hat{s}}$ and $\frac{\partial \xi}{\partial^2 \hat{s} \partial \hat{t}}$ at $\hat{s} = 0$ are plotted vs. \hat{t} where m denotes number of points in the θ direction.	97
3.14	L^2 norm of the interpolation error for the function $\mathcal{W} = R^4 + R^3 + R^2 + R + Z^4 + Z^3 + Z^2 + Z$ plotted vs element size h . The interpolation of a function is computed using new basis functions derived for elements on the polar grid center.	98
4.1	(a) The density (blue circles) and temperature (red circles) profiles from the JET experiment (pulse no. 73569), with the corresponding fitted profiles used for simulations (plain black lines). [75] (b) Interpretations for the coefficients of profiles of the density and temperature (c) Interpretations for the coefficients of profiles of FF'	101

4.2	For a circular equilibrium 1: (a) The density, temperature and FF' profiles plotted vs ψ_N . (b) Numerically computed equilibrium ψ	106
4.3	For a circular equilibrium 2: (a) The density, temperature and FF' profiles plotted vs ψ_N . (b) Numerically computed equilibrium ψ . . .	107
4.4	For a circular equilibrium 3 (cbm18): (a) The density, temperature and FF' profiles plotted vs ψ_N . (b) Numerically computed equilibrium ψ . .	108
4.5	For a JET like equilibrium: (a) The density, temperature and FF' profiles plotted vs ψ_N . (b) Boundary conditions specified for ψ on the polar grid. (c) Polar grid on which Grad-Shafranov equation is solved and contours for numerical solution ψ . (d) Grid aligned to numerical solution ψ shown in red color. (e) Pseudocolor plot of ψ on the flux aligned grid.	109
4.6	Linear runs for internal kink mode: (a) q profile showing the location of $q = 1$ surface roughly at $\psi_N = 0.5$ (b) magnetic energies (ME) vs resistivity for full MHD (FMHD) and reduced MHD (RMHD) models.	116
4.7	Visualizations for the perturbations in internal kink simulations plotted on the poloidal plane $\phi = 0$. The first, second and third row show results for $\eta = 10^{-5}$, 10^{-6} and 10^{-7} (in normalized) units respectively. The first, second and third columns show the perturbations in A_3 , T and v_R respectively.	118
4.8	Linear runs for tearing mode: (a) q profile showing the location of $q = 1$ surface roughly at $\psi_N \approx 0.28$ (this corresponds to $R \approx 10.5$) (b) magnetic energies (ME) vs resistivities for full MHD (FMHD) and reduced MHD (RMHD) models.	119
4.9	Visualizations for the perturbations in tearing mode simulations plotted on the poloidal plane $\phi = 0$. The first and second row show results for $\eta = 10^{-6}$ and 10^{-7} (in normalized) units respectively. The first, second and third columns show the perturbations in A_3 , T and v_ϕ respectively.	120
4.10	Flux aligned grid used for circular ballooning mode where magnetic axis is shifted to $R \approx 3.68$ m. Pseudocolor shows the temperature field at the $t = 0$. The grid is clustered around the sharp gradient in the temperature to capture ballooning modes.	121

4.11	Linear runs for circular ballooning mode: (a) q profile (b) magnetic energies (ME) vs resistivities for full MHD (FMHD) and reduced MHD (RMHD) models.	122
4.12	Visualizations for the perturbations in circular ballooning mode simulations plotted on the poloidal plane $\phi = 0$. The first and second row show results for $n = 4$ and 16 respectively. The first, second and third columns show the perturbations in A_3 , T and ρ respectively.	122
4.13	Linear runs for ballooning modes in JET like X-point plasma (a) q profile (b) magnetic energies (ME) vs number of harmonics n for full and reduced MHD models.	123
4.14	Visualizations for the perturbations in X-point plasma for ballooning mode simulations for $n = 10$. The left and right window shows $ \nabla p $ and perturbations in A_3 respectively plotted on a poloidal plane $\phi = 0$	124
4.15	Comparison of growth rates of magnetic energies γ_{ME} plotted vs t for internal kink modes obtained using Gears method with $r_n = 1$ and $r_n \neq 1$ for the 3 tests described.	127
4.16	Grids used for tearing mode simulations with new basis for the elements of the polar grid center. These grids are zoomed near grid center to show the effect of parameter a on grid accumulation. As a reduces, grid is accumulated near the center, while $a = 99$ denotes no accumulation.	128
4.17	Magnetic energies for (a) linear and (b) nonlinear tearing mode run with $n = 0, 1$. The factor a in the legends denote amount grid accumulation near the polar grid center. With old basis functions at the grid center numerical noise is seen. With new basis functions at the grid center the noise is removed.	128
4.18	Effect of polar grid center treatment: First and second row show visualizations for linear and nonlinear runs for tearing modes respectively. First and second column show visualizations without and with polar grid center treatment respectively. (a) and (b) show perturbations in A_3 for linear tearing mode runs. (c) and (d) show perturbations in v_ϕ for nonlinear tearing mode runs.	129
4.19	Perturbations in v_ϕ with (a) old and (b) new basis functions at the polar grid center. With the new basis functions the noise at the grid center disappears.	130

4.20	(a) Flux surface aligned polar grid used for nonlinear simulation of internal kink mode (b) Evolution of energies with (solid lines) and without (dotted lines) numerical stabilization.	132
4.21	Evolution of energies showing nonlinear saturation phase after linear growth of internal kink modes.	132
5.1	JET like equilibrium used for MMI simulations: (a) ρ , T and FF' profiles plotted vs ψ_N . (b) Boundary conditions specified to solve Grad-Shafranov equation on the polar grid. (c) Contours showing the numerical solution of the Grad-Shafranov equation ψ plotted upon polar grid. (d) Flux aligned grid with the contours of ψ_N highlighting $q = 1, 2, \dots, 6$ surfaces (drawn radially outwards) (e) Numerical solution ψ plotted on the flux aligned grid. (f) q profile plotted vs ψ_N	137
5.2	MGI with full MHD: (a) T_e at the magnetic axis. (b) T_e profiles at midplane plotted vs R . Evolution of : (c) magnetic energies (solid lines) and kinetic energies (dotted lines) for $n = 1, 2, 3, 4$ (d) plasma current I_p	139
5.3	MGI with full MHD: First, second and third column shows T_e [keV], n_e (10^{20}) and Poincaré plots respectively. First, second, third and fourth row corresponds to $t = 1.48, 2.37, 2.97, 3.86$ in ms respectively.	141
5.4	The data obtained from CE assumption and openADAS [1] database: (a) the charge state distribution function $\mathcal{P}(z)$ plotted vs electron temperature (in $\log_{10}(K)$) where $z \in 0, 10$ for Neon atom. The legend 'sum' denotes summation of $\mathcal{P}(z)$ over all charge states. (b) Z_{eff} plotted vs electron temperature. (c) Radiation function plotted vs electron temperature (in $\log_{10}(K)$).	143
5.5	Sketch illustrating SPI: (a) Distribution of initial position and velocity of the SPI fragments (b) The direction and the extent of SPI fragments propagation.	143
5.6	(a) Ablation rate plotted vs t (b) Total number of Ne atom in plasma plotted vs t	144

5.7	First, second, third and fourth row show visualization of $n_{\text{imp}} [10^{20}]$, T [keV], A_3 and Z_{eff} while first, second and third columns shows the quantities plotted at $t = 0.83, 0.88$ and 1 ms. All the figures are plotted at $\phi = 0$ plane.	146
5.8	Poicaré plot of magnetic field plotted at $t = 1$ ms along with the position of SPI fragments marked by blue dots.	147
5.9	SPI with full MHD: Evolution of (a) magnetic energies (solid lines) and kinetic energies (dotted lines) for $n = 1, 2, 3, 4, 5, 6, 7$ (b) T at the magnetic axis. (c) T profiles at midplane plotted vs R . (d) $j = -Rj_\phi$ profiles at midplane plotted vs R . Smoothing operation is performed on this profile.	148
5.10	SPI with full MHD: Evolution of (a) thermal energy (b) radiation energy (c) plasma current I_p . These are integrated quantities over plasma volume.	148
5.11	Effect of η in A_R and A_Z equations: (a) ablation rates (b) Total impurities injected (c) plasma current I_p (d) plasma thermal energy (e) magnetic energies (ME) (f) kinetic energies (KE). For ME and KE solid lines denote the energies obtained using the same value of η in all equations A_R , A_Z and A_3 . While, dashed lines denote the energies obtained by the use of smaller value of η in A_R and A_Z equation. . .	152
5.12	Poicaré plots of the magnetic field at $t = 0.94$ ms showing effect of η in A_R and A_Z equations.	153
5.13	Effect of η on SPI simulations: (a) ablation rates (b) Total impurities injected (c) plasma current I_p (d) plasma thermal energy (e) magnetic energies (ME) (f) kinetic energies (KE). For ME and KE solid lines, dashed lines and dotted-dashed lines denote the energies obtained using $\eta = 10^{-6}, 10^{-7}$ and 10^{-9}	155
5.14	Effect of T and Z_{eff} dependence on the resistivity (a) T (in normalized units) plotted in log scale at $t \approx 0.72$ ms (b) Z_{eff} plotted at $t \approx 0.72$ ms (c) ratio of resistivities (in normalized units) $\eta(t \approx 0.72)/\eta(t \approx 0.057)$	155
5.15	SPI simulations run on a series of grids for $\eta = 10^{-7}$ (a) physical time for which simulation is run (b) ablation rates (c) total impurities injected (d) radiation energy (e) plasma current I_p (f) plasma thermal energy.	157

5.16	SPI simulations run on a series of grids for $\eta = 10^{-7}$ (a) magnetic energies (b) kinetic energies. Dotted, dashed, dashed-dotted and solid lines represents energies plotted for grid 2, 3, 4 and 5 respectively.	157
5.17	Poincare plots of the magnetic field plotted for the simulation with $\eta = 10^{-7}$ at the mentioned time instants and grids.	159
5.18	SPI simulations to show effect of D_{\perp} with $\eta = 10^{-7}$ (a) physical time for which simulation is run (b) ablation rates (c) total impurities injected (d) radiation energy (e) plasma current I_p (f) plasma thermal energy.	160
5.19	SPI simulations to show effect of D_{\perp} with $\eta = 10^{-7}$ (a) magnetic energies (b) kinetic energies. Solid, dashed and dashed-dotted lines represents energies plotted for the simulations ($D_{\perp} = 10^{-5}, \Delta t = 5$), ($D_{\perp} = 2 \times 10^{-5}, \Delta t = 5$) and ($D_{\perp} = 2 \times 10^{-5}, \Delta t = 2$) respectively.	161
5.20	SPI simulations to show effect of D_{\perp} with $\eta = 10^{-7}$ (a) T (b) $j = -R j_{\phi}$ plotted at midplane vs R for ($D_{\perp} = 2 \times 10^{-5}, \Delta t = 2$).	161
5.21	SPI simulations to show effect of the numerical stabilization : (a) physical time for which simulation is run (b) ablation rates (c) total impurities injected (d) radiation energy (e) plasma current I_p (f) plasma thermal energy.	163
5.22	SPI simulations to show effect of the numerical stabilization (a) magnetic energies (b) kinetic energies. Solid and dashed represents energies plotted for the sim1 and sim2 respectively.	164
5.23	SPI simulations to show effect of the numerical stabilization. Poincaré plots shown for (a) sim1 at $t = 2.118$ ms and for (b) sim2 at $t = 2.088$ ms.	164
5.24	SPI simulation with $\eta = 10^{-8}$: (a) The ablation rates (b) total impurities injected (c) radiation energy (d) plasma current I_p (e) plasma thermal energy (f) T at the magnetic axis.	166
5.25	The temperature and current profiles plotted at midplane at the mentioned time instants for the SPI simulation with $\eta = 10^{-8}$: (a) T vs R (b) $j(= -R J_{\phi})$ vs R	167

5.26	Visualizations of SPI simulation with $\eta = 10^{-8}$. 1st, 2nd and 3rd columns show T [keV], n_{imp} [10^{20}] and ρ_{imp}/ρ while 1st, 2nd, 3rd and 4th row show snapshots at $t = 0.651, 1.207, 1.95$ and 2.381 ms respectively.	169
5.27	Visualizations of SPI simulation with $\eta = 10^{-8}$. 1st, 2nd and 3rd columns show $Z_{\text{eff}}, (\gamma - 1) \rho_{\text{imp}} E_{\text{ion}}$ and P_{rad} while 1st, 2nd, 3rd and 4th row show snapshots at $t = 0.651, 1.207, 1.95$ and 2.381 ms respectively.	170
5.28	Visualizations of SPI simulation with $\eta = 10^{-8}$. 1st, 2nd and 3rd columns show $A_3, \mathbf{B} \cdot \nabla T$ and $\mathbf{v} \cdot \nabla \rho_{\text{imp}}$ while 1st, 2nd, 3rd and 4th row show snapshots at $t = 0.651, 1.207, 1.95$ and 2.381 ms respectively.	171
5.29	SPI simulation with $\eta = 10^{-8}$: (a) magnetic energies (b) kinetic energies.	172
5.30	Poincaré plots of the magnetic field at mentioned time instants along with the projected position of SPI fragments shown by blue dots. . .	173
5.31	Two SPI configurations used each using different initial position and SPI velocity.	174
5.32	SPI simulations compared with two different injection set ups: (a) physical time for which simulations are run (b) ablation rates (c) total impurities injected (d) radiation energy (e) plasma current I_p (f) plasma thermal energy.	175
5.33	The comparison of the evolution of the energies with SPI simulations with two different injection set ups: (a) magnetic energies (b) kinetic energies. Solid and dashed represents energies plotted for the old and new SPI set up respectively.	176
5.34	Visualizations of SPI simulation with $\eta = 10^{-9}$ and different configuration. 1st, 2nd and 3rd columns show T [keV], n_{imp} [10^{20}] and ρ_{imp}/ρ while 1st, 2nd, 3rd and 4th row show snapshots at $t = 0.336, 0.93, 1.638$ and 1.762 ms respectively.	179
5.35	Visualizations of SPI simulation with $\eta = 10^{-9}$ and different configuration. 1st, 2nd and 3rd columns show $Z_{\text{eff}}, (\gamma - 1) \rho_{\text{imp}} E_{\text{ion}}$ and P_{rad} while 1st, 2nd, 3rd and 4th row show snapshots at $t = 0.336, 0.93, 1.638$ and 1.762 ms respectively.	180

5.36	Visualizations of SPI simulation with $\eta = 10^{-9}$ and different configuration. 1st, 2nd and 3rd columns show A_3 , $\mathbf{B} \cdot \nabla T$ and v_ϕ [km/s] while 1st, 2nd, 3rd and 4th row show snapshots at $t = 0.336, 0.93, 1.638$ and 1.762 ms respectively.	181
5.37	The temperature and current profiles plotted at midplane at the mentioned time instants for the SPI simulation with $\eta = 10^{-9}$ and a new SPI set up: (a) T vs R (b) $j(= -R J_\phi)$ vs R	182
5.38	Poincaré plots of the magnetic field for the simulation with a new SPI set up: (a) $t = 1.638$ ms and (b) at $t = 1.761$ ms.	182
6.1	Evolution of (a) ablation rates (b) total impurities injected (c) radiation energy (d) plasma thermal energy (e) plasma current I_p (f) temperature at the magnetic axis for the cases shown in Table (6.1).	187
6.2	Comparison of the evolution (a) magnetic energies (b) kinetic energies for SPI simulations with $\eta_0 = 10^{-6}$. Solid, dashed and dashed dotted lines denote ‘case 1.0’, ‘case 1.1’ and ‘case 2.1’ respectively.	188
6.3	Discontinuity detecting criterion k_{SC} plotted to show the local nature of the shock-capturing stabilization scheme. Top row shows the estimate of k_{SC} with $C = 1$ for ‘case 1.0’ while the bottom row shows the same for ‘case 1.1’.	189
6.4	Comparison of the evolution (a) magnetic energies (b) kinetic energies for SPI simulations with $\eta_0 = 10^{-6}$. Solid, dashed and dashed dotted lines denote ‘case 2.1’, ‘case 2.5’ and ‘case 2.10’ respectively.	190
6.5	Visualizations of SPI simulation with $\eta = 10^{-6}$ for ‘case 2.5’. 1st, 2nd and 3rd columns show T [keV], n_{imp} [10^{20}] and v_ϕ [km/s] at the mentioned time instants.	191
6.6	Profiles of temperature and current plotted at midplane at the mentioned time steps for SPI simulations with $\eta = 10^{-6}$ for ‘case 2.5’.	192
6.7	Poincaré plots of the magnetic field for the SPI simulation with constant resistivity specified by $\eta_0 = 10^{-6}$ for ‘case 2.5’. The color maps denote the plasma temperature (in keV) and solid black circles denote the projection of the position of SPI fragments in $\phi = 0$ plane.	193

6.8	SPI simulations to show effect of shock-capturing stabilization with temperature dependent resistivity specified by $\eta_0 = 10^{-8}$: (a) physical time for which simulation is run (b) ablation rates (c) total impurities injected (d) radiation energy (e) plasma thermal energy (f) plasma current I_p	194
6.9	Effect of shock-capturing stabilization on SPI simulation with temperature dependent resistivity specified by $\eta_0 = 10^{-8}$. For ‘case 1.0’ and ‘case 1.1’, comparison of the evolution of (a) magnetic and (b) kinetic energies. For ‘case 2.0’ and ‘case 2.1’, comparison of the evolution of (c) magnetic and (e) kinetic energies. Solid lines corresponds to $C = 0$ while dashed lines corresponds to $C = 1$	195
6.10	Visualizations of SPI simulation with $\eta = 10^{-8}$ for the ‘case 1.1’. 1st, 2nd and 3rd columns show T [keV], n_{imp} [10^{20}] and v_ϕ [km/s] at the mentioned time instants.	197
6.11	Visualizations of SPI simulation with $\eta = 10^{-8}$ for the ‘case 1.1’. 1st, 2nd and 3rd columns show A_3 , Z_{eff} and η (in normalized units) at the mentioned time instants.	198
6.12	SPI simulations with temperature dependent resistivity specified by $\eta_0 = 10^{-8}$: (a) Evolution of T at magnetic axis for ‘case 1.1’ and ‘case 2.1’. (b) temperature and (c) current profile plotted at midplane at the mentioned time instants for ‘case 1.1’.	199
6.13	Poicaré plots of the magnetic field for the SPI simulation with temperature dependent resistivity specified by $\eta_0 = 10^{-8}$ for ‘case 1.1’. The color maps denote the plasma temperature (in keV) and solid black circles denote the projection of the position of SPI fragments in $\phi = 0$ plane.	200

Chapter 1

Introduction

At present day, the major electricity production technologies use natural resources like fossil fuels and uranium. These resources are depleting and their constant burning is causing a threat of severe environmental risks. Nevertheless, the demand of energy is ever growing as humans are becoming more and more dependent on electricity for daily activities and comfort. With the current rate of energy consumption, the energy demand around the year 2100 is predicted to be about four times higher than its present level [65]. Therefore a sustainable, abundant and clean energy source is needed to meet the growing demand of energy. Fusion offers the prospect of an intrinsically safe, virtually inexhaustible and environmentally acceptable energy source [6]. Figure (1.1a) shows consumption, in percentage, of the different energy resources used in 2001 and figure (1.1b) shows carbon dioxide (CO₂) emissions per kW-hr from different energy sources. Fusion is one of the energy sources that has a low specific carbon dioxide emission.

1.1 Fusion and plasma confinement

1.1.1 Fusion energy

The sun is powered by fusion reactions and humankind is putting efforts to construct ‘artificial suns’ on Earth to harness fusion energy. Under certain conditions atoms or nuclei of lighter elements undergo a reaction in which constituent atoms or nuclei may fuse to become atoms or nuclei of a heavier element. In the process, some amount

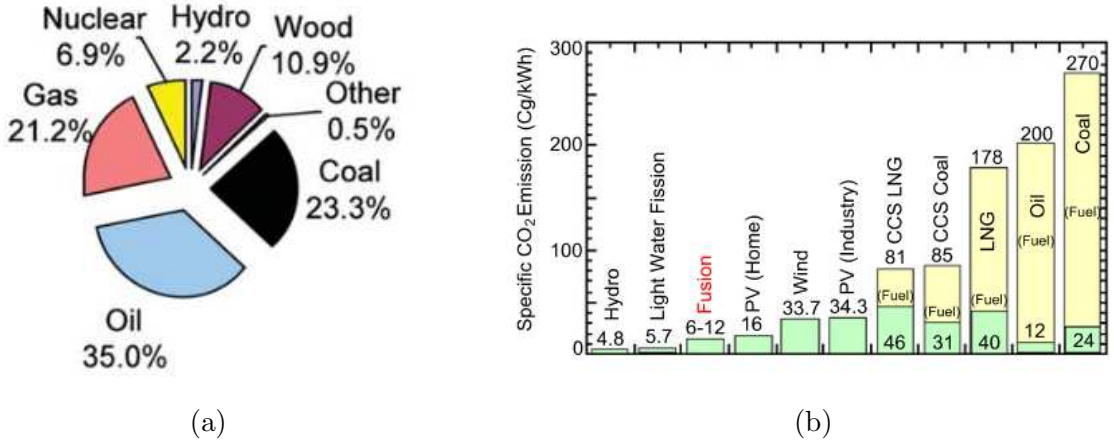


Figure 1.1: (a) Global energy consumption in the year 2001. The sector marked ‘other’ includes geothermal, solar, and wind energy [65]. (b) Specific carbon dioxide emissions (PV: photo voltaics; CCS: carbon capture and storage; LNG: liquefied natural gas) [58].

of mass is converted into pure energy which is quantified by Einstein’s famous mass-energy relation $E = mc^2$. This is the mechanism of fusion and energy liberated in fusion reaction is known as fusion energy. Fusion of hydrogen isotopes deuterium (D) and tritium (T) are of particular interest:



where n denotes a neutron and the amount of energy liberated in the reaction is 17.6 MeV.

For fusion to take place, particles (atoms or nuclei of fusion fuel) should have sufficient energy to overcome the repulsion barrier due to the electrostatic Coulomb forces (≈ 0.01 MeV). For particles to achieve such amount of energy a fusion fuel is heated to a very high temperature. The fusion reaction rate per unit volume can be written as [85]:

$$R = n_1 n_2 \langle \sigma v \rangle_{12}$$

where n_1 and n_2 are the particle densities of species 1 and 2, respectively, and $\langle \sigma v \rangle_{12}$ is the fusion reactivity of the two species. Figure (1.2) shows that the reactivity is higher for D2-T3 reaction than deuterium-deuterium (D2-D2) and deuterium-helium (D2-He³) reactions at a given temperature. This is why achieving the necessary conditions for D2-T3 reaction is the goal of present phase of fusion research [85]. The necessary conditions for fusion to take place include the temperature of the order 100 million degrees Celsius and the particle density of the order 10^{20} m^{-3} .

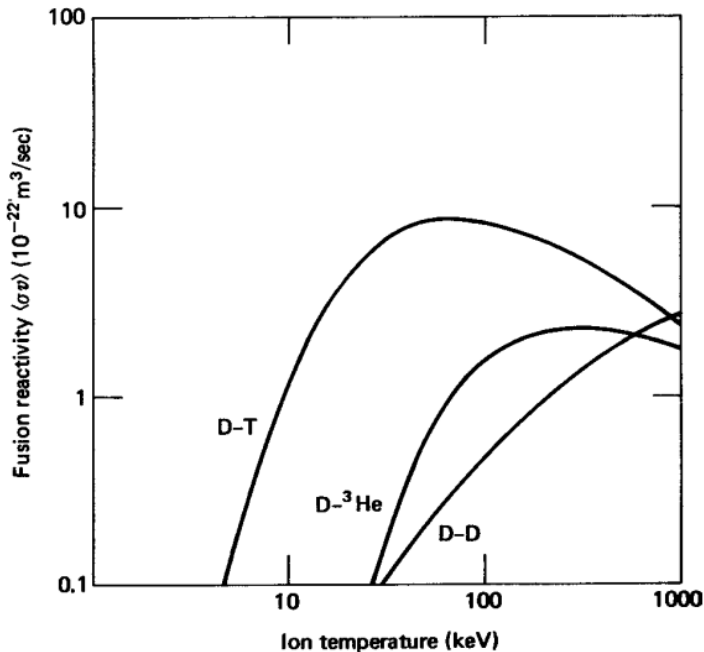


Figure 1.2: Fusion reactivity plotted vs ion temperature [85].

1.1.2 Plasma

At the temperatures of the order 100 million degrees Celsius, a gaseous fuel exists as a macroscopically neutral collection of ions, electrons and very few neutral particles known as plasma. A plasma contains sufficiently many charged particles which undergo long range Coulomb interactions. A collective behavior of a plasma is characterized by these long range interactions and the statistics of many particles in presence of the average electromagnetic field. The motion of charged particles in a plasma is influenced by electromagnetic fields, moreover moving charged particles produce their own electromagnetic fields altering the net field. This makes plasma dynamics highly non-linear and rich in physics. For more precise description of a plasma, the following requirements have to be satisfied [20, 37]

- 1) The time scales (\mathcal{T}) of plasma dynamics (Coulomb interactions) are sufficiently small with respect to collision times with neutrals (\mathcal{T}_n): $\mathcal{T} \ll \mathcal{T}_n$.
- 2) The length scale λ of plasma dynamics is much larger than the Debye length λ_D such that quasi neutrality holds: $\lambda \gg \lambda_D$. The Debye length is estimated by comparing the thermal energy of particles with their electrostatic energy.
- 3) There are many particles in a sphere with radius of Debye length: $N_D \gg 1$.

To harness fusion energy, a fusion reactor has to be built in which high temperature plasma can be confined in a limited volume. Therefore, understanding plasma physics is a key to harness fusion energy [58].

1.1.3 Plasma confinement

The *amplification factor* Q of a fusion reactor is defined as:

$$Q = \frac{\text{power obtained from fusion reactions}}{\text{power input to the reactor}}$$

The reactor is beneficial if $Q > 1$. In such case a reactor will use part of the power produced by itself so that the input power may progressively be diminished. However, to keep a reactor with $Q > 1$ in operation for a long time poses further challenges. The *confinement time* τ_E gives the rate at which energy is lost. It is written as

$$\tau_E = \frac{\text{energy content of the plasma}}{\text{power lost in the process}}$$

The *Lawson Criterion* gives the condition needed for a reactor such that the fusion reactions can provide enough energy to maintain the temperature of plasma against all power losses. This condition is $n \tau_E T > 3 \times 10^{21} \text{ m}^{-3} \text{ keV}$ where n is the particle density and T is the temperature of the plasma.

The Sun holds its dense hot plasma by a gravitational field for which the Lawson Criterion is well satisfied. For fusion reactors on the Earth two ways to confine plasma are *inertial confinement* and *magnetic confinement*. In an *inertial confinement*, D2-T3 gases at high densities are fired with a laser beam, however confinement times for such reactors are low. In a *magnetic confinement* D2-T3 gases are brought at high temperatures and a resulting plasma is confined using a strong magnetic field. In this work, we are interested in a magnetic confinement configuration used in tokamaks, a torus shaped fusion reactor.

1.2 Tokamaks and some terminologies

1.2.1 Tokamaks

The word tokamak is the Russian acronym of TOroidal'naya KAmera s MAgnitnymi Katushkami (toroidal chamber with magnetic coils). A tokamak is essentially a

toroidal chamber in which the plasma is confined by a magnetic field. Figure (1.3a) shows a schematic of a tokamak device and (1.3b) shows the toroidal and cylindrical coordinate systems in which physics relevant to tokamaks is described. The coordinate ϕ denotes the toroidal direction whereas the plane formed by R and Z (or θ) denotes the poloidal plane. Since the poloidal plane is perpendicular to the toroidal direction, any vector is often represented in terms of poloidal and toroidal parts. The combination of the toroidal magnetic field B_ϕ and poloidal magnetic field B_θ gives rise to ‘magnetic field lines’ with helical trajectories around a torus.

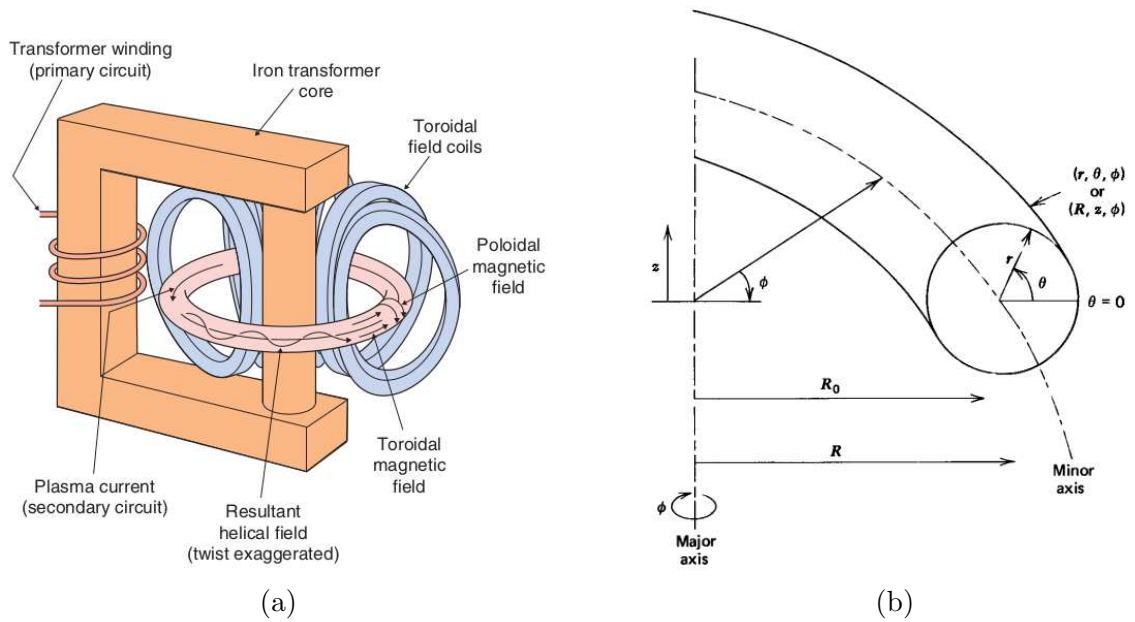


Figure 1.3: (a) A schematic view of a tokamak [65] (b) Toroidal (r, θ, ϕ) and cylindrical (R, Z, ϕ) coordinate systems. The geometric axis of a tokamak is identified by $R_0 = (R_{max} + R_{min})/2$ while the minor radius is identified by $a = (R_{max} - R_{min})/2$.

The amplitude of B_ϕ is given by Ampere’s theorem as:

$$B_\phi = \frac{\mu_0 I_t}{2\pi R}$$

where, I_t is the current running in the toroidal field coils and R is the radial coordinate of a device as shown in Figure (1.3b). Therefore, it can be seen that

$$B_\phi \propto \frac{1}{R}$$

Confinement is not possible with a purely toroidal field because the particles progressively drift vertically due to the $1/R$ variation of B_ϕ . Since ions and electrons are drifted in opposite directions, a vertical current is created and it carries the plasma

to the wall of a device. In order to have an equilibrium, it is necessary also to have a poloidal magnetic field [96], which is produced mainly by current in the plasma itself, flowing in the toroidal direction.

As mentioned before, the amplification factor Q should be more than 1 in order to gain net power from a tokamak device. After decades of tokamak experiments, now $Q \approx 1$ is achievable and it brings a good prospect for building and operating a high Q reactor. The goal of International Thermonuclear Experimental Reactor (ITER) is to achieve $Q = 10$. Figure (1.4a) shows a summary of the progress towards the goal of controlled fusion where triple product ($n\tau_E T$) achieved vs temperatures is shown for different tokamaks. Empirical scaling may be used to extrapolate the quantities of critical importance such as confinement time τ_E and performance of the future devices. Data from many tokamaks is analyzed using statistical methods to determine the dependence of τ_E on parameters like plasma current (I_p), major radius (R_0), particle density (n), inverse aspect ratio ($\epsilon = a/R_0$), heating power, toroidal magnetic field (B_ϕ) etc. The figure (1.4b) shows that this extrapolation predicts the confinement time for ITER as 3.7 to 6 seconds.

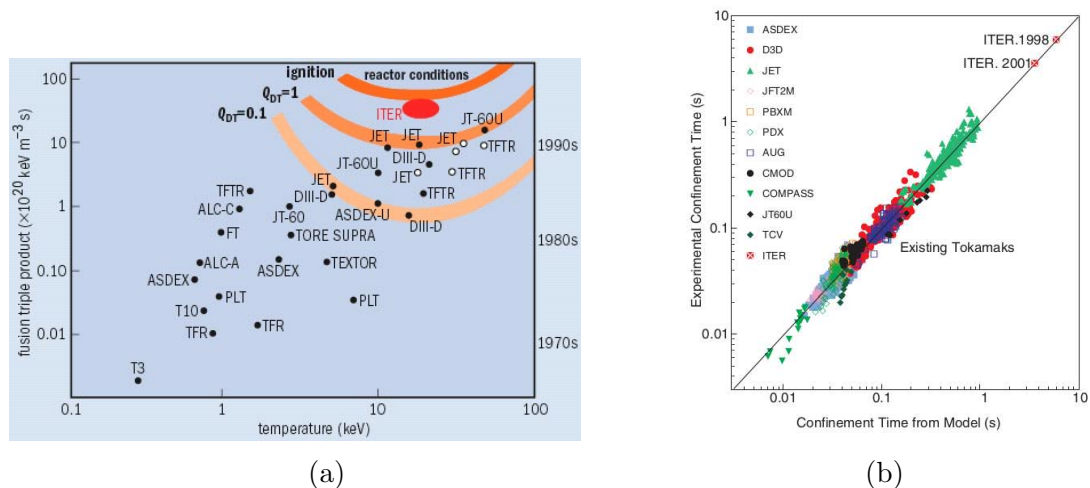


Figure 1.4: (a) Fusion triple product as a function of the core ion temperature for different tokamaks [80] (b) Experimental data from all the major tokamaks in the international fusion program showing how the confinement time scales with physical parameters [65].

Major steps to achieve commercial fusion power plants are sketched in Figure (1.5). Scientific feasibility of fusion reactors have been demonstrated by smaller tokamak devices so far like JET, TFTR and JT-60U. The objective of the ITER is to demonstrate the scientific and technical feasibility of fusion energy. In the next step,

a full-size prototype fusion power plant DEMO will show that fusion is commercially feasible. Apart from ITER, the biggest tokamak so far is JET with major radius $R_0 = 3$ m while ITER has $R_0 = 6$ m and DEMO is expected to have $R_0 = 9$ m.

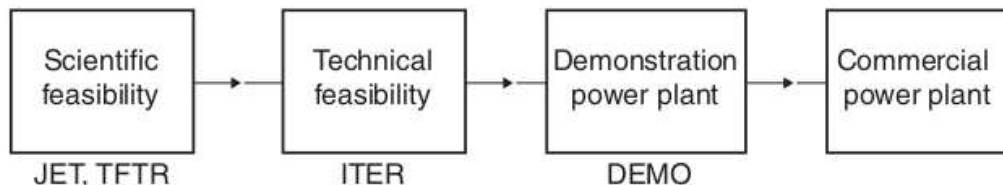


Figure 1.5: Outline of the development of the fusion power program [65].

1.2.2 Magnetic surfaces and some definitions

Tokamak plasma can be described by a single fluid model called magneto-hydrodynamics (MHD). The details of the MHD model and the relevant assumption are given in Chapter 2. In the case of ideal (dissipationless perfectly conducting) MHD, it can be shown that the particles in the plasma move along ‘magnetic field lines’, the condition often referred to as the ‘frozen flux’ constraint. This flux refers to the poloidal magnetic flux ψ_θ which, in axisymmetric cylindrical coordinates, is given by:

$$\psi_\theta = 2\pi \int_0^a \mathbf{B}_\theta \cdot \nabla\theta R dR$$

where, a is a radial (r) coordinate. Moreover, the topology of the magnetic field is conserved which means that the field lines may be distorted or compressed, but they may not reconnect with one another (reconnection is possible in resistive MHD). The magnetic field lines lie on the *magnetic surfaces* with constant ψ_θ and pressure. Such nested surfaces are depicted in the illustration (1.6) and ψ_θ may be used as radial coordinate.

One of the quantities of interest associated with the flux surfaces is *safety factor*. It describes the pitch angle of the magnetic field lines and determines whether, on a given flux surface, a magnetic field line will be closed or not. The safety factor q is related to the number of turns n in the toroidal direction required to make exactly m turns in the poloidal direction and is given by

$$q(\psi) = \frac{d\phi}{d\theta}$$

The surfaces with rational values of q , that means the surfaces on which the field lines are closed, are of particular importance for tokamak instabilities.

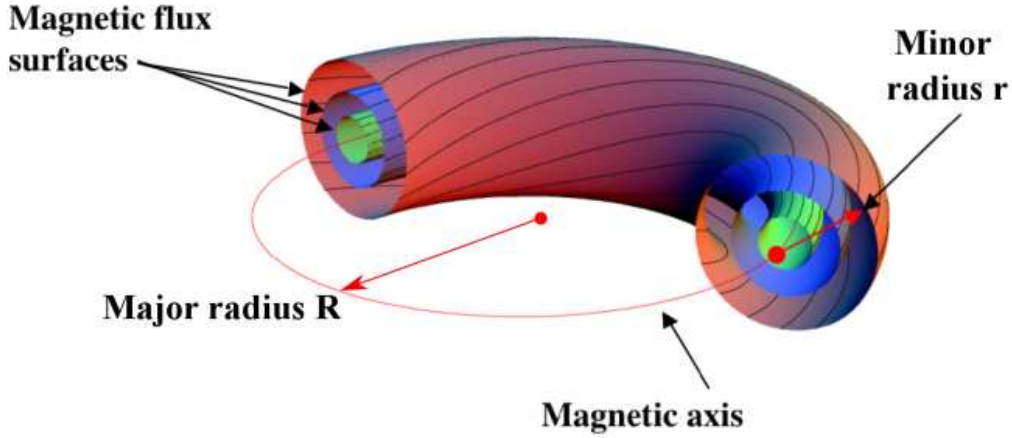


Figure 1.6: Nested magnetic flux surfaces with magnetic lines on them.

Another important quantity in plasma physics is the *plasma beta* β which gives the ratio of the thermal pressure over the magnetic pressure and is defined as

$$\beta = \frac{\int p dV}{B_0/2\mu_0}$$

where integration is evaluated over plasma volume, B_0 is the amplitude of the magnetic field at the magnetic axis and μ_0 is the permeability of free space.

1.2.3 Limiter and divertor configurations

In tokamak devices direct contact between a plasma and the wall of a device is avoided by means of either a material limiter or by a divertor which leads magnetic field lines away from the surface of a plasma to a dump plate more remote from a plasma [96]. In the ‘core’ region the flux surfaces are closed (Figure 1.7) and plasma is confined. The last closed flux surface forms a plasma boundary or a separatrix that separates regions of closed and open flux surfaces. These surfaces open onto plasma facing component (PFCs) and inner wall of a tokamak. The region with open flux surfaces is called Scrape-Off -Layer (SOL).

In the limiter configuration, plasma boundary is formed by a limiter, a material structure. The tokamak, Tore Supra in Cadarache, France is an example of limiter configuration. The divertor configuration is characterized by a presence of saddle points (X-points) in the plasma equilibrium. The flux surface that forms X-point is called separatrix. This configuration avoids direct interaction between the plasma core and PFCs. When plasma particles escape from the core region, they are transported

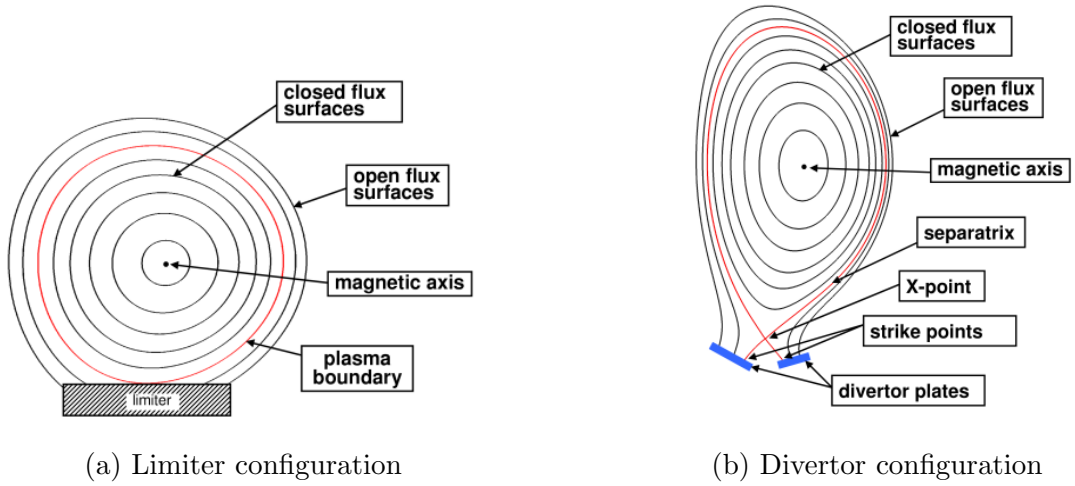


Figure 1.7: Tokamak configurations.

to the *divertor* via open field lines. The points where the separatrix meets the divertor are called the strike points. The poloidal magnetic field B_θ vanishes at the separatrix and the safety factor q diverges to infinity. Thus, in order to quantify q at the edge of the plasma, the $q_{95} = q(\psi_N = 0.95)$ is defined as the safety factor, where ψ_N is the poloidal flux normalized between ψ at the magnetic axis and ψ at the separatrix. The recent tokamaks have one or two X-points, for example, ITER in France will have one X-point while, DIII-D in USA has two X-points.

1.3 Disruptions and their mitigation

1.3.1 Disruptions

Plasma instabilities that arise in tokamaks are typically driven by parallel current or pressure gradients [96]. Current driven instabilities can lead to the growth of kink and tearing modes. If the pressure gradients are high near the separatrix, ballooning modes can develop and lead to repetitive crashes and loss of pressure. Such instabilities are called Edge-Localised Modes (ELMs) which can be related to transition from low to high modes. When a plasma is heated beyond certain threshold value, a transport barrier forms at the edge of a plasma causing the pressure gradients to rise. This transport barrier forms a pedestal region as shown in Figure (1.8). In this situation, the confinement time is improved and therefore the associated modes are called as High confinement modes (H-modes). Similarly the name L-mode is associated with

low confinement. Both situations are sketched in Figure (1.8).

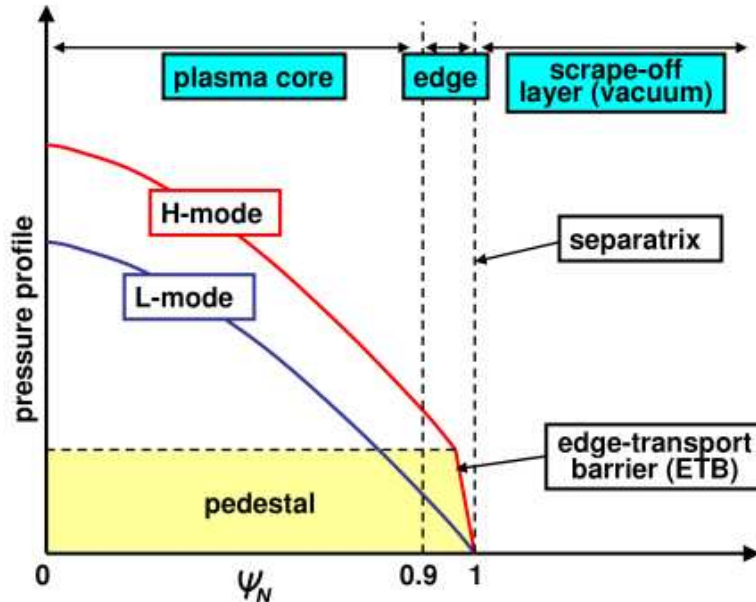


Figure 1.8: L-mode and H-mode confinement [77].

It is desirable that a plasma remains confined inside a vacuum space of a tokamak, however there are different kinds of disruptive events which affect global plasma confinement, for example sawtooth oscillations, ELMs etc. Major disruptions affect plasma confinement severely and lead to the termination of tokamak discharge. Disruptions are unavoidable and occur when certain limits on tokamak operating parameters (such as plasma current I_p , plasma beta β_N and particle density n) are exceeded, causing loss of a large fraction of the plasma energy [12, 45]. This results in dramatic fall of the temperature, plasma current I_p and the loss of confinement.

1.3.2 Sequence of events during major disruptions

An increase in the level of MHD activity is a sign of onset of a major disruption. Such disruptions are characterized by a well-defined sequence of events: thermal quench (TQ) and current quench (CQ) as sketched in Figure (1.9).

Thermal quench

After MHD activities reach a critical point, events occur on a much faster time scale typically of the order of 1 ms [65]. Plasma confinement deteriorates, temperatures

go down to sub-keV in less than 1 ms, and plasma losses several orders of magnitude of the thermal energy. This phase is called thermal quench (TQ) and is sketched in Figure (1.9). The thermal energy is transferred onto the PFC or lost by radiation, which can damage them. A spike in the plasma current (I_p) associated with TQ is observed in experiments. The dynamics of the TQ is complex and depends on plasma parameters and disruption causes.

Current quench

After the TQ phase follows the current quench (CQ) in which the plasma current (I_p) decays to zero rapidly as shown in Figure (1.9). Plasma resistivity has Spitzer like dependence upon the temperature: $\eta \propto T^{-3/2}$ [96, 47]. During TQ phase plasma cools down and as a consequence the resistivity of plasma increases. Plasma current cannot be supported by such resistivities and a rapid CQ occurs whose rates can be as high as 1000 MA/s [45]. Plasma loses its magnetic energy during CQ, part of which can be converted into thermal energy and dissipated as radiation or convected and conducted to the PFCs. Rapid decrease in the plasma current also induces currents in the tokamak structure which may lead to damaging $\mathbf{J} \times \mathbf{B}$ forces.

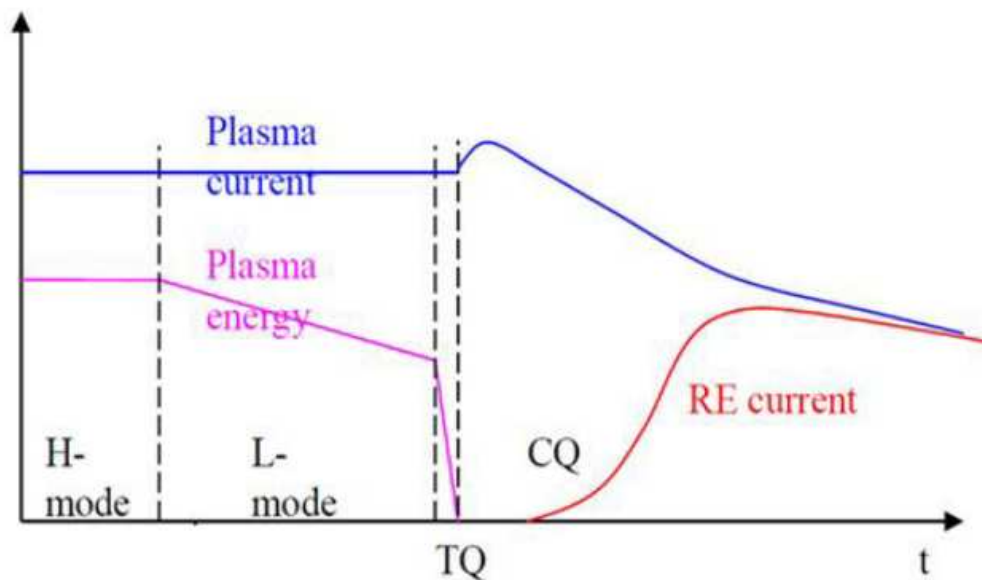


Figure 1.9: Phases of disruptions: the thermal quench (TQ) and current quench (CQ)

Another distinct phase of a disruption may be due to *runaway electrons*. The CQ can cause a large toroidal electric field which can accelerate electrons. These electrons can gain relativistic speeds and damage the tokamak walls.

It will be discussed later that a tokamak magnetic configuration can become unstable to helical perturbations of the form

$$w(r, t) = w(r) e^{i(\gamma t + m\theta - n\phi)}$$

where θ and ϕ are the poloidal and toroidal angles, whereas m and n are the corresponding poloidal and toroidal harmonics. The rapid and nonlinear growth of such instabilities gives rise to the rapid loss of thermal energy that starts the disruption sequence [45]. In the precursor growth phase that triggers the TQ, magnetic reconnection of plasma is possible under the nonlinear development of helical instabilities (non-linear tearing mode). The TQ occurs due to the growth of core modes such as internal kink mode $m/n = 1/1$, tearing modes $m/n = 2/1$ and $m/n = 3/1$. Their growth triggers the breaking of magnetic surfaces and a loss of confinement.

1.3.3 Disruptions control

As discussed above, disruptions can have damaging effects on the tokamak walls and structure. Large thermal loads occur during the TQ and large mechanical loads occur during the CQ on PFCs and the tokamak structures. Moreover, the severity of damage increases as the size of a device increases. Therefore, disruptions need to be avoided for smooth running of a reactor or at least they should be mitigated to reduce the damaging of the device and its components. The subject of disruption avoidance or mitigation is divided into three considerations [45]:

- Avoidance of the operating conditions that lead to disruption.
- Intervention to avoid disruptions either before disruption precursors occur or before onset of TQ
- Mitigation in which actions are taken after the disruption onset to reduce the severity or consequential effects of a disruption.

Disruption avoidance and/or mitigation is highly desirable for ITER design and its operational goals. The ITER Disruption Mitigation System (DMS) is designed to inject massive amounts of material into plasma to reduce heat loads by dissipating most of the thermal energy by radiation, to increase the plasma density to prevent the formation of runaway electron (RE) beams, and to control the duration of the CQ to reduce electromagnetic loads. The current design of the ITER DMS uses two kinds

of injection techniques: Massive Gas Injection (MGI) and Shattered Pellet Injection (SPI) as shown in the illustration (1.10a).

In MGI a massive amount (10-1000 times the initial plasma content) of neutral gas, usually Argon (Ar) or Neon (Ne), is injected at the plasma edge. The objective of MGI is to reduce heat loads by dissipating most of the plasma thermal energy by radiation. The ability of MGI to mitigate TQ and CQ loads has been demonstrated in tokamaks [45, 62]. The focus of the present work is mainly on the numerical simulations of SPI.

1.3.4 Shattered pellet injection

SPI involves frozen pellets of D₂ or Ne or Ar or their mixture in a specially designed cryogenic pipe gun. The technology of forming and firing such cryogenic pellets that are shattered before entering into a plasma has been developed at Oak Ridge National Laboratory for mitigating disruptions [22, 8]. DMS is designed such that the pellet will be injected into plasma at a given speed when a disruption is detected. These pellets are shattered in a curved tube before the frozen pellets enter plasma, as shown in Figure (1.10b). Shattering of pellets forms the fragments of pellet material consequently increasing the ablation surface of neutrals/impurities and avoids the damage of wall components from direct impact by a large solid pellet.

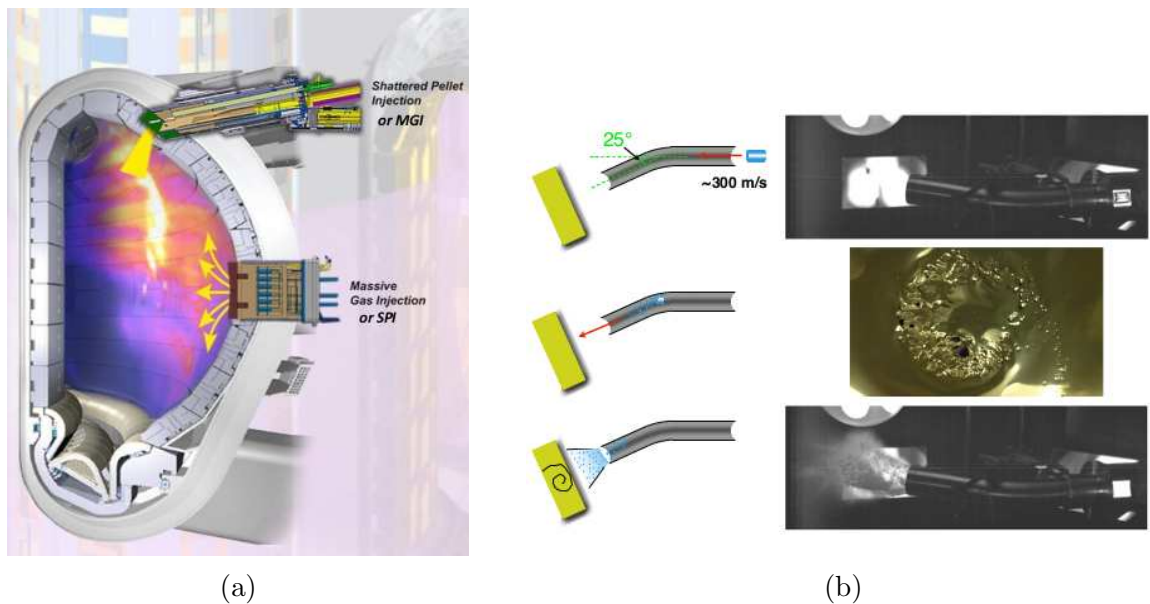


Figure 1.10: (a) Illustration for SPI and MGI set ups in ITER. (b) Simple breaker tube with single bend to shatter large pellets in DIII-D (figure from [28])

Basic physical process of plasma interaction with SPI fragments is as follows: The electrons in plasma collide with the injected fragments and heat them. Consequently, heated fragments begin to ablate neutral molecules forming dense clouds around the surface of fragments and shielding them from plasma. In the present work, the ablation of the fragments is modeled by the strongly shielded neutral gas shielding (NGS) model in a Maxwellian plasma [78, 33] meaning that the neutral gas cloud dissipates almost all the incoming heat flux before it reaches the pellet surface due to the smallness of the material's ablation energy [49]. For a given electron temperature T_e and density n_e , the ablation rate (in the number of ablated atoms per second) for a spherical deuterium fragment with radius r_p is given by

$$\partial_t N \propto n_e^{1/3} T_e^{5/3} r_p^{4/3}$$

This ablation rate will be used to model the source term for SPI in MHD equations. One consequence of the presence of impurities in plasma is radiation power loss. In the presence of impurities the bremsstrahlung radiation [96] is enhanced. It is a type of radiation that electrons emit when they are accelerated due to collisions. Also, there are losses due to 'line radiation' and 'recombination radiation' associated with atomic processes [96].

Using SPI, successful mitigation has been achieved in DIII-D and hence SPI has been selected as the baseline for ITER DMS. Since the plasma volume of ITER is ten times greater than that of JET, to achieve injection of sufficient quantity, multiple shattered pellets will be injected in ITER [2]. JET has been equipped with SPI in 2019 and will serve as an important demonstration and extrapolation tool for the future ITER SPI design.

Remark: Impurities

Plasma in tokamaks (assuming D plasma) can quickly be contaminated with other elements which are called as *impurities*. These impurities arise from the wall surfaces as plasma interacts with PFCs and can penetrate into the plasma core. Presence of impurities in the core can degrade the performance of a reactor. Experiments show evidence of the effects due to impurity transport [96]. SPI involves injection of impurities (inert gases) in the plasma for the purpose of mitigation of disruptions. Transport of such impurities in SPI, atomic processes involved and radiation losses are discussed in Chapter 2.

1.4 Numerical modeling

Numerical simulations can give insights into nonlinear physical phenomena and can play a complementary role to interpret experimental observations. To date, there exist many nonlinear MHD codes for tokamak modeling. The following few concern with magnetically confined tokamak and stellarator plasmas:

- BOUT++ [26] is a finite volume code that can handle unstructured grids.
- MEGA [89] is a linear as well as particle-MHD code developed to study interactions between energetic ions and MHD modes using finite difference methods.
- M3D-C1 [57] is a two fluid MHD code that uses high-order $C1$ finite elements and semi implicit time integration method.
- NIMROD [35] is a semi implicit MHD code that uses spectral finite elements in the poloidal plane and Fourier series for the toroidal direction.
- XTOR-2F [64] is a fully implicit two fluid MHD code that uses finite differences in radial coordinate and Fourier representation in poloidal and toroidal directions.
- JOREK [24, 47] is a fully implicit MHD code with extended physics that uses bicubic Bézier elements in the poloidal plane and Fourier series in the toroidal direction.

1.4.1 JOREK

The goal of this work is to implement a so called full MHD model with sources to simulate SPI using JOREK. The code uses the Bicubic Bézier finite element method in the poloidal plane, Fourier representation in the toroidal direction and a fully implicit time stepping algorithm. Simulations can be run in hybrid parallel computing framework coded using message passing interface (MPI) and OpenMP. It can be used to run versatile simulations for studying large-scale plasma instabilities and their control. Realistic geometries with divertor configurations can be handled and grids can be generated with curved elements with the isoparametric mapping so that grid elements can be made aligned to flux surfaces. The numerical methods used in JOREK, relevant for the present work, are described in Chapter 3.

Historically JOEREK uses reduced MHD models [40] for a wide range of applications like ELMs and their control, disruptions and their control and many other applications [47]. However, the full MHD model suitable for production level simulations is a recent addition in JOEREK. The first implementations of a full MHD model in JOEREK have been done in [44, 43] for simple geometries. The stabilization method based on variable multi scale decomposition have been implemented in [23]. It has been shown in [74] that the full MHD model is numerically robust and can be used for nonlinear simulations. The benchmark of the reduced and full MHD models is shown in [74] and is also presented in Chapter 4. It is shown that for certain types of instabilities such as the internal kink (in a high plasma β regime), it is necessary to use the full MHD model [74]. In addition to validation and benchmark of full MHD model, in this work we present SPI simulations taking into account impurity transport.

1.5 Organization of the manuscript

The manuscript is organized as follows:

Chapter 2 focuses on the governing equations for plasma physics and plasma interactions. A hierarchy of plasma physics models starting from kinetic equations are described and assumptions are outlined which are relevant for writing MHD equations. These equations are then written for tokamak modeling in the cylindrical coordinate system, normalized units and are referred to as full MHD model. The equation for the equilibrium for axisymmetric plasma, ‘Grad-Shafranov equation’, is derived and it is highlighted that the major task of the present work is to study evolution of the perturbed plasma equilibrium. The difference between full and reduced MHD model is emphasized. Finally MHD equations are written with source terms to model SPI. The process of SPI is described via atomic reactions taking place in a plasma and the physical significance of source and transport quantities is described.

Chapter 3 focuses on Galerkin finite element method (FEM) implemented in JOEREK. First, the governing equations are written as a system of partial differential equations (PDEs) and the motivation for the choice of FEM is described. Brief description of Galerkin FEM is given along with the stabilized FEM based on Variable Multi-Scale (VMS) and shock capturing approach. Then the construction of the finite dimensional space is described with the details of FEM used in the poloidal plane and Fourier representation used in the toroidal direction. Variable time step second

order backward difference (BDF2) method is derived and implemented. Grid generation is described in the context of Bézier formulation with main focus on the flux surface aligned grids. Finally, the issue of grid singularity is discussed and numerical treatment for polar grid center is proposed.

In Chapter 4, the details of the implementation of FEM on Grad-Shafranov equation along with few numerical equilibria are presented. This is followed by the details of FEM implementation on the full MHD equations. Then the numerical results for standard instability problems are presented which have been validated with the results obtained using the previously implemented reduced MHD model. Later, the advantage of using variable time step BDF2 method and numerical treatment for polar grid center is demonstrated. Finally, nonlinear simulations of the internal kink mode are discussed.

In Chapter 5, the numerical results for MMI obtained using single and two temperature models are presented. The numerical results for SPI obtained using single temperature full MHD model are discussed for the effect of the resistivity, grid, numerical stabilization and SPI configuration. The long run simulations showing pre-TQ phase and the characteristics of related physics are discussed.

In Chapter 6, the numerical results for SPI obtained with shock-capturing stabilization are presented. It is demonstrated that shock-capturing stabilization terms helps capture the TQ physics. The thesis is ended with the global conclusions and future perspectives.

Chapter 2

Physical models

A plasma consists of a set of charged and uncharged particles (atoms, molecules, ions and electrons) and exhibits a collective behavior due to the interactions among these particles. If a plasma is fully ionized then it contains only charged particles, i.e., ions (i) and electrons (e) and they interact via ‘Coulomb collisions’ [37]. If a plasma is partially ionized, in addition to charged particles, it contains neutral particles (atoms or molecules of same or different gases). Such plasma can occur naturally, for example: astrophysical plasma, or it can be produced in a laboratory, for example: by injecting neutral gases in a tokamak plasma. Many types of interactions are possible when a plasma contains charged as well as neutral particles. These particles can interact with each other via elastic collisions, Coulomb collisions and atomic reactions. These atomic reactions can be excitation, ionization, recombination and charge exchange.

- An excitation involves collision of an electron with an atom in which an electron transfers part of its energy to an atom.
- An ionization involves collision of an electron with a particle (atom or ion) in which an electron is removed from a particle, thereby changing the ionization level of a particle. The energy required to remove one electron so that the particle goes from ionization level z to $z + 1$ is denoted by E_z^{z+1} .
- In a recombination process, an ion can absorb an electron to change its charge state (ionization level).
- A charge exchange is possible between two colliding ions or ion-atom/molecule in which one ion transfers a charge to another.

Each of these atomic reactions are characterized by a reaction cross-section $\sigma(v)$ which defines the collision frequency for each process. This cross-section depends on the relative speed v of interacting particles and is usually averaged over a Maxwellian velocity distribution to give the reaction rate per time and volume units [66, 30]:

$$\Gamma_{z,z'} = n_z n_{z'} \langle \sigma(v) v \rangle$$

where n_z and $n_{z'}$ are the particle densities of two interacting species. The evolution of each species can be calculated from reaction rates for ionization $\Gamma_{z,z'}^{\text{ion}}$, recombination $\Gamma_{z,z'}^{\text{rec}}$ and charge exchange $\Gamma_{z,z'}^{\text{cx}}$.

A plasma also emits radiation that results in the loss of its energy. Main radiative processes are the bremsstrahlung and ‘line radiation’. The ‘bremsstrahlung radiation’ [96] is emitted when a charged particle is accelerated due to its Coulomb interaction with other particles. The ‘line radiation’ is emitted by ions and atoms when an electron is moving from one energy level to a lower one, as a result of de-excitation.

In summary, the charge state or ionization level of ions and neutral particles can change due to atomic reactions in a plasma. Ions, electrons and neutral particles in a plasma can be further subdivided into many species, where each species can be identified based on physical properties of its particles such as charge, mass, velocity etc. For example, a plasma in the core of a tokamak can have two species, D ions (i) and electrons (e). In certain situations, a plasma in tokamaks can have so called ‘runaway electrons’ [96]. In such a case plasma can be thought to have three species: ions, electron and fast moving electrons. When a neutral gas is injected in a tokamak plasma, atomic reactions can change the charge state of ions and neutrals. In this case, a plasma can contain electrons, neutral particles and many different species of ions each characterized by their charge, mass and velocities. Transfer of mass, momentum and energy is also possible among all these species, such that the total mass, momentum and energy is conserved.

Governing equations for a multi species plasma described above can be written on various levels: from kinetic to fluid modeling. In subsections below, kinetic and fluid equations are described. Multi species equations are sometimes referred to as multi fluid equations. A single fluid equations, which are also called as magneto-hydrodynamics (MHD) equations, are derived from multi species equations. Finally, MHD equations are described for tokamak modeling.

2.1 Physical models for plasma

2.1.1 Kinetic model

It is noted in Chapter 1 that the collective behavior of a plasma is affected by long as well as short range interactions and is a result of the statistics of many particles moving in the average electromagnetic field created by all other particles. In statistical description, the physical information of a plasma is expressed in terms of time-dependent distribution functions $f_\alpha(\mathbf{r}, \mathbf{u}, t)$ such that the total number of particles $N_\alpha = \int \int f_\alpha dr^3 du^3$ is assumed constant. The index α denotes the type of particles (or species) and the distribution functions represent the density of the representative points in six dimensional phase space formed by three space \mathbf{r} and three velocity \mathbf{u} coordinates. The governing equation for the evolution of f_α in the phase space is given by Boltzmann equation and is written as [11]

$$\frac{\partial f_\alpha}{\partial t} + \nabla \cdot (f_\alpha \mathbf{u}) + \nabla_u \cdot (f_\alpha \mathbf{a}) = C_\alpha \quad (2.1)$$

with

$$\mathbf{a} = \frac{q_\alpha}{m_\alpha} (\mathbf{E} + \mathbf{u} \times \mathbf{B})$$

where, q_α and m_α denotes the charge and mass of each particle of species α , respectively. C_α denotes the ‘collisions’ due to short-range inter-particle interactions. The vectors \mathbf{E} and \mathbf{B} denote electric and magnetic fields governed by Maxwell’s equations for electrodynamics [39]:

$$\text{Poisson's eq:} \quad \nabla \cdot \mathbf{E} = \frac{\tau}{\epsilon_0} \quad (2.2)$$

$$\text{Induction eq:} \quad \nabla \times \mathbf{E} = -\frac{\partial \mathbf{B}}{\partial t} \quad (2.3)$$

$$\text{Gauss Law:} \quad \nabla \cdot \mathbf{B} = 0 \quad (2.4)$$

$$\text{Ampère's law:} \quad \nabla \times \mathbf{B} = \mu_0 \mathbf{J} \quad (2.5)$$

The charge density τ and current density \mathbf{J} in the Maxwell’s equations are defined as:

$$\tau = \sum_{\alpha} q_{\alpha} n_{\alpha} \quad \text{and} \quad \mathbf{J} = \sum_{\alpha} q_{\alpha} n_{\alpha} \mathbf{v}_{\alpha}$$

where, the particle densities n_α and average particle velocities \mathbf{v}_α are the zeroth and first moments of the distribution functions f_α respectively:

$$n_\alpha(\mathbf{r}, t) = \int f_\alpha(\mathbf{r}, \mathbf{u}, t) d\mathbf{u} \quad (2.6)$$

$$\mathbf{v}_\alpha = \frac{1}{n_\alpha(\mathbf{r}, t)} \int \mathbf{u} f_\alpha(\mathbf{r}, \mathbf{u}, t) d\mathbf{u} \quad (2.7)$$

Poisson's equation (2.2) gives the relation between electric field \mathbf{E} produced by the charge density τ . The induction equation denotes Faraday's law of induction and means that changing magnetic field induces an electric field. The assumption is made in writing Faraday's law that the velocities under concern are non-relativistic [39]. Gauss law gives the divergence free condition that magnetic field \mathbf{B} satisfies. Finally, Ampère's law gives the relation between magnetic fields and moving charges, i.e. currents. The constants ϵ_0 and μ_0 are the permittivity and permeability of free space and their values in SI units are $8.85 \times 10^{-12} \text{ C}^2/\text{N m}^2$ and $4\pi \times 10^{-7} \text{ N/A}^2$ respectively. Another useful law in electrodynamics is the Lorentz force law [39]. It says that the net force \mathbf{F} acting on the charge q in the presence of both electric and magnetic fields is given by:

$$\mathbf{F} = q (\mathbf{E} + \mathbf{v} \times \mathbf{B})$$

The collision term in Equation (2.1) is decomposed into contributions due to collisions of particles of species α with particles of species β : $C_\alpha = \sum_\beta C_{\alpha,\beta}(f_\alpha, f_\beta)$. The explicit form of a collision term $C_{\alpha,\beta}$ may be given by 'Landau collision integral' [37]. However for the purpose of this study, few general properties of collision terms such as the conservation of mass, momentum and energy [37] are enough. In the process of collisions, conservation of mass holds and it implies that the total number of particles of each species α at a certain position is unchanged:

$$\int C_{\alpha,\beta} d\mathbf{u} = 0 \quad (2.8)$$

The conservation of momentum applied to collisions of the particles of the same and different species respectively implies:

$$\int m_\alpha \mathbf{u} C_{\alpha,\alpha} d\mathbf{u} = 0 \quad (2.9)$$

$$\int m_\alpha \mathbf{u} C_{\alpha,\beta} d\mathbf{u} + \int m_\beta \mathbf{u} C_{\beta,\alpha} d\mathbf{u} = 0 \quad (2.10)$$

The conservation of energy applied to collisions of the particles of the same and different species respectively implies:

$$\int \frac{1}{2} m_\alpha u^2 C_{\alpha,\alpha} d\mathbf{u} = 0 \quad (2.11)$$

$$\int \frac{1}{2} m_\alpha u^2 C_{\alpha,\beta} d\mathbf{u} + \int \frac{1}{2} m_\beta u^2 C_{\beta,\alpha} d\mathbf{u} = 0 \quad (2.12)$$

Boltzmann's equation (2.1) along with Maxwell's Equations (2.2-2.5) give a microscopic description of plasma and in principle can be solved for the distribution function $f_\alpha(\mathbf{r}, \mathbf{u}, t)$. In case of collisionless or weakly collisional plasmas, i.e., $C_\alpha = 0$, Boltzmann equations reduce to Vlasov equations:

$$\frac{\partial f_\alpha}{\partial t} + \nabla \cdot (f_\alpha \mathbf{u}) + \nabla_u \cdot (f_\alpha \mathbf{a}) = 0 \quad (2.13)$$

Equations (2.1) or (2.13) are difficult to analyze as they are written in six dimensional phase space with the time being the additional independent variable. Moreover, the length scales λ_D and time scales \mathcal{T} that govern the evolution of f_α are very small. The codes LIGKA [61], GYSELA [60] etc. are based on the kinetic modeling of magnetized plasma. In this work we focus on the macroscopic description of a plasma. A macroscopic description of plasma is obtained from a kinetic model by taking the moments of Boltzmann's or Vlasov equations to get fluid equations. In such a description, the dynamics occurs over the larger (hydrodynamic) length scales $\lambda_H \gg \lambda_D$ and time scales $\mathcal{T}_H \gg \mathcal{T}$.

2.1.2 Multi fluid model

For a generic function of velocity $g(\mathbf{u})$, the moments of Boltzmann equation can be written as:

$$\int \left[\frac{\partial f_\alpha}{\partial t} + \nabla \cdot (\mathbf{u} f_\alpha) + \nabla_u \cdot (\mathbf{a}_\alpha f_\alpha) \right] g(\mathbf{u}) d\mathbf{u} = \int \sum_\beta C_{\alpha,\beta} g(\mathbf{u}) d\mathbf{u} \quad (2.14)$$

By setting $g(\mathbf{u}) = 1$, one writes the zeroth moment of Boltzmann's equation:

$$\int \left[\frac{\partial f_\alpha}{\partial t} + \nabla \cdot (\mathbf{u} f_\alpha) + \nabla_u \cdot (\mathbf{a}_\alpha f_\alpha) \right] d\mathbf{u} = \int \sum_\beta C_{\alpha,\beta} d\mathbf{u}$$

Since, \mathbf{r} , \mathbf{u} and t are independent variables, integrals and derivatives can be commuted in order to simplify the equation.

$$\frac{\partial}{\partial t} \left(\int f_\alpha d\mathbf{u} \right) + \nabla \cdot \left(\int \mathbf{u} f_\alpha d\mathbf{u} \right) + \int \nabla_u \cdot (\mathbf{a}_\alpha f_\alpha) d\mathbf{u} = \sum_\beta \int C_{\alpha,\beta} d\mathbf{u}$$

Gauss theorem suggests that the third term on the left hand side will be zero, because $f_\alpha \rightarrow 0$ as $v \rightarrow \infty$ and the surface integral vanish in velocity space. Using definitions (2.6), (2.7) and relation (2.8), the above equation can be written as:

$$\frac{\partial n_\alpha}{\partial t} + \nabla \cdot (n_\alpha \mathbf{v}_\alpha) = 0 \quad (2.15)$$

This is the equation for the evolution of the particle density of a species α and it represents the conservation of mass. Now, the first moment is obtained by letting $g(\mathbf{u}) = \mathbf{u}$ in equation (2.14):

$$\int \mathbf{u} \left[\frac{\partial f_\alpha}{\partial t} + \nabla \cdot (\mathbf{u} f_\alpha) + \nabla_u \cdot (\mathbf{a}_\alpha f_\alpha) \right] d\mathbf{u} = \int \mathbf{u} \sum_\beta C_{\alpha,\beta} d\mathbf{u}$$

This equation is then multiplied by the mass of a particle m_α and further simplified using the definitions (2.6) and (2.7) to write:

$$\frac{\partial}{\partial t} (n_\alpha m_\alpha \mathbf{v}_\alpha) + m_\alpha \nabla \cdot \int (\mathbf{u} \otimes \mathbf{u} f_\alpha) d\mathbf{u} - n_\alpha q_\alpha (\mathbf{E} + \mathbf{v}_\alpha \times \mathbf{B}) = \mathbf{R}_\alpha \quad (2.16)$$

The first term is straightforward. The third term results from an integration by parts and the expression for \mathbf{a}_α is used. The term on the right hand side $\mathbf{R}_\alpha = m_\alpha \int \mathbf{u} \sum_\beta C_{\alpha,\beta} d\mathbf{u}$ is a friction coefficient which is the effect of collisions. The velocity from the tensor quantity in the second term is decomposed into the average \mathbf{v}_α and random part \mathbf{v}' part: $\mathbf{u} = \mathbf{v}_\alpha + \mathbf{v}'$ such that $d\mathbf{u} = d\mathbf{v}'$ and by definition $\int \mathbf{v}' f_\alpha d\mathbf{v}' = 0$. Now the tensor quantity from the second term can be expanded and the definition (2.7) is used to write:

$$\begin{aligned} \int (\mathbf{u} \otimes \mathbf{u} f_\alpha) d\mathbf{u} &= \int (\mathbf{v}_\alpha \otimes \mathbf{v}_\alpha + \mathbf{v}_\alpha \otimes \mathbf{v}' + \mathbf{v}' \otimes \mathbf{v}_\alpha + \mathbf{v}' \otimes \mathbf{v}') f_\alpha d\mathbf{v}' \\ &= \int (\mathbf{v}_\alpha \otimes \mathbf{v}_\alpha) f_\alpha d\mathbf{v}' + 0 + 0 + \int (\mathbf{v}' \otimes \mathbf{v}') f_\alpha d\mathbf{v}' \\ &= \int (n_\alpha \mathbf{v}_\alpha \otimes \mathbf{v}_\alpha) + \int (\mathbf{v}' \otimes \mathbf{v}') f_\alpha d\mathbf{v}' \end{aligned}$$

The random part of velocity \mathbf{v}' gives rise to a quantity measuring the mean kinetic energy of the particles, which is the temperature (T_α):

$$T_\alpha = m_\alpha \frac{\langle v'^2 \rangle}{3k}$$

and the stress tensor $\underline{\mathbf{P}}_\alpha$ is given by:

$$\underline{\mathbf{P}}_\alpha = - \int (m_\alpha f_\alpha \mathbf{v}' \otimes \mathbf{v}') d\mathbf{v}'$$

where, k is Boltzmann's constant. The stress tensor is further decomposed into isotropic and anisotropic parts: $\underline{\mathbf{P}}_\alpha = -p_\alpha \mathbb{I} + \underline{\boldsymbol{\pi}}_\alpha$. For an isotropic function f_α , the stress tensor becomes a diagonal tensor with identical terms on the diagonal, each being pressure:

$$p_\alpha = \int m_\alpha \frac{v'^2}{3} f_\alpha d\mathbf{v}'$$

The relation between the pressure and temperature is then written as $p_\alpha = k n_\alpha T_\alpha$. The term $\underline{\boldsymbol{\pi}}_\alpha$ denotes the viscous tensor. Substituting the definition of the stress tensor $\underline{\mathbf{P}}_\alpha$ into the second term of equation (2.16), the equation for the momentum of the particles of species α is obtained as:

$$\begin{aligned} \frac{\partial}{\partial t} (n_\alpha m_\alpha \mathbf{v}_\alpha) + \nabla \cdot (n_\alpha m_\alpha \mathbf{v}_\alpha \otimes \mathbf{v}_\alpha) + \nabla p_\alpha - n_\alpha q_\alpha (\mathbf{E} + \mathbf{v}_\alpha \times \mathbf{B}) \\ = \nabla \cdot \underline{\boldsymbol{\pi}}_\alpha + \mathbf{R}_\alpha \end{aligned} \quad (2.17)$$

The equation of the particle density (2.15) can be removed from the above equation, to write the equation in terms of the velocity \mathbf{v}_α as:

$$n_\alpha m_\alpha \frac{\partial \mathbf{v}_\alpha}{\partial t} + n_\alpha m_\alpha \mathbf{v}_\alpha \cdot \nabla \mathbf{v}_\alpha + \nabla p_\alpha - n_\alpha q_\alpha (\mathbf{E} + \mathbf{v}_\alpha \times \mathbf{B}) = \nabla \cdot \underline{\boldsymbol{\pi}}_\alpha + \mathbf{R}_\alpha \quad (2.18)$$

The second moment is obtained by taking $g(\mathbf{u}) = \frac{m_\alpha}{2} u^2$ in equation (2.14):

$$\int \frac{m_\alpha}{2} u^2 \left[\frac{\partial f_\alpha}{\partial t} + \nabla \cdot (\mathbf{u} f_\alpha) + \nabla_u \cdot (\mathbf{a}_\alpha f_\alpha) \right] d\mathbf{u} = \int \frac{m_\alpha}{2} u^2 \sum_\beta C_{\alpha,\beta} d\mathbf{u}$$

It can be treated in a similar way to first moment and steps for its simplification can be found in [37, 32, 11]. The simplification of second moment gives the equation of the total energy \mathcal{E}_α which is written as:

$$\frac{\partial \mathcal{E}_\alpha}{\partial t} + \nabla \cdot [(\mathcal{E}_\alpha + p_\alpha) \mathbf{v}_\alpha] - q_\alpha n_\alpha \mathbf{v}_\alpha \cdot \mathbf{E} = \nabla \cdot (\underline{\boldsymbol{\pi}}_\alpha \cdot \mathbf{v}_\alpha) + \nabla \cdot \mathbf{h}_\alpha + \mathbf{v}_\alpha \cdot \mathbf{R}_\alpha + Q_\alpha \quad (2.19)$$

with,

$$\mathcal{E}_\alpha = \frac{n_\alpha m_\alpha v_\alpha^2}{2} + \frac{1}{\gamma_\alpha - 1} p_\alpha$$

where, γ_α is the ratio of specific heats of a species α . The quantity $\mathbf{h}_\alpha = \int \frac{1}{2} n_\alpha m_\alpha v'^2 \mathbf{v}' d\mathbf{u}$ denotes heat flow due to fluctuating motion of the particles of species α and the last two terms come from the collision term, where \mathbf{R}_α denotes the momentum transfer and $Q_\alpha = \int \frac{1}{2} C_{\alpha,\beta} m_\alpha v_\alpha^2 d\mathbf{u}$ denotes the heat transfer. The equation for the total

energy can be simplified using the particle density equation (2.15) and momentum equation (2.17) to obtain the equation for the temperature evolution as:

$$\frac{kn_\alpha}{\gamma_\alpha - 1} \left(\frac{\partial T_\alpha}{\partial t} + \mathbf{v}_\alpha \cdot \nabla T_\alpha \right) + kn_\alpha T_\alpha \nabla \cdot \mathbf{v}_\alpha = \underline{\boldsymbol{\pi}}_\alpha : \nabla \mathbf{v}_\alpha + \nabla \cdot \mathbf{h}_\alpha + Q_\alpha \quad (2.20)$$

By defining the partial mass densities as $\rho_\alpha = n_\alpha m_\alpha$ and including source terms, the multi fluid equations are written as a system of the equations for mass, momentum and total energy as:

$$\begin{aligned} \frac{\partial \rho_\alpha}{\partial t} + \nabla \cdot (\rho_\alpha \mathbf{v}_\alpha) &= \dot{\rho}_\alpha \\ \frac{\partial}{\partial t} (\rho_\alpha \mathbf{v}_\alpha) + \nabla \cdot (\rho_\alpha \mathbf{v}_\alpha \otimes \mathbf{v}_\alpha) + \nabla p_\alpha - n_\alpha q_\alpha (\mathbf{E} + \mathbf{v}_\alpha \times \mathbf{B}) &= \nabla \cdot \underline{\boldsymbol{\pi}}_\alpha + \mathbf{R}_\alpha + \dot{\mathbf{m}}_\alpha \\ \frac{\partial \mathcal{E}_\alpha}{\partial t} + \nabla \cdot [(\mathcal{E}_\alpha + p_\alpha) \mathbf{v}_\alpha] &= \nabla \cdot (\underline{\boldsymbol{\pi}}_\alpha \cdot \mathbf{v}_\alpha) + \nabla \cdot \mathbf{h}_\alpha + \left(\frac{q_\alpha \rho_\alpha}{m_\alpha} \mathbf{E} + \mathbf{R}_\alpha \right) \cdot \mathbf{v}_\alpha + Q_\alpha + \dot{\mathcal{E}}_\alpha \end{aligned} \quad (2.21)$$

along with Maxwell's equations (2.2)-(2.5) to describe electromagnetic fields. The terms $\dot{\rho}_\alpha$, $\dot{\mathbf{m}}_\alpha$ and $\dot{\mathcal{E}}_\alpha$ denote the sources for the densities, momenta and energies respectively. Atomic reactions through which particles can be added or removed from the species (described at the beginning of this section) can be modeled using these sources. The equation of the total energy can be written in terms of the temperature evolution equation (2.20).

The diffusive and dissipative terms $\underline{\boldsymbol{\pi}}_\alpha$, \mathbf{R}_α , \mathbf{h}_α and Q_α have not been yet specified in terms of macroscopic variables. Doing so, in order to bring closure to fluid system, is a vast topic of 'transport theory' and has many approaches [37]. They are described later for the single fluid equations.

2.1.3 Two fluid model

The multi fluid model can be used to write the equations for a plasma consisting of two species ($\alpha = e, i$): electrons with the charge $q_e = -e$ and ions with the charge $q_i = Ze$, where Z is the ion charge number. From the momentum conservation of collision terms (2.10) it can be deduced that $\mathbf{R}_e = -\mathbf{R}_i$ and energy conservation of the collision terms (2.12) implies that $Q_e = -(\mathbf{v}_e - \mathbf{v}_i) \cdot \mathbf{R}_e - Q_i$. Using these relations and ignoring source terms in (2.21), the two-fluid model for electron-ion plasma can

be written as a system of equations of the mass, momentum and temperature as:

$$\frac{\partial \rho_e}{\partial t} + \nabla \cdot (\rho_e \mathbf{v}_e) = 0 \quad (2.22)$$

$$\frac{\partial \rho_i}{\partial t} + \nabla \cdot (\rho_i \mathbf{v}_i) = 0 \quad (2.23)$$

$$\frac{\partial}{\partial t}(\rho_e \mathbf{v}_e) + \nabla \cdot (\rho_e \mathbf{v}_e \otimes \mathbf{v}_e) + \nabla p_e + en_e(\mathbf{E} + \mathbf{v}_e \times \mathbf{B}) = \nabla \cdot \underline{\boldsymbol{\pi}}_e + \mathbf{R}_e \quad (2.24)$$

$$\frac{\partial}{\partial t}(\rho_i \mathbf{v}_i) + \nabla \cdot (\rho_i \mathbf{v}_i \otimes \mathbf{v}_i) + \nabla p_i - Zen_i(\mathbf{E} + \mathbf{v}_i \times \mathbf{B}) = \nabla \cdot \underline{\boldsymbol{\pi}}_i - \mathbf{R}_e \quad (2.25)$$

$$\frac{kn_e}{\gamma_e - 1} \left(\frac{\partial T_e}{\partial t} + \mathbf{v}_e \cdot \nabla T_e \right) + kn_e T_e \nabla \cdot \mathbf{v}_e = \underline{\boldsymbol{\pi}}_e : \nabla \mathbf{v}_e + \nabla \cdot \mathbf{h}_e - (\mathbf{v}_e - \mathbf{v}_i) \cdot \mathbf{R}_e - Q_i \quad (2.26)$$

$$\frac{kn_i}{\gamma_i - 1} \left(\frac{\partial T_i}{\partial t} + \mathbf{v}_i \cdot \nabla T_i \right) + kn_i T_i \nabla \cdot \mathbf{v}_i = \underline{\boldsymbol{\pi}}_i : \nabla \mathbf{v}_i + \nabla \cdot \mathbf{h}_i + Q_i \quad (2.27)$$

along with Maxwell's equations (2.2)-(2.5). The pressure due to electrons and ions is given as $p_e = n_e k T_e$ and $p_i = n_i k T_i$ respectively. The charge density is given by $\tau = -e(n_e - Zn_i)$ while the current density is given by $\mathbf{J} = -e(n_e \mathbf{v}_e - Zn_i \mathbf{v}_i)$.

2.1.4 Single fluid model

The single fluid equations or MHD equations can be derived from the two-fluid equations by taking linear combinations of equations of the mass, momentum and total energy or pressure of each species. Recalling that charges of electrons and ions are $-e$ and Ze respectively, some useful definitions to obtain single fluid variables are:

$$\rho \equiv \rho_e + \rho_i = n_e m_e + n_i m_i$$

$$\rho \mathbf{v} \equiv n_e m_e \mathbf{v}_e + n_i m_i \mathbf{v}_i$$

$$p \equiv p_e + p_i = n_e k T + n_i k T$$

$$\tau \equiv q_e n_e + q_i n_i = -e(n_e - Zn_i)$$

$$\mathbf{J} \equiv q_e n_e \mathbf{u}_e + q_i n_i \mathbf{u}_i = -e(n_e \mathbf{v}_e - Zn_i \mathbf{v}_i)$$

where, ρ is the total density, \mathbf{v} is center of mass or average velocity and p is the total pressure of a plasma. In general, the derivation of single fluid equations is a huge task and depending upon assumptions made a hierarchy of single fluid equations can be obtained. The systematic derivation at each assumption level can be found in [37]. Here, we only note the assumptions that are relevant to tokamak plasmas and describe the final model of interest. These assumptions are as follows:

- Plasma maintains quasi-neutrality, i.e., $|n_e - Zn_i| \ll n_e$. This assumption holds upto high degree in plasmas on account of the property of plasma that any charge imbalance is neutralized almost instantaneously [37].
- The mass of electron is much smaller than the mass of ions, i.e., $m_e \ll m_i$.
- The relative velocity of ions and electrons is small as compare to the center of mass velocity:

$$|\mathbf{v}_i - \mathbf{v}_e| \ll |\mathbf{v}|$$

- The velocities of plasma dynamics under concern are non-relativistic, i.e., $|\mathbf{v}| \ll c$, where c is the speed of light.
- The temperature equilibration time \mathcal{T}_{eq} is significantly smaller than other characteristic times, i.e. $\mathcal{T}_{\text{eq}} \ll \mathcal{T}_H$ and hence $T_e = T_i$. This assumption makes a considerable simplification to the single fluid model, without which one would get a single fluid but two temperature MHD model.

The equation for total density is obtained by adding the equation for electron density (2.22) and ion density (2.23) and then using the definitions for density ρ and center of mass velocity \mathbf{v} :

$$\frac{\partial \rho}{\partial t} + \nabla \cdot (\rho \mathbf{v}) = 0$$

The equation for the total momentum is obtained by adding momentum equation for electrons (2.24) and ions (2.25) to get:

$$\frac{\partial}{\partial t}(\rho \mathbf{v}) + \nabla \cdot (\rho \mathbf{v} \otimes \mathbf{v}) + \nabla p - \mathbf{J} \times \mathbf{B} = \nabla \cdot \underline{\boldsymbol{\pi}}$$

where the definition of the center of mass or average velocity is used in the first term, the definition of the total pressure is used in the third term while the definition of the total current is used in the fourth term on the left hand side. The second term is obtained by the decomposition of particle velocity into mean and random parts: $\mathbf{v}_\alpha = \mathbf{v} - \mathbf{v}'_\alpha$. The additional terms coming from this decomposition are used in the definition of viscous tensor on the right hand side as: $\underline{\boldsymbol{\pi}} = \sum_\alpha \underline{\boldsymbol{\pi}}_\alpha + \sum_\alpha \rho_\alpha \mathbf{v}'_\alpha \otimes \mathbf{v}'_\alpha$. Finally, adding the equations of the electron temperature (2.26) and ion temperature (2.27) gives evolution of the total pressure as:

$$\frac{\partial p}{\partial t} + \mathbf{v} \cdot \nabla p + \gamma p \nabla \cdot \mathbf{v} = (\gamma - 1) \left((\underline{\boldsymbol{\pi}}_e : \nabla \mathbf{v}_e + \underline{\boldsymbol{\pi}}_i : \nabla \mathbf{v}_i) + \nabla \cdot (\mathbf{h}_e + \mathbf{h}_i) + \eta \mathbf{J} \cdot \mathbf{J} \right)$$

The assumption $T_i = T_e$ is used to derive the above equation. The last term in the equation of pressure denotes Ohmic heating and it arises from the ion-electron transfer term \mathbf{R}_e which can be written as [37]:

$$\mathbf{R}_e = \eta \frac{1}{1 + \mu} \frac{Ze}{m_i} \rho \mathbf{J}$$

where, μ is the ratio of masses over charges, η is the resistivity of a plasma. The viscosity ($\underline{\boldsymbol{\pi}}_{e,i}$) and heat conduction ($\mathbf{h}_{e,i}$) terms have not been represented in terms of macroscopic variables yet. Neglecting viscosities $\underline{\boldsymbol{\pi}}_{e,i} \rightarrow 0$ and heat conduction terms $\mathbf{h}_{e,i} \rightarrow 0$ gives a resistive MHD modeling. Collecting the equations for density, velocity (or momentum), pressure along with Maxwell's laws forms the MHD model for plasma which is written as:

$$\begin{aligned} \frac{\partial \rho}{\partial t} + \nabla \cdot (\rho \mathbf{v}) &= 0 \\ \rho \frac{\partial \mathbf{v}}{\partial t} + \rho \mathbf{v} \cdot \nabla \mathbf{v} + \nabla p - \mathbf{J} \times \mathbf{B} &= 0 \\ \frac{\partial p}{\partial t} + \mathbf{v} \cdot \nabla p + \gamma p \nabla \cdot \mathbf{v} &= (\gamma - 1)(\eta \mathbf{J} \cdot \mathbf{J}) \\ \frac{\partial \mathbf{B}}{\partial t} + \nabla \times \mathbf{E} &= 0 \\ \nabla \cdot \mathbf{B} &= 0 \\ \mathbf{E} + \mathbf{v} \times \mathbf{B} &= \eta \mathbf{J} \\ \mu_0 \mathbf{J} &= \nabla \times \mathbf{B} \end{aligned}$$

where the sixth equation is the Ohm's law $\mathbf{E} + \mathbf{v} \times \mathbf{B} = \eta \mathbf{J}$ and the last equation gives the definition of current $\mu_0 \mathbf{J} = \nabla \times \mathbf{B}$. The Ohm's law can be used in induction equation to write the system of resistive full MHD equations as:

$$\begin{aligned} \frac{\partial \rho}{\partial t} + \nabla \cdot (\rho \mathbf{v}) &= 0 \\ \rho \frac{\partial \mathbf{v}}{\partial t} + \rho \mathbf{v} \cdot \nabla \mathbf{v} + \nabla p - \mathbf{J} \times \mathbf{B} &= 0 \\ \frac{\partial p}{\partial t} + \mathbf{v} \cdot \nabla p + \gamma p \nabla \cdot \mathbf{v} &= (\gamma - 1)(\eta \mathbf{J} \cdot \mathbf{J}) \\ \frac{\partial \mathbf{B}}{\partial t} - \nabla \times \mathbf{v} \times \mathbf{B} &= -\eta \nabla \times \mathbf{J} \end{aligned} \tag{2.28}$$

along with Gauss's law $\nabla \cdot \mathbf{B} = 0$ and Ampère's law $\mu_0 \mathbf{J} = \nabla \times \mathbf{B}$. With $\eta = 0$, one recovers the system of ideal MHD equations:

$$\begin{aligned}
\frac{\partial \rho}{\partial t} + \nabla \cdot (\rho \mathbf{v}) &= 0 \\
\rho \frac{\partial \mathbf{v}}{\partial t} + \rho \mathbf{v} \cdot \nabla \mathbf{v} + \nabla p - \mathbf{J} \times \mathbf{B} &= 0 \\
\frac{\partial p}{\partial t} + \mathbf{v} \cdot \nabla p + \gamma p \nabla \cdot \mathbf{v} &= 0 \\
\frac{\partial \mathbf{B}}{\partial t} - \nabla \times (\mathbf{v} \times \mathbf{B}) &= 0
\end{aligned} \tag{2.29}$$

The above equations can be normalized with respect to μ_0 such that μ_0 can be dropped from MHD equations without altering their form. Normalization of MHD equations is described in detail later. The ideal MHD equations (2.29) can be written in the conservative form:

$$\partial_t \mathbf{y} + \nabla \cdot \underline{\mathbf{f}}(\mathbf{y}) = 0$$

where, the conserved variables $\mathbf{y} = \{\rho, \rho \mathbf{v}, \mathcal{E}_T, \mathbf{B}\}^T$ represent the vector containing the density ρ , momentum $\rho \mathbf{v}$, total energy \mathcal{E} and magnetic field \mathbf{B} . The total energy is given by:

$$\mathcal{E}_T = \frac{\rho}{\gamma - 1} + \frac{1}{2} \rho \mathbf{v} \cdot \mathbf{v} + \frac{1}{2} \mathbf{B} \cdot \mathbf{B}$$

In order to find the characteristic wave speeds of the ideal MHD system, it can be written in quasi-linear form:

$$\partial_t \tilde{\mathbf{y}} + \underline{\mathbf{A}}_i(\tilde{\mathbf{y}}) \partial_{x_i} \tilde{\mathbf{y}} = 0$$

for the vector of variables $\tilde{\mathbf{y}} = \{\rho, \mathbf{v}, p, \mathbf{B}\}^T$. For any dimension $d \in \{1, 2, 3\}$, the row for B_d equation will be zero for the matrix $\underline{\mathbf{A}}_i(\tilde{\mathbf{y}})$ as the equation for B_d becomes $\partial_t B_d = 0$. Therefore, the respective row and column can be removed from $\underline{\mathbf{A}}_i(\tilde{\mathbf{y}})$ to get a matrix of rank 7. This matrix can be diagonalized with seven eigenvalues corresponding to one entropy wave, two Alfvén waves and four magneto-acoustic (two slow and two fast) waves traveling with speeds [81]:

$$\lambda_4 = v_1, \quad \lambda_{2,6} = v_1 \mp c_a, \quad \lambda_{3,5} = v_1 \mp c_s, \quad \lambda_{1,7} = v_1 \mp c_f$$

respectively, where,

$$c_a = \frac{|B_1|}{\sqrt{\rho}}, \quad c_{s,f}^2 = \frac{1}{2} \left(\frac{\gamma p + \mathbf{B} \cdot \mathbf{B}}{\rho} \pm \sqrt{\left(\frac{\gamma p + \mathbf{B} \cdot \mathbf{B}}{\rho} \right)^2 - \frac{4\gamma p B_1^2}{\rho^2}} \right)$$

Since all eigenvalues are real, the system of ideal MHD equations is a hyperbolic one with the wave speed ordering:

$$\lambda_1 \leq \lambda_2 \leq \lambda_3 \leq \lambda_4 \leq \lambda_5 \leq \lambda_6 \leq \lambda_7$$

These inequalities reveal that some eigenvalues may coincide and therefore the conservative system of ideal MHD equations is not strictly hyperbolic. The computation of the complete set of eigenvectors is not straightforward (see, for example, [17], [5]).

2.2 Tokamak modeling

2.2.1 Co-ordinate system

The physical equations written so far are in coordinate free vector notations. From the application to tokamak point of view, the cylindrical (or toroidal) coordinate system is used. The base cylindrical coordinate system (R, Z, ϕ) , shown in Figure (2.1), is given by $x = R \cos \phi$, $y = -R \sin \phi$ and $z = Z$, where (x, y, z) denotes Cartesian coordinates. Thus, ϕ is oriented clockwise if viewed from the top. According to the definitions in [82], this convention correspond to a COCOS number of 8. The orthonormal basis vectors for this cylindrical coordinate system are denoted by $\mathbf{e}_R = \nabla R$, $\mathbf{e}_Z = \nabla Z$ and $\mathbf{e}_\phi = R \nabla \phi$. Some useful identities for this set of basis vectors are as follows:

$$\begin{aligned} \nabla \mathbf{e}_R &= \frac{1}{R} \mathbf{e}_\phi \otimes \mathbf{e}_\phi; & \nabla \mathbf{e}_Z &= 0; & \nabla \mathbf{e}_\phi &= -\frac{1}{R} \mathbf{e}_\phi \otimes \mathbf{e}_R \\ \nabla \cdot \mathbf{e}_R &= \frac{1}{R}; & \nabla \cdot \mathbf{e}_Z &= 0; & \nabla \cdot \mathbf{e}_\phi &= 0 \\ \nabla \times \mathbf{e}_R &= 0; & \nabla \times \mathbf{e}_Z &= 0; & \nabla \times \mathbf{e}_\phi &= -\frac{1}{R} \mathbf{e}_Z \end{aligned}$$

It is also useful to represent a vector in contra variant basis $\mathbf{a}^1 = \nabla R$, $\mathbf{a}^2 = \nabla Z$ and $\mathbf{a}^3 = \nabla \phi$ which are orthogonal but not normalized. A vector \mathbf{A} can be represented in both basis as: $\mathbf{A} = A_R \mathbf{e}_R + A_Z \mathbf{e}_Z + A_\phi \mathbf{e}_\phi = A_R \mathbf{a}^1 + A_Z \mathbf{a}^2 + R A_\phi \mathbf{a}^3$. Some useful identities for contra variant basis are as follows:

$$\begin{aligned} \nabla \mathbf{a}^1 &= R \mathbf{a}^3 \otimes \mathbf{a}^3; & \nabla \mathbf{a}^2 &= 0; & \nabla \mathbf{a}^3 &= -\frac{1}{R} \mathbf{a}^3 \otimes \mathbf{a}^1 - \frac{1}{R} \mathbf{a}^1 \otimes \mathbf{a}^3 \\ \nabla \cdot \mathbf{a}^1 &= \frac{1}{R}; & \nabla \cdot \mathbf{a}^2 &= 0; & \nabla \cdot \mathbf{a}^3 &= 0 \\ \nabla \times \mathbf{a}^1 &= 0; & \nabla \times \mathbf{a}^2 &= 0; & \nabla \times \mathbf{a}^3 &= 0 \end{aligned}$$

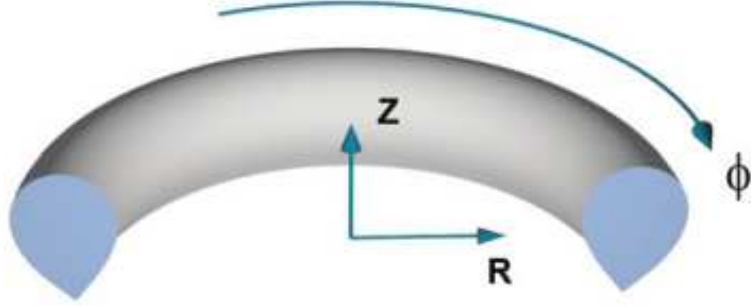


Figure 2.1: The coordinate system used for representation of plasma physics equations.

2.2.2 MHD instabilities

For tokamaks, it is of great interest to know whether a given plasma equilibrium, if perturbed by a small amount, is stable or not. In stability theory, a physical variable is decomposed into two parts, a time independent equilibrium \mathbf{w}_0 and small time dependent perturbation $\mathbf{w}' \ll \mathbf{w}_0$ as:

$$\mathbf{w}(\mathbf{x}) = \mathbf{w}_0(\mathbf{x}) + \mathbf{w}'(\mathbf{x})e^{\gamma t} \quad (2.30)$$

where γ may be a complex number and denotes the growth rate of perturbations. Using this decomposition, the system of MHD equations can be linearized and analyzed for the growth rates γ . If $\text{Re}(\gamma) > 0$ then perturbations will grow exponentially and MHD system is said to be unstable. A decomposition given by equation (2.30) can be used in ideal MHD equations and all perturbed quantities can be expressed as a function of \mathbf{w}' . Then the potential energy δW can be expressed in terms of the perturbations \mathbf{w}' [32] as:

$$\delta W = \delta W_F + \delta W_S + \delta W_V$$

where δW_F , δW_S and δW_V denote potential energy of plasma, plasma-vacuum surface and vacuum respectively. Of particular interest here is the potential energy of plasma given by:

$$\begin{aligned} \delta W_F = \frac{1}{2\mu_0} \int \left[|\mathbf{B}'_{\perp}|^2 + B_0^2 |\nabla \cdot \mathbf{w}'_{\perp} + 2\mathbf{w}'_{\perp} \cdot (\mathbf{b} \cdot \nabla \mathbf{b})|^2 \right. \\ \left. + \mu_0 \gamma p_0 |\nabla \cdot \mathbf{w}'|^2 - 2 \mu_0 (\mathbf{w}'_{\perp} \cdot \nabla p_0) (\mathbf{w}'_{\perp} \cdot (\mathbf{b} \cdot \nabla \mathbf{b})) \right. \\ \left. - \mu_0 J_{0\parallel} \mathbf{w}'_{\perp} \times \mathbf{b} \cdot \mathbf{B}'_{\perp} \right] dV \end{aligned} \quad (2.31)$$

where \mathbf{b} is the unit vector in the direction of equilibrium magnetic field \mathbf{B}_0 . The integral is taken over plasma volume and quantities with subscripts \perp and \parallel denote the components perpendicular and parallel to \mathbf{B}_0 . The quantities with starred superscript denote complex conjugates. The energy principle states that an MHD equilibrium is unstable if the total potential energy $\delta W < 0$. The first three terms in δW_F are positive whereas the last two terms may be negative and hence can lead to an instability. Therefore the possible sources of instabilities can be the pressure gradient and the parallel current density.

Plasma instabilities caused by the pressure gradient may lead to ballooning modes which are highly relevant to tokamaks. They appear in the low field side where the curvature ($\mathbf{b} \cdot \nabla \mathbf{b}$) is unfavorable and can lead to violent and repetitive crashes and loss of pressure. Such instabilities are called Edge-Localised Modes. The instabilities driven by parallel currents are called kink modes.

In the core of tokamak plasma, the magnetic field lines are closed. They are periodic in the toroidal direction as well as in the poloidal plane. Therefore, perturbations maybe represented using Fourier series such that:

$$\mathbf{w}'(\mathbf{x}) = \sum_{m,n} \hat{\mathbf{w}}'_{m,n}(r) e^{i(m\theta - n\phi)}$$

where m and n are the poloidal and toroidal mode numbers, θ and ϕ are the poloidal and toroidal angles respectively and $\hat{\mathbf{w}}'_{m,n}$ are functions of the radial coordinate r . The set of mode numbers (m, n) are often seen to be unstable, in experiments as well as in numerical simulations, on the rational surfaces of the plasma where $q = m/n$, where q is the plasma safety factor. At these rational surfaces the instability structures are similar to the structure of the magnetic field lines.

JOREK simulates the evolution of perturbations added to initial plasma equilibrium numerically. Therefore, the first step is to compute the plasma equilibrium which is described next.

2.2.3 Grad-Shafranov Equation

The static equilibrium for ideal MHD equations is written by setting $\partial/\partial t = 0$ and plasma velocity $\mathbf{v} = 0$ in ideal MHD equations (2.29):

$$\nabla p = \mathbf{J} \times \mathbf{B} \tag{2.32}$$

with Gauss law $\nabla \cdot \mathbf{B} = 0$ and Ampère's law $\mathbf{J} = \nabla \times \mathbf{B}$. This equation balances pressure with magnetic forces. It is immediately clear that $\mathbf{B} \cdot \nabla p = 0$ and $\mathbf{J} \cdot \nabla p = 0$ meaning that magnetic field lines and current lines lie on the surfaces of constant pressure. These surfaces are called magnetic surfaces. At the center of a plasma the pressure is maximum and this point is called the magnetic axis.

In the toroidal coordinate system described in (2.2.1), Gauss's law is written as:

$$\frac{1}{R} \frac{\partial(RB_R)}{\partial R} + \frac{\partial B_Z}{\partial Z} + \frac{1}{R} \frac{\partial B_\phi}{\partial \phi} = 0$$

In order to derive Grad-Shafranov equations a toroidal symmetry i.e., $\partial_\phi(\cdot) = 0$ is assumed [38, 84]. This implies that $\partial_\phi B_\phi = 0$ and hence B_ϕ is a function of R and Z only. Therefore, Gauss law reduces to:

$$\frac{1}{R} \frac{\partial(RB_R)}{\partial R} + \frac{\partial B_Z}{\partial Z} = \frac{1}{R} \frac{\partial(RB_R)}{\partial R} + \frac{1}{R} \frac{\partial(RB_Z)}{\partial Z} = 0$$

and the poloidal field can be represented in terms of a stream function $\psi(R, Z)$ such that:

$$B_R = -\frac{1}{R} \frac{\partial \psi}{\partial Z} \quad \text{and} \quad B_Z = \frac{1}{R} \frac{\partial \psi}{\partial R} \quad (2.33)$$

The stream function ψ is analogous to the poloidal magnetic flux Ψ and therefore, ψ is often referred to as poloidal magnetic flux. Now, the magnetic field may be represented as:

$$\mathbf{B} = \frac{1}{R} \nabla \psi \times \mathbf{e}_\phi + B_\phi \mathbf{e}_\phi$$

This expression can be compared with the $\mathbf{B} = \text{grad} \times \mathbf{A}$ to get the relation between poloidal flux ψ and A_ϕ as: $\psi = RA_\phi$.

Similarly, the divergence of current $\nabla \cdot \mathbf{J} = \nabla \cdot \nabla \times \mathbf{B} = 0$ can be explored with toroidal symmetry to write:

$$\nabla \cdot \mathbf{J} = \frac{1}{R} \frac{\partial(RJ_R)}{\partial R} + \frac{\partial J_Z}{\partial Z} = \frac{1}{R} \frac{\partial(RJ_R)}{\partial R} + \frac{1}{R} \frac{\partial(RJ_Z)}{\partial Z} = 0$$

This gives rise to another poloidal current stream function $F(R, Z)$ such that:

$$J_R = -\frac{1}{R} \frac{\partial F}{\partial Z} \quad \text{and} \quad J_Z = \frac{1}{R} \frac{\partial F}{\partial R}$$

Hence the expression for the current in terms of F can be written as:

$$\mathbf{J} = \frac{1}{R} \nabla F \times \mathbf{e}_\phi + J_\phi \mathbf{e}_\phi$$

and can be compared with the definition of the current, under the assumption of toroidal symmetry:

$$\mathbf{J} = \nabla \times \mathbf{B} = \frac{\partial B_\phi}{\partial Z} \mathbf{e}_R - \frac{1}{R} \frac{\partial(RB_\phi)}{\partial R} \mathbf{e}_Z + R \left(\frac{\partial B_Z}{\partial R} - \frac{\partial B_R}{\partial Z} \right) \mathbf{e}_\phi$$

to get the relation between F and B_ϕ as: $F = RB_\phi$. Substituting B_ϕ in the expression for the magnetic field, we can write:

$$\mathbf{B} = \frac{1}{R} \nabla \psi \times \mathbf{e}_\phi + \frac{F}{R} \mathbf{e}_\phi = \nabla \psi \times \nabla \phi + F \nabla \phi \quad (2.34)$$

Now the toroidal component of the current can be written from above expression of the current as:

$$J_\phi = R \left(\frac{\partial B_Z}{\partial R} - \frac{\partial B_R}{\partial Z} \right)$$

and equations (2.33) can be used to represent it in terms of ψ as:

$$J_\phi = - \left[\frac{\partial}{\partial R} \left(\frac{1}{R} \frac{\partial \psi}{\partial R} \right) + \frac{1}{R} \frac{\partial^2 \psi}{\partial Z^2} \right] = - \frac{1}{R} \Delta^* \psi$$

where Δ^* is an elliptic operator known as Grad-Shafranov operator and is defined as:

$$\Delta^* \psi = R \nabla \cdot \left(\frac{1}{R^2} \nabla \psi \right) = R \frac{\partial}{\partial R} \left(\frac{1}{R} \frac{\partial \psi}{\partial R} \right) + \frac{\partial^2 \psi}{\partial Z^2}$$

The projections of the momentum equation (2.32) with the magnetic field and current vector derived above are written as:

$$\begin{aligned} \mathbf{B} \cdot \nabla p &= \mathbf{e}_\phi \cdot (\nabla \psi \times \nabla p) = 0 \\ \mathbf{J} \cdot \nabla p &= \mathbf{e}_\phi \cdot \left(\nabla F \times \nabla p \right) = 0 \end{aligned}$$

where toroidal symmetry is used while simplifying above projections. These equations imply that the pressure and poloidal current stream function F are functions of ψ : $p = p(\psi)$ and $F = R B_\phi = F(\psi)$. The Grad-Shafranov equation is then obtained by taking the projection of the force balance equation (2.32) with $\nabla \psi$ and it is written as:

$$\Delta^* \psi = R^2 \frac{\partial p}{\partial \psi} - F \frac{\partial F}{\partial \psi} \quad (2.35)$$

This is a nonlinear elliptic PDE that governs equilibrium between plasma pressure and magnetic forces. The functions $p(\psi)$ and $F(\psi)$ are completely arbitrary at this point and may be defined from the experimental conditions of a tokamak device under concern. If $p(\psi)$ and $F(\psi)$ are nonlinear functions, there is no theoretical guarantee of the existence and/or uniqueness of the solution for Grad-Shafranov equation (2.35), even with Dirichlet boundary conditions. In practice, these functions are constructed by a polynomial fitting over experimental data.

2.2.4 Full MHD model with Potential vector formulation

The induction equation in MHD models: $\partial_t \mathbf{B} + \nabla \times \mathbf{E} = 0$, after taking divergence gives: $\partial_t \nabla \cdot \mathbf{B} = 0$, since $\nabla \cdot (\nabla \times \mathbf{E}) = 0$. This means that if the initial condition satisfies the divergence free constrain $\nabla \cdot \mathbf{B} = 0$, it will be satisfied at any $t > 0$. Since the divergence free constrain on the magnetic field is to be satisfied at all times, the magnetic field can also be represented in terms of a vector potential \mathbf{A} such that $\nabla \cdot (\nabla \times \mathbf{A}) = 0$. Moreover, plasma equilibrium in tokamaks given by magnetic flux ψ is related to the toroidal component of a magnetic vector potential as: $\psi = RA_\phi$. The expression for magnetic field based on ideal MHD equilibrium for a tokamak application is defined to have the form given by equation (2.34). It can be rearranged as:

$$\mathbf{B} = \nabla \times (\psi \nabla \phi) + F \nabla \phi$$

using the vector identity: $\nabla \times (\psi \nabla \phi) = \nabla \psi \times \nabla \phi + \psi \nabla \times \nabla \phi$. In terms of the the magnetic vector potential $\mathbf{A} = \psi \nabla \phi$ the magnetic field can be further re-written as:

$$\mathbf{B} = \nabla \times \mathbf{A} + F(\psi) \nabla \phi \quad (2.36)$$

It can be easily verified that, this form of the magnetic field satisfies Gauss's law $\nabla \cdot \mathbf{B} = 0$ when $F(\psi)$ is a toroidally axisymmetric function. It is emphasized again that F is a function of poloidal coordinates R and Z but is a constant in time. Substituting the definition of the magnetic field (2.36) in the induction equation (2.3) gives:

$$\nabla \times \left(\frac{\partial \mathbf{A}}{\partial t} + \mathbf{E} \right) = 0$$

Since curl of the gradient of any scalar function vanish, the above equation is satisfied if there exists Φ such that:

$$\frac{\partial \mathbf{A}}{\partial t} + \mathbf{E} = -\nabla \Phi$$

where, Φ is an electric potential. Moreover, the magnetic vector potential \mathbf{A} is not uniquely defined and can be added with gradient of any scalar function $\mathbf{A} = \mathbf{A}' + \nabla \chi$ without altering the magnetic field. In order to uniquely define potentials, a 'gauge' needs to be fixed [39] for Φ and χ and there can be many choices depending upon the problem at hand. One convenient choice is to use Weyl's gauge $\Phi = 0$ and since

χ is left free, Weyl's gauge is also called as incomplete gauge. Another choice is the Coulomb's gauge $\nabla \cdot \mathbf{A} = 0$. By taking divergence of the induction equation:

$$\frac{\partial}{\partial t}(\nabla \cdot \mathbf{A}) + \nabla \cdot \mathbf{E} = -\nabla \cdot \nabla \Phi$$

and using Poisson's equation (2.2) and Coulomb gauge, the induction equation reduces to another Poisson equation:

$$\nabla^2 \Phi = \frac{\tau}{\epsilon_0}$$

Therefore, the use of Coulomb gauge require the solution of this Poisson equation. For a quasi-neutral plasma, this equation is reduced to a Laplace equation where $\tau \approx 0$. In this work, we choose Weyl's gauge and use Ohm's Law $\mathbf{E} = \mathbf{v} \times \mathbf{B} + \eta \mathbf{J}$ to write the induction equation as:

$$\frac{\partial \mathbf{A}}{\partial t} - \mathbf{v} \times \mathbf{B} = -\eta \mathbf{J}$$

This induction equation replaces the induction equation in resistive MHD equations (2.28) so that the system of equations becomes:

$$\begin{aligned} \frac{\partial \rho}{\partial t} + \nabla \cdot (\rho \mathbf{v}) &= 0 \\ \rho \frac{\partial \mathbf{v}}{\partial t} + \rho \mathbf{v} \cdot \nabla \mathbf{v} + \nabla p - \mathbf{J} \times \mathbf{B} &= 0 \\ \frac{\partial p}{\partial t} + \mathbf{v} \cdot \nabla p + \gamma p \nabla \cdot \mathbf{v} &= (\gamma - 1)(\eta \mathbf{J} \cdot \mathbf{J}) \\ \frac{\partial \mathbf{A}}{\partial t} - \mathbf{v} \times \mathbf{B} &= -\eta \mathbf{J} \end{aligned} \tag{2.37}$$

with Gauss's law $\nabla \cdot \mathbf{B} = 0$ and Ampère's law: $\mu_0 \mathbf{J} = \nabla \times \mathbf{B}$. This system of equations is implemented in JOEK as the full MHD model with the potential vector formulation. The equilibrium function $F(\psi)$ in the definition of the magnetic field (2.36) is constant in time.

2.2.5 Visco-resistive full MHD model with sources

So far, for simplicity we neglected dissipative and diffusive effects and focused upon the resistive and ideal MHD equations. In this subsection, visco-resistive full MHD

equations are written with dissipative, diffusive and source terms as follows:

$$\begin{aligned}
\frac{\partial \rho}{\partial t} + \nabla \cdot (\rho \mathbf{v}) &= \nabla \cdot (\underline{\mathbf{D}} \nabla \rho) + S_\rho \\
\rho \frac{\partial \mathbf{v}}{\partial t} + \rho \mathbf{v} \cdot \nabla \mathbf{v} + \nabla p - \mathbf{J} \times \mathbf{B} &= \nabla \cdot \underline{\boldsymbol{\pi}} + \mathbf{S}_v \\
\frac{\partial p}{\partial t} + \mathbf{v} \cdot \nabla p + \gamma p \nabla \cdot \mathbf{v} &= \nabla \cdot (\underline{\boldsymbol{\kappa}} \nabla T) + (\gamma - 1) \nabla \underline{\boldsymbol{\pi}} : \nabla \mathbf{v} + S_T \\
\frac{\partial \mathbf{A}}{\partial t} - \mathbf{v} \times \mathbf{B} &= -\eta (\mathbf{J} - \mathbf{S}_J)
\end{aligned} \tag{2.38}$$

with Gauss law $\nabla \cdot \mathbf{B} = 0$ and Ampère's law $\mu_0 \mathbf{J} = \nabla \times \mathbf{B}$. The particle source S_ρ and the heating source S_T can be used to maintain axisymmetric equilibrium. They can also be used to model phenomena like massive gas injection [74] or shattered pellet injection [49]. Similarly, a current source vector \mathbf{S}_J can be used to preserve the original current profile approximately throughout the simulation when specified as $\mathbf{S}_J = \mathbf{J}(t = 0)$. Consistently evolving bootstrap current can also be modeled using the current source term [47]. The source term in the velocity equation contains the contribution of diffusion and density source S_ρ as well as momentum source \mathbf{S}_m (recall that the velocity equation is derived from the momentum equation by removing the density equation from it) :

$$\mathbf{S}_v = \mathbf{S}_m - (\nabla \cdot (\underline{\mathbf{D}} \nabla \rho + S_\rho)) \mathbf{v}$$

The source term in the pressure equation contains Ohmic heating term and the terms with density, momentum and energy source:

$$S_T = (\gamma - 1) \left[\eta \mathbf{J} \cdot \mathbf{J} + S_E - \mathbf{S}_m \cdot \mathbf{v} + \frac{\mathbf{v} \cdot \mathbf{v}}{2} (\nabla \cdot (\underline{\mathbf{D}} \nabla \rho + S_\rho)) \right]$$

The heat diffusion tensor is decomposed into parallel and perpendicular part with respect to the magnetic field as:

$$\underline{\boldsymbol{\kappa}} = \kappa_{\parallel} (\mathbf{b} \otimes \mathbf{b}) + \kappa_{\perp} (\mathbb{I} - \mathbf{b} \otimes \mathbf{b}) \tag{2.39}$$

where \mathbf{b} denotes the unit vector in the direction of \mathbf{B} . Note that the factor $(\gamma - 1)$ in the heat diffusion term is absorbed in the coefficients κ_{\parallel} and κ_{\perp} . The ratio of specific heats is specified as $\gamma = 5/3$. Coefficients in the heat diffusion term may or may not be constants. Radial profiles for κ_{\perp} can be used to mimic various levels of cross-field kinetic turbulent transport, which cannot be described by MHD [47]. The temperature dependence in accordance with Spitzer-Härm is used for parallel heat diffusion coefficient κ_{\parallel} :

$$\kappa_{\parallel} = \kappa_0 \left(\frac{T}{T_0} \right)^{\frac{5}{2}}$$

where κ_0 is defined at the magnetic axis and is calculated according to the Spitzer-Härm formula. κ_0 has well defined values for electrons and ions, however in single fluid single temperature MHD model their average of value may be used for κ_0 .

The particle diffusion tensor has analogous form as that of the heat diffusion tensor:

$$\underline{\mathbf{D}} = D_{\parallel}(\mathbf{b} \otimes \mathbf{b}) + D_{\perp}(\mathbb{I} - \mathbf{b} \otimes \mathbf{b}) \quad (2.40)$$

As particle transport is dominated by convection, the parallel particle diffusion coefficient D_{\parallel} is generally not used. Similar to κ_{\perp} , the radial profile for D_{\perp} may also be used to mimic the turbulent transport phenomena.

The viscous stress tensor $\underline{\boldsymbol{\pi}}$ may be decomposed into three main parts that model respectively the Newtonian-fluid type, neoclassical and gyro-viscous effects. The details of these tensors and their implementation for reduced MHD models can be found in [47] and references therein. In the full MHD model considered here, the viscous stress tensor is modeled as:

$$\underline{\boldsymbol{\pi}} = \mu \nabla \mathbf{v} \quad (2.41)$$

where μ is the coefficient of viscosity. In general, μ is a tensor of higher order that can be decomposed into the direction parallel and perpendicular to \mathbf{B} and effects of neoclassical and gyro-viscous terms can also be taken into account [47]. However, the coefficient of viscosity is assumed here to be a scalar quantity. The coefficient of viscosity and resistivity both can be constants or can have a Spitzer-like dependence on temperature to keep Prandtl number constant:

$$\eta = \eta_0 \left(\frac{T}{T_0} \right)^{-3/2} ; \quad \mu = \mu_0 \left(\frac{T}{T_0} \right)^{-3/2}$$

where η_0 and μ_0 are resistivity and viscosity at the magnetic axis.

2.2.6 Normalization

Full MHD equations (2.37) can be normalized using typical scales for length l_0 , density ρ_0 , time t_0 and magnetic field B_0 . The density scale is chosen as the density at the center of the plasma ρ_0 . The scales for magnetic field and length are chosen as $B_0 = 1$ and $l_0 = 1$. The scales for other physical variables can be derived now. To derive the times scale, Alfvén wave speed is considered which is given by

$$v_0 = \frac{B_0}{\sqrt{\rho_0 \mu_0}}$$

Inserting, $B_0 = 1$ and $l_0 = 1$, the scales for speed v_0 and time t_0 are written as:

$$v_0 = \frac{1}{\sqrt{\rho_0 \mu_0}}, \quad t_0 = \frac{l_0}{v_0} = \sqrt{\rho_0 \mu_0}$$

The constant μ_0 is the permeability of free space and its value in SI units is $4\pi \times 10^{-7} \text{ N/A}^2$. The scale for the pressure can be derived to get:

$$p_0 = \rho_0 v_0^2 = \frac{1}{\mu_0}$$

and the relation between the pressure and temperature gives:

$$T_0 = \frac{\rho_0}{p_0} = \mu_0 \rho_0$$

Now, Ampère's law in SI units $\mathbf{J}_{[\text{SI}]} = \frac{1}{\mu_0} \nabla \times \mathbf{B}_{[\text{SI}]}$ is normalized using length and magnetic field scales to write:

$$\mathbf{J} = \nabla \times \mathbf{B}$$

such that the current scale becomes $J_0 = 1/\mu_0$. The conversion of other physical variables from SI to normalized units can be derived to write:

$$\begin{aligned} t &= \frac{t_{[\text{SI}]}}{\sqrt{\rho_0 \mu_0}} \\ \rho &= \frac{\rho_{[\text{SI}]}}{\rho_0} \\ \mathbf{v} &= \mathbf{v}_{[\text{SI}]} \sqrt{\rho_0 \mu_0} \\ p &= p_{[\text{SI}]} \mu_0 \\ \mathbf{J} &= \mathbf{J}_{[\text{SI}]} \mu_0 \\ T &= T_{[\text{SI}]} \rho_0 \mu_0 \\ \eta &= \eta_{[\text{SI}]} \sqrt{\frac{\rho_0}{\mu_0}} \\ \mu &= \mu_{[\text{SI}]} \sqrt{\frac{\mu_0}{\rho_0}} \\ \underline{\mathbf{D}} &\rightarrow \underline{\mathbf{D}}_{[\text{SI}]} \sqrt{\rho_0 \mu_0} \\ \underline{\boldsymbol{\kappa}} &\rightarrow \underline{\boldsymbol{\kappa}}_{[\text{SI}]} \sqrt{\frac{\mu_0}{\rho_0}} \end{aligned} \tag{2.42}$$

The temperature is often written in electron volts in plasma physics and the unit conversion associated with it is: $T = T_{[\text{eV}]} e n_0 \mu_0$, where e is the electron charge and

$n_0 = \rho_0 \times 10^{20}$ is the scale for particle density. Full MHD equations in normalized units are now written as:

$$\begin{aligned}
\frac{\partial \rho}{\partial t} + \nabla \cdot (\rho \mathbf{v}) &= \nabla \cdot (\underline{\mathbf{D}} \nabla \rho) + S_\rho \\
\rho \frac{\partial \mathbf{v}}{\partial t} + \rho \mathbf{v} \cdot \nabla \mathbf{v} + \nabla p - \mathbf{J} \times \mathbf{B} &= \nabla \cdot \underline{\boldsymbol{\pi}} + \mathbf{S}_v \\
\frac{\partial p}{\partial t} + \mathbf{v} \cdot \nabla p + \gamma p \nabla \cdot \mathbf{v} &= \nabla \cdot (\underline{\boldsymbol{\kappa}} \nabla T) + (\gamma - 1) \nabla \underline{\boldsymbol{\pi}} : \nabla \mathbf{v} + S_T \\
\frac{\partial \mathbf{A}}{\partial t} - \mathbf{v} \times \mathbf{B} &= -\eta(\mathbf{J} - \mathbf{S}_J)
\end{aligned} \tag{2.43}$$

with Gauss's law $\nabla \cdot \mathbf{B} = 0$ and the definition of the current $\mathbf{J} = \nabla \times \mathbf{B}$. From the mathematical point of view, the only change in the system is that μ_0 is eliminated from the current definition and the structure of the equations is preserved.

For D2 plasma with particle density $n_0 = 6 \times 10^{19} \text{ m}^{-3}$, the unit normal time corresponds to about $0.7 \mu\text{s}$. Hence a typical JOREK simulation needs to be run for approximately 10^4 normalized time units to get the dynamics over a few milli seconds in physical time.

2.2.7 Reduced MHD model

The aim of this subsection is only to highlight the differences in full and reduced MHD models rather than to derive or present reduced models. The reduced models have 6 to 7 variables whereas the full MHD model has 8 variables and hence reduced models give advantages in terms of computational costs and memory requirements for simulations. These models are based on the following assumptions that are relevant to tokamaks:

- The toroidal magnetic field B_ϕ is significantly greater than the poloidal magnetic field B_θ , i.e. $B_\phi \gg B_\theta$. This assumption implies that the poloidal plasma current does not appear in the reduced MHD equations.
- The toroidal magnetic field is constant in space as well as time, i.e., $F(\psi) = F_0$. This assumption eliminates the fast magneto-acoustic waves while retaining the relevant physics. With this assumption, the magnetic field is defined to have the form:

$$\mathbf{B} = \frac{1}{R} \nabla \psi \times \mathbf{e}_\phi + \frac{F_0}{R} \mathbf{e}_\phi$$

The velocity in reduced MHD models is defined to have parallel (to magnetic field) and perpendicular velocity as:

$$\mathbf{v} = \mathbf{v}_\perp + v_\parallel \mathbf{B}$$

The reduced MHD equations implemented in JOREK can be found in [47] and many references therein and their derivation can be found in [77, 4]. They are the system of MHD equations consisting the equations of poloidal magnetic flux (ψ), perpendicular momentum (in terms of velocity stream function u), toroidal current density ($j = \Delta^* \psi$), toroidal component vorticity (w), density (ρ), temperature (T) and parallel velocity (v_\parallel). Another difference to be noted between reduced and full MHD models is that the Coulomb gauge $\nabla \cdot \mathbf{A} = 0$ has been used to derive reduced MHD equations whereas Weyl's gauge is used in full MHD model.

2.3 Full MHD: Massive Material Injection

As mentioned earlier, the source terms in full MHD equations can be used to model Massive Gas Injection (MGI) or Shattered Pellet Injection (SPI) in which a massive amount of material is injected into a tokamak plasma. A plasma in a tokamak mostly consists of electrons and main core ions which are the ions in the plasma core (usually D ions). The injected species may be D or Ne or Ar whose atoms (neutral/impurity particles) interact with hot plasma via atomic reactions explained at the beginning of this Chapter. The ions at different charge level can be formed when the impurity particles interact with plasma electrons. To model MGI or SPI in a plasma, we must consider the effects of transport of impurities and atomic processes including radiation losses. The ionization energy and radiation power is determined as a function of the electron temperature (T_e) and electron density (n_e) under the assumption of coronal equilibrium (CE) [49]. Following we describe detailed derivation of full MHD model with the transport of impurities.

Let us consider a tokamak plasma consisting electrons e , main core ions i and impurities. Here, impurities are neutral particles of an injected gas (with charge number higher than D) and ions resulting from these atoms (impurity ions). Injected impurity neutral particles may undergo ionization to various levels due to atomic processes. The charge associated with each ionization level is denoted by $q_z = Ze$. Let $z \in \{0, \dots, N_z\}$ be ionization level where $z = 0$ denotes no ionization, i.e. neutral impurity particles and N_z denotes maximum level of ionization that can be attained.

Let E_α be the total ionization energy required to fully ionize an atom from the neutral state to the ionization state z such that:

$$E_\alpha = \sum_{z=1}^{\alpha} E_{z-1}^z$$

where E_{z-1}^z is the ionization energy required to move an ion from the level $z - 1$ up to level z . In such a situation, we have a multi fluid system with the evolution equation for the impurity of each charge state and would result in a large number of equations. However, under CE assumption, rapid change in temperature or strong density source may cause artificially fast evolution of charge state distribution, thus result in artificially high recombination radiation. To avoid this, we treat E_α as a potential energy and use the recombination radiation function at CE from the open ADAS data to model the corresponding radiation power. Such treatment ensures the energy conservation and prevents artificially large recombination radiation [49].

The system of multi fluid equations (2.21) is re-written here for the evolution of each species $\alpha \in \{e, i\} \cup \{0, \dots, N_z\}$ along with the induction equation in vector potential form as:

$$\begin{aligned} \frac{\partial \rho_\alpha}{\partial t} + \nabla \cdot (\rho_\alpha \mathbf{v}_\alpha) &= \dot{\rho}_\alpha^A + \dot{\rho}_\alpha^{NA} \\ \frac{\partial (\rho_\alpha \mathbf{v}_\alpha)}{\partial t} + \nabla \cdot (\rho_\alpha \mathbf{v}_\alpha \otimes \mathbf{v}_\alpha) + \nabla p_\alpha - \frac{\rho_\alpha}{m_\alpha} q_\alpha (\mathbf{E} + \mathbf{v}_\alpha \times \mathbf{B}) &= \nabla \cdot \boldsymbol{\pi}_\alpha + \mathbf{R}_\alpha \\ &\quad + \dot{\mathbf{m}}_\alpha^A + \dot{\mathbf{m}}_\alpha^{NA} \\ \frac{\partial \mathcal{E}_\alpha}{\partial t} + \nabla \cdot \left((\mathcal{E}_\alpha + p_\alpha) \mathbf{v}_\alpha \right) &= \nabla \cdot (\boldsymbol{\pi}_\alpha \mathbf{v}_\alpha) + \nabla \cdot \mathbf{h}_\alpha + Q_\alpha + \dot{\mathcal{E}}_\alpha^A + \dot{\mathcal{E}}_\alpha^{NA} \\ &\quad + \left(\frac{q_\alpha \rho_\alpha}{m_\alpha} \mathbf{E} - \mathbf{R}_\alpha \right) \cdot \mathbf{v}_\alpha \\ \frac{\partial \mathbf{A}}{\partial t} - \mathbf{v} \times \mathbf{B} &= -\eta \mathbf{J} \end{aligned} \tag{2.44}$$

with Gauss's law $\nabla \cdot \mathbf{B} = 0$ and Ampère's law $\mathbf{J} = \nabla \times \mathbf{B}$. These equations are written in normalized units. The equation for the total energy (\mathcal{E}_α) now has the contribution due to ionization potential energy E_α as:

$$\mathcal{E}_\alpha = \frac{p_\alpha}{(\gamma_\alpha - 1)} + \frac{1}{2} \rho_\alpha \mathbf{v}_\alpha \cdot \mathbf{v}_\alpha + \rho_\alpha E_\alpha$$

The terms $\dot{\rho}_\alpha^{NA}$, $\dot{\mathbf{m}}_\alpha^{NA}$ and $\dot{\mathcal{E}}_\alpha^{NA}$ denote sources for densities, momenta and energies associated with non atomic reactions respectively, whereas the terms $\dot{\rho}_\alpha^A$, $\dot{\mathbf{m}}_\alpha^A$ and $\dot{\mathcal{E}}_\alpha^A$ denote sources for densities, momenta and energies associated with atomic reactions.

The terms R_α , \mathbf{h}_α and Q_α denote momentum transfer, heat flow and heat transfer respectively.

Using the equations for densities and momenta in the equations of total energies, the equations for pressures p_α evolution are obtained as follows:

$$\begin{aligned} \frac{1}{(\gamma_\alpha - 1)} \left(\frac{\partial p_\alpha}{\partial t} + \mathbf{v}_\alpha \cdot \nabla p_\alpha + \gamma p_\alpha \nabla \cdot \mathbf{v}_\alpha \right) &= \underline{\boldsymbol{\pi}}_\alpha : \nabla \mathbf{v}_\alpha + \nabla \cdot \mathbf{h}_\alpha + Q_\alpha \\ &+ \left(\frac{q_\alpha \rho_\alpha}{m_\alpha} \mathbf{E} - \mathbf{R}_\alpha \right) \cdot \mathbf{v}_\alpha + \dot{\mathcal{E}}_\alpha^{NA} - (\dot{\mathbf{m}}_\alpha^A + \dot{\mathbf{m}}_\alpha^{NA}) \cdot \mathbf{v}_\alpha + \frac{\dot{\rho}_\alpha^A + \dot{\rho}_\alpha^{NA}}{2} \mathbf{v}_\alpha \cdot \mathbf{v}_\alpha \\ &+ \dot{\mathcal{E}}_\alpha^A - \left(\frac{\partial(\rho_\alpha E_\alpha)}{\partial t} + \nabla \cdot (\rho_\alpha E_\alpha \mathbf{v}_\alpha) \right) \end{aligned}$$

We consider the situation in which atomic reactions do not affect the evolution of the pressure of the impurity species $\alpha \in \{0, 1, \dots, N_z\}$. Therefore we can write:

$$\dot{\mathcal{E}}_\alpha^A = \frac{\partial(\rho_\alpha E_\alpha)}{\partial t} + \nabla \cdot (\rho_\alpha E_\alpha \mathbf{v}_\alpha) \quad \text{for } \alpha \in \{0, \dots, N_z\} \quad (2.45)$$

From the conservation of energy, sum of ionization potential energies over all species $\alpha \in \{i, e\} \cup \{0, 1, \dots, N_z\}$ is zero and hence we can write:

$$\dot{\mathcal{E}}_e^A = - \sum_{\alpha=0}^{N_z} \dot{\mathcal{E}}_\alpha^A = - \frac{\partial}{\partial t} \left(\sum_{\alpha=0}^{N_z} \rho_\alpha E_\alpha \right) - \nabla \cdot \left(\sum_{\alpha=0}^{N_z} \rho_\alpha E_\alpha \mathbf{v}_\alpha \right)$$

Note that the main core ions are already ionized and hence the ionization energy associated $\alpha = i$ is zero. Now we define the average quantities as:

$$\rho_{\text{imp}} E_{\text{ion}} = \sum_{\alpha=0}^{N_z} \rho_\alpha E_\alpha \quad \text{and} \quad \rho_{\text{imp}} E_{\text{ion}} \mathbf{v}_{\text{imp}} = \sum_{\alpha=0}^{N_z} \rho_\alpha E_\alpha \mathbf{v}_\alpha$$

where ρ_{imp} is the total impurity density, E_{ion} is the average ionization potential energy and \mathbf{v}_{imp} is the average velocity of all species α . Therefore, the pressure evolution for electrons can be written as follows:

$$\begin{aligned} \frac{1}{(\gamma_e - 1)} \left(\frac{\partial p_e}{\partial t} + \mathbf{v}_e \cdot \nabla p_e + \gamma p_e \nabla \cdot \mathbf{v}_e \right) &= \underline{\boldsymbol{\pi}}_e : \nabla \mathbf{v}_e + \nabla \cdot \mathbf{h}_e + Q_e + \eta \mathbf{J} \cdot \mathbf{J} \\ &+ \dot{\mathcal{E}}_e^{NA} - (\dot{\mathbf{m}}_e^A + \dot{\mathbf{m}}_e^{NA}) \cdot \mathbf{v}_e + \frac{\dot{\rho}_e^A + \dot{\rho}_e^{NA}}{2} \mathbf{v}_e \cdot \mathbf{v}_e \\ &- \left(\frac{\partial(\rho_{\text{imp}} E_{\text{ion}})}{\partial t} + \nabla \cdot (\rho_{\text{imp}} E_{\text{ion}} \mathbf{v}_{\text{imp}}) \right) \end{aligned} \quad (2.46)$$

and the pressure evolution for the species other than electrons $\alpha \in \{i\} \cup \{0, 1, \dots, N_z\}$ is written as:

$$\begin{aligned} \frac{1}{(\gamma_\alpha - 1)} \left(\frac{\partial p_\alpha}{\partial t} + \mathbf{v}_\alpha \cdot \nabla p_\alpha + \gamma p_\alpha \nabla \cdot \mathbf{v}_\alpha \right) &= \underline{\boldsymbol{\pi}}_\alpha : \nabla \mathbf{v}_\alpha + \nabla \cdot \mathbf{h}_\alpha + Q_\alpha \\ &+ \dot{\mathcal{E}}_\alpha^{NA} - (\dot{\mathbf{m}}_\alpha^A + \dot{\mathbf{m}}_\alpha^{NA}) \cdot \mathbf{v}_\alpha + \frac{\dot{\rho}_\alpha^A + \dot{\rho}_\alpha^{NA}}{2} \mathbf{v}_\alpha \cdot \mathbf{v}_\alpha \end{aligned} \quad (2.47)$$

The relation between the pressure and temperature: $p_\alpha = kn_\alpha T_\alpha$ can be used to write equation of the electron temperature as follows:

$$\begin{aligned} \frac{n_e k}{(\gamma_e - 1)} \left(\frac{\partial T_e}{\partial t} + \mathbf{v}_e \cdot \nabla T_e + (\gamma_e - 1) T_e \nabla \cdot \mathbf{v}_e \right) &= \underline{\boldsymbol{\pi}}_e : \nabla \mathbf{v}_e + \nabla \cdot \mathbf{h}_e + Q_e + \eta \mathbf{J} \cdot \mathbf{J} \\ + \dot{\mathcal{E}}_e^{NA} - (\dot{\mathbf{m}}_e^A + \dot{\mathbf{m}}_e^{NA}) \cdot \mathbf{v}_e + \frac{\dot{\rho}_e^A + \dot{\rho}_e^{NA}}{2} \mathbf{v}_e \cdot \mathbf{v}_e - \frac{k T_e}{(\gamma_e - 1) m_e} \left(\frac{\partial \rho_e}{\partial t} + \mathbf{v}_e \cdot \nabla \rho_e \right) \\ - \left(\frac{\partial (\rho_{\text{imp}} E_{\text{ion}})}{\partial t} + \nabla \cdot (\rho_{\text{imp}} E_{\text{ion}} \mathbf{v}_{\text{imp}}) \right) \end{aligned} \quad (2.48)$$

and equations for temperatures of rest of the species $\alpha \in \{i\} \cup \{0, 1, \dots, N_z\}$ as follows:

$$\begin{aligned} \frac{n_\alpha k}{(\gamma_\alpha - 1)} \left(\frac{\partial T_\alpha}{\partial t} + \mathbf{v}_\alpha \cdot \nabla T_\alpha + (\gamma_\alpha - 1) T_\alpha \nabla \cdot \mathbf{v}_\alpha \right) &= \underline{\boldsymbol{\pi}}_\alpha : \nabla \mathbf{v}_\alpha + \nabla \cdot \mathbf{h}_\alpha + Q_\alpha + \dot{\mathcal{E}}_\alpha^{NA} \\ - (\dot{\mathbf{m}}_\alpha^A + \dot{\mathbf{m}}_\alpha^{NA}) \cdot \mathbf{v}_\alpha + \frac{\dot{\rho}_\alpha^A + \dot{\rho}_\alpha^{NA}}{2} \mathbf{v}_\alpha \cdot \mathbf{v}_\alpha - \frac{k T_\alpha}{(\gamma_\alpha - 1) m_\alpha} \left(\frac{\partial \rho_\alpha}{\partial t} + \mathbf{v}_\alpha \cdot \nabla \rho_\alpha \right) \end{aligned} \quad (2.49)$$

Following a similar approach to the previous subsection, the multi fluid equations can be combined to derive the single fluid (MHD) equations. A series of assumptions for modeling source terms for MGI/SPI into full MHD model are written now:

Coronal Equilibrium:

The assumption of CE requires the plasma to be dominated by radiative recombination and to exist in an ionization equilibrium [67, 49]. The contributions from these atomic reactions are contained in the source terms $\dot{\rho}$, $\dot{\mathbf{m}}$ and $\dot{\mathcal{E}}$. The atomic reactions conserve the mass, momentum and energy, therefore:

$$\sum_\alpha \dot{\rho}_\alpha = 0; \quad \sum_\alpha \dot{\mathbf{m}}_\alpha = 0; \quad \sum_\alpha \dot{\mathcal{E}}_\alpha = 0$$

We consider the time-dependent ionization and recombination reactions among the species as described at the beginning of this section. These atomic reactions can be represented in terms of a system of Ordinary Differential Equations (ODEs) as:

$$\frac{dW_{\text{imp}}}{dt} = \frac{1}{\epsilon} \underline{\mathbf{F}}_e W_{\text{imp}} \quad \text{and} \quad \frac{dW_e}{dt} = \frac{1}{\epsilon} \underline{\mathbf{F}}_{\text{imp}} W_e$$

where,

$$\begin{aligned} W_{\text{imp}} &= \{n_z, \mathbf{v}_z, T_z\}^T & z \in \{1, 2, \dots, N_z\}^T \\ W_e &= \{n_e, \mathbf{v}_e, T_e\}^T \\ \underline{\mathbf{F}}_e &= \underline{\mathbf{F}}_e(W_e); & \underline{\mathbf{F}}_{\text{imp}} &= \underline{\mathbf{F}}_{\text{imp}}(W_{\text{imp}}, W_e) \end{aligned}$$

The right hand side of the equations are given by ionization and recombination rates as described at the beginning of this Chapter. In practice, this system is solved by setting velocities to zero. CE assumes that the time over which the macroscopic plasma parameter vary is large enough as compared to the atomic reaction relaxation time scale. Therefore, the distribution of ionization levels is determined by a balance between ionization, radiative and recombination processes:

$$\underline{\mathbf{F}}_e W_{\text{imp}} = 0 \quad \text{and} \quad \underline{\mathbf{F}}_{\text{imp}} W_e = 0$$

By solving these equations, the density distribution of ionization levels $z(T_e, n_e)$ is obtained [49] as a function of the electron temperature T_e and weak function of the electron density n_e .

Quasi-neutrality:

The assumption of quasi-neutrality says that the plasma is neutral at the macroscopic scales and the net resulting electric charge is zero.

$$q_e n_e + q_i n_i + \sum_{z=1}^{N_z} q_z n_z = -en_e + Zen_i + \sum_{z=1}^{N_z} z n_z \approx 0$$

This can be further simplified to get:

$$n_e \approx Zn_i + Z_{\text{imp}} n_{\text{imp}} \quad (2.50)$$

where impurity particle density n_{imp} and mean charge Z_{imp} of impurity ions are defined as:

$$n_{\text{imp}} = \sum_{z=1}^{N_z} n_z \quad \text{and} \quad Z_{\text{imp}} = \sum_{z=1}^{N_z} z \frac{n_z}{n_{\text{imp}}}$$

Using CE assumption the ratio n_z/n_{imp} is given by a charge state distribution function $\mathcal{P}(z, n_e, T_e)$. This function can be obtained from open ADAS [1] atomic data for a given n_e and T_e . The ionization potential energy E_{ion} is then determined as:

$$E_{\text{ion}}(n_e, T_e) = \sum_{z=1}^{N_z} \mathcal{P}(z, n_e, T_e) E_z \quad (2.51)$$

with E_z being the accumulated ionization potential energy of a charge state z .

Total density:

The total density ρ is obtained by summing over all partial densities, for electrons ρ_e , ions ρ_i and each impurity species ρ_z and is written as:

$$\rho = \rho_e + \rho_i + \sum_{z=0}^{N_z} \rho_z = \rho_e + \rho_i + \rho_n + \rho_c = \rho_e + \rho_i + \rho_{\text{imp}}$$

with

$$\rho_{\text{imp}} = \sum_{z=0}^{N_z} \rho_z = \rho_n + \sum_{z=1}^{N_z} \rho_z = \rho_n + \rho_c = m_{\text{imp}} n_{\text{imp}} \quad (2.52)$$

where ρ_n is the density of neutral particles ($z = 0$); ρ_{imp} and m_{imp} is the total density and total mass of impurities (including neutrals) respectively. The assumption that allows to add the neutral and impurity density is that the mass of electron is very small as compared to the mass of any impurity particle ($m_e \ll m_{\text{imp}}$) and addition or removal of an electron does not change the mass of a impurity particle significantly.

Quasi-neutrality assumption (2.50) can be used in the definition of the total density to write it in terms of the ion density ρ_i and impurity density ρ_{imp} as:

$$\rho = \rho_e + \rho_i + \rho_n + \sum_1^{N_z} \rho_\alpha = \left(1 + \frac{m_e}{m_i} Z\right) \rho_i + \left(1 + \frac{m_e}{m_{\text{imp}}} Z_{\text{imp}}\right) \rho_{\text{imp}}$$

With the assumption $m_e \ll m_i$ and $m_e \ll m_{\text{imp}}$, the total density can be further approximated as:

$$\rho \approx \rho_i + \rho_{\text{imp}}$$

Average velocity:

The average or center of mass velocity of all species is defined as:

$$\rho \mathbf{v} = \rho_e \mathbf{v}_e + \rho_i \mathbf{v}_i + \sum_{z=0}^{N_z} \rho_z \mathbf{v}_z = \rho_e \mathbf{v}_e + \rho_i \mathbf{v}_i + \rho_n \mathbf{v}_n + \rho_c \mathbf{v}_c \quad (2.53)$$

where, \mathbf{v}_n is the velocity of neutral particles ($z = 0$) and \mathbf{v}_c is the average velocity of the charged particles ($z \neq 0$) which is given by:

$$\mathbf{v}_c = \frac{1}{\rho_c} \sum_{z=1}^{N_z} \rho_z \mathbf{v}_z \quad (2.54)$$

Since the neutral particles are not affected by electromagnetic fields, \mathbf{v}_n can be different from \mathbf{v}_c . The average velocity of the neutral particles and charged species is defined as:

$$\mathbf{v}_{\text{imp}} = \frac{1}{\rho_{\text{imp}}}(\rho_n \mathbf{v}_n + \rho_c \mathbf{v}_c) \quad (2.55)$$

Total pressure:

The total pressure is obtained using Dalton's law by summing partial pressures for all species to write:

$$p = p_e + p_i + \sum_{z=0}^{N_z} p_z = k(n_e T_e + n_i T_i + \sum_{z=0}^{N_z} n_z T_z) \quad (2.56)$$

Using the relation obtained from quasi-neutrality assumption (2.50), the total pressure can be written as:

$$p = k \left(Z \frac{\rho_i}{m_i} T_e + Z_{\text{imp}} \frac{\rho_{\text{imp}}}{m_{\text{imp}}} T_e + \frac{\rho_i}{m_i} T_i + \sum_{z=0}^{N_z} \frac{\rho_z}{m_z} T_z \right)$$

Since the removal or gain of electrons does not affect the mass of each impurity species, it can be assumed that $m_z = m_{\text{imp}}$ and the total pressure becomes:

$$p = k \left(Z \frac{\rho_i}{m_i} T_e + Z_{\text{imp}} \frac{\rho_{\text{imp}}}{m_{\text{imp}}} T_e + \frac{\rho_i}{m_i} T_i + \frac{\rho_{\text{imp}}}{m_{\text{imp}}} T_i \right)$$

Further, it can be assumed that the main core ions and impurities are at the same temperature $T_i = T_z$, then the expression of the total pressure becomes:

$$p = \frac{k}{m_i} \left[\rho_i (Z T_e + T_i) + \rho_{\text{imp}} \frac{m_i}{m_{\text{imp}}} (Z_{\text{imp}} T_e + T_i) \right]$$

Finally, it can be assumed that the temperature equilibration time of ions and electrons is very small as compared to the MHD time scales which implies that $T_i = T_e$, then the total pressure for single fluid modeling becomes:

$$p = \frac{kT}{m_i} \left[\rho_i (Z + 1) + \rho_{\text{imp}} \frac{m_i}{m_{\text{imp}}} (Z_{\text{imp}} + 1) \right]$$

Without the last assumption, one would get a two temperature model. Making use of $\rho \approx \rho_i + \rho_{\text{imp}}$ and for deuterium plasma $Z = 1$, the definition of the pressure becomes:

$$p = \frac{2k}{m_i} (\rho + \alpha_{\text{imp}} \rho_{\text{imp}}) T \quad \text{with} \quad \alpha_{\text{imp}} = \frac{1}{2} \frac{m_i}{m_{\text{imp}}} (Z_{\text{imp}} + 1) - 1$$

Total current

The total current is defined as:

$$\mathbf{J} = q_e n_e \mathbf{v}_e + q_i n_i \mathbf{v}_i + \sum_{z=1}^{N_z} q_z n_z \mathbf{v}_z = e \left(-n_e \mathbf{v}_e + Z n_i \mathbf{v}_i + \sum_{z=1}^{N_z} z n_z \mathbf{v}_z \right) \quad (2.57)$$

where $q_e = -e$, $q_i = eZ$ and $q_z = ez$. We assume that all the charged impurities have the same velocity, $\mathbf{v}_z = \mathbf{v}_c$ and use the definition of mean charge Z_{imp} to write:

$$\mathbf{J} = -e \left(n_e \mathbf{v}_e + Z n_i \mathbf{v}_i + Z_{\text{imp}} n_{\text{imp}} \mathbf{v}_c \right)$$

If it is further assumed that the main ion velocity is equal to the charged particles velocity ($\mathbf{v}_i = \mathbf{v}_c$), then the expression for the current simplifies to:

$$\mathbf{J} = -e \left(n_e \mathbf{v}_e + (Z n_i + Z_{\text{imp}} n_{\text{imp}}) \mathbf{v}_i \right)$$

Further using the quasi neutrality (2.50), the expression of current can be written as:

$$\mathbf{J} = -en_e \left(\mathbf{v}_e + \mathbf{v}_i \right) \quad (2.58)$$

This expression allows us to write velocity of electrons \mathbf{v}_e in terms of the velocity of ions \mathbf{v}_i and greatly simplifies the derivation of single fluid equations.

Impurity density equation

The equation of the density of neutral particles ρ_n is written by setting $\alpha = 0$ in the partial density equation in (2.44) as:

$$\frac{\partial \rho_n}{\partial t} + \nabla \cdot (\rho_n \mathbf{v}_n) = \dot{\rho}_n^{NA} + \dot{\rho}_n^A$$

Similarly, the equation for evolution of the charged impurity species ρ_c is written from the partial density equation in (2.44) by summing over $\alpha \in \{1, 2, \dots, N_z\}$ as:

$$\frac{\partial \rho_c}{\partial t} + \nabla \cdot (\rho_c \mathbf{v}_c) = \sum_{\alpha=1}^{N_z} \dot{\rho}_\alpha^{NA} + \sum_{\alpha=1}^{N_z} \dot{\rho}_\alpha^A$$

where, \mathbf{v}_c is the average velocity of charged impurity species given by (2.54). The source term related to atomic reactions $\dot{\rho}_\alpha^A$ involves the production or elimination of electrons as a result of the transfer of electrons from one species to another during

atomic processes. Since the mass of electron is assumed very small as compared to neutrals and charge impurities, the effect of sources due to atomic reaction can be neglected in the equation for neutrals density and charged species to write:

$$\begin{aligned}\frac{\partial \rho_n}{\partial t} + \nabla \cdot (\rho_n \mathbf{v}_n) &= \dot{\rho}_n^{NA} \\ \frac{\partial \rho_c}{\partial t} + \nabla \cdot (\rho_c \mathbf{v}_c) &= \dot{\rho}_c^{NA}\end{aligned}$$

Source terms in above equations can be combined to write:

$$\dot{\rho}_{\text{imp}} = \dot{\rho}_n^{NA} + \dot{\rho}_c^{NA} = \sum_{\alpha=1}^{N_z} \dot{\rho}_\alpha^{NA} \quad (2.59)$$

where $\dot{\rho}_{\text{imp}}$ is the source term that include the effect of neutral particles s as well charged impurities. Now, the evolution equation for total impurity density ρ_{imp} is obtained by summing the above two equations and using the definitions (2.52), (2.55) and (2.59) to write:

$$\frac{\partial \rho_{\text{imp}}}{\partial t} + \nabla \cdot (\rho_{\text{imp}} \mathbf{v}_{\text{imp}}) = \dot{\rho}_{\text{imp}}$$

The variable \mathbf{v}_{imp} is an additional vector variable that can be removed using Fick's law. By adding and subtracting the average velocity \mathbf{v} , the above equation becomes:

$$\frac{\partial \rho_{\text{imp}}}{\partial t} + \nabla \cdot (\rho_{\text{imp}} \mathbf{v}) = \nabla \cdot (\rho_{\text{imp}} (\mathbf{v} - \mathbf{v}_{\text{imp}})) + \dot{\rho}_{\text{imp}}$$

Here, \mathbf{v}_{imp} can be thought as the random velocity about the average velocity \mathbf{v} . Again, for each species α , the mass fraction is defined as:

$$Y_\alpha = \frac{\rho_\alpha}{\rho} \quad \text{s.t.} \quad \sum_{\alpha} Y_\alpha = 1$$

Now, defining the mass fraction for impurity density as $Y_{\text{imp}} = \rho_{\text{imp}}/\rho$, the first term at the right hand side in the impurity density equation can be written as

$$\nabla \cdot (\rho_{\text{imp}} (\mathbf{v} - \mathbf{v}_{\text{imp}})) = \nabla \cdot (\rho Y_{\text{imp}} (\mathbf{v} - \mathbf{v}_{\text{imp}}))$$

According to the Fick's law, this term can be modeled as a diffusion of Y_{imp} as:

$$\nabla \cdot (\rho Y_{\text{imp}} (\mathbf{v} - \mathbf{v}_{\text{imp}})) = \nabla \cdot (\rho \underline{\mathbf{D}}_{\text{imp}} \nabla Y_{\text{imp}})$$

with the density diffusion tensor $\underline{\mathbf{D}}_{\text{imp}}$. This term is approximated further as:

$$\nabla \cdot (\rho \underline{\mathbf{D}}_{\text{imp}} \nabla Y_{\text{imp}}) \approx \nabla \cdot (\underline{\mathbf{D}}_{\text{imp}} \nabla \rho_{\text{imp}})$$

and substituted in the impurity density equation to write:

$$\frac{\partial \rho_{\text{imp}}}{\partial t} + \nabla \cdot (\rho_{\text{imp}} \mathbf{v}) = \nabla \cdot (\underline{\mathbf{D}}_{\text{imp}} \nabla \rho_{\text{imp}}) + \dot{\rho}_{\text{imp}}$$

The impurity source $\dot{\rho}_{\text{imp}}$ is given by an ablation scaling law for ‘strongly shielded’ neutral gas shielding (NGS) model in a Maxwellian plasma which is used to determine the ablation rate [49, 83, 73]. Strongly shielded means the neutral gas cloud dissipates almost all the incoming heat flux before it reaches the pellet surface due to the smallness of the material’s ablation energy [49]. The exact ablation rate depends upon the material being injected in the plasma. The ablation models used in our study are: Sergeev’s model for full impurity pellets [83] and Parks’s model for mixed pellets [73]. The mathematical form of the impurity source is written as:

$$\begin{aligned} \dot{\rho}_{\text{imp}} &= m_{\text{imp}} \dot{n}_{\text{imp}} \\ &= m_{\text{imp}} \sum_{s=1}^N \partial_t N_s \exp\left(-\frac{(R - R_s)^2 + (Z - Z_s)^2}{\Delta R^2}\right) \exp\left(-\frac{(\phi - \phi_s)^2}{\Delta \phi^2}\right) \end{aligned} \quad (2.60)$$

where, s is the index over number of fragments N . The term $\partial_t N_s$ denotes ablation rate (i.e. the number of ablated atoms per second) of a fragment that depends upon electron temperature T_e and weakly upon the density n_e . The ablation rate for a spherical fragment with radius r_s is given by:

$$\partial_t N_s = f(X) r_s^{4/3} n_e^{1/3} T_e^{5/3}$$

A mixed injection of different gases considered is realized through $f(X)$ which is the function of the mixture of gases X . In this work, pellets with single impurity are considered ($f(X) = 1$) and details for the mixture of impurities can be found in [49]. The exponential term in the equation (2.60) denotes a Gaussian shape of an ablated cloud of a fragment. The coordinates R_s , Z_s and ϕ_s denote the location of the deposited fragments. We choose the neutral cloud parameter ΔR and $\Delta \phi$ to determine an elongated Gaussian shape of the neutral gas clouds. Such a choice of shape of deposit is justified due to the limited resolution in the toroidal direction. Moreover, the fast expansion of neutral clouds can not be modeled using fluid equations.

The coordinates R_s , Z_s and ϕ_s evolve in time as pellets/fragments are injected at some velocity \mathbf{u} . In principle, a following system of ODEs determines the evolution

of positions, velocity and size of ablated fragments:

$$\begin{aligned}\frac{d\boldsymbol{\mathcal{X}}}{dt} &= f(t, \boldsymbol{\mathcal{U}}) \\ \frac{d\boldsymbol{\mathcal{U}}}{dt} &= \boldsymbol{\mathcal{A}} \\ \frac{dr}{dt} &= g(r, \rho_e, T_e)\end{aligned}$$

where, the vector $\boldsymbol{\mathcal{X}} = \{R_s, Z_s, \phi_s\}$ denotes the position of the fragment, $\boldsymbol{\mathcal{A}}$ denotes the acceleration and r is the size of ablated cloud. For a situation considered here the injection velocity $\boldsymbol{\mathcal{U}}$ is assumed constant and the system of ODE reduces to:

$$\begin{aligned}\frac{d\boldsymbol{\mathcal{X}}}{dt} &= \boldsymbol{\mathcal{U}} \\ \frac{dr}{dt} &= g(r, \rho_e, T_e)\end{aligned}$$

The evolution of a fragment size is governed by the conservation of mass:

$$n_s 4 \pi r_s^2 \frac{dr_s}{dt} = \partial_t N_s$$

where n_s is the particle density of the fragments.

Total density equation

The equation of the total density ρ is obtained by summing the partial densities in equation (2.44) over all species $\alpha \in \{0, 1, \dots, N_z\}$ and is written using the definition for total density and average velocity (2.53), as:

$$\frac{\partial \rho}{\partial t} + \nabla \cdot (\rho \mathbf{v}) = \sum_{\alpha} \dot{\rho}_{\alpha}^A + \sum_{\alpha} \dot{\rho}_{\alpha}^{NA}$$

Sum of the sources from atomic reactions is zero on the account of conservation of mass, i.e., $\sum_{\alpha} \dot{\rho}_{\alpha}^A = 0$. The source terms for non atomic processes can be further decomposed into sources for main ions and impurities and the definition (2.59) can be used to write:

$$\sum_{\alpha} \dot{\rho}_{\alpha}^{NA} = \dot{\rho}_i^{NA} + \sum_0^{N_z} \dot{\rho}_z^{NA} = \dot{\rho}_i + \dot{\rho}_{\text{imp}}$$

Finally, substituting above term into the equation of the total density:

$$\frac{\partial \rho}{\partial t} + \nabla \cdot (\rho \mathbf{v}) = \dot{\rho}_i + \dot{\rho}_{\text{imp}}$$

Total momentum equation

The equation for the total momentum is obtained by summing the momentum equations in (2.44) over all species $\alpha \in \{i, e\} \cup \{0, 1, \dots, N_z\}$ to write:

$$\frac{\partial(\rho\mathbf{v})}{\partial t} + \nabla \cdot (\rho\mathbf{v} \otimes \mathbf{v}) + \nabla p - \mathbf{J} \times \mathbf{B} = \nabla \cdot \underline{\boldsymbol{\pi}} + \dot{\mathbf{m}}$$

where, the definitions of the average velocity (2.53), total pressure (2.56) and total current (2.58) are used in the first, third and fourth terms on the left hand side, respectively. Using the decomposition of particle velocities into average and random part about the average velocity as: $\mathbf{v}_\alpha = \mathbf{v} + \mathbf{v}'_\alpha$, the second term at the right hand side is written and the viscous stress tensor is defined as:

$$\underline{\boldsymbol{\pi}} = \sum_{\alpha} \underline{\boldsymbol{\pi}}_{\alpha} - \sum_{\alpha} \rho_{\alpha} \mathbf{v}'_{\alpha} \otimes \mathbf{v}'_{\alpha}$$

The source terms $\dot{\mathbf{m}}$ contain the sum of sources from all species with contributions only from the non atomic parts because the sum of sources due to atomic reactions vanishes due to conservation of the momentum:

$$\dot{\mathbf{m}} = \sum_{\alpha} \dot{\mathbf{m}}_{\alpha}^A + \sum_{\alpha} \dot{\mathbf{m}}_{\alpha}^{NA}$$

Energy equation

We assume that the ratio of specific heats of all species is equal $\gamma_i = \gamma_e = \gamma_{\alpha} = 5/3$. The energy equations are written in terms of the pressure, as can be seen from equation for electron pressure (2.46) and ions pressure (2.47). The electron pressure equation can be simplified using quasi-neutrality assumption on the current given by equation (2.58) and the assumption that electron mass is negligible to write:

$$\frac{1}{(\gamma - 1)} \left(\frac{\partial p_e}{\partial t} + \mathbf{v} \cdot \nabla p_e + \gamma p_e \nabla \cdot \mathbf{v} \right) = \underline{\boldsymbol{\pi}}_e : \nabla \mathbf{v} + \nabla \cdot \mathbf{h}_e + Q_e + S_{T_e} - C_{\text{ion}} \quad (2.61)$$

where the term S_{T_e} contains the sources due to non atomic processes along with Ohmic heating:

$$S_{T_e} = \eta \mathbf{J} \cdot \mathbf{J} + P(T_e) - \dot{\mathbf{m}}_e \cdot \mathbf{v} + \frac{\dot{\rho}_i + \dot{\rho}_{\text{imp}}}{2} \mathbf{v} \cdot \mathbf{v}$$

where $P(T_e)$ denotes radiation power loss. The last term in the equation (2.61) contains energy sources due to atomic reactions that are modeled in terms of ionization

potential energy E_{imp} as :

$$C_{\text{ion}} = \left(\frac{\partial(\rho_{\text{imp}}E_{\text{ion}})}{\partial t} + \nabla \cdot (\rho_{\text{imp}}E_{\text{ion}}\mathbf{v}_{\text{imp}}) \right)$$

The ion temperature equation is obtained from equation (2.49) by summing over all the species other than electrons with the additional assumption that all ion species are at the same temperature to write:

$$\frac{1}{(\gamma - 1)} \left(\frac{\partial p_I}{\partial t} + \mathbf{v} \cdot \nabla p_I + \gamma p_I \nabla \cdot \mathbf{v} \right) = \underline{\boldsymbol{\pi}}_I : \nabla \mathbf{v} + \nabla \cdot \mathbf{h}_I + Q_I + S_{T_I} \quad (2.62)$$

here, the pressure p_I denotes the pressure due to all the species except electrons and S_{T_I} contains the sources due to non atomic processes.

$$S_{T_I} = -\dot{\mathbf{m}}_I \cdot \mathbf{v} + \frac{\dot{\rho}_i + \dot{\rho}_{\text{imp}}}{2} \mathbf{v} \cdot \mathbf{v}$$

Finally summing the equations of T_e (2.48) and T_I (2.49), the equation for the total pressure is obtained which is written as:

$$\frac{1}{(\gamma - 1)} \left(\frac{\partial p}{\partial t} + \mathbf{v} \cdot \nabla p + \gamma p \nabla \cdot \mathbf{v} \right) = \underline{\boldsymbol{\pi}} : \nabla \mathbf{v} + \nabla \cdot \mathbf{h} + S_T - C_{\text{ion}} \quad (2.63)$$

where, the term S_T contains the sources due to Ohmic heating and non atomic processes:

$$S_T = \eta \mathbf{J} \cdot \mathbf{J} + P(T_e) - \dot{\mathbf{m}} \cdot \mathbf{v} + \frac{\dot{\rho}_i + \dot{\rho}_{\text{imp}}}{2} \mathbf{v} \cdot \mathbf{v} \quad (2.64)$$

The term $P(T_e)$ is given by

$$P(T_e) = -n_e n_{\text{imp}} L_{\text{rad}}(T_e) \quad (2.65)$$

where, L_{rad} represents the radiation power function obtained via the CE assumption and includes the contribution from line radiation, recombination radiation and bremsstrahlung radiation. The term C_{ion} has the additional variable \mathbf{v}_{imp} . It can be eliminated using Fick's law. The last term in C_{ion} can be rearranged by adding and subtracting \mathbf{v} as:

$$C_{\text{ion}} = \left(\frac{\partial(\rho_{\text{imp}}E_{\text{ion}})}{\partial t} + \nabla \cdot (\rho_{\text{imp}}E_{\text{ion}}\mathbf{v}) + \nabla \cdot (\rho_{\text{imp}}E_{\text{ion}}(\mathbf{v}_{\text{imp}} - \mathbf{v})) \right)$$

Using the definition of mass fraction for impurity species Y_{imp} the last term can be written as: $\nabla \cdot (\rho Y_{\text{imp}} E_{\text{ion}} (\mathbf{v}_{\text{imp}} - \mathbf{v}))$ so that the Fick's law can be applied to write the expression for C_{ion} as:

$$C_{\text{ion}} = \left(\frac{\partial(\rho_{\text{imp}}E_{\text{ion}})}{\partial t} + \nabla \cdot (\rho_{\text{imp}}E_{\text{ion}}\mathbf{v}) + \nabla \cdot (\rho E_{\text{ion}} \underline{\mathbf{D}}_{\text{imp}} \nabla Y_{\text{imp}}) \right)$$

Further, the last term can be approximated to $\nabla \cdot (E_{\text{ion}} \underline{D}_{\text{imp}} \nabla \rho_{\text{imp}})$ and the remaining terms can be simplified to write the expression for C_{ion} as:

$$C_{\text{ion}} = E_{\text{ion}} \left(\frac{\partial \rho_{\text{imp}}}{\partial t} + \mathbf{v} \cdot \nabla \rho_{\text{imp}} \right) + \rho_{\text{imp}} \left(\frac{\partial E_{\text{ion}}}{\partial t} + \nabla \cdot (E_{\text{ion}} \mathbf{v}) \right) + \nabla \cdot (E_{\text{ion}} D_{\text{imp}} \nabla \rho_{\text{imp}}) \quad (2.66)$$

This expression is substituted in the equation for the total pressure (2.63) where E_{ion} is given by the equation (2.51).

Induction equation

The induction equation is not affected by summation over species. The resistivity, apart from Spitzer like dependence, is also considered to depend upon the effective charge Z_{eff} which is defined as:

$$Z_{\text{eff}} = \frac{\sum_{\alpha} n_{\alpha} Z_{\alpha}^2}{\sum_{\alpha} n_{\alpha} Z_{\alpha}}$$

where n_{α} and Z_{α} are the particle densities and charge of each species α . The expression for the resistivity is written as [96, 49]:

$$\eta = \frac{\sqrt{2m_e} Z_{\text{eff}} e^2 \ln(\Lambda)}{12 \pi^{3/2} \epsilon_0^2 T_e^{3/2}} \frac{1 + 1.198 Z_{\text{eff}} + 0.222 Z_{\text{eff}}^2}{1 + 2.966 Z_{\text{eff}} + 0.753 Z_{\text{eff}}^2} \quad (2.67)$$

The equations for ρ , ρ_{imp} , \mathbf{v} , T , \mathbf{A} along with Gauss law and Ampère's law forms the MHD model with sources to be used for SPI simulations.

Single and two temperature models

In summary, we re-write equations by collecting them as a system of MHD equation with single temperature and two temperature model. The single temperature model is written below by collecting the equations for impurity density, total density, total

momentum, total pressure and the induction equation as follows:

$$\begin{aligned}
\frac{\partial \rho_{\text{imp}}}{\partial t} + \nabla \cdot (\rho_{\text{imp}} \mathbf{v}) &= \nabla \cdot (\underline{\mathbf{D}}_{\text{imp}} \nabla \rho_{\text{imp}}) + \dot{\rho}_{\text{imp}} \\
\frac{\partial \rho}{\partial t} + \nabla \cdot (\rho \mathbf{v}) &= \nabla \cdot (\underline{\mathbf{D}} \nabla \rho) + \dot{\rho}_i + \dot{\rho}_{\text{imp}} \\
\frac{\partial (\rho \mathbf{v})}{\partial t} + \nabla \cdot (\rho \mathbf{v} \otimes \mathbf{v}) + \nabla p - \mathbf{J} \times \mathbf{B} &= \mu \nabla^2 \mathbf{v} + \dot{\mathbf{m}} \\
\frac{1}{(\gamma - 1)} \left(\frac{\partial p}{\partial t} + \mathbf{v} \cdot \nabla p + \gamma p \nabla \cdot \mathbf{v} \right) &= \mu \nabla \mathbf{v} : \nabla \mathbf{v} + \nabla \cdot (\underline{\boldsymbol{\kappa}} \nabla T) + S_T - C_{\text{ion}} \\
\frac{\partial \mathbf{A}}{\partial t} - \mathbf{v} \times \mathbf{B} &= -\eta \mathbf{J}
\end{aligned} \tag{2.68}$$

with Gauss law $\nabla \cdot \mathbf{B} = 0$ and Ampères law $\nabla \times \mathbf{B} = \mathbf{J}$. The definition of viscous tensor: $\underline{\boldsymbol{\pi}} = \mu \nabla \mathbf{v}$ and as heat conduction flux: $\mathbf{h} = \underline{\boldsymbol{\kappa}} \nabla T$ is used in the equation for velocity and pressure respectively. The density diffusion is added in the equation of ρ . The form of the total density and impurity density diffusion tensor is given by equation (2.40) and that of heat diffusion tensor is given by equation (2.39). The source term S_T is given by equations (2.64) and (2.65) while C_{ion} is given by equations (2.66) and (2.51).

The two temperature model is written below by collecting the equations for impurity density, total density, total momentum, electron pressure, ion pressure and the induction equation as follows:

$$\begin{aligned}
\frac{\partial \rho_{\text{imp}}}{\partial t} + \nabla \cdot (\rho_{\text{imp}} \mathbf{v}) &= \nabla \cdot (\underline{\mathbf{D}}_{\text{imp}} \nabla \rho_{\text{imp}}) + \dot{\rho}_{\text{imp}} \\
\frac{\partial \rho}{\partial t} + \nabla \cdot (\rho \mathbf{v}) &= \nabla \cdot (\underline{\mathbf{D}} \nabla \rho) + \dot{\rho}_i + \dot{\rho}_{\text{imp}} \\
\frac{\partial (\rho \mathbf{v})}{\partial t} + \nabla \cdot (\rho \mathbf{v} \otimes \mathbf{v}) + \nabla p - \mathbf{J} \times \mathbf{B} &= \nabla \cdot \underline{\boldsymbol{\pi}} + \dot{\mathbf{m}} \\
\frac{1}{(\gamma - 1)} \left(\frac{\partial p_e}{\partial t} + \mathbf{v} \cdot \nabla p_e + \gamma p_e \nabla \cdot \mathbf{v} \right) &= \underline{\boldsymbol{\pi}}_e : \nabla \mathbf{v} + \nabla \cdot \mathbf{h}_e + Q_e + S_{T_e} - C_{\text{ion}} \\
\frac{1}{(\gamma - 1)} \left(\frac{\partial p_I}{\partial t} + \mathbf{v} \cdot \nabla p_I + \gamma p_I \nabla \cdot \mathbf{v} \right) &= \underline{\boldsymbol{\pi}}_I : \nabla \mathbf{v} + \nabla \cdot \mathbf{h}_I + Q_I + S_{T_I} \\
\frac{\partial \mathbf{A}}{\partial t} - \mathbf{v} \times \mathbf{B} &= -\eta \mathbf{J}
\end{aligned} \tag{2.69}$$

All the source, diffusive and dissipative terms have the same meaning and form as in case of single temperature model, except that the source terms due to Ohmic heating and atomic reaction are to be included in the equation for electron pressure.

2.4 Conclusion

This Chapter is introduced with the plasma interactions and basic atomic process that take place in plasma. The equations for plasma physics are described on microscopic and macroscopic level in the section (2.1). The series of assumptions are noted to get a hierarchy of models from kinetic to multi fluid to single fluid model. The focus of the present work is on plasma dynamics that can be modeled using MHD equations.

In the section (2.2), full MHD model is described including resistive and dissipative terms and the variables are normalized with respect to the scales relevant for tokamak modeling. It is emphasized that a magnetic vector potential formulation is used to write the induction equation in terms of magnetic vector potential \mathbf{A} instead of magnetic field \mathbf{B} . The Grad-Shafranov equation that governs ideal MHD equilibrium in axisymmetric configuration is described. Plasma equilibrium, if perturbed, can develop instabilities that are related to parallel current and pressure gradient. It is noted that rational q surfaces are the likely locations of plasma instabilities. The difference between full and reduced MHD models is briefly noted.

Finally, the neutrals and impurity transport terms are included in full MHD model which can be used for MGI and SPI simulations. The detailed derivation of transport and source terms is presented in the section (2.3) with the discussion of atomic reactions involved. Underlying assumption of CE is described. The assumption that the ionization potential energy does not effect the pressure of impurities is crucial in obtaining a closed system of equations that does not involve evolution of each charged state.

The governing equations for plasma physics written in this Chapter are nonlinear PDEs. In the next Chapter, numerical methods used to discretize these PDEs are discussed.

Chapter 3

Numerical methods

The purpose of this Chapter is to describe numerical approximation techniques of full magneto-hydrodynamic (MHD) equations described in Chapter 2. These MHD equations nonlinear hyperbolic partial differential equations (PDEs), except Grad-Shafranov equation which is a non-linear elliptic PDE. The strong form of MHD equations for the vector of variables: $\mathbf{y}(\mathbf{x}, t)$, where $(\mathbf{x}, t) \in \mathbb{R}^{nv} \times \mathbb{R}_+$, defined over the spatial domain $\Omega \subset \mathbb{R}^d$ is written as:

$$\begin{aligned}\forall \mathbf{x} \in \Omega, t > 0 : & \quad \mathcal{R}(\mathbf{y}) = 0 \\ \forall \mathbf{x} \in \Omega, t = 0 : & \quad \mathbf{y} = \mathbf{y}_0 \\ \forall \mathbf{x} \in \Gamma_D, t > 0 : & \quad \mathbf{y} = \mathbf{y}_D \\ \forall \mathbf{x} \in \Gamma_N, t > 0 : & \quad \mathbf{n} \cdot \underline{\kappa} \nabla \mathbf{y} = \mathbf{y}_N\end{aligned}\tag{3.1}$$

Here, nv and d represent the number of variables and spatial dimensions respectively; \mathcal{R} is residual of the strong form. The second equation specifies initial condition \mathbf{y}_0 . The boundary of the domain is $\partial\Omega = \Gamma_D \cup \Gamma_N$ with $\Gamma_D \cap \Gamma_N = \emptyset$ where, Γ_D and Γ_N are parts of the boundary where Dirichlet and Neumann (or Robin) boundary conditions are to be applied respectively. This decomposition of the boundary is for representation purpose. In practice, boundary conditions can be applied separately for each variable i.e. given $\mathbf{y} \in \{y_k\}$, for each variable y_k there can be a division of boundary such that $\partial\Omega_k = \Gamma_{D_k} \cup \Gamma_{N_k}$ with $\Gamma_{D_k} \cap \Gamma_{N_k} = \emptyset$. The problem in strong form (3.1) is assumed to be well-posed in the sense that it describes relevant MHD physics for plasma dynamics and boundary conditions are taken from experimental data. The vector \mathbf{y} denotes the variables: $\mathbf{y} = \{\rho, \rho\mathbf{v}, p, \mathbf{A}\}^T$ for which MHD equations are written in Chapter 2.

The residual of the strong form above can be also represented in transport, advective, diffusive and reactive (TADR) [90] form:

$$\mathcal{R}(\mathbf{w}) = \underline{\mathbf{M}} \frac{\partial \mathbf{w}}{\partial t} + \underline{\mathbf{C}}(\mathbf{w}) \nabla \mathbf{w} - \mathbf{d}(\mathbf{w}) - \mathbf{s}(\mathbf{w}) = 0 \quad (3.2)$$

where, \mathbf{w} is another set of variables such that: $\partial_t \mathbf{y} = \underline{\mathbf{M}}(\mathbf{w}) \partial_t \mathbf{w}$. The notations $\underline{\mathbf{C}}(\mathbf{w}) \nabla$, $\mathbf{d}(\mathbf{w})$ and $\mathbf{s}(\mathbf{w})$ denote convective operator, diffusive terms and source terms respectively. For example, for the full MHD system (2.38) the vector of variables \mathbf{w} can be given as: $\mathbf{w} = \{\rho, \mathbf{v}, T, \mathbf{A}\}^T$, whereas the matrix $\underline{\mathbf{M}}(\mathbf{w})$ and the operator $\underline{\mathbf{C}}(\mathbf{w}) \nabla$ can be given as:

$$\underline{\mathbf{M}}(\mathbf{w}) = \begin{bmatrix} 1 & 0 & 0 & 0 \\ 0 & \rho \mathbf{I} & 0 & 0 \\ T & 0 & \rho & 0 \\ 0 & 0 & 0 & \mathbf{I} \end{bmatrix}, \quad \underline{\mathbf{C}}(\mathbf{w}) \nabla = \begin{bmatrix} \mathbf{v} \cdot \nabla & \rho \nabla \cdot & 0 & 0 \\ T \nabla & \rho \mathbf{v} \cdot \nabla & \rho \nabla & 0 \\ T \mathbf{v} \cdot \nabla & \gamma p \nabla \cdot & \rho \mathbf{v} \cdot \nabla & 0 \\ 0 & 0 & 0 & -\mathbf{v} \times \nabla \times \end{bmatrix}$$

The operator $\underline{\mathbf{C}}(\mathbf{w}) \nabla$ is associated with the convective (hyperbolic) terms. The vector of diffusive terms $\mathbf{d}(\mathbf{w})$ and source terms $\mathbf{s}(\mathbf{w})$ are written as:

$$\mathbf{d}(\mathbf{w}) = \begin{pmatrix} \nabla \cdot (\underline{\mathbf{D}} \nabla \rho) \\ \nabla \cdot (\mu \nabla \mathbf{v}) \\ \nabla \cdot (\underline{\boldsymbol{\kappa}} \nabla T) \\ -\eta (\nabla \times \nabla \times \mathbf{A}) \end{pmatrix}, \quad \mathbf{s}(\mathbf{w}) = \begin{pmatrix} S_\rho \\ -\mathbf{J} \times \mathbf{B} + \mathbf{S}_v \\ S_T \\ \eta \mathbf{S}_J \end{pmatrix}$$

The diffusive and source terms are described in Section (2.2.5) for visco-resistive full MHD model. Except the last term from the induction equation, the vector of diffusive terms $\mathbf{d}(\mathbf{w})$ can be written as divergence of diffusive fluxes $\underline{\boldsymbol{\Gamma}}(\mathbf{w}) = \{\underline{\mathbf{D}} \nabla \rho, \mu \nabla \mathbf{v}, \underline{\boldsymbol{\kappa}} \nabla T, 0\}^T$.

The properties of MHD phenomena like convection dominated flows, presence of strong anisotropies in magnetized plasma and divergence free constrain on the magnetic field, motivates the choices of certain numerical schemes to be used. For convection dominated flows, numerical schemes must take into account the effects of unresolved scales in order to insure stability of the numerical approach. In the context of compressible hydrodynamics, the pioneering work of von-Neumann and Richtmyer [93] and its 2D extension by Wilkins [97, 98], the effects of unresolved scale on the

resolved scales are formulated as artificial viscosity. In [55], explicit evaluation of sub-scale effects is made on the resolved scales via the resolution of the so-called Riemann problems. However, these popular formulations are mainly applicable in finite volume and discontinuous Galerkin methods. Riemann problems are defined in the directions normal to the mesh faces and have inherent numerical stabilization and hence are highly dependent on the mesh topology. Such stabilizing effect can be undesirable for the flows with strong anisotropic processes, as in strongly magnetized plasma.

In this context, the high-order Galerkin finite element method (FEM) can provide a suitable framework for the numerical approximation. Galerkin FEM however gives rise to the centered approximations of differential operators which can lead to dispersion errors for convection dominated flows. Galerkin FEM alone does not provide a mechanism for the control of the sub-scales effects on the resolved scales: ‘stabilization’. The variational multi-scale (VMS) formulation [18, 53, 51] provides attractive guidelines for the development of stabilized schemes that take into account the effect of unresolved scales. Within the VMS framework, stabilization of waves is achieved by an additional contribution in the weak formulation. In this way, an upwinding process is introduced which leads to numerical diffusion essentially in the flow direction, so as to avoid crosswind diffusion effects for multidimensional flows over non-aligned meshes. In the section (3.1), we describe general formulation for Galerkin FEM and VMS based stabilization terms.

The divergence free constrain $\nabla \cdot \mathbf{B} = 0$ is another important factor deciding the numerical scheme. At the discrete level, the divergence free constrain is not guaranteed to satisfy and even small errors in $\nabla_h \cdot \mathbf{B}$ can cause large errors in numerical simulations [14, 25]. There are strategies to overcome this difficulty for finite volume methods as described in [91]. In case of FEM a special space of basis functions to be satisfied divergence free constrain at discrete level may be used. The vector potential formulation, as described in Chapter 2, can lead to a MHD system with third order derivative terms (in reduced MHD models) and the divergence free constraint to be satisfied becomes:

$$\nabla_h \cdot (\nabla_h \times \mathbf{A}) = 0$$

Therefore, a design of FEM with at least continuous gradients ($\mathcal{C}1$ -continuity) over the finite elements is desired. In the section (3.2) we describe the construction of a finite dimensional space for FEM to achieve this goal. In section (3.3), the time integration method adapted to variable time stepping is described.

The grid generation for realistic geometries is described in the section (3.4). With the iso-parametric mapping, the grid and physical variables are interpolated using the same order of interpolation. This allows us to construct curved finite elements so that a grid can be aligned to flux surfaces and curved boundaries can be accurately represented. The issue with grid singularities is then addressed and a strategy is proposed to cure numerical problems arising at the polar grid center.

3.1 Finite element method and stabilization

3.1.1 Galerkin finite element method

The variational form of the problem (3.2) is obtained by multiplying the strong form by a test function \mathbf{w}^* (with a certain level of regularity) and integrating over the domain Ω to write:

$$\int_{\Omega} \mathbf{w}^* \cdot \mathcal{R}(\mathbf{w}) \, d\Omega = 0$$

Defining the L^2 scalar product: $(f, g) = \int_{\Omega} f \cdot g \, d\Omega$, the weak formulation of the problem can be written as: Find trial functions $\mathbf{w} \in \mathcal{S}$ where

$$\mathcal{S} := \{\mathbf{w} | \mathbf{w}(\mathbf{x}, t) \in (H(\Omega)^{nv} \times (0, \infty)), \forall \mathbf{x} \in \Gamma_p : \mathbf{w}(\mathbf{x}, 0) = \mathbf{w}_0\}$$

such that, for all test functions $\mathbf{w}^* \in \mathcal{V}$ where

$$\mathcal{V} := \{\mathbf{w}^* | \mathbf{w}^*(\mathbf{x}) \in (H(\Omega)^{nv} \times (0, \infty)), \forall \mathbf{x} \in \Gamma_p : \mathbf{w}^*(\mathbf{x}) = 0\}$$

the residual evaluated with the trial function is orthogonal to the test function space, i.e.:

$$(\mathbf{w}^*, \mathcal{R}(\mathbf{w}))_{\Omega} = 0 \tag{3.3}$$

Galerkin FEM consists of taking a projection of this infinite dimensional (continuous) weak form to get a finite dimensional (discretized) weak form. The domain Ω is ‘triangulated’ by dividing into finite number of non-overlapping elements Ω_e such that:

$$\Omega_h = \bigcup_e \Omega_e$$

Then the discrete weak form becomes: Find trial functions $\mathbf{w}_h \in \mathcal{S}_h$ where

$$\mathcal{S}_h := \{\mathbf{w}_h | \mathbf{w}_h(\mathbf{x}, t) \in (H(\Omega)^{nv} \times (0, \infty)), \forall \mathbf{x} \in \Gamma_p : \mathbf{w}_h = \mathbf{w}_0\}$$

such that, for all test functions $\mathbf{w}_h^* \in \mathcal{V}_h$ where

$$\mathcal{V}_h := \{\mathbf{w}_h^* | \mathbf{w}_h^*(\mathbf{x}) \in (H(\Omega)^{nv} \times (0, \infty)), \forall \mathbf{x} \in \Gamma_p : \mathbf{w}_h^* = 0\}$$

the residual evaluated with the trial function is orthogonal to the test function space, i.e.:

$$(\mathbf{w}_h^*, \mathcal{R}(\mathbf{w}_h))_{\Omega_h} = 0 \quad (3.4)$$

The discretized domain Ω_h , construction or choice of the space of test functions \mathcal{V}_h and the basis for nodal variables (\mathcal{N}) defines the FEM and the capability of the method to resolve the scales in the physical problem. Before describing the space of test functions and basis functions for FEM, we describe the stabilized FEM based on VMS formulation in the following subsection.

3.1.2 Variable Multi-scale formulation

VMS formulation [18, 53, 51] consists of a decomposition of scales in the problem. The purpose of scale decomposition can be development of physical/mathematical models, for example, Reynolds stresses for incompressible flows. Here, we are concerned with the modeling of unresolved or sub-grid scales, which involves approximations to the local numerical solution of the problem. We consider the decomposition of the solution \mathbf{w} as large scales ($\bar{\mathbf{w}}$) which are resolved by FEM and fine scales (\mathbf{w}') that FEM can not capture i.e.

$$\mathbf{w} = \bar{\mathbf{w}} + \mathbf{w}'$$

Test functions \mathbf{w}^* are decomposed in the similar way.

$$\mathbf{w}^* = \bar{\mathbf{w}}^* + \mathbf{w}'^*$$

The decomposition for the trial and test functions are such that $\mathcal{S} = \bar{\mathcal{S}} \oplus \mathcal{S}'$ and $\mathcal{V} = \bar{\mathcal{V}} \oplus \mathcal{V}'$, where $\bar{\mathcal{S}}$ and $\bar{\mathcal{V}}$ are the function spaces for large scales while \mathcal{S}' and \mathcal{V}' are function spaces for fine scales. Now the weak formulation (3.3) can be re-written as:

$$((\bar{\mathbf{w}}^* + \mathbf{w}'^*), \mathcal{R}(\bar{\mathbf{w}} + \mathbf{w}'))_{\Omega} = 0$$

The orthogonality of the spaces allows us to separate the problem into two different ones, i.e., the problem for large and fine scales:

$$\forall \bar{\mathbf{w}} \in \bar{\mathcal{S}}, \mathbf{w}' \in \mathcal{S}', \bar{\mathbf{w}}^* \in \bar{\mathcal{V}} \quad (\bar{\mathbf{w}}^*, \mathcal{R}(\bar{\mathbf{w}} + \mathbf{w}'))_{\Omega} = 0 \quad (3.5)$$

$$\forall \bar{\mathbf{w}} \in \bar{\mathcal{S}}, \mathbf{w}' \in \mathcal{S}', \bar{\mathbf{w}}^* \in \mathcal{V}' \quad (\mathbf{w}'^*, \mathcal{R}(\bar{\mathbf{w}} + \mathbf{w}'))_{\Omega} = 0 \quad (3.6)$$

The VMS approach can be used to obtain an equation for large scales alone. The residual can be approximated as:

$$\mathcal{R}(\bar{\mathbf{w}} + \mathbf{w}') = \mathcal{R}(\bar{\mathbf{w}}) + \underline{\mathbf{L}}(\bar{\mathbf{w}}, \partial)\mathbf{w}'$$

where, $\underline{\mathbf{L}}(\bar{\mathbf{w}}, \partial)\mathbf{w}'$ is the effect of unresolved scales and $\underline{\mathbf{L}}$ is the transport operator for the residual \mathcal{R} . Using above expansion into Eq. (3.5), large scale problem becomes:

$$(\bar{\mathbf{w}}^*, \mathcal{R}(\bar{\mathbf{w}}))_{\Omega} + (\bar{\mathbf{w}}^*, \underline{\mathbf{L}}(\bar{\mathbf{w}}, \partial)\mathbf{w}')_{\Omega} = 0$$

Further, using adjoint duality:

$$(\bar{\mathbf{w}}^*, \mathcal{R}(\bar{\mathbf{w}}))_{\Omega} + (\underline{\mathbf{L}}^T(\bar{\mathbf{w}}, \partial)\bar{\mathbf{w}}^*, \mathbf{w}')_{\Omega} = 0$$

where $\underline{\mathbf{L}}^T$ is the adjoint operator of $\underline{\mathbf{L}}$. Using the decomposition of the residual $\mathcal{R}(\bar{\mathbf{w}} + \mathbf{w}')$ into Eq. (3.6) the problem statement for fine scale is written as:

$$(\mathbf{w}'^*, \mathcal{R}(\bar{\mathbf{w}}) + \underline{\mathbf{L}}(\bar{\mathbf{w}}, \partial)\mathbf{w}')_{\Omega} = 0$$

Since this equation is true for any \mathbf{w}'^* , we can write:

$$\mathcal{R}(\bar{\mathbf{w}}) + \underline{\mathbf{L}}(\bar{\mathbf{w}}, \partial)\mathbf{w}' = 0$$

which gives the estimation for fine scales:

$$\mathbf{w}' = -\underline{\mathbf{L}}^{-1}(\bar{\mathbf{w}}, \partial) \mathcal{R}(\bar{\mathbf{w}})$$

If $\underline{\mathbf{L}}$ is a linear operator, then it is possible to express $\underline{\mathbf{L}}^{-1}$ in terms of the Green's function for the operator $\underline{\mathbf{L}}$ [52] and the projector operator onto the finite elements space. Now the VMS formulation can be written in terms of large scales alone:

$$(\bar{\mathbf{w}}^*, \mathcal{R}(\bar{\mathbf{w}}))_{\Omega} - (\underline{\mathbf{L}}^T(\bar{\mathbf{w}}, \partial)\bar{\mathbf{w}}^*, \underline{\mathbf{L}}^{-1}(\bar{\mathbf{w}}, \partial) \mathcal{R}(\bar{\mathbf{w}}))_{\Omega} = 0$$

where $\underline{\mathbf{L}}^T$ is the transpose of the operator $\underline{\mathbf{L}}$. The operator $\underline{\mathbf{L}}$ is not always simple to invert and may lead to a problem which is more complex than the original problem and therefore to obtain a tractable and computationally efficient method, the VMS

formulation relies on approximations for the \mathbf{w}' . In practice, algebraic formulations are used in which the operator $\underline{\mathbf{L}}^{-1}$ is approximated as intrinsic time-scale matrix $\underline{\mathbf{T}}$ and hence the approximate estimation of fine scale becomes:

$$\mathbf{w}' = -\underline{\mathbf{T}} \mathcal{R}(\bar{\mathbf{w}})$$

Using this estimate, the VMS formulation is then written as:

$$\forall \bar{\mathbf{w}}^* \in \mathcal{V}_h, \bar{\mathbf{w}} \in \mathcal{S}_h \quad (\bar{\mathbf{w}}^*, \mathcal{R}(\bar{\mathbf{w}}))_{\Omega} - (\underline{\mathbf{L}}^T(\bar{\mathbf{w}}, \partial)\bar{\mathbf{w}}^*, \underline{\mathbf{T}} \mathcal{R}(\bar{\mathbf{w}}))_{\Omega} = 0 \quad (3.7)$$

The first term in above equation comes from FEM while the second term give is the stabilization scheme for a FEM based on VMS formulation. Many stabilization approaches can be obtained from the VMS stabilization scheme depending upon the choice of the stabilization operator, for example, if one chooses the operator $\underline{\mathbf{L}}$ instead of the adjoint $\underline{\mathbf{L}}^T$ then streamline-upwind/Petrov-Galerkin (SUPG) scheme is retrieved.

3.2 Finite Element Method for tokamak modeling

3.2.1 Mixed Bi-cubic Bézier-spectral FEM

Recalling the discrete weak form (3.4): Find $\mathbf{w}_h \in \mathcal{S}_h$ such that

$$(\mathbf{w}_h^*, \mathcal{R}(\mathbf{w}_h))_{\Omega_h} = \int_{\Omega_h} \mathbf{w}_h^* \cdot \mathcal{R}(\mathbf{w}_h) d\Omega_h = 0 \quad \forall \mathbf{w}_h^* \in \mathcal{V}_h \quad (3.8)$$

First, the domain Ω needs to be discretized. Geometry of a tokamak device is toroidal and hence the domain Ω can be decomposed as a poloidal plane ($\boldsymbol{\xi} = \{R, Z\}^T \in \Omega_{\boldsymbol{\xi}}$) and the periodic toroidal direction ($\phi \in [0, 2\pi[$) such that $\Omega = \Omega_{\boldsymbol{\xi}} \times \Omega_{\phi}$. Therefore, the differential $d\Omega$ is written as: $d\Omega = d\Omega_{\boldsymbol{\xi}} d\Omega_{\phi} = d\Omega_{\boldsymbol{\xi}} d\phi$. The grid generation in JOREK, discussed later in detail, is essentially a discretization of 2D poloidal plane $\Omega_{\boldsymbol{\xi}}$ into non-overlapping elements Ω_e such that:

$$\Omega_{\boldsymbol{\xi}_h} = \bigcup_e \Omega_e$$

In the periodic direction, the grid is realized via Fourier representation. Therefore, the space \mathcal{V}_h is a tensor product of the space of functions in the poloidal plane ($\mathcal{V}_{\boldsymbol{\xi}}$) and that in the toroidal direction (\mathcal{V}_{ϕ}). The space \mathcal{V}_h is spanned by the basis functions V_i such that:

$$\mathcal{V}_h = \mathcal{V}_{\boldsymbol{\xi}}(\Omega_{\boldsymbol{\xi}}) \times \mathcal{V}_{\phi}([0, 2\pi[) = \text{SPAN}\{V_i(\boldsymbol{\xi}, \phi)\}$$

where,

$$V_i(\boldsymbol{\xi}, \theta) = N_{i_{2D}}(\boldsymbol{\xi}) C_{i_\phi}(\phi)$$

and the spaces \mathcal{V}_ξ and \mathcal{V}_ϕ are spanned by the functions $N_{i_{2D}}(\boldsymbol{\xi})$ and $C_{i_\phi}(\phi)$ respectively. The index i is a multi-component index such that $i = (i_{2D}, i_\phi)$ with $i_{2D} \in \{1, \dots, N_{2D}\}$ and $i_\phi \in \{1, \dots, N_\phi\}$ where N_{2D} and N_ϕ denote the dimensions of the poloidal and toroidal spaces respectively. A trial function for FEM is then written as:

$$\mathbf{w}_h(\boldsymbol{\xi}, \phi, t) = \sum_{i=1}^{N_{2D} N_\phi} \mathbf{w}_i(t) V_i(\boldsymbol{\xi}, \phi) = \sum_{i=1}^{N_{2D} N_\phi} \mathbf{w}_i(t) N_{i_{2D}}(\boldsymbol{\xi}) C_{i_\phi}(\phi)$$

where, degrees of freedom $\mathbf{w}_i(t)$ are function of time t . In Galerkin FEM the trial and test functions belong to the same space and hence the test functions are written as:

$$\mathbf{w}_h^*(\boldsymbol{\xi}, \phi) = \sum_{i=1}^{N_{2D} N_\phi} \mathbf{w}_i^* V_i(\boldsymbol{\xi}, \phi) = \sum_{i=1}^{N_{2D} N_\phi} \mathbf{w}_i^* N_{i_{2D}}(\boldsymbol{\xi}) C_{i_\phi}(\phi)$$

Now, the discrete weak form (3.8) is written as:

$$\int_{\phi} \int_{\Omega_{\boldsymbol{\xi}_h}} \mathbf{w}_i^* V_i \cdot \mathcal{R} \left(\sum_j \mathbf{w}_j(t) V_j \right) d\Omega_{\boldsymbol{\xi}} d\phi = 0 \quad \forall i \quad (3.9)$$

The basis functions $N_{i_{2D}}$ are constructed such that continuous representation of a function \mathbf{w}_h and their gradients is obtained. From algorithmic implementation point of view, it is necessary to know what is the form of these functions on any given element Ω_e in $\Omega_{\boldsymbol{\xi}_h}$ and how the restrictions of these functions match across adjacent elements. The idea is to evaluate the weak form written above for any given element Ω_e and then assemble the contributions of all elements to get the global system of discrete equations. In order to do so, the ‘finite element’ (Ω_e, Q, Σ) is defined [21] as follows:

- 1) Ω_e is a subdivision of a domain $\Omega_{\boldsymbol{\xi}_h}$ with piecewise smooth boundary and this sub division is often called as element domain.
- 2) $Q = \{\mathcal{B}_1, \mathcal{B}_2, \dots, \mathcal{B}_k\}$ is a finite dimensional space of functions on Ω_e and these functions are called as shape functions or basis functions of the finite element.
- 3) $\Sigma = \{P_1, P_2, \dots, P_k\}$ is a finite set of so called nodal variables such that: $P_i(\mathcal{B}_j) = \delta_{ij}$.

There are several choices of finite elements that provide $\mathcal{C}1$ continuity [21, 16]. The finite element implemented in JOREK [24] uses Bézier basis functions and is described below:

■ The finite element in poloidal plane

Let us consider a decomposition of the poloidal domain Ω_ξ into non-overlapping quadrangular elements : $\Omega_\xi = \bigcup_e \Omega_e$, where $\xi = \{R, Z\}^T$. In the framework of the iso-geometrical analysis, we consider that there exists a global, non-singular mapping between the physical domain Ω_ξ and the parametric domain $\Omega_\zeta = \bigcup_e \tau_e$, where $\zeta = \{s, t\}^T$. This global mapping transforms the straight quadrangular element τ_e to a curved quadrangular element Ω_e in the physical space. Moreover, any element τ_e can be mapped by a non-singular transformation to the unit reference square $\hat{\tau}(\hat{\zeta}) = [0, 1] \times [0, 1]$, where $\hat{\tau} = \{\hat{s}, \hat{t}\}^T$. Elements in all three spaces are sketched into the figure (3.1).

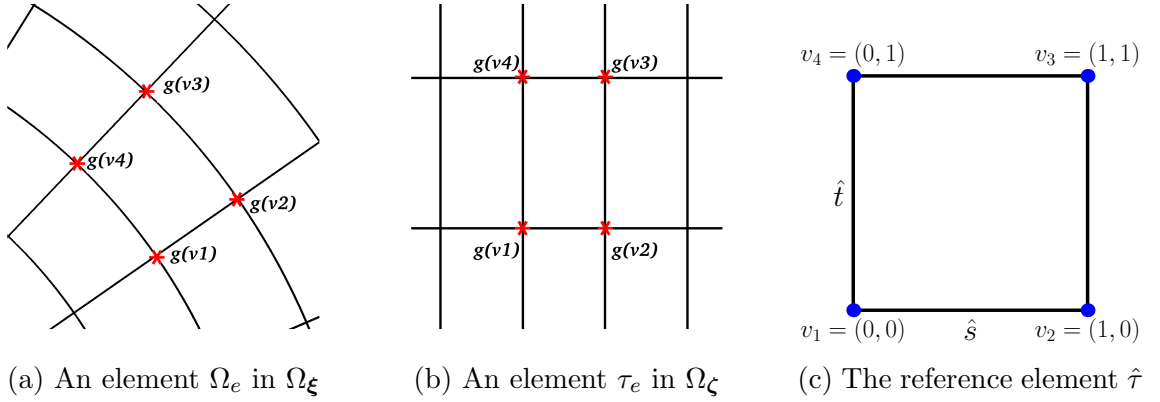


Figure 3.1: (a) A curved element Ω_e in physical plane Ω_ξ is marked by the vertices $g(v_1)$, $g(v_2)$, $g(v_3)$ and $g(v_4)$. (b) An element τ_e in the parametric plane Ω_ζ formed by the same vertices. (c) The unit reference element $\hat{\tau}$.

The space of bi-cubic polynomials Q_3 is considered on $\hat{\tau}$. The choice of Bernstein polynomials gives the Bézier basis functions on the reference element $\hat{\tau}$.

$$Q_3 \equiv \text{SPAN}\{\mathcal{B}_{v,d}(\hat{s}, \hat{t}), \quad 1 \leq v, d \leq 4\}$$

The basis functions $\mathcal{B}_{v,d}$ in 2D are natural extension of 1D Bernstein polynomials and are obtained by taking tensor product of 1D Bernstein polynomials in \hat{s} and \hat{t} direction. Using Bézier basis functions, a bicubic Bézier patch on the reference

element can be represented as:

$$\mathbf{P}(\hat{s}, \hat{t}) = \sum_{v=1}^4 \sum_{d=1}^4 \mathbf{P}_{v,d} \mathcal{B}_{v,d}(\hat{s}, \hat{t}), \quad 0 \leq \hat{s}, \hat{t} \leq 1$$

In the context of iso-parametric formulation, the grid data and physical variables are

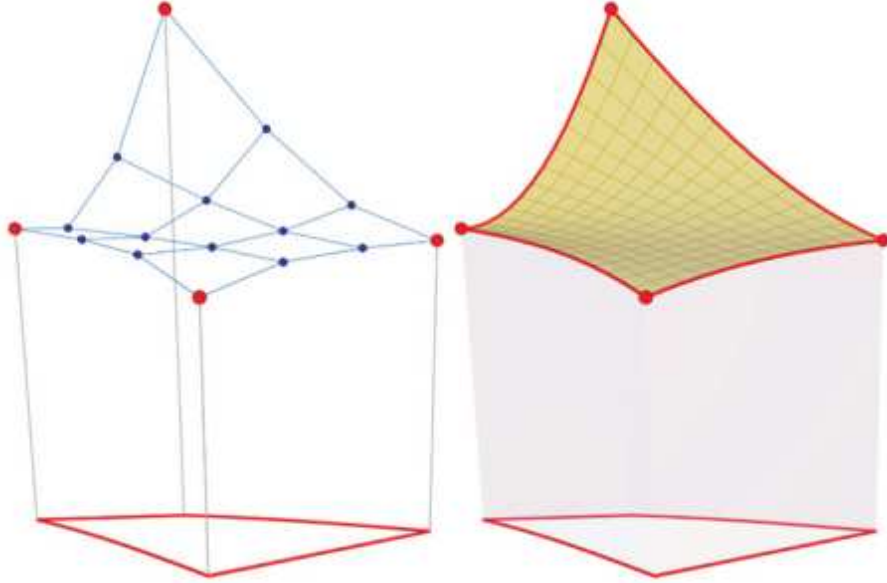


Figure 3.2: A Bézier patch shown in 3D space: The left plot represent the control points of the patch highlighted in blue color. The red control points define the grid nodes. The right plot depicts the resulting Bézier surface. The projection of the surface bounded by red curves at the bottom represents a grid cell in (R, Z) plane. The elevation represents the spatial distribution of any physical variable. The figure is taken from [47].

represented by the same basis functions. Hence, the components of the control points $\mathbf{P}_{i,j}$ include poloidal mesh coordinates $\boldsymbol{\xi} = \{R, Z\}$ as well as variables of PDEs. One such Bézier patch is shown in the Figure (3.2).

Bézier formulation is a generalization of the Hermite cubic elements such that it relaxes the strong constraint of the continuity of the local coordinates in each finite element. As a consequence, the functions and their gradients are continuous in real (physical) space but not in the parametric coordinates. This generalization of Hermite elements to bi-cubic Bézier elements is formulated in [24] and can very briefly be summarized as:

- The adjacent Bézier patches share common control points on the common edge. This continuity condition is said to be geometric continuity of order zero G^0 .

- In addition to above requirement, the order of continuity G^1 or ‘tangent plane condition’ gives continuity of surface gradients. This means that the planes tangent to both surfaces are identical along the edge. This situation is illustrated in the figure (3.3). The left plots represent the control points of the elements and the right plots depict the resulting surface. In the plots at the top, the neighboring Bézier elements share the control points at the common boundary such that values are continuous across the boundary between the elements (G^0 continuity). However, since the control points around the boundary are not aligned to each other, i.e., green lines exhibit bends, derivatives are not continuous across the element boundary. The plots at the bottom correspond to the discretization where both values and derivatives are continuous across the element boundaries (G^1). Here, the control points at the element boundaries are aligned, i.e., the green lines do not exhibit bends.

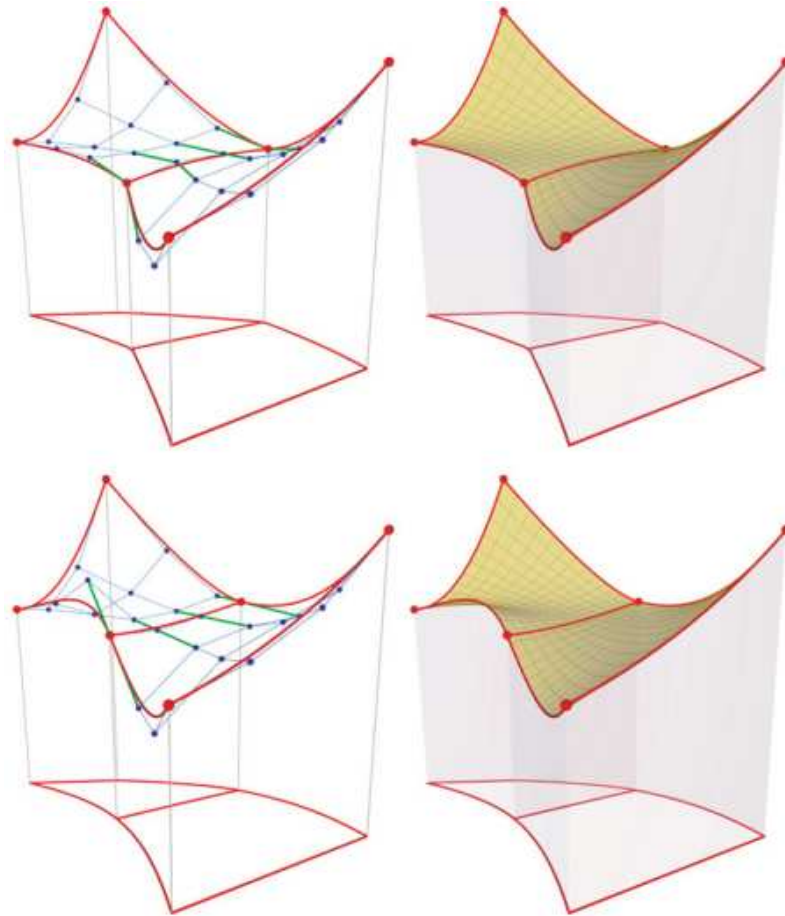


Figure 3.3: Two neighboring Bézier elements are shown. The figure is taken from [47].

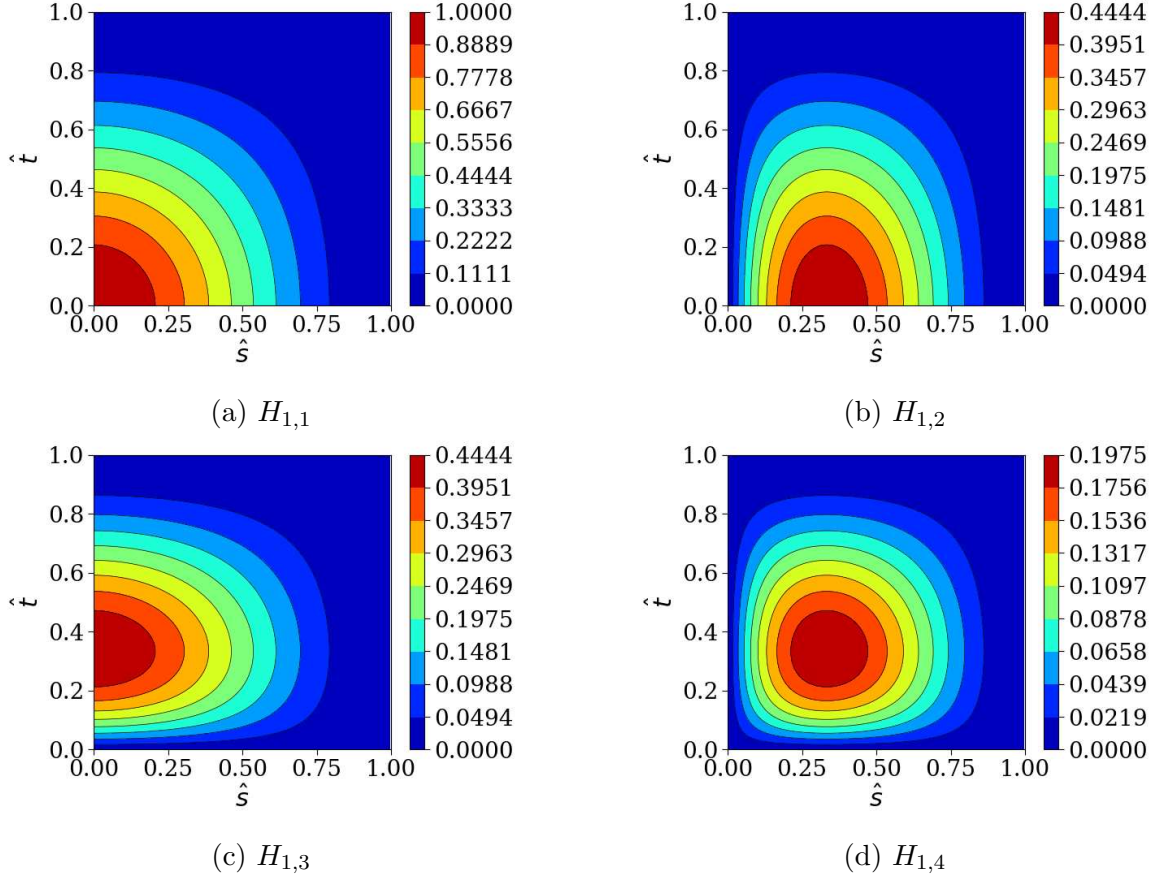


Figure 3.4: Bézier basis functions associated with vertex 1 of the reference element $\hat{\tau}$. The coordinate ($\hat{s} = 0$, $\hat{t} = 0$) corresponds to vertex 1.

Moreover, the number of degrees of freedom can also be reduced using G^1 continuity condition. In the figure (3.5), a corner $P_{0,0}$ is shown where 4 Bézier elements meet. This corner is associated with 9 control points. Using G^1 continuity, it can be shown that [24], only 4 degrees of freedom are required to determine all 9 control points associated with this corner $P_{0,0}$.

In practice, for any element e , the mesh and physical variables can be expanded in the Bézier basis as:

$$\mathbf{P}(\hat{s}, \hat{t})|_e = \sum_{v=1}^4 \sum_{d=1}^4 \mathbf{P}_{g(v),d} \sigma_{v,d}^e H_{v,d}(\hat{s}, \hat{t})$$

where, the index v denotes local numbering of vertices of each element and d denotes the degrees of freedom associated with the each vertex. The index $g(v)$ denotes the global numbering of the vertex v in the mesh. The scale factors $\sigma_{v,d}^e$ corresponding to the same node are different for each element to guarantee the G^1 continuity. It is important to remark here that these scale factors are a geometric property and

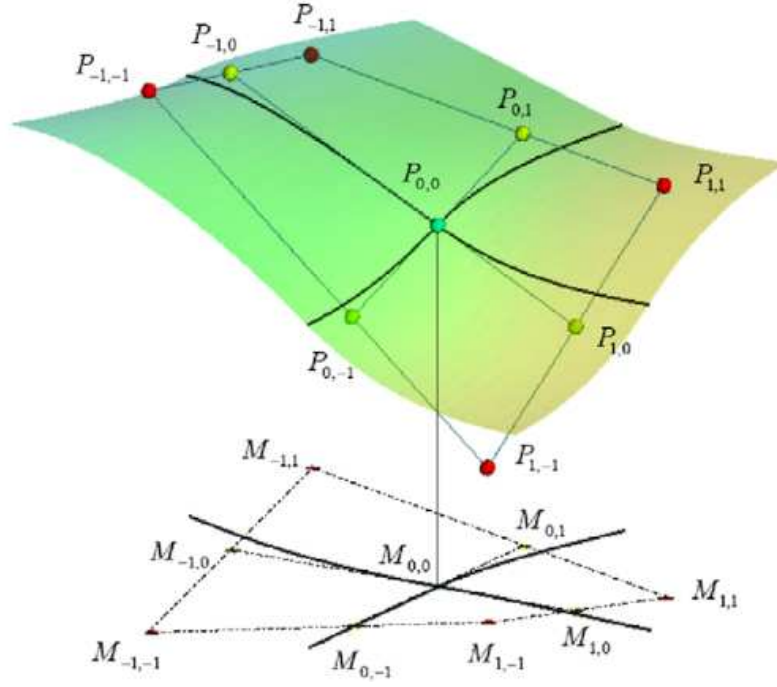


Figure 3.5: Corner between four Bézier patches with G^1 continuity. The figure is taken from [24].

therefore independent of time and identical for each physical quantity. The presence of the scale factors $\sigma_{v,d}^e$ is a consequence of reduction of the number of DoFs to 4 from 9. The basis functions $H_{v,d}(\hat{s}, \hat{t})$ are written in the Table (3.1) and the figure (3.4) shows plots of the 4 basis functions associated with vertex 1. Each vertex has 4 basis functions associated with it which can be seen in the Table (3.1) and they can be obtained by substitutions:

- $\hat{s} \rightarrow (1 - \hat{s}) \implies H_{2,d}(\hat{s}, \hat{t}) = H_{1,d}(1 - \hat{s}, \hat{t})$
- $\hat{s} \rightarrow (1 - \hat{s})$ and $\hat{t} \rightarrow (1 - \hat{t}) \implies H_{3,d}(\hat{s}, \hat{t}) = H_{1,d}(1 - \hat{s}, 1 - \hat{t})$
- $\hat{t} \rightarrow (1 - \hat{t}) \implies H_{4,d}(\hat{s}, \hat{t}) = H_{1,d}(\hat{s}, 1 - \hat{t})$

The DoFs $\mathbf{P}_{g(v),d}$ are written with global index $g(v)$ to emphasis that they are node properties and they are shared among all elements containing that respective node. The DoFs $\mathbf{P}_{g(v),d}$ associated to any element e are related to the derivatives with respect to parametric coordinates

$$\zeta = \{s, t\}^T$$

as follows,

$$\mathbf{P}_{g(v),1} \rightarrow \mathbf{P}|_{g(v)}, \quad \mathbf{P}_{g(v),2} \rightarrow \frac{\partial \mathbf{P}}{\partial s} \Big|_{g(v)}, \quad \mathbf{P}_{g(v),3} \rightarrow \frac{\partial \mathbf{P}}{\partial t} \Big|_{g(v)}, \quad \mathbf{P}_{g(v),4} \rightarrow \frac{\partial^2 \mathbf{P}}{\partial s \partial t} \Big|_{g(v)}$$

which again highlights the equivalence between bicubic Bézier and Hermite finite element.

$H_{1,1} = (1 - \hat{s})^2 (1 + 2\hat{s}) (1 - \hat{t})^2 (1 + 2\hat{t})$	$H_{2,1} = \hat{s}^2 (3 - 2\hat{s}) (1 - \hat{t})^2 (1 + 2\hat{t})$
$H_{1,2} = 3 \hat{s} (1 - \hat{s})^2 (1 - \hat{t})^2 (1 + 2\hat{t})$	$H_{2,2} = 3 \hat{s}^2 (1 - \hat{s}) (1 - \hat{t})^2 (1 + 2\hat{t})$
$H_{1,3} = 3 (1 + 2\hat{s}) (1 - \hat{s})^2 \hat{t} (1 - \hat{t})^2$	$H_{2,3} = 3 \hat{s}^2 (3 - 2\hat{s}) \hat{t} (1 - \hat{t})^2$
$H_{1,4} = 9 \hat{s} (1 - \hat{s})^2 \hat{t} (1 - \hat{t})^2$	$H_{2,4} = 9 \hat{s}^2 (1 - \hat{s}) \hat{t} (1 - \hat{t})^2$
$H_{3,1} = \hat{s}^2 (3 - 2\hat{s}) \hat{t}^2 (3 - 2\hat{t})$	$H_{4,1} = (1 - \hat{s})^2 (1 + 2\hat{s}) \hat{t}^2 (3 - 2\hat{t})$
$H_{3,2} = 3 \hat{s}^2 (1 - \hat{s}) \hat{t}^2 (3 - 2\hat{t})$	$H_{4,2} = 3 (1 - \hat{s})^2 \hat{s} \hat{t}^2 (3 - 2\hat{t})$
$H_{3,3} = 3 \hat{s}^2 (3 - 2\hat{s}) \hat{t}^2 (1 - \hat{t})$	$H_{4,3} = 3 (1 - \hat{s})^2 (1 + 2\hat{s}) \hat{t}^2 (1 - \hat{t})$
$H_{3,4} = 9 \hat{s}^2 (1 - \hat{s}) \hat{t}^2 (1 - \hat{t})$	$H_{4,4} = 9 (1 - \hat{s})^2 \hat{s} \hat{t}^2 (1 - \hat{t})$

Table 3.1: Bézier basis functions $H_{v,d}$ where $1 \leq v \leq 4$ and $1 \leq d \leq 4$.

The space \mathbf{V}_ξ is spanned by the functions $N_{i_{2D}}(\xi)$ such that the restrictions of $N_{i_{2D}}(\xi)$ on an element e , when mapped to the unit reference element, corresponds to the functions $\sigma_{v,d}^e H_{gv,d}$. The index $i_{2D} = (g(v), d)$ corresponds to four basis functions that are associated with the vertex $g(v)$ and $d = \{1, 2, 3, 4\}$, hence $N_{2D} = 4n_p$, where n_p is the number of vertices in the grid. Therefore the global basis function $N_{i_{2D}}(\xi)$ is written as:

$$N_{i_{2D}}(\xi) = \bigcup \sigma_{v,d}^e H_{v,d} \quad \text{where, } i_{2D} = (g(v), d)$$

with $H_{v,d} = 0 \forall v$ if $g(v)$ does not belong to an element e .

The error estimate for bicubic Bézier FEM discussed here is given as [87]:

$$h_e^{p+1-s} + h_e^{2p+2-2m}$$

where h_e is the characteristic length of one element, p is the order of the approximation functions, s is the order of the derivatives and m denotes the order of the equation to be solved. For cubic functions and second order elliptic operators like Grad-Shafranov equations, the error in the solution (H^0 norm) scales as h_e^4 while that in the derivative (H^1 norm) scales as h_e^3 . The fourth order convergence obtained for full MHD model by performing numerical tests on the standard MHD is shown in [74].

■ *Toroidal basis functions:*

The sine and cosine functions are used as the basis functions in the periodic toroidal direction. Therefore, the approximated space \mathbf{V}_ϕ is spanned by the functions C_{i_ϕ} :

$$\mathbf{V}_\phi([0, 2\pi[) = \text{SPAN}\{C_{i_\phi}, \quad 1 \leq i_\phi \leq 2n_H + 1 = N_\phi\}$$

where n_H is the number of harmonics and C_{i_ϕ} are:

$$C_{i_\phi}(\phi) = \begin{cases} 1, & \text{if } i_\phi = 1, & n = 0 \\ \cos(n\phi), & \text{if } i_\phi = 2n, & n \in 0, 1, \dots, n_H \\ \sin(n\phi), & \text{if } i_\phi = 2n + 1, & n \in 0, 1, \dots, n_H \end{cases}$$

Now, the description of poloidal and toroidal basis functions is completed. The function \mathbf{w}_h on any element e is represented as:

$$\mathbf{w}_h(\hat{s}, \hat{t}, \phi, t) = \sum_{i_\phi=1}^{N_\phi} \sum_{v=1}^4 \sum_{d=1}^4 \mathbf{w}_{v,d,i_\phi}(t) H_{v,d}^e(\hat{s}, \hat{t}) C_{i_\phi}(\phi)$$

here t refers to time and for conciseness $H^e(\hat{s}, \hat{t}) = \sigma_{v,d} H_{v,d}(\hat{s}, \hat{t})$. The test function is represented as:

$$\mathbf{w}_h^*(\hat{s}, \hat{t}, \phi) = \sum_{i_\phi=1}^{N_\phi} \sum_{v=1}^4 \sum_{d=1}^4 \mathbf{w}_{v,d,i_\phi}^* H_{v,d}^e(\hat{s}, \hat{t}) C_{i_\phi}(\phi)$$

The weak form written in the equation (3.9) can be represented as sum of weak forms on all elements:

$$\sum_e \int_\phi \int_{\hat{\tau}} \mathbf{w}_{v,d,i_\phi}^* H_{v,d}^e C_{i_\phi} \cdot \mathcal{R} \left(\sum_{v', d', j_\phi} \mathbf{w}_{v',d',j_\phi}(t) H_{v',d'}^e C_{j_\phi} \right) \det(\mathcal{J}) d\Omega_{\hat{\tau}} d\phi = 0 \quad (3.10)$$

$\forall v, d, i_\phi$ and \mathcal{J} is the jacobian of transformation from physical coordinates $\boldsymbol{\xi}$ to the reference coordinates (\hat{s}, \hat{t}) and is given as:

$$\mathcal{J} = \begin{bmatrix} \partial_{\hat{s}} R & \partial_{\hat{t}} R \\ \partial_{\hat{s}} Z & \partial_{\hat{t}} Z \end{bmatrix}$$

Using the weak form (3.10) and the residual of TADR system given by equation (3.2), computational details of each term are written below. First, the contribution from

the ‘mass matrix’ term is written as:

$$\begin{aligned} & \int_{\phi} \int_{\hat{\tau}} \mathbf{w}_{v,d,i_{\phi}}^* H_{v,d}^e C_{i_{\phi}} \cdot \underline{\mathbf{M}}(\mathbf{w}_h) \left(\sum_{v',d',j_{\phi}} \partial_t \mathbf{w}_{v',d',j_{\phi}}(t) H_{v',d'}^e C_{j_{\phi}} \right) \det(\mathcal{J}) d\Omega_{\hat{\tau}} d\phi \\ & = \mathbf{w}_{v,d,i_{\phi}}^* \underline{\mathbf{M}}^e(\mathbf{w}_h) \partial_t \mathbf{w}_{v',d',j_{\phi}}(t) \quad \forall v,d,i_{\phi} \end{aligned}$$

where the element mass matrix $\underline{\mathbf{M}}^e(\mathbf{w}_h)$ is identified as:

$$\underline{\mathbf{M}}_{v,d,i_{\phi},v',d',j_{\phi}}^e(\mathbf{w}_h) = \int_{\phi} \int_{\hat{\tau}} H_{v,d}^e C_{i_{\phi}} \underline{\mathbf{M}}(\mathbf{w}_h) H_{v',d'}^e C_{j_{\phi}} \det(\mathcal{J}) d\Omega_{\hat{\tau}} d\phi$$

Now the convective terms are written as:

$$\begin{aligned} & \int_{\phi} \int_{\hat{\tau}} \mathbf{w}_{v,d,i_{\phi}}^* H_{v,d}^e C_{i_{\phi}} \cdot \underline{\mathbf{C}}(\mathbf{w}_h, \nabla) \left(\sum_{v',d',j_{\phi}} \mathbf{w}_{v',d',j_{\phi}}(t) H_{v',d'}^e C_{j_{\phi}} \right) \det(\mathcal{J}) d\Omega_{\hat{\tau}} d\phi \\ & = \mathbf{w}_{v,d,i_{\phi}}^* \underline{\mathbf{C}}^e(\mathbf{w}_h) \mathbf{w}_{v',d',j_{\phi}}(t) \quad \forall v,d,i_{\phi} \end{aligned}$$

The matrix $\underline{\mathbf{C}}^e(\mathbf{w}_h)$ associated with the convective terms is identified as:

$$\underline{\mathbf{C}}_{v,d,i_{\phi},v',d',j_{\phi}}^e(\mathbf{w}_h) = \int_{\phi} \int_{\hat{\tau}} H_{v,d}^e C_{i_{\phi}} \underline{\mathbf{C}}(\mathbf{w}_h) \partial(H_{v',d'}^e C_{j_{\phi}}) \det(\mathcal{J}) d\Omega_{\hat{\tau}} d\phi$$

Note that the convective terms written here contain first derivatives only and hence are not integrated by parts, see form of the term $\underline{\mathbf{C}}(\mathbf{w})\nabla\mathbf{w}$ at the beginning of the section. The diffusive terms however are integrated by parts as they contain second derivatives.

$$\begin{aligned} & \int_{\phi} \int_{\hat{\tau}} \mathbf{w}_{v,d,i_{\phi}}^* H_{v,d}^e C_{i_{\phi}} \cdot \nabla \cdot \left[\underline{\mathbf{\Gamma}}\nabla \left(\sum_{v',d',j_{\phi}} \mathbf{w}_{v',d',j_{\phi}}(t) H_{v',d'}^e C_{j_{\phi}} \right) \right] \det(\mathcal{J}) d\Omega_{\hat{\tau}} d\phi \\ & = -\mathbf{w}_i^* \underline{\mathbf{\Gamma}}_{v,d,i_{\phi},v',d',j_{\phi}}^e \mathbf{w}_j + \mathbf{w}^* \underline{\mathbf{\Gamma}}_{v,d,i_{\phi},v',d',j_{\phi}}^{e,b} \mathbf{w}_j \quad \forall v,d,i_{\phi} \end{aligned}$$

The matrix $\underline{\mathbf{\Gamma}}_{i,j}^e$ is identified as:

$$\underline{\mathbf{\Gamma}}_{v,d,i_{\phi},v',d',j_{\phi}}^e(\mathbf{w}_h) = - \int_{\phi} \int_{\hat{\tau}} \partial(H_{v,d}^e C_{i_{\phi}}) \underline{\mathbf{\Gamma}}(\mathbf{w}_h) \partial(H_{v',d'}^e C_{j_{\phi}}) \det(\mathcal{J}) d\Omega_{\hat{\tau}} d\phi$$

and the second term is a boundary integral coming from integration by parts performed to get rid of second derivatives. This boundary integral is given as:

$$\underline{\mathbf{\Gamma}}_{v,d,i_{\phi},v',d',j_{\phi}}^{e,b}(\mathbf{w}_h) = - \int_{\phi} \int_{\partial\hat{\tau}} H_{v,d}^e C_{i_{\phi}} \underline{\mathbf{\Gamma}}(\mathbf{w}_h) \partial(H_{v',d'}^e C_{j_{\phi}}) \cdot \hat{\mathbf{n}} \det(\mathcal{J}) dS d\phi$$

where, $\hat{\mathbf{n}}$ is the unit normal to the surface S of an element. The second integral vanishes for internal cells as the unit vectors $\hat{\mathbf{n}}$ will be equal and opposite for neighboring cells and the terms $\underline{\mathbf{\Gamma}}$ will match on the boundaries. This integral will have

non-zero contributions only on the boundaries of the entire domain Ω_ξ . Finally, the contribution from the source term is written as:

$$-\int_{\phi} \int_{\hat{\tau}} \mathbf{w}_{v,d,i_\phi}^* H_{v,d}^e C_{i_\phi} \cdot \mathbf{s}(\mathbf{w}_h) \det(\mathcal{J}) d\Omega_{\hat{\tau}} d\phi = -\mathbf{w}_{v,d,i_\phi}^* \cdot \mathbf{s}^e(\mathbf{w}_h) \quad \forall v, d, i_\phi$$

and the vector $\mathbf{s}(\mathbf{w}_h)_i^e$ is identified as:

$$\mathbf{s}_{v,d,i_\phi}^e(\mathbf{w}_h) = \int_{\phi} \int_{\hat{\tau}} H_{v,d}^e C_{i_\phi} \mathbf{s}(\mathbf{w}_h) \det(\mathcal{J}) d\Omega_{\hat{\tau}} d\phi$$

The integrals over unit reference element in above matrices $\underline{\mathbf{M}}_{v,d,i_\phi,v',d',j_\phi}^e$, $\underline{\mathbf{C}}_{v,d,i_\phi,v',d',j_\phi}^e$, $\underline{\mathbf{\Gamma}}_{v,d,i_\phi,v',d',j_\phi}^e$ and the vector $\mathbf{s}_{v,d,i_\phi}^e$ are evaluated using Gauss quadrature. The integrals in the toroidal direction $\mathbb{A}_{i_\phi,j_\phi}^{e,k,l}$:

$$\mathbb{A}_{i_\phi,j_\phi}^{e,k,l} = \int_0^{2\pi} \mathbb{A}_{v,d,v',d'}^{e,k,l}(\phi) \partial_\phi^k C_{i_\phi} \partial_\phi^l C_{j_\phi} d\phi$$

where, $\mathbb{A}_{v,d,v',d'}^{e,k,l}(\phi)$ can be poloidal integrals from any matrix: mass, convective or diffusive. The index k and l denotes the order of the derivative with respect to ϕ and $1 \leq i_\phi, j_\phi \leq N_\phi$. These integrals are estimated either by a direct summation over equidistant toroidal planes or by Discrete Fourier Transform (DFT) using the input data as $\mathbb{A}_{v,d,v',d'}^{e,k,l}(\phi_p)$ where $p \in \{1, \dots, N_p\}$ and N_p denotes number of equidistant planes in the toroidal direction. The details of DFT implementation can be found in Appendix B of [23].

3.2.2 Time stepping and matrix solver

The global mass matrix is obtained by adding the entries of all element mass matrices $\underline{\mathbf{M}}_{v,d,i_\phi,v',d',j_\phi}^e$ at respective locations depending on the vertices $g(v)$ and $g(v')$ as follows:

$$\mathbb{P} = \left[\sum_e \underline{\mathbf{M}}_{v,d,i_\phi,v',d',j_\phi}^e \right]$$

The global mass matrix \mathbb{P} has non zero entries only if $g(v)$ and $g(v')$ are vertices of an element e so that the matrix is sparse. The summation on poloidal elements suggest how the assembling procedure is implemented. Similarly, the other matrices $\underline{\mathbf{C}}_{v,d,i_\phi,v',d',j_\phi}^e$, $\underline{\mathbf{\Gamma}}_{v,d,i_\phi,v',d',j_\phi}^e$ and the vector $\mathbf{s}_{v,d,i_\phi}^e$ can be assembled to write the global system of discrete equations as:

$$\mathbb{P}(\mathbf{W}) \frac{\partial \mathbf{W}}{\partial t} = \mathbf{Q}(\mathbf{W})$$

where, \mathbf{W} is the vector of DoFs and $\mathbf{Q}(\mathbf{W})$ contains contributions from convective, diffusive, reactive and source terms. This system of semi discrete equations is discretized in time using a general implicit two step second order method [9] as:

$$\begin{aligned} & \mathbb{P}(\mathbf{W}^n) \left((1 + \xi) \mathbf{W}^{n+1} - (1 + 2\xi) \mathbf{W}^n + \xi \mathbf{W}^{n-1} \right) \\ & = \Delta t_n \left(\theta \mathbf{Q}(\mathbf{W})^{n+1} + (1 - \theta) \mathbf{Q}(\mathbf{W})^n \right) \end{aligned}$$

The term $\mathbf{Q}(\mathbf{W})^{n+1}$ can be linearized by using the approximation:

$$\mathbf{Q}(\mathbf{W})^{n+1} \approx \mathbf{Q}(\mathbf{W})^n + \left(\frac{\partial \mathbf{Q}}{\partial \mathbf{W}} \right)^n \delta \mathbf{W}^n \quad (3.11)$$

where, $\delta \mathbf{W}^n = \mathbf{W}^{n+1} - \mathbf{W}^n$. Substituting the approximation of $\mathbf{Q}(\mathbf{W})^{n+1}$, a second order method is written as:

$$\left[(1 + \xi) \mathbb{P}(\mathbf{W}^n) - \Delta t_n \theta \left(\frac{\partial \mathbf{Q}}{\partial \mathbf{W}} \right)^n \right] \delta \mathbf{W}^n = \Delta t_n \mathbf{Q}(\mathbf{W}^n) + \xi \mathbb{P}(\mathbf{W}^n) \delta \mathbf{W}^{n-1} \quad (3.12)$$

The choice of parameters ξ and θ decides the numerical method and its accuracy.

- $\xi = 0$ and $\theta = 1$ recovers implicit Euler method
- $\xi = 0$ and $\theta = 0.5$ recovers Crank-Nicholson method
- $\xi = 0.5$ and $\theta = 1$ recovers second order backward difference (BDF2)

The system of linear equations (3.11) can be represented as a sparse matrix system and is solved for $\delta \mathbf{W}^n$ using iterative solvers. The solution of the linear system is then used to update the DoFs at the next time level: $\mathbf{W}^{n+1} = \mathbf{W}^n + \delta \mathbf{W}^n$ and thereby using the interpolation to determine the variables \mathbf{w}_h at the next time level. Several matrix solvers are implemented in JOREK for solving the linear sparse matrix system. For 2D axisymmetric simulations the whole matrix system is treated by a direct solver and may be solved using interfaces to PaStiX [54] or MUMPS [3] for direct sparse matrix solvers. PaStiX uses Cholesky method if the matrix is symmetric positive-definite or LU decomposition if the matrix is non-symmetric. For the non-axisymmetric practical simulations, GMRES [31] iterative method is used along with the physics based preconditioner [47]. The matrix is written into blocks corresponding to the toroidal harmonics. The diagonal blocks describing the interaction of each harmonic with itself are kept while all off-diagonal blocks are dropped in the preconditioning. Each block matrix is solved by one or several MPI tasks on one

or several compute nodes, with the number of cores inside a compute node being exploited via the built-in thread support of the sparse matrix libraries (pthreads in case of PaStiX). The detailed aspects of implementations of matrix solvers and their performance can be found in [47, 71, 48].

3.2.3 Stabilized FEM for full MHD

VMS based stabilization:

In this subsection, VMS based stabilized FEM is applied to the full MHD model (2.43). The residual for this system in TADR form (3.2) is pre-multiplied by $\underline{\mathbf{M}}^{-1}$ to define a new residual $\mathcal{R}_1(\mathbf{w})$ as:

$$\mathcal{R}_1(\mathbf{w}) = \underline{\mathbf{M}}^{-1} \mathcal{R}(\mathbf{w}) = \frac{\partial \mathbf{w}}{\partial t} + \underline{\mathbf{A}}(\mathbf{w}) \nabla \mathbf{w} - \mathbf{d}_1(\mathbf{w}) - \mathbf{s}_1(\mathbf{w}) = 0$$

where, the new convective operator $\underline{\mathbf{A}}(\mathbf{w}) \nabla$ is written as:

$$\underline{\mathbf{A}}(\mathbf{w}) \nabla = \begin{bmatrix} \mathbf{v} \cdot \nabla & \rho \nabla \cdot & 0 & 0 \\ \frac{T}{\rho} \nabla & \mathbf{v} \cdot \nabla & \nabla & 0 \\ 0 & (\gamma - 1) T \nabla \cdot & \mathbf{v} \cdot \nabla & 0 \\ 0 & 0 & 0 & -\mathbf{v} \times \nabla \times \end{bmatrix} \quad (3.13)$$

Consequently, the weak form of full MHD model can be re-written in terms of the new residual $\mathcal{R}_1(\mathbf{w})$ as:

$$(\mathbf{w}^*, \underline{\mathbf{M}} \mathcal{R}_1(\mathbf{w}))_{\Omega} = (\mathbf{v}^*, \mathcal{R}_1(\mathbf{w}))_{\Omega} = 0$$

where, $\mathbf{v}^* = \underline{\mathbf{M}}^T \mathbf{w}^*$ are the test functions projected with the transpose of the mass matrix. The VMS approach described in the subsection (3.1.2) can be followed to write a stabilized FEM as:

$$(\bar{\mathbf{v}}^*, \mathcal{R}_1(\bar{\mathbf{w}}))_{\Omega} - (\underline{\mathbf{L}}_1^T(\bar{\mathbf{w}}, \partial) \bar{\mathbf{v}}^*, \underline{\mathbf{T}} \mathcal{R}_1(\bar{\mathbf{w}}))_{\Omega'} = 0 \quad (3.14)$$

where, the second term in above equation provides stabilization and the transport operator $\underline{\mathbf{L}}_1^T(\bar{\mathbf{w}}, \partial)$ is based on the definition of the residual $\mathcal{R}_1(\bar{\mathbf{w}})$. The symbol $\Omega' = \bigcup \Omega_e$ denotes element interiors, since the terms involving integrals over the element interior boundaries are neglected. Equation (3.14) is the weak form of the full MHD model in vector potential form with stabilization terms based on VMS approach. From this VMS formulation, it is possible to recover the other stabilization schemes as special cases like streamwise upwind/Petrov Galerkin (SUPG) and Galerkin least square (GLS).

- SUPG: As mentioned before, if one uses operator $\underline{\mathbf{L}}$ instead of its adjoint $\underline{\mathbf{L}}_1^T$ then the SUPG scheme is recovered.
- Additionally, if instead of the residual $\mathcal{R}_1(\bar{\mathbf{w}})$, the transport operator $\underline{\mathbf{L}}$ is used then the Galerkin least square method is recovered.

Simplifications of VMS stabilization used in this work are as follows:

- 1) Instead of the residual $\mathcal{R}_1(\bar{\mathbf{w}})$, an approximated residual is used in the equation (3.14) such that:

$$\mathcal{R}_1(\bar{\mathbf{w}}) \approx \underline{\mathbf{A}}(\mathbf{w})\nabla\mathbf{w} - \mathbf{S}$$

where, in time marching \mathbf{S} is approximated as $\mathbf{S} = \underline{\mathbf{A}}(\mathbf{w})\nabla\mathbf{w}^n$. This accounts to the following stabilization scheme as:

$$(\bar{\mathbf{v}}^*, \mathcal{R}_1(\bar{\mathbf{w}}))_\Omega - ([\underline{\mathbf{A}}(\bar{\mathbf{w}}, \partial)]^T \bar{\mathbf{v}}^*, \underline{\mathbf{T}} \underline{\mathbf{A}}(\mathbf{w})\nabla(\mathbf{w} - \mathbf{w}^n))_{\Omega'} = 0 \quad (3.15)$$

Therefore, this scheme involves the stabilization terms only in the implicit part of the discrete system.

- 2) Another simplification used involves the use of only convective terms $\underline{\mathbf{A}}(\mathbf{w})\nabla\mathbf{w}$ in the definition of \mathcal{R}_1 and the adjoint operator based on convective terms $\underline{\mathbf{L}}_1^T(\bar{\mathbf{w}}, \partial)$. Then the equation (3.14) gives the stabilization scheme as follows:

$$(\bar{\mathbf{v}}^*, \mathcal{R}_1(\bar{\mathbf{w}}))_\Omega - \left([\underline{\mathbf{A}}(\mathbf{w})\nabla]^T \bar{\mathbf{v}}^*, \underline{\mathbf{T}} \underline{\mathbf{A}}(\mathbf{w})\nabla\mathbf{w} \right)_{\Omega'} = 0 \quad (3.16)$$

The convective operator is given by the equation (3.13). The stabilization scheme can be further specialized to focus upon convective $\underline{\mathbf{A}}_c\nabla$ and acoustic $\underline{\mathbf{A}}_a\nabla$ part separately. Each of this part is written as:

$$\underline{\mathbf{A}}_c\nabla = \begin{bmatrix} \mathbf{v} \cdot \nabla & 0 & 0 & 0 \\ 0 & \mathbf{v} \cdot \nabla & \nabla & 0 \\ 0 & 0 & \mathbf{v} \cdot \nabla & 0 \\ 0 & 0 & 0 & -\mathbf{v} \times \nabla \times \end{bmatrix}; \quad \underline{\mathbf{A}}_a\nabla = \begin{bmatrix} 0 & \rho\nabla \cdot & 0 & 0 \\ \frac{T}{\rho}\nabla & 0 & \nabla & 0 \\ 0 & (\gamma - 1)T\nabla \cdot & 0 & 0 \\ 0 & 0 & 0 & 0 \end{bmatrix}$$

Determining the stabilization coefficient matrix $\underline{\mathbf{T}}$ is usually a more difficult task than the original problem itself and is a active area of research. Usually this matrix is either given heuristic arguments or simplified analysis [90]. The stabilization coefficient matrix is simply chosen here as $\underline{\mathbf{T}} = \mathcal{T} \mathbb{I}$ where \mathcal{T} is a time scale to guarantee the consistency of the formulation and is written as:

$$\underline{\mathbf{T}} = k_c \frac{h_e}{\lambda_{\max}} \mathbb{I} \quad (3.17)$$

where, h_e is the element size, λ_{\max} is the maximum of fastest characteristic speed over an element and k_c is the small real number to be set to control the amount of stabilization added.

In additions to VMS based stabilization, shock capturing and fourth order stabilization terms are also added in the FEM and are described as follows:

Shock capturing stabilization:

While VMS stabilization provides L^2 stability, it is useful to have a mechanism for BV stability as MHD equations can admit discontinuous solutions [34, 88, 95]. A presence of discontinuities or shocks can give rise to oscillations in the numerical solution around the region of discontinuity and can affect the accuracy and stability of a numerical method adversely. The shock-capturing stabilization term introduces artificial viscosity to be added only in the regions surrounding shocks/discontinuities. These stabilization terms can also be added in a certain direction giving rise to anisotropic stabilization terms. The isotropic stabilization terms can be written as:

$$\mathbf{d}_{\text{isc}} = \sum_e \int_{\Omega_e} \nabla \mathbf{w}^* : (\underline{\mathbf{T}}_{\text{SC}} \nabla \mathbf{w}_h) d\Omega_e$$

and anisotropic stabilization terms can be written as:

$$\mathbf{d}_{\text{asc}} = \sum_e \int_{\Omega_e} (\mathbf{b} \cdot \nabla \mathbf{w}^*) : (\underline{\mathbf{T}}_{\text{SC}} (\mathbf{b} \cdot \nabla \mathbf{w}_h)) d\Omega_e$$

where, the vector \mathbf{b} denotes the direction of which the stabilization is to be added. In case of a strongly magnetized plasma, this direction may be the direction of the magnetic field. Many choices are available for stabilization matrix $\underline{\mathbf{T}}_{\text{SC}}$ as can be seen in [88, 7, 34]. In this work a simplified choice for the stabilization coefficient matrix is used as:

$$\underline{\mathbf{T}}_{\text{SC}} = k_{\text{SC}} \mathbb{I}$$

where, k_{SC} is the shock sensor. Many choices can be found in literature to determine this term [88]. A simplistic choice of $h |\nabla p/p|$ maybe used as a criteria for the detection of discontinuities.

Fourth order diffusion terms:

The fourth order stabilization terms are effective in removing very high oscillations from the numerical solution as it damps high wave numbers quickly. The fourth order stabilization terms is written in weak form as:

$$\mathbf{d}_4 = \sum_e k_c \int_{\Omega_e} \nabla^2 \mathbf{w}^* \cdot \nabla^2 \mathbf{w}_h \, d\Omega_e$$

where k_c is a small real number to be specified to control the amount of the stabilization.

3.3 Time integration method with variable time step

The second order implicit method is already described in section 3.2.2, however it uses a constant time stepping. Often it is the case in a non-linear phase of MHD simulations that a time step needs to be reduced as the time scale of MHD dynamics reduces. Across a jump in the time step, the constant time stepping time integration method becomes inconsistent. In this section, we derive the second order time integration method for variable time stepping.

The derivation of a two step method for first order ordinary differential equation (ODE), that allows variable time steps, is presented first. Let us consider an initial value problem given by a first order ODE:

$$\frac{du}{dt} = f(u, t), \quad u(t=0) = u_0$$

for which a two step difference method is to be derived. Following the procedure in [9], the difference equation for the approximation of a first order ODE is written as follows:

$$\rho(E) u^n = \Delta t \sigma(E) f^n$$

where, $\rho(E)$ and $\sigma(E)$ denote the generating polynomials and E is the shifting operator in time such that $E(u^n) = u^{n+1} = u(t + \Delta t)$. The generating polynomial $\rho(E)$ takes the form: $\rho(E) = \sum_{j=0}^2 \alpha_j E_j$ and the second generating polynomial $\sigma(E)$ takes the form $\sigma(E) = \sum_{j=0}^2 \beta_j E_j$. Using the forms of two generating polynomials, the difference equation for a two step method can be written as:

$$\alpha_2 u^{n+2} + \alpha_1 u^{n+1} + \alpha_0 u^n = \Delta t \left(\beta_2 f^{n+2} + \beta_1 f^{n+1} + \beta_0 f^n \right)$$

Let us assume that the time discretization allows unequal intervals and the time step is given by $\Delta t_n = t_{n+1} - t_n$. Therefore, a two step method becomes:

$$\alpha_2 u^{n+2} + \alpha_1 u^{n+1} + \alpha_0 u^n = \Delta t_{n+1} \left(\beta_2 f^{n+2} + \beta_1 f^{n+1} + \beta_0 f^n \right) \quad (3.18)$$

Using Taylor's series for unequal intervals, u^{n+2} and u^{n+1} can be approximated as:

$$\begin{aligned} u^{n+2} &\approx u^n + s_n \frac{du}{dt} \Big|_n + \frac{s_n^2}{2!} \frac{du^2}{dt^2} \Big|_n \\ u^{n+1} &\approx u^n + \Delta t_n \frac{du}{dt} \Big|_n + \frac{\Delta t_n^2}{2!} \frac{du^2}{dt^2} \Big|_n \end{aligned}$$

where, $s_n = \Delta t_n + \Delta t_{n+1}$ is the sum of two successive time steps. These expansions can be put into Eq. (3.18) and the coefficients of the first three terms can be equated in order to get a second order method as:

$$\begin{aligned} \alpha_2 + \alpha_1 + \alpha_0 &= 0 \\ \alpha_2(1 + r_n) + \alpha_1 r_n &= \left(\beta_2 + \beta_1 + \beta_0 \right) = 1 \\ \alpha_2(1 + r_n^2) + \alpha_1 r_n^2 &= 2 \left(\beta_2(1 + r_n) + \beta_1 r_n \right) \end{aligned}$$

where, $r_n = \frac{\Delta t_n}{\Delta t_{n+1}}$ denotes the ratio of successive time steps. The first relation is the consistency condition. Since we have 3 equations in 6 unknowns, some of the variables may be set free. Letting $\alpha_0 = \xi$ gives $\alpha_1 = -\xi - \alpha_2$ from the consistency condition. Then, using the second relation in terms of α_j it is easy to see that $\alpha_2 = 1 + \xi r_n$.

$$\alpha_1 = -(1 + \xi(1 + r_n)) \quad \text{and} \quad \alpha_2 = 1 + \xi r_n$$

By letting $\beta_2 = \theta$, the second relation in terms of β_j gives $\beta_1 = 1 - \theta - \beta_0$. Finally, by putting all these expressions in the third relation and after some simplification, we get:

$$\beta_0 = \frac{\theta}{r_n} + 1 - \frac{(1 + \xi r_n)(1 + r_n)^2}{2r_n} + \frac{(1 + \xi(1 + r_n))r_n}{2}$$

The above relation needs to be satisfied for the resulting method to be second order accurate. Further, letting $\beta_0 = 0$ gives:

$$\xi = \frac{2\theta - 1}{r_n(1 + r_n)}$$

Putting the expressions for all coefficients into Eq. (3.18), a consistent two-step method for variable time-step can be written as:

$$(1 + r_n\xi) u^{n+2} - [1 + \xi(1 + r_n)] u^{n+1} + \xi u^n = \Delta t_{n+1} \left(\theta f^{n+2} + (1 - \theta) f^{n+1} \right) \quad (3.19)$$

where,

$$\xi = \frac{2\theta - 1}{r_n(1 + r_n)} \quad \text{and} \quad r_n = \frac{\Delta t_n}{\Delta t_{n+1}}$$

It can be readily verified that, for a constant time stepping $\Delta t = \Delta t_n$, the ratio r_n becomes 1 and the second order method for constant time stepping is recovered, where the requirement for second order accuracy reduces to:

$$\xi = \theta - \frac{1}{2}$$

Further, $\theta = \frac{1}{2}$ gives the Crank-Nicholson method and $\theta = 1$ given classical Gears (BDF2) method for constant time stepping. The stability of this method can be investigated for a constant time stepping scheme using a model problem $\dot{u} = f(u, t) = \lambda u$ with the exact solution $u(t) \propto e^{\lambda t}$, where λ is a complex number. Dividing the equation (3.19) by u_{n+1} :

$$(1 + \xi) \frac{u^{n+2}}{u^{n+1}} - (1 + 2\xi) + \xi \frac{u^n}{u^{n+1}} = \lambda \Delta t \left(\theta \frac{u^{n+2}}{u^{n+1}} + (1 - \theta) \right)$$

The ratio of numerical solutions at two time steps u^{n+2}/u^{n+1} and u^{n+1}/u^n denote the ‘growth’ in the solution and are called as amplification factor G . Further, the difference equation becomes:

$$(1 + \xi - \lambda \Delta t \theta) G^2 - (1 + 2\xi + \lambda \Delta t (1 - \theta)) G + \xi = 0$$

which can be solved for the roots of G :

$$G_{1,2} = \frac{-b \pm \sqrt{b^2 - 4ac}}{2a}$$

where,

$$a = (1 + \xi - \lambda\Delta t\theta), \quad b = -(1 + 2\xi + \lambda\Delta t(1 - \theta)), \quad c = \xi$$

For a stable scheme, $|G| \leq 1$ when $\text{Re}(\lambda) < 0$ and it is shown in [9] that the condition holds if $1 \leq 2\theta$ and $-1 \leq 2\xi \leq 2\theta - 1$. The convergence of the methods (with constant time stepping) is shown by numerically solving a simple ODE:

$$\frac{du}{dt} = -u, \quad u(t=0) = 1$$

the exact solution for which is $u_{\text{exact}} = e^{-t}$. The errors $\text{abs}(u - u_{\text{exact}})$ are plotted for series of time steps Δt in Figure (3.6) and they show that implicit Euler method shows first order convergence while Crank-Nicholson and BDF2 show second order convergence. From the equation (3.19) it can be seen that for BDF knowledge of the solution at $n - 1$ -th time level is needed as ξ is non-zero and hence at the first step it has to be started with a two time level method. Figure (3.6) also shows the advantage of starting the computations with Crank-Nicholson over implicit Euler.

It can be seen that for a variable time step method the stability analysis is not straight forward. It depends upon the equation to be solved as well as ratio of the time steps [10, 27, 63]. In [72] it is shown that the variable time step BDF2 method can generate large errors if started with BDF1 even if the initial time step is small and it is recommended to start BDF2 with the self-starting second-order implicit Runge-Kutta method in order to guarantee the second order convergence.

The method can be applied in a straight-forward manner to a system of PDEs given by:

$$\frac{\partial \mathbf{A}(\mathbf{u})}{\partial t} = \mathbf{B}(t, \mathbf{u})$$

where $\mathbf{A}(\mathbf{u})$ and $\mathbf{B}(t, \mathbf{u})$ are the vectors of dimension equal to the number of variables. The second order method for the system of PDE is then written as:

$$\begin{aligned} & (1 + r_n\xi) \mathbf{A}(\mathbf{u})^{n+1} - [1 + \xi(1 + r_n)] \mathbf{A}(\mathbf{u})^n + \xi \mathbf{A}(\mathbf{u})^{n-1} \\ & = \Delta t_n \left(\theta \mathbf{B}(\mathbf{u})^{n+1} + (1 - \theta) \mathbf{B}(\mathbf{u})^n \right) \end{aligned}$$

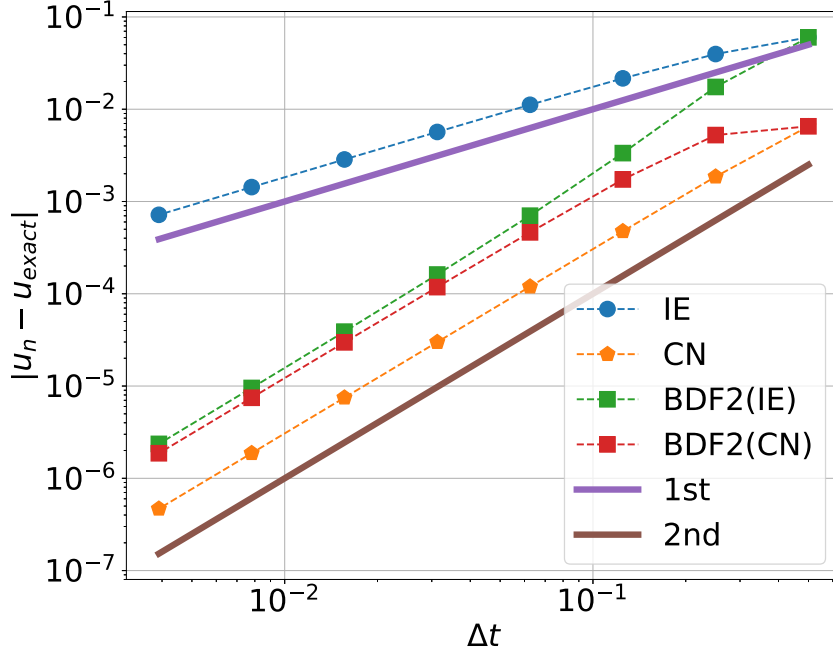


Figure 3.6: Convergence of time integration methods shown by plotting absolute value of the error computed for a series of time steps Δt . Implicit Euler (IE) shows first order convergence, Crank-Nicholson (CE) and second order back-word difference (BDF2) show second order convergence. Since knowledge of $n - 1$ -th time level is needed for BDF2, at the first time step the simulation maybe started with either IE or CN. Starting a simulation with CN shows advantage as the errors in this case are lower.

where, $r_n = \frac{\Delta t_{n-1}}{\Delta t_n}$. Above system of equations can be linearized by using the approximations:

$$\begin{aligned} \mathbf{A}(\mathbf{u})^{n+1} &\approx \mathbf{A}(\mathbf{u})^n + \left(\frac{\partial \mathbf{A}}{\partial \mathbf{u}}\right)^n \delta \mathbf{u}^n \\ \mathbf{A}(\mathbf{u})^{n-1} &\approx \mathbf{A}(\mathbf{u})^n - \left(\frac{\partial \mathbf{A}}{\partial \mathbf{u}}\right)^n \delta \mathbf{u}^{n-1} \\ \mathbf{B}(\mathbf{u})^{n+1} &\approx \mathbf{B}(\mathbf{u})^n + \left(\frac{\partial \mathbf{B}}{\partial \mathbf{u}}\right)^n \delta \mathbf{u}^n \end{aligned}$$

where, $\delta \mathbf{u}^n = \mathbf{u}^{n+1} - \mathbf{u}^n$. After linearization, the second order method is written as:

$$\left[(1 + r_n \xi) \left(\frac{\partial \mathbf{A}}{\partial \mathbf{u}}\right)^n - \Delta t_n \theta \left(\frac{\partial \mathbf{B}}{\partial \mathbf{u}}\right)^n \right] \delta \mathbf{u}^n = \Delta t_n \mathbf{B}(\mathbf{u})^n + \xi \left(\frac{\partial \mathbf{A}}{\partial \mathbf{u}}\right)^n \delta \mathbf{u}^{n-1} \quad (3.20)$$

with

$$\xi = \frac{2\theta - 1}{r_n(1 + r_n)} \quad \text{and} \quad r_n = \frac{\Delta t_{n-1}}{\Delta t_n} \quad (3.21)$$

Finally, it is the choice of θ that will specify the second order method. $\theta = \frac{1}{2}$ gives the analogue for Crank-Nicholson method and $\theta = 1$ gives the analogue for Gears method for variable time stepping. The equivalence between the form of equation (3.12) and (3.21) suggest that the implementation of the second order time integration method with variable time step involves only redefinition of ξ and making use of the ratio r_n in the formula. In this work simulations mostly use constant time stepping and the variable time step method is active only when there is a jump in the time step. However, the method can also be used if the time step is to be determined by Courant condition and the successive time steps can be different.

3.4 Grid generation

As mentioned before, grid generation involves building 2D grids in a poloidal plane as Fourier representation is used in toroidal direction. In recent developments, building 3D grid is also a possibility [47], however we focus our attention on 2D grids in poloidal planes for this study. The poloidal domain Ω_ξ is discretized into quadrangular cells Ω_e (also referred as element). We recall that JOEREK uses iso-parametric mapping, i.e., the same mapping is used for the geometry and the physical unknowns. The isoparametric mapping allows accurate alignment of finite elements to the magnetic flux surfaces and hence curved elements can be constructed. This strategy is similar to isoparametric Hermite elements but gives more flexibility with the grid generation with the possibility of refinement [24].

Recalling the definition of the finite element, the description of a grid for any element e can be written as:

$$\boldsymbol{\xi}(\hat{s}, \hat{t})|_e = \sum_{v=1}^4 \sum_{d=1}^4 \boldsymbol{\xi}_{v,d}^e H_{v,d}(\hat{s}, \hat{t}) = \sum_{v=1}^4 \sum_{d=1}^4 \boldsymbol{\xi}_{g(v),d} \sigma_{v,d}^e H_{v,d}(\hat{s}, \hat{t})$$

The relation between the ‘local’ ($\boldsymbol{\xi}_{v,d}^e$) and ‘global’ ($\boldsymbol{\xi}_{g(v),d}$) DoFs can be interpreted in a following way:

$$\boldsymbol{\xi}_{v,d}^e = \left. \frac{\partial \boldsymbol{\xi}}{\partial \zeta} \frac{\partial \zeta}{\partial \hat{\zeta}} \right|_e = \boldsymbol{\xi}_{g(v),d} \sigma_{v,d}^e$$

where,

$$\sigma_{v,d}^e = \left. \frac{\partial \zeta}{\partial \hat{\zeta}} \right|_e$$

such that $s = s(\hat{s})$ and $t = t(\hat{t})$. The grid data or DoFs of a grid along with the scale factors $\sigma_{v,d}^e$ are known to FEM solver and are computed as a part of grid generation. The DoFs of a grid are associated to the grid vertices so that advantages of compressed numerical graph and block formulation can be taken for computational efficiency purposes [47]. DoFs for the grid are written as:

$$\boldsymbol{\xi}_{g(v),1} = \boldsymbol{\xi}|_{g(v)} ; \quad \boldsymbol{\xi}_{g(v),2} = \left. \frac{\partial \boldsymbol{\xi}}{\partial s} \right|_{g(v)} ; \quad \boldsymbol{\xi}_{g(v),3} = \left. \frac{\partial \boldsymbol{\xi}}{\partial t} \right|_{g(v)} ; \quad \boldsymbol{\xi}_{g(v),4} = \left. \frac{\partial^2 \boldsymbol{\xi}}{\partial s \partial t} \right|_{g(v)} \quad (3.22)$$

while the scale factors are written as:

$$\sigma_{v,1}^e = 1 ; \quad \sigma_{v,2}^e = \left. \frac{\partial s}{\partial \hat{s}} \right|_v^e ; \quad \sigma_{v,3}^e = \left. \frac{\partial t}{\partial \hat{t}} \right|_v^e ; \quad \sigma_{v,4}^e = \left. \frac{\partial s}{\partial \hat{s}} \right|_v^e \left. \frac{\partial t}{\partial \hat{t}} \right|_v^e \quad (3.23)$$

Following, we describe briefly few types of grids those can be generated in JOREK and are relevant for this study.

3.4.1 Rectangular grids

For a rectangular grid, let N_R and N_Z be the number of points in R and Z directions respectively. The poloidal plane is represented by $\boldsymbol{\xi} = \boldsymbol{\xi}(\boldsymbol{\zeta}) = \boldsymbol{\xi}_o + \Delta \boldsymbol{\xi} \boldsymbol{\zeta}$ where $\boldsymbol{\xi}$ is the linear functions of s and t such that the vertices of a grid can be represented as:

$$\boldsymbol{\xi}_{i,j} = \begin{pmatrix} R_i \\ Z_j \end{pmatrix} = \begin{pmatrix} R_o \\ Z_o \end{pmatrix} + \begin{pmatrix} (R - R_o)s_i \\ (Z - Z_o)t_j \end{pmatrix} \quad 1 \leq i \leq N_R, 1 \leq j \leq N_Z$$

Then, the DoFs and scale factors are given by relations (3.22) and (3.23) respectively.

3.4.2 Polar grids

For a polar grid, let N_R and N_θ be the number of points in the radial and poloidal direction respectively. The parametric domain, in this case, is denoted by $\boldsymbol{\zeta} = \{r, \theta\}^T$, where $r = \sqrt{(R - R_o)^2 + (Z - Z_o)^2}$ and $\theta = \tan^{-1}(-Z/R)$. The domain is represented as $\boldsymbol{\xi} = \boldsymbol{\xi}_o + \boldsymbol{\xi}(\boldsymbol{\zeta}(\hat{\boldsymbol{r}}))$ such that each point of a polar grid is given by:

$$\boldsymbol{\xi}_i = \begin{pmatrix} R_o \\ Z_o \end{pmatrix} + \begin{pmatrix} r_i \cos \theta_j \\ r_i \sin \theta_j \end{pmatrix}$$

Let the radius r and angle θ be smooth functions: $r = f(s)$ and $\theta = \theta(t)$. Then the data required for Bézier representation becomes:

$$\begin{aligned}\boldsymbol{\xi}_{g(v),1} &= f(s) \begin{pmatrix} \cos \theta \\ \sin \theta \end{pmatrix} \\ \left. \frac{\partial \boldsymbol{\xi}}{\partial s} \right|_{g(v),2} &= f'(s) \begin{pmatrix} \cos \theta \\ \sin \theta \end{pmatrix} \\ \left. \frac{\partial \boldsymbol{\xi}}{\partial t} \right|_{g(v),3} &= f(s) \theta'(t) \begin{pmatrix} -\sin \theta \\ \cos \theta \end{pmatrix} \\ \left. \frac{\partial^2 \boldsymbol{\xi}}{\partial s \partial t} \right|_{g(v),4} &= f'(s) \theta'(t) \begin{pmatrix} -\sin \theta \\ \cos \theta \end{pmatrix}\end{aligned}$$

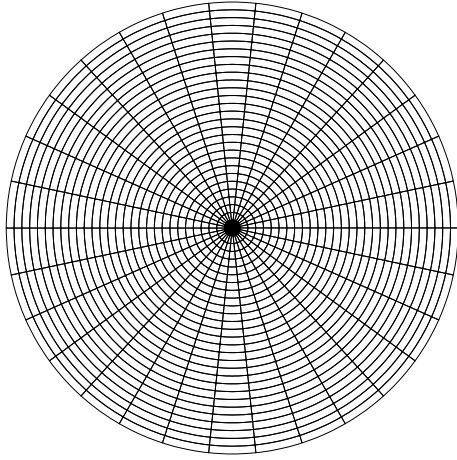
Polar grids represented by this Bézier formulation give a quite good accuracy and it is also possible to build a non-circular polar grids based on Soloviev equilibrium [24]. For such grids $\boldsymbol{\zeta} = \{r(s, t), \theta(t)\}^T$ where $r = \sqrt{(R - R_o)^2 + (Z - Z_o)^2}$. The boundary of the grid corresponds to $\psi = 0$ and can be specified in terms of the ellipticity, quadrangularity and triangularity as follows:

$$\begin{aligned}R &= \cos(\theta + T_u \sin \theta + Q_u \sin(2\theta)), \quad 0 \leq \theta < \pi \\ &= \cos(\theta + T_l \sin \theta + Q_l \sin(2\theta)), \quad \pi \leq \theta < 2\pi \\ Z &= E \sin \theta\end{aligned}$$

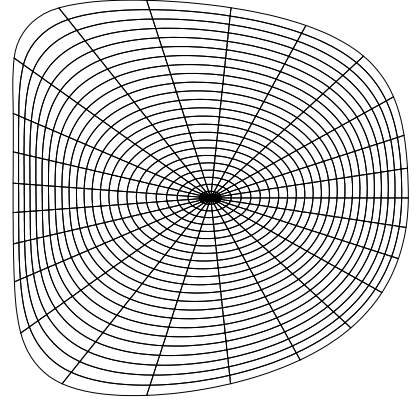
where, T_u , T_l are upper and lower triangularities respectively, Q_u and Q_l are upper and lower quadrangularities respectively and E is the ellipticity. The grid data for Bézier representation of such a grid can be computed in a similar way as described above for a circular grid. Polar grids described in this subsection can be used to solve Grad-Shafranov equation and then to simulate MHD flows. The grids shown in Figure (3.7a) and (3.7b) show examples of circular and non-circular grids respectively.

3.4.3 Flux-aligned grids

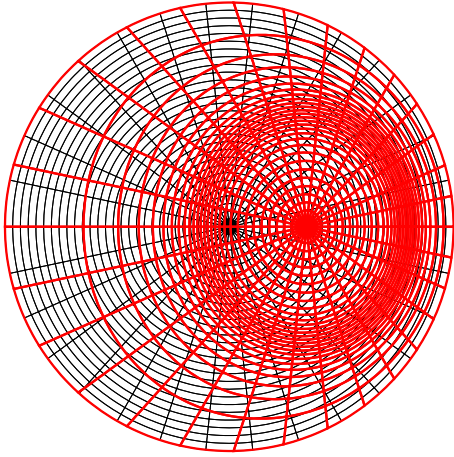
A grid that is aligned to the magnetic flux ψ can be constructed for MHD simulations. To build a flux aligned grid, first Grad-Shafranov equation (2.35) needs to be solved on a polar grids to obtain poloidal magnetic flux $\psi(\boldsymbol{\xi})$. If the ψ field does not have a X-point, then generation of new flux-aligned grid is similar to that of polar grids



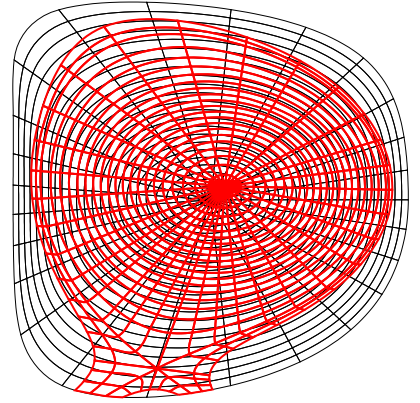
(a) Circular polar grid



(b) Non circular polar grid



(c) Flux aligned polar grid



(d) Flux aligned grid with one X-point

Figure 3.7: Polar grids generated in JOEREK. First row shows circular and noncircular polar grids on which Grad-Shafranov equation is solved for poloidal magnetic flux (ψ). Second row shows grids aligned to the flux surfaces in red color plotted on the top of previous grids.

described before, except that the parametric domain is now: $\zeta = \{\psi(s), \theta(t)\}^T$. The poloidal domain is represented by $\xi = \xi_o + \xi(\zeta(\hat{\tau}))$ such that each point of a flux aligned grid is given by:

$$\xi_i = \begin{pmatrix} R_o \\ Z_o \end{pmatrix} + \begin{pmatrix} R(\psi_i, \theta_j) \\ Z(\psi_i, \theta_j) \end{pmatrix}$$

Flux surfaces ψ_i are distributed between a flux surface at the magnetic axis ψ_a and a suitable last flux surface ψ_x . The grid data is then written as:

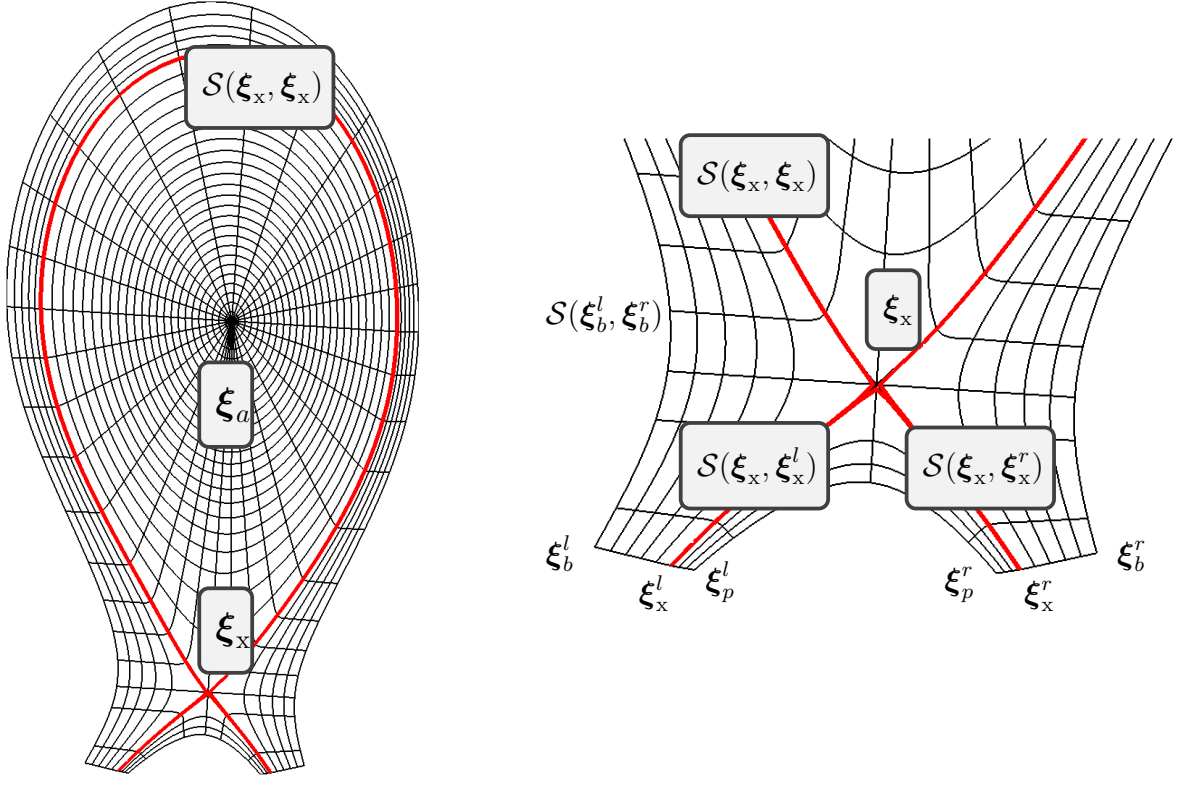
$$\begin{aligned}\xi_{g(v),1} &= \xi|_{g(v)} \\ \xi_{g(v),2} &= \left. \frac{\partial \xi}{\partial \psi} \frac{\partial \psi}{\partial s} \right|_{g(v)} \\ \xi_{g(v),3} &= \left. \frac{\partial \xi}{\partial \theta} \frac{\partial \theta}{\partial t} \right|_{g(v)} \\ \xi_{g(v),4} &= \left. \frac{\partial^2 \xi}{\partial \psi \partial \theta} \frac{\partial \psi}{\partial s} \frac{\partial \theta}{\partial t} \right|_{g(v)}\end{aligned}$$

where, the data $\frac{\partial \xi}{\partial \psi}$, $\frac{\partial \xi}{\partial \theta}$ and $\frac{\partial^2 \xi}{\partial \psi \partial \theta}$ is determined from the jacobian of the coordinate transformation between ξ and ζ . An example of a polar flux aligned grid is shown in Figure (3.7c).

3.4.4 Flux-aligned grids with X-points

If ψ field contains X-points, then the domain is decomposed into several sub-domains and the meshing of each sub-domain is preformed step by step. In this case, ψ -isosurfaces for X-points play an important role to identify sub-domains. For simplicity of description, we focus upon the procedure for grid generation with one X-point only.

The grid center is marked by the position of magnetic axis ξ_a where $\psi = \psi_a$ has an extremum. The separatrix is also identified as the iso-surface $\psi = \psi_x$ which separates the closed field lines (inside the core region) and open field lines. The X-point on the separatrix is marked by the position ξ_x . The iso-surface associated with the X-point (the separatrix) crosses the divertor plates at two different points ξ_x^l and ξ_x^r as shown in Figure (3.8b), where superscripts l and r are denote the left and right leg of tokamak device. The separatrix can be decomposed into three parts: the curves $\mathcal{S}(\xi_x^l, \xi_x)$ and $\mathcal{S}(\xi_x^r, \xi_x)$ and the remaining part that can be thought as a closed curve $\mathcal{S}(\xi_x, \xi_x)$. The value $\psi_b > \psi_x$ is chosen such that the iso-surface for ψ_b is a smooth curve $\mathcal{S}(\xi_b^l, \xi_b^r)$ where ξ_b^l and ξ_b^r denote the locations on the divertor plates as shown in Figure (3.8a). This surface is a last open flux surface and forms the part of the boundary of the domain. Similarly, the value $\psi_p < \psi_x$ is chosen such that the iso-surface for ψ_p is a smooth curve $\mathcal{S}(\xi_p^l, \xi_p^r)$ where ξ_p^l and ξ_p^r also denote the locations on the divertor plates as shown in Figure 3.8b. The divertor plates are defined by the curves $\mathcal{S}(\xi_b^l, \xi_x^l)$, $\mathcal{S}(\xi_x^l, \xi_p^l)$, $\mathcal{S}(\xi_p^r, \xi_x^r)$ and $\mathcal{S}(\xi_x^r, \xi_b^r)$ those form part of the boundaries which are not flux aligned.



(a) Flux-aligned grid with one X-point

(b) Zoomed view of flux aligned grid

Figure 3.8: Flux aligned grid generated in JOREK with one X-point. The magnetic axis and X-point are marked by ξ_a and ξ_x . The red curve in a) denotes the separatrix. The left divertor cuts the last open field line, separatrix and end of private region at ξ_b^l , ξ_x^l and ξ_p^l respectively. Similarly, the right divertor cuts the last open field line, separatrix and end of private region at ξ_b^r , ξ_x^r and ξ_p^r respectively. The separatrix constitutes three curves: the curve that closes on X-point ($\mathcal{S}(\xi_x, \xi_x)$), the curves joining X-point with left ($\mathcal{S}(\xi_x, \xi_x^l)$) and right legs ($\mathcal{S}(\xi_x, \xi_x^r)$). Other strategic curve are: $\mathcal{S}(\xi_b^l, \xi_b^r)$, $\mathcal{S}(\xi_b^l, \xi_x^l)$, $\mathcal{S}(\xi_b^r, \xi_x^r)$, $\mathcal{S}(\xi_x^l, \xi_p^l)$ and $\mathcal{S}(\xi_x^r, \xi_p^r)$.

Marking above points and curves now allow the domain to decompose into three distinct sub-domains: core region Ω_c , scrape-off layer (SOL) Ω_s and private region Ω_p . The SOL is formed by $\psi > \psi_x$ while private region is formed by $\psi < \psi_x$. The boundary of entire domain $\partial\Omega$ is formed by several parts as follows:

$$\partial\Omega = \mathcal{S}(\xi_x^l, \xi_b^l) \cup \mathcal{S}(\xi_b^l, \xi_b^r) \cup \mathcal{S}(\xi_b^r, \xi_x^r) \cup \mathcal{S}(\xi_x^r, \xi_p^r) \cup \mathcal{S}(\xi_p^r, \xi_p^l) \cup \mathcal{S}(\xi_p^l, \xi_x^l)$$

To construct a flux-aligned grid, the radial discretization is done by simply taking a chosen set of flux contours, both inside and outside the separatrix. The poloidal discretization is done in several steps. The poloidal plane is separated into two parts

by a line from the X-point. The upper part is composed of the sub-domains with both closed and open flux surfaces. The sub-domain inside the separatrix is meshed as a polar grid by taking straight lines from the magnetic axis out to the separatrix. The lower part of the grid, below the X-point, is separated into two regions from SOL and the private region. The meshing of these parts and the SOL region from upper part is done in straight-forward way, i.e., by curved mapping on real domain from rectangular parametric domains. A flux aligned grid with one X-point is shown in Figure (3.7d) using red color.

3.4.5 Grid singularities:

In the FEM described above, continuity of functions and their gradients is achieved on the account of certain conditions satisfied when 4 elements share a common vertex as shown in Figure (3.5). At any such vertex, the unit vectors of $\frac{\partial \xi}{\partial s}$, $\frac{\partial \xi}{\partial t}$ and $\frac{\partial^2 \xi}{\partial s \partial t}$ form a frame associated to each of four elements. Figure (3.9) shows frames drawn with the unit vectors of $\frac{\partial \xi}{\partial s}$ (red arrows) and $\frac{\partial \xi}{\partial t}$ (blue arrows) at a vertex associated to one of the element. It is clear that reversing the signs of these unit vectors one by one will give the frames associated with other 3 elements shared by a vertex. However, such a pattern of frames is not possible at the grid center of a polar grid and at the X-point as shown in Figures (3.9a) and (3.9b) respectively, highlighting the points of concern.

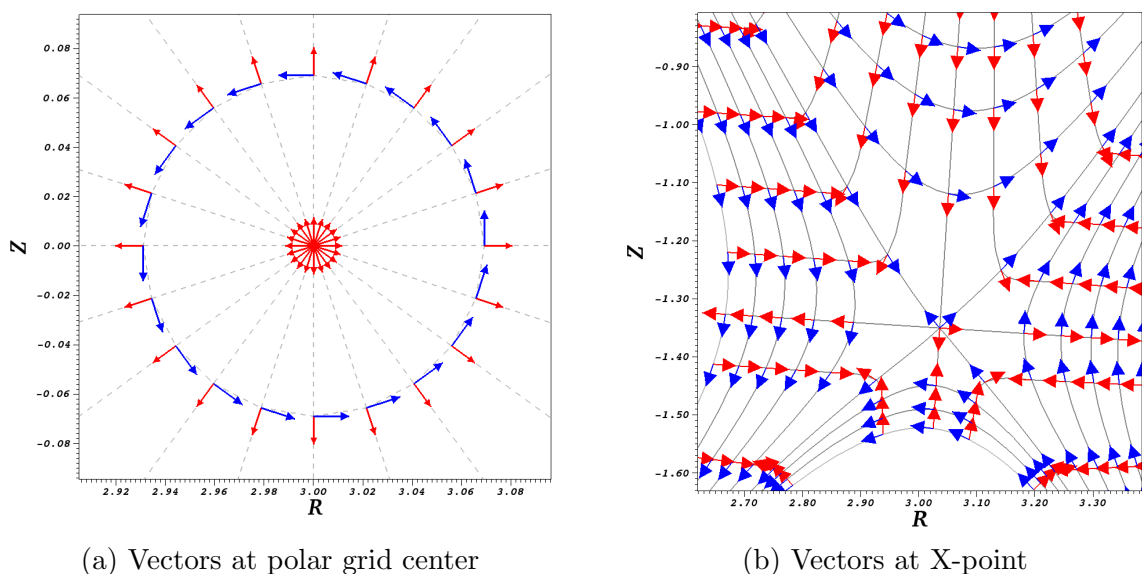


Figure 3.9: Grid singularities

In practice there may be vertices in the grid where number of elements sharing a vertex may be different than 4, for example the vertex denoting the location of the X-point, where 8 elements meet together as shown in Figure (3.8b) and (3.9b). Therefore, continuity of the gradients is not guaranteed at such points and the accuracy of the finite element method may be degraded. Moreover, the mapping from physical domain to parametric domain is assumed non-singular, a condition which is not satisfied at the polar grid center. At the polar grid center each element has one edge on the grid axis that collapses to a single vertex and as a consequence many elements meet at the same vertex. Precisely, the number of vertices that meet at the polar grid center is equal to the number of elements N_θ in the θ direction. Therefore, the number of DoFs at the polar grid center is $4N_\theta$, instead of 4, resulting in an over determined system. The global basis functions V_{i2D} are plotted at the polar grid center and shown in Figure (3.11 (a)-(d)). It can be seen that the 3rd and 4th basis functions are oscillatory across elements and are not continuous at the grid center. Such a basis can be a source of numerical instabilities and sometimes cause simulations to crash. A strategy developed to treat such singular points is presented in this section.

A situation is depicted in Figure (3.10a) where a curved element falls on the polar grid center as radius $r \rightarrow \epsilon$ where ϵ is a small real number. The edge of a curved element, joining vertex v_1 and v_4 , falls on the grid center (although in practice it can be any edge). This edge when mapped onto the unit reference element denotes the line $\hat{s} = 0$. Therefore, we focus on the representations of a grid and interpolation of a function at $\hat{s} = 0$.

Theorem 1: The entire curve $\xi(\hat{s} = 0, \hat{t})$ will asymptotically collapse to a single point ξ_* as $\epsilon \rightarrow 0$, if and only if

$$\xi_{g(1),1} = \xi_{g(4),1} = \xi_*; \quad \xi_{g(1),3} \sigma_{1,3}^3 = \xi_{g(4),3} \sigma_{4,3}^3 = 0$$

As a consequence we asymptotically have

$$\frac{\partial \xi}{\partial \hat{t}}(\hat{t}) = 0 \quad \forall t \in [0, 1]$$

Proof: By looking at the interpolation for $\hat{s} = 0$:

$$\xi(\hat{s} = 0, \hat{t}) = \sum_{v=1}^4 \sum_{d=1}^4 \xi_{g(v),d} \sigma_{v,d}^e H_{v,d}(\hat{s} = 0, \hat{t})$$

following relations can be written:

$$\xi(\hat{t}) = \xi_{g(1),1} H_{1,1}(\hat{t}) + \xi_{g(1),3} \sigma_{1,3}^e H_{1,3}(\hat{t}) + \xi_{g(4),1} H_{4,1}(\hat{t}) + \xi_{g(4),3} \sigma_{4,3}^e H_{4,3}(\hat{t})$$

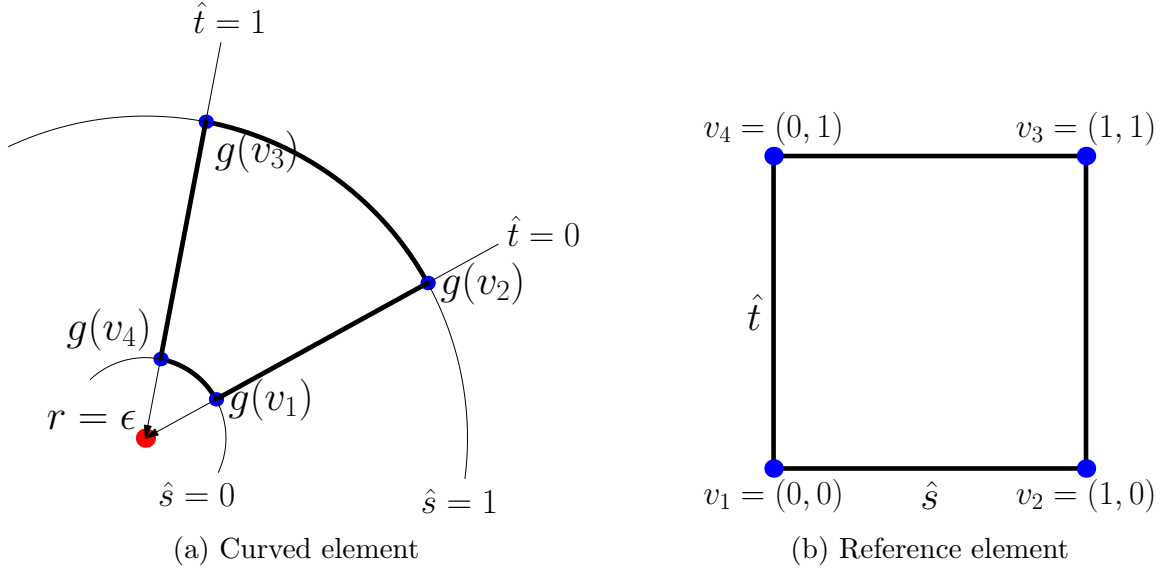


Figure 3.10: An element on the polar grid center. A typical situation where the edge of an element on the axis is formed by vertex v_1 and v_4 falls on the polar grid center which in the reference element forms the edge $\hat{s} = 0$.

It is easy to see that $H_{1,1}(\hat{t})$ and $H_{4,1}(\hat{t})$ form partition of unity : $H_{1,1}(\hat{t}) + H_{4,1}(\hat{t}) = 1 \quad \forall \hat{t} \in [0, 1]$. Therefore, we can rewrite the above relations as:

$$\begin{aligned} \boldsymbol{\xi}(\hat{t}) &= \boldsymbol{\xi}_* + (\boldsymbol{\xi}_{g(1),1} - \boldsymbol{\xi}_*) H_{1,1}(\hat{t}) + \boldsymbol{\xi}_{g(1),3} \sigma_{1,3}^e H_{1,3}(\hat{t}) \\ &\quad + (\boldsymbol{\xi}_{g(4),1} - \boldsymbol{\xi}_*) H_{4,1}(\hat{t}) + \boldsymbol{\xi}_{g(4),3} \sigma_{4,3}^e H_{4,3}(\hat{t}) \end{aligned}$$

where, $\boldsymbol{\xi}_*$ is the coordinates of the grid center and $\sigma_{1,1}^e = \sigma_{4,1}^e = 1$ by the construction of a grid. Since, the entire curve asymptotically falls on the single point $\boldsymbol{\xi}_*$, it follows that:

- $\boldsymbol{\xi}_{g(1),1} \rightarrow \boldsymbol{\xi}_*$ and $\boldsymbol{\xi}_{g(4),1} \rightarrow \boldsymbol{\xi}_*$
- $\boldsymbol{\xi}_{g(1),3} \rightarrow 0$ and $\boldsymbol{\xi}_{g(4),3} \rightarrow 0$ (since $\sigma_{1,3}^e \neq 0$ and $\sigma_{4,3}^e \neq 0$)

Now, let us look at the \hat{t} derivative at $\hat{s} = 0$:

$$\frac{\partial \boldsymbol{\xi}}{\partial \hat{t}}(\hat{t}) = \boldsymbol{\xi}_{g(1),1} \frac{\partial H_{1,1}}{\partial \hat{t}}(\hat{t}) + \boldsymbol{\xi}_{g(1),3} \sigma_{1,3}^e \frac{\partial H_{1,3}}{\partial \hat{t}}(\hat{t}) + \boldsymbol{\xi}_{g(4),1} \frac{\partial H_{4,3}}{\partial \hat{t}}(\hat{t}) + \boldsymbol{\xi}_{g(4),3} \sigma_{4,3}^e \frac{\partial H_{4,3}}{\partial \hat{t}}(\hat{t})$$

Using the deduction from $\boldsymbol{\xi}(0, \hat{t})$ and $\frac{\partial H_{1,1}}{\partial \hat{t}}(\hat{s} = 0, \hat{t}) + \frac{\partial H_{4,1}}{\partial \hat{t}}(\hat{s} = 0, \hat{t}) = 0$, it can be further deduced that:

$$\frac{\partial \boldsymbol{\xi}}{\partial \hat{t}}(\hat{s} = 0, \hat{t}) = 0$$

This completes the proof of the theorem. The condition $\partial_i \boldsymbol{\xi} = 0$ plays an important part in achieving the continuity of gradients at the grid center.

Lemma 1: As the entire curve $\boldsymbol{\xi}(\hat{s} = 0, \hat{t})$ asymptotically collapses to the single point $\boldsymbol{\xi}_*$, the DoFs $\boldsymbol{\xi}_{g(v),2}$ and $\boldsymbol{\xi}_{g(v),4}$ at the grid center can be written in terms of only $\frac{\partial \boldsymbol{\xi}}{\partial \hat{s}}$ and $\frac{\partial^2 \boldsymbol{\xi}}{\partial \hat{s} \partial \hat{t}}$.

Proof: Let us look at \hat{s} and mixed derivative of $\boldsymbol{\xi}$ at $\hat{s} = 0$:

$$\begin{aligned} \frac{\partial \boldsymbol{\xi}}{\partial \hat{s}}(\hat{t}) &= \boldsymbol{\xi}_{g(1),2} \sigma_{1,2}^e \frac{\partial H_{1,2}}{\partial \hat{s}}(\hat{t}) + \boldsymbol{\xi}_{g(1),4} \sigma_{1,4}^e \frac{\partial H_{1,4}}{\partial \hat{s}}(\hat{t}) \\ &\quad + \boldsymbol{\xi}_{g(4),2} \sigma_{4,2}^e \frac{\partial H_{4,2}}{\partial \hat{s}}(\hat{t}) + \boldsymbol{\xi}_{g(4),4} \sigma_{4,4}^e \frac{\partial H_{4,4}}{\partial \hat{s}}(0, \hat{t}) \end{aligned}$$

$$\begin{aligned} \frac{\partial^2 \boldsymbol{\xi}}{\partial \hat{s} \partial \hat{t}}(\hat{t}) &= \boldsymbol{\xi}_{g(1),2} \sigma_{1,2}^e \frac{\partial^2 H_{1,2}}{\partial \hat{s} \partial \hat{t}}(\hat{t}) + \boldsymbol{\xi}_{g(1),4} \sigma_{1,4}^e \frac{\partial^2 H_{1,4}}{\partial \hat{s} \partial \hat{t}}(\hat{t}) \\ &\quad + \boldsymbol{\xi}_{g(4),2} \sigma_{4,2}^e \frac{\partial^2 H_{4,2}}{\partial \hat{s} \partial \hat{t}}(\hat{t}) + \boldsymbol{\xi}_{g(4),4} \sigma_{4,4}^e \frac{\partial^2 H_{4,4}}{\partial \hat{s} \partial \hat{t}}(\hat{t}) \end{aligned}$$

Since, the curve $\hat{s} = 0$ collapses to a single point $\boldsymbol{\xi}_*$, we can write $\boldsymbol{\xi}_{g(1),2} = \boldsymbol{\xi}_{g(4),2} = \boldsymbol{\xi}_{*,2}$ and $\boldsymbol{\xi}_{g(1),4} = \boldsymbol{\xi}_{g(4),4} = \boldsymbol{\xi}_{*,4}$. Therefore, above relations can be written as:

$$\begin{bmatrix} \frac{\partial \boldsymbol{\xi}}{\partial \hat{s}}(\hat{t}) \\ \frac{\partial^2 \boldsymbol{\xi}}{\partial \hat{s} \partial \hat{t}}(\hat{t}) \end{bmatrix}_{\hat{s}=0} = \begin{bmatrix} \sigma_{1,2}^e \frac{\partial H_{1,2}}{\partial \hat{s}} + \sigma_{4,2}^e \frac{\partial H_{4,2}}{\partial \hat{s}} & \sigma_{1,4}^e \frac{\partial H_{1,4}}{\partial \hat{s}} + \sigma_{4,4}^e \frac{\partial H_{4,4}}{\partial \hat{s}} \\ \sigma_{1,2}^e \frac{\partial^2 H_{1,2}}{\partial \hat{s} \partial \hat{t}}(\hat{t}) + \sigma_{4,2}^e \frac{\partial^2 H_{4,2}}{\partial \hat{s} \partial \hat{t}} & \sigma_{1,4}^e \frac{\partial^2 H_{1,4}}{\partial \hat{s} \partial \hat{t}} + \sigma_{4,4}^e \frac{\partial^2 H_{4,4}}{\partial \hat{s} \partial \hat{t}} \end{bmatrix}_{\hat{s}=0} \begin{bmatrix} \boldsymbol{\xi}_{g(*),2} \\ \boldsymbol{\xi}_{g(*),4} \end{bmatrix}$$

Alternatively, rewriting the inverse equations:

$$\begin{bmatrix} \boldsymbol{\xi}_{g(*),2} \\ \boldsymbol{\xi}_{g(*),4} \end{bmatrix} = \begin{bmatrix} \sigma_{1,2}^e \frac{\partial H_{1,2}}{\partial \hat{s}} + \sigma_{4,2}^e \frac{\partial H_{4,2}}{\partial \hat{s}} & \sigma_{1,4}^e \frac{\partial H_{1,4}}{\partial \hat{s}} + \sigma_{4,4}^e \frac{\partial H_{4,4}}{\partial \hat{s}} \\ \sigma_{1,2}^e \frac{\partial^2 H_{1,2}}{\partial \hat{s} \partial \hat{t}}(\hat{t}) + \sigma_{4,2}^e \frac{\partial^2 H_{4,2}}{\partial \hat{s} \partial \hat{t}} & \sigma_{1,4}^e \frac{\partial^2 H_{1,4}}{\partial \hat{s} \partial \hat{t}} + \sigma_{4,4}^e \frac{\partial^2 H_{4,4}}{\partial \hat{s} \partial \hat{t}} \end{bmatrix}_{\hat{s}=0}^{-1} \begin{bmatrix} \frac{\partial \boldsymbol{\xi}}{\partial \hat{s}} \\ \frac{\partial^2 \boldsymbol{\xi}}{\partial \hat{s} \partial \hat{t}} \end{bmatrix}_{\hat{s}=0}$$

Hence it can be seen that at $\hat{s} = 0$, 2nd and 4th DoFs can be written only in terms of \hat{s} derivatives and mixed derivatives.

Before we look the interpolation of any scalar function $W(\hat{s}, \hat{t})$ at $\hat{s} = 0$, we note the following relations between DoFs and alternate DoFs:

$$\begin{aligned} W_{g(v),1} &= \mathcal{W}(g(v)) \\ W_{g(v),2} &= \frac{\partial W}{\partial \hat{s}} = \nabla_{\boldsymbol{\xi}} \mathcal{W} \cdot \frac{\partial \boldsymbol{\xi}}{\partial \hat{s}} \\ W_{g(v),3} &= \frac{\partial W}{\partial \hat{t}} = \nabla_{\boldsymbol{\xi}} \mathcal{W} \cdot \frac{\partial \boldsymbol{\xi}}{\partial \hat{t}} \\ W_{g(v),4} &= \frac{\partial^2 \mathcal{W}}{\partial \hat{s} \partial \hat{t}} = \nabla_{\boldsymbol{\xi}} \mathcal{W} \cdot \frac{\partial^2 \boldsymbol{\xi}}{\partial \hat{s} \partial \hat{t}} + \mathcal{H}_{\boldsymbol{\xi}}(\mathcal{W}) : \left(\frac{\partial \boldsymbol{\xi}}{\partial \hat{s}} \otimes \frac{\partial \boldsymbol{\xi}}{\partial \hat{t}} \right) \end{aligned} \tag{3.24}$$

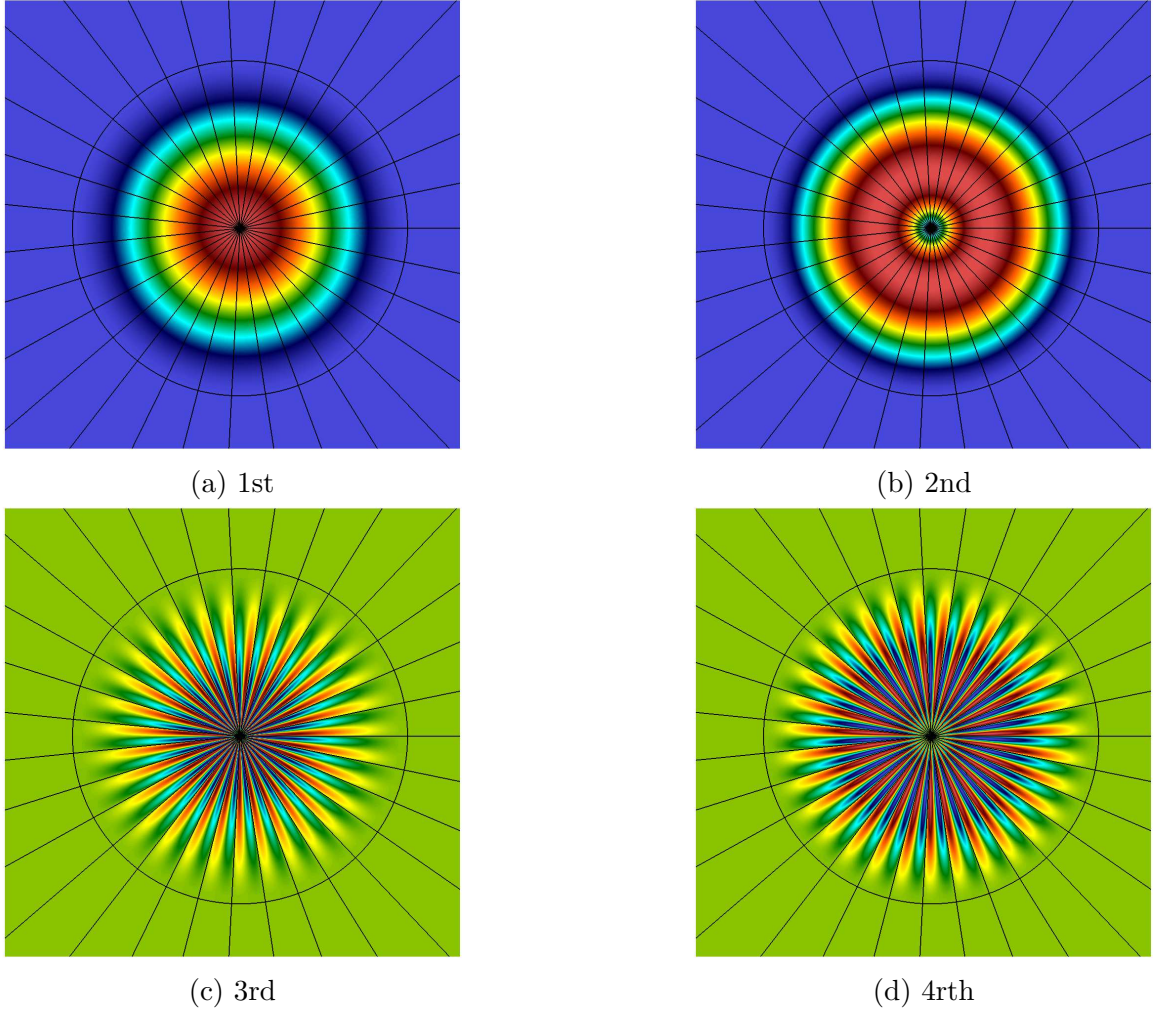


Figure 3.11: Basis function plotted at the polar grid center. The third and fourth basis functions are oscillatory in the θ direction and are not continuous at the grid center.

where, $W(\tilde{\tau}) = \mathcal{W}(\boldsymbol{\xi})$ is the function in the physical space and $\mathcal{H}_{\boldsymbol{\xi}}(\mathcal{W})$ is a Hessian matrix for W with respect to $\boldsymbol{\xi}$ given by:

$$\mathcal{H}_{\boldsymbol{\xi}}(\mathcal{W}) = \begin{bmatrix} \partial_{RR}\mathcal{W} & \partial_{RZ}\mathcal{W} \\ \partial_{RZ}\mathcal{W} & \partial_{ZZ}\mathcal{W} \end{bmatrix}$$

These relations imply that bicubic Bézier FEM can be written alternatively in terms six DoFs: \mathcal{W} , $\nabla_{\boldsymbol{\xi}}\mathcal{W}$, $\mathcal{H}_{\boldsymbol{\xi}}(\mathcal{W})$ those corresponds to derivatives in the physical space $\boldsymbol{\xi}$.

Theorem 2: If the entire curve $\boldsymbol{\xi}(\hat{s} = 0, \hat{t})$ asymptotically collapse to a single point $\boldsymbol{\xi}_*$ as $\epsilon \rightarrow 0$, then for a scalar function W one gets:

$$W_{g(1),1} = W_{g(4),1} = W_*; \quad W_{g(1),3} \sigma_{1,3}^3 = W_{g(4),3} \sigma_{4,3}^3 = 0$$

where, W_* is the value of the function W at the polar grid center. As a consequence we asymptotically have

$$\frac{\partial W}{\partial \hat{t}}(\hat{t}) = 0 \quad \forall \hat{t} \in [0, 1]$$

This theorem can be proved similar to Theorem 1.

Theorem 3: Assuming that the edge formed by vertices $v = 1$ and $v = 4$ of an element lies on the polar grid center, the interpolation of a function W in the element on the grid center is given by:

$$W(\hat{s}, \hat{t}) = \sum_{v=2}^3 \sum_{d=1}^4 W_{g(v),d} \sigma_{v,d}^e B_{v,d}(\hat{s}, \hat{t}) + \sum_{d=1}^4 W_{g(1),d} N_{1,d}^e + \sum_{d=1}^4 W_{g(4),d} N_{4,d}^e$$

where, $N_{v,d}^e$ are given by the equation (3.25).

Proof: Looking at the equations (3.24) at $\hat{s} = 0$ for vertex $v = 1$ and $v = 4$:

$$\begin{aligned} W_{g(v),1} &= \mathcal{W}(g(v)) \Big|_{\hat{s}=0} \\ W_{g(v),2} &= \nabla_{\xi} \mathcal{W} \cdot \frac{\partial \xi}{\partial \hat{s}} \Big|_{\hat{s}=0} \\ W_{g(v),3} &= \nabla_{\xi} \mathcal{W} \cdot \frac{\partial \xi}{\partial \hat{t}} \Big|_{\hat{s}=0} \\ W_{g(v),4} &= \nabla_{\xi} \mathcal{W} \cdot \frac{\partial^2 \xi}{\partial \hat{s} \partial \hat{t}} \Big|_{\hat{s}=0} + \mathcal{H}_{\xi}(\mathcal{W}) : \left(\frac{\partial \xi}{\partial \hat{s}} \otimes \frac{\partial \xi}{\partial \hat{t}} \right) \Big|_{\hat{s}=0} \end{aligned}$$

From Theorem 2, it is clear that the first and fourth DoFs are the same at the grid center: $W_{g(1),1} = W_{g(4),1} = W_*$. From Theorem 1, we have

$$\frac{\partial \xi}{\partial \hat{t}}(\hat{t}) = 0 \quad \forall \hat{t} \in [0, 1]$$

which implies that the 3rd DoF become zero: $W_{g(1),3} = W_{g(4),3} = W_{g(*)},3 = 0$ and the remaining two equations are written as:

$$\begin{aligned} W_{g(v),2} &= \nabla_{\xi} \mathcal{W} \cdot \frac{\partial \xi}{\partial \hat{s}} \Big|_{\hat{s}=0} \\ W_{g(v),4} &= \nabla_{\xi} \mathcal{W} \cdot \frac{\partial^2 \xi}{\partial \hat{s} \partial \hat{t}} \Big|_{\hat{s}=0} \end{aligned}$$

Using Lemma 1, these equations can be rewritten as:

$$\begin{aligned}
\begin{pmatrix} W_{g(v),2} \\ W_{g(v),4} \end{pmatrix} &= \begin{bmatrix} \frac{\partial \xi}{\partial \hat{s}} \\ \frac{\partial^2 \xi}{\partial \hat{s} \partial \hat{t}} \end{bmatrix}_{\hat{s}=0} \cdot \nabla_{\xi} \mathcal{W} \\
&= \begin{bmatrix} \sigma_{1,2}^e \frac{\partial H_{1,2}}{\partial \hat{s}} + \sigma_{4,2}^e \frac{\partial H_{4,2}}{\partial \hat{s}} & \sigma_{1,4}^e \frac{\partial H_{1,4}}{\partial \hat{s}} + \sigma_{4,4}^e \frac{\partial H_{4,4}}{\partial \hat{s}} \\ \sigma_{1,2}^e \frac{\partial^2 H_{1,2}}{\partial \hat{s} \partial \hat{t}}(\hat{t}) + \sigma_{4,2}^e \frac{\partial^2 H_{4,2}}{\partial \hat{s} \partial \hat{t}} & \sigma_{1,4}^e \frac{\partial^2 H_{1,4}}{\partial \hat{s} \partial \hat{t}} + \sigma_{4,4}^e \frac{\partial^2 H_{4,4}}{\partial \hat{s} \partial \hat{t}} \end{bmatrix}_{\hat{s}=0} \begin{bmatrix} \xi_{g(*),2} \\ \xi_{g(*),4} \end{bmatrix} \cdot \nabla_{\xi} \mathcal{W} \\
\begin{pmatrix} W_{g(v),2} \\ W_{g(v),4} \end{pmatrix} &= \begin{bmatrix} N_{1,2}^e & N_{4,2}^e \\ N_{1,4}^e & N_{4,4}^e \end{bmatrix}_{\hat{s}=0} \cdot \begin{pmatrix} \partial_R \mathcal{W} \\ \partial_Z \mathcal{W} \end{pmatrix}
\end{aligned}$$

where,

$$\begin{aligned}
N_{1,2}^e(\hat{t}) &= \xi_{g(*),2} \sigma_{1,2}^e \frac{\partial H_{1,2}}{\partial \hat{s}}(\hat{t}) + \xi_{g(*),4} \sigma_{1,4}^e \frac{\partial H_{1,4}}{\partial \hat{t}}(\hat{t}) \\
N_{4,2}^e(\hat{t}) &= \xi_{g(*),2} \sigma_{4,2}^e \frac{\partial H_{4,2}}{\partial \hat{s}}(\hat{t}) + \xi_{g(*),4} \sigma_{4,4}^e \frac{\partial H_{4,4}}{\partial \hat{t}}(\hat{t}) \\
N_{1,4}^e(\hat{t}) &= \xi_{g(*),2} \sigma_{1,2}^e \frac{\partial^2 H_{1,2}}{\partial \hat{s} \partial \hat{t}}(\hat{t}) + \xi_{g(*),4} \sigma_{1,4}^e \frac{\partial^2 H_{1,4}}{\partial \hat{s} \partial \hat{t}}(\hat{t}) \\
N_{4,4}^e(\hat{t}) &= \xi_{g(*),2} \sigma_{4,2}^e \frac{\partial^2 H_{4,2}}{\partial \hat{s} \partial \hat{t}}(\hat{t}) + \xi_{g(*),4} \sigma_{4,4}^e \frac{\partial^2 H_{4,4}}{\partial \hat{s} \partial \hat{t}}(\hat{t})
\end{aligned} \tag{3.25}$$

Above equations can be thought as the new basis functions for the new 2nd and 4th DoFs given by $\partial_R W$ and $\partial_Z W$ respectively. Now, the interpolation of a sufficiently smooth scalar function for an element on the polar grid center can be written as:

$$\begin{aligned}
W(\hat{s}, \hat{t}) &= \sum_{v=1}^4 \sum_{d=1}^4 W_{g(v),d} \sigma_{v,d}^e B_{v,d}(\hat{s}, \hat{t}) \\
&= \sum_{v=2}^3 \sum_{d=1}^4 W_{g(v),d} \sigma_{v,d}^e B_{v,d} + \sum_{d=1}^4 W_{g(1),d} \sigma_{1,d}^e B_{1,d} + \sum_{d=1}^4 W_{g(4),d} \sigma_{4,d}^e B_{4,d}
\end{aligned}$$

Using the results of Theorem 1, 2 and Lemma 1, the interpolation can be written in terms of new basis functions and DoFs as:

$$\begin{aligned}
W(\hat{s}, \hat{t}) &= \sum_{v=2}^3 \sum_{d=1}^4 W_{g(v),d} \sigma_{v,d}^e B_{v,d}(\hat{s}, \hat{t}) \\
&\quad + \sum_{d=1}^4 W_{g*,d} N_{1,d}^e(\hat{t}) + \sum_{d=1}^4 W_{*,d} N_{4,d}^e(\hat{t})
\end{aligned}$$

The new DoFs and new basis functions are summarized in Table (3.2). Note that the basis function associated with 3rd DoF do not play any role as 3rd DoF is set to zero. In practice this is done by penalization. These new basis functions impose continuity of gradients at the polar grid center in the physical plane and are shown in Figure (3.12).

Node 1			Node 4		
DoF	Scales	Basis functions	DoF	Scales	Basis functions
$W_{g(*)},1 = \mathcal{W}_*$	1	$N_{1,1}^e = H_{1,1}$	$W_{g(*)},1 = \mathcal{W}_*$	1	$N_{1,1}^e = H_{4,1}$
$W_{g(*)},2 = \frac{\partial \mathcal{W}}{\partial R} \Big _*$	1	$N_{1,2}^e$	$W_{g(*)},2 = \frac{\partial \mathcal{W}}{\partial R} \Big _*$	1	$N_{4,2}^e$
$W_{g(*)},3 = 0$	1	$N_{1,3}^e = \sigma_{1,3}^e H_{1,3}$	$W_{g(*)},3 = 0$	1	$N_{4,3}^e = \sigma_{4,3}^e H_{4,3}$
$W_{g(*)},4 = \frac{\partial \mathcal{W}}{\partial Z} \Big _*$	1	$N_{1,4}^e$	$W_{g(*)},4 = \frac{\partial \mathcal{W}}{\partial Z} \Big _*$	1	$N_{4,4}^e$

Table 3.2: Summary of new DoFs, scales and basis functions to be applied at the polar grid center. The basis functions $N_{1,2}^e$, $N_{1,4}^e$, $N_{4,2}^e$ and $N_{4,4}^e$ are given by the equations (3.25).

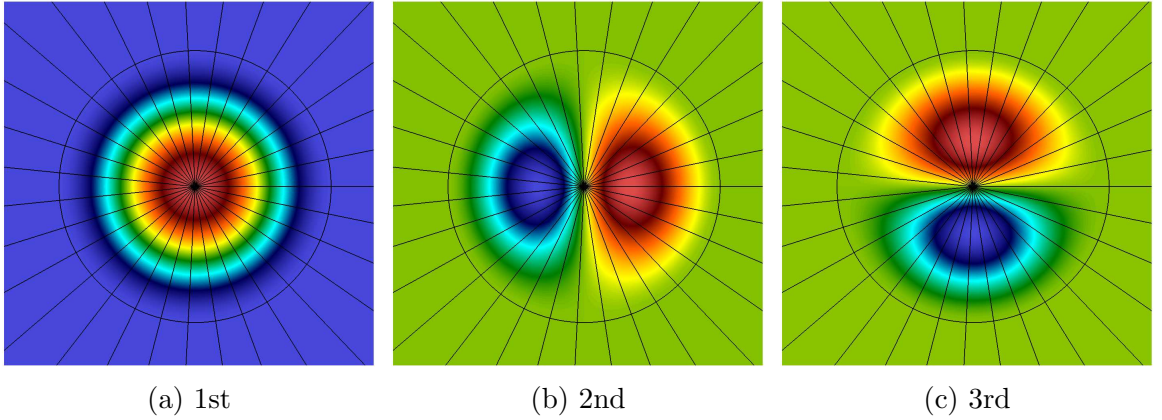


Figure 3.12: New global basis functions plotted at the polar grid center. The first basis function is unchanged. The second and fourth basis functions are linear combinations of original basis functions. The third basis function is not to be used as the DoF associate it with 0.

A simple demonstration is shown in Figure (3.13) where the errors in the quantities $\frac{\partial \xi}{\partial \hat{s}}$ and $\frac{\partial^2 \xi}{\partial \hat{s} \partial \hat{t}}$ at $\hat{s} = 0$ for a circular polar grid are plotted vs \hat{t} where m denotes number of points in the θ direction. It can be seen that the errors in the grid data even for $m = 20$ are sufficiently small. Here, the errors refer to the difference between exact polar representation and bicubic Bézier representation of a polar grid.

Figure (3.14) shows the L^2 norm of the interpolation error in the function

$$\mathcal{W} = R^4 + R^3 + R^2 + R + Z^4 + Z^3 + Z^2 + Z$$

for any element on the polar grid center plotted vs element size h . The parametric (r, θ) plane is discretized by equi-spaced points such that the rectangular elements have sides of length:

$$dr = \frac{1}{2^{m+1}} \quad \text{and} \quad d\theta = \frac{2\pi}{2^{m+1}}$$

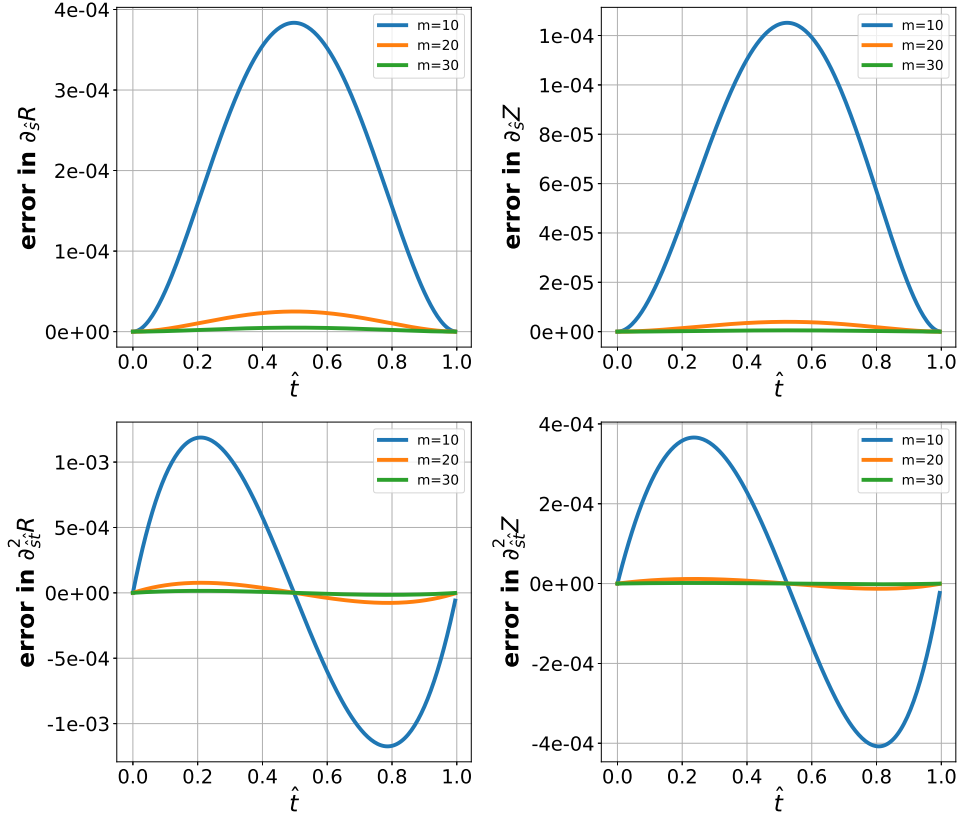


Figure 3.13: Error in the grid representation at the polar grid center. Errors in $\frac{\partial \xi}{\partial \hat{s}}$ and $\frac{\partial \xi}{\partial \hat{s} \partial \hat{t}}$ at $\hat{s} = 0$ are plotted vs. \hat{t} where m denotes number of points in the θ direction.

The interpolation is computed using new basis functions derived above and it can be seen in Figure (3.14) that errors follow convergence of order 4. For the sake of discussion, the numerical tests to demonstrate the effect of the new basis functions proposed are presented in Chapter 4.

3.5 Conclusions

In this Chapter numerical methods used for nonlinear modeling of MHD equations are discussed. Chapter introduces the motivation for the choice of numerical methods from the spatial and temporal discretization point of view. In section (3.1) a general framework of Galerkin FEM is discussed while in section (3.2) mixed bicubic Bézier-Spectral FEM used in JOEAK is described and the stabilization term are based on VMS and shock-capturing strategies are formulated. In section (3.3) the implicit time integration method adapted for variable time step is derived whereas section

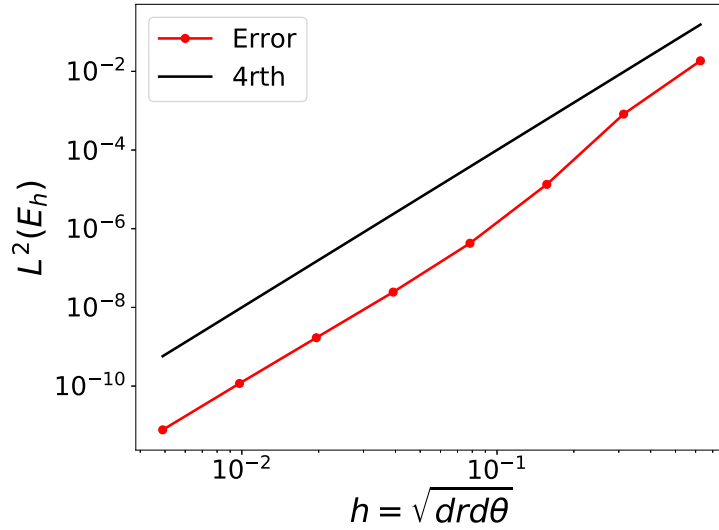


Figure 3.14: L^2 norm of the interpolation error for the function $\mathcal{W} = R^4 + R^3 + R^2 + R + Z^4 + Z^3 + Z^2 + Z$ plotted vs element size h . The interpolation of a function is computed using new basis functions derived for elements on the polar grid center.

(3.4) describes the multi-block grid generation for the realistic tokamak geometries. The choice of FEM allows one to generate grids with curved elements so that accurate representation of boundaries can be made and grid elements can be aligned to magnetic flux surfaces. Finally, issues of grid singularities is discussed and a strategy is proposed to overcome the numerical problems due to grid singularities.

This Chapter sets all the numerical tools required to simulated nonlinear MHD phenomena. On the top of the bicubic Bézier FEM used in JOREK, we have implemented the stabilization terms as an additional contribution to the weak form, adapted the time integration method for variable time stepping and proposed a numerical treatment for the grid singularities encountered. These tools are applied on the MHD equations discussed in Chapter 2 and the numerical results obtained are presented in next Chapters.

Chapter 4

Implementation and validation of full MHD model

In this Chapter we describe the implementation of numerical methods discussed in Chapter 3 on the governing equations discussed in Chapter 2 along with the details of the FEM implementation. Then we present the numerical results for standard MHD instabilities. The main idea is to perturb a plasma equilibrium and evolve perturbations numerically about an equilibrium. Energy principle tells us that the MHD instabilities can be driven by parallel current or pressure gradient [32, 96]. Moreover, in tokamak plasma, probable locations of MHD instabilities are rational q surfaces and hence grids used in the simulations are often refined in the region of rational q surfaces.

Since Fourier representation is used in the toroidal direction, finite number of toroidal harmonics, denoted by n , are included in the simulations. Linear runs refer to the simulations in which axisymmetric $n = 0$ kept stationary and $n \neq 0$ modes are evolved in time. Usually this is done to investigate the growth rates of a single harmonic. When all harmonics including $n = 0$ are evolved in time, the simulation is referred to as a nonlinear run.

In section (4.1) we describe implementation of bicubic Bézier finite element method (FEM) on Grad-Shafranov equation, which is a nonlinear elliptic partial differential equation (PDE) that governs axisymmetric plasma equilibrium in 2D. In section (4.2), implementation of FEM on full MHD model is described focusing upon the weak form and projections used in vector test functions. In section (4.3), we present numerical results of linear simulations for standard MHD instability problems such as internal

kink, tearing and ballooning modes. The growth rates of energies for these modes are computed as dE/dt where E can be kinetic or magnetic energy and are compared for full and reduced MHD models. Finally, in section (4.4) nonlinear simulations are presented for internal kink modes.

4.1 Solving Grad-Shafranov equation

Grad-Shafranov equation (2.35) for ideal MHD equilibrium is a nonlinear elliptic PDE, re-written here in a strong form as:

$$\Delta^* \psi = R^2 \left(\nabla \cdot \frac{1}{R^2} \nabla \psi \right) = f(\psi) \quad \text{in } \Omega_\xi$$

where f in the right hand side is given by

$$f = R^2 p' - F F'$$

where prime denotes the derivative with respect to ψ . Three essential inputs required to solve Grad-Shafranov equations are:

- boundary conditions on ψ
- pressure profile $p(\psi)$
- $FF'(\psi)$ profile

Boundary conditions on ψ along with the R and Z coordinates of the boundary may be obtained from ‘geqdsk’ files or from equilibria created with CLISTE code. The functions p and F are specified as the profiles of normalized magnetic flux surface ψ_N :

$$\psi_N = \frac{\psi - \psi_a}{\psi_e - \psi_a}$$

where, ψ_a denotes the flux at the magnetic axis and ψ_e refers to the separatrix (in case of a divertor configuration) or the last closed surface (a limiter configuration). The profiles are usually constructed by fitting with the experimental data. The fitting assumes polynomial profile for the density ρ , temperature T and square of the poloidal current flux $G = (F(\psi))^2$. The profile for density is specified as:

$$\rho(\psi_N) = (\rho_0 - \rho_1) \left(1 + \sum_{i=1}^3 C(i) \psi_N^i \right) \left(0.5 - 0.5 \tanh \left(\frac{\psi_N - C(5)}{C(4)} \right) \right) + \rho_1 \quad (4.1)$$

where,

ρ_0 : Density at the magnetic axis

ρ_1 : Density outside the separatrix or at the last closed flux surface

$C(1)$: linear slope of modified tanh

$C(2)$: quadratic slope of modified tanh

$C(3)$: cubic slope of modified

$C(4)$: width of tanh

$C(5)$: position of tanh

In the similar way, a temperature profile is also specified. Finally, the equation of the

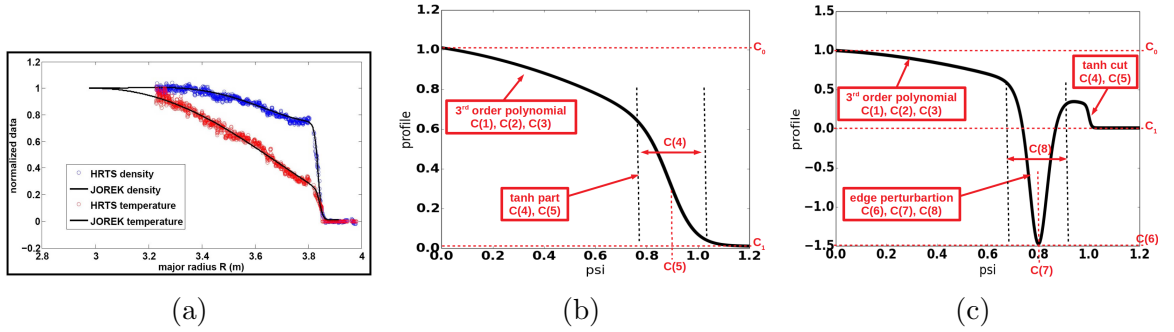


Figure 4.1: (a) The density (blue circles) and temperature (red circles) profiles from the JET experiment (pulse no. 73569), with the corresponding fitted profiles used for simulations (plain black lines). [75] (b) Interpretations for the coefficients of profiles of the density and temperature (c) Interpretations for the coefficients of profiles of FF'

state $p = \rho T$ gives the pressure profile as:

$$\frac{dp}{d\psi} = \frac{d\rho}{d\psi} T + \rho \frac{dT}{d\psi} = \frac{1}{\psi_e - \psi_a} \left(\frac{d\rho}{d\psi_N} T + \rho \frac{dT}{d\psi_N} \right)$$

The fit of density and temperature profiles with the experimental data of a particular JET run is shown in Figure (4.1a). Each of the density and temperature profile is constructed with the coefficients whose interpretations are shown in Figure (4.1b). The profile for FF' is obtained from the profile of $G = F^2$ which is written as:

$$G(\psi_N) = G_0 + 2(\psi_e - \psi_a) \sum_{i=1}^3 C_i \frac{\psi_N^i}{i}$$

which after deriving with respect to ψ becomes:

$$FF'(\psi_N) = \frac{1}{2(\psi_e - \psi_a)} \frac{\partial G}{\partial \psi_N} = \sum_{i=1}^3 C_i \psi_N^{i-1}$$

An additional perturbation at the plasma edge may be added in FF' profile to account for the bootstrap current and the profile is precisely given as:

$$FF'(\psi_N) = ((C_0 - C_1)f_{poly} + f_{pert}) f_{tanh} + C_1 \quad (4.2)$$

where

$$\begin{aligned} f_{poly}(\psi_N) &= 1 + C(1) \psi_N + C(2) \psi_N^2 + C(3) \psi_N^3 \\ f_{tanh}(\psi_N) &= 0.5 - 0.5 * \tanh\left(\frac{\psi_N - C(5)}{C(4)}\right) \\ f_{pert}(\psi_N) &= \frac{C(6)}{2C(8)} \cosh\left(\frac{\psi_N - C(7)}{C(8)}\right)^{-2} \end{aligned}$$

The meaning of the coefficients for FF' profile are:

C_0 : Value at magnetic axis

C_1 : Value outside separatrix

$C(1)$: linear slope of modified tanh

$C(2)$: quadratic slope of modified tanh

$C(3)$: cubic slope of modified

$C(4)$: width of tanh (to switch off profile in SOL)

$C(5)$: position of tanh

$C(6)$: amplitude of edge perturbation

$C(7)$: position of edge perturbation

$C(8)$: width of edge perturbation

Figure (4.1c) shows the role of coefficients in defining FF' profile. We now seek a weak formulation of Grad-Shafranov equation. Let \mathcal{W} be the space of functions such that $\mathcal{W} = \{\psi^* \in [H^1(\Omega_\xi)]\}$ where ψ^* is a test function. Multiplying the strong form with a test function and then integrating over the domain gives:

$$\int_{\Omega_\xi} \frac{1}{R^2} \psi^* R^2 \left(\nabla \cdot \frac{1}{R^2} \nabla \psi \right) d\Omega_\xi = \int_{\Omega_\xi} \frac{1}{R^2} \psi^* f d\Omega_\xi$$

The factor $1/R^2$ is multiplied at the both sides for convenience. Using integration by parts the weak form is written as:

$$- \int_{\Omega_\xi} \frac{1}{R^2} \nabla \psi^* \cdot \nabla \psi d\Omega_\xi + \oint \frac{1}{R^2} \psi^* \nabla \psi \cdot \hat{n} dS = \int_{\Omega_\xi} \frac{1}{R^2} \psi^* (R^2 p' - FF') d\Omega_\xi$$

For a homogeneous Dirichlet boundary condition, the boundary integral term vanishes and then the weak form becomes: Find $\psi \in \mathcal{V}$ such that:

$$- \int_{\Omega_\xi} \frac{1}{R^2} \nabla \psi^* \cdot \nabla \psi d\Omega_\xi = \int_{\Omega_\xi} \frac{1}{R^2} \psi^* f d\Omega_\xi \quad \forall \psi^* \in \mathcal{W}$$

To formulate a FEM we need finite-dimensional subspace $\mathcal{V}_h \subset \mathcal{V}$ and $\mathcal{W}_h \subset \mathcal{W}$. Now, the discrete weak form becomes: Find $\psi_h \in \mathcal{V}_h$ such that:

$$- \int_{\Omega_\xi} \frac{1}{R^2} \nabla \psi^* \cdot \nabla \psi_h \, d\Omega_\xi = \int_{\Omega_\xi} \frac{1}{R^2} \psi^* f \, d\Omega_\xi \quad \forall \psi^* \in \mathcal{W}_h$$

where, \mathcal{W}_h is a space for test functions yet to be specified. The function ψ_h is represented in terms of shape functions as:

$$\psi_h(\boldsymbol{\xi}) = \sum_{p=1}^{np} \sum_{d=1}^4 \psi_{p,d} N_{p,d}(\boldsymbol{\xi})$$

where, np are number vertices in poloidal plane. Substituting this expansion, the weak form then becomes:

$$- \int_{\Omega_\xi} \sum_{p=1}^{np} \sum_{d=1}^4 \psi_{p,d} \frac{1}{R^2} \nabla \psi^* \cdot \nabla N_{p,d} \, d\Omega_\xi = \int_{\Omega_\xi} \frac{1}{R^2} \psi^* f \, d\Omega_\xi \quad \forall \psi^* \in \mathcal{W}_h$$

In Galerkin FEM, the test functions ψ^* are chosen from the same space as trial functions and hence $\mathcal{W}_h = \mathcal{V}_h$. Now, the Galerkin FEM is written as:

$$- \int_{\Omega_\xi} \sum_{p=1}^{np} \sum_{d=1}^4 \psi_{p,d} \frac{1}{R^2} \nabla N_{p',d'} \cdot \nabla N_{p,d} \, d\Omega_\xi = \int_{\Omega_\xi} \frac{1}{R^2} N_{p',d'} f \, d\Omega_\xi \quad \forall N_{p',d'} \in \mathcal{V}_h$$

To discretize the weak form above one needs to construct a finite dimensional subspace on the domain Ω_ξ which is described in Chapter 3. To construct \mathcal{V}_h , first the domain is subdivided into non overlapping quadrangular elements Ω_e such that $\Omega_\xi = \bigcup \Omega_e$. In order to achieve higher order of approximation, curved elements represented by bicubic Bézier polynomials are constructed. A curved finite element is defined as (Ω_e, Q, Σ) where Q is a finite dimensional space of shape functions \mathcal{B}_k on Ω_e and Σ is a finite set of nodal variables. The shape functions \mathcal{B}_k are such that the restrictions of $N_{p,d}$ on any element gives shape functions for that particular element. Therefore, the discrete weak form on any element Ω_e is written as:

$$- \int_{\Omega_e} \sum_{v=1}^4 \sum_{d=1}^4 \psi_{g(v),d} \frac{1}{R^2} \nabla \mathcal{B}_{g(v'),d'} \cdot \nabla \mathcal{B}_{g(v),d} \, d\Omega_e = \int_{\Omega_e} \frac{1}{R^2} \mathcal{B}_{g(v'),d'} f \, d\Omega_e \quad \forall \mathcal{B}_{g(v'),d'}$$

Above equation can be rewritten in the matrix-vector form as:

$$\sum_{v=1}^4 \sum_{d=1}^4 A_{g(v'),d',g(v),d}^e \psi_{g(v),d}^e = \mathbf{r}_{g(v'),d'}^e \quad \forall \mathcal{B}_{g(v'),d'}$$

where,

$$A_{g(v'),d',g(v),d}^e = - \int_{\Omega_e} \frac{1}{R^2} \nabla \mathcal{B}_{g(v'),d'} \cdot \nabla \mathcal{B}_{g(v),d} d\Omega_e$$

$$\mathbf{r}_{g(v'),d'}^e = \int_{\Omega_e} \frac{1}{R^2} \mathcal{B}_{g(v'),d'} f d\Omega_e$$

These integrals are computed by mapping a curved element Ω_e onto a unit reference element $\hat{\tau}$. The reference finite element is defined as $(\hat{\tau}, Q, \hat{\Sigma})$ where $\hat{\tau}(\hat{s}, \hat{t})$ is a biunit reference element as shown in Figure (3.1c). Let \mathcal{M} denote one-to-one mapping of $\hat{\tau}$ onto a curved element Ω_e in $\boldsymbol{\xi}$ plane as:

$$\mathcal{M} : \Omega_e(\boldsymbol{\xi}) \rightarrow \hat{\tau}$$

The jacobian matrix of the mapping is then given by:

$$J = \begin{bmatrix} \partial_{\hat{s}} R & \partial_{\hat{t}} R \\ \partial_{\hat{s}} Z & \partial_{\hat{t}} Z \end{bmatrix}$$

The space of shape function Q is then written as:

$$Q = \{ \mathcal{B} : \mathcal{B}(\boldsymbol{\xi}) = B(\mathcal{M}^{-1}(\boldsymbol{\xi})), \quad \boldsymbol{\xi} \in \Omega_e, B \in Q(\hat{\tau}) \}$$

and nodal variables are given by:

$$\hat{\Sigma} = \{ \psi : \psi_{i_{2D}}(B_{j_{2D}}) = \delta_{i_{2D}, j_{2D}} \}$$

where $i_{2D} = (g(v), d)$ is a multi index that denotes the index of the shape function associated to vertex $g(v)$ and DoF d . Representing the integrals in the reference element:

$$A_{g(v'),d',g(v),d}^e = - \int_{\hat{\tau}} \frac{1}{R^2} \nabla B_{v',d'} \cdot \nabla B_{v,d} |J| d\hat{\tau}$$

$$\mathbf{r}_{g(v'),d'}^e = \int_{\hat{\tau}} \frac{1}{R^2} B_{v',d'} f |J| d\hat{\tau}$$

These integrals are evaluated using Gauss quadrature as:

$$I \approx \sum_{p=1}^{Ng} \sum_{q=1}^{Ng} w_p w_q \hat{I}(\hat{s}_p, \hat{t}_q)$$

where, I is any integral with integrand \hat{I} , Ng is the order of the Gauss quadrature and $w_{p/q}$ are the weights for the Gaussian quadrature. Due to the choice of bicubic polynomials, Ng must be at least 4. The contributions from all elements can be

computed in the same manner and are assembled to obtain the global system of equations:

$$[\mathbb{A}] \{\psi\} = \{\mathbf{r}(\psi^{(k)})\}$$

This is a system of nonlinear equations which is solved using Picard iterations by inverting the following linear system for $\psi_{i2D}^{(k+1)}$:

$$[\mathbb{A}] \{\psi^{(k+1)}\} = \{\mathbf{r}(\psi^{(k)})\}$$

The right hand side vector \mathbf{r} contains the contribution due to profiles p' and FF' which are functions $\psi_N(\psi)$ and hence $\psi_N(\psi)$ is computed at each iteration. When the quantity $\psi^{(k+1)} - \psi^{(k)}$ is below a certain tolerance, the approximate solution ψ_{eq} of Grad-Shafranov equation is assumed to be obtained. This solution is used as a starting point of tokamak modeling and is used to determine the initial conditions for numerical simulations. It can also be used to construct a grid which is aligned to flux surfaces.

Following are some of the tokamak equilibria described for which Grad-Shafranov equation is numerically solved and these equilibria are used for MHD simulations later.

Equilibrium 1:

This equilibrium is for cylindrical plasma with major radius 10 m and minor radius of plasma 1 m. The density and temperature profiles are specified using the form of profile given by equation (4.1) whereas the FF' profile is given by equation (4.2). The coefficients used for the density profile are:

$$\rho_0 = 1, \rho_1 = 0.1, C(1) = -1, C(2) = 0, C(3) = 0, C(4) = 1, C(5) = 5$$

The coefficients used for the temperature profile are:

$$T_0 = 0.002, T_1 = 10^{-8}, C(1) = -0.8, C(2) = 0, C(3) = 0, C(4) = 1, C(5) = 5$$

The coefficients used for the FF' profile are:

$$FF_0 = 2, FF_1 = 0, C(1) = -1, C(2) = 0, C(3) = 0, \\ C(4) = 0.03, C(5) = 5, C(6) = 0.4793, C(7) = 10, C(8) = 1$$

With $F_0 = 10$, resulting profiles are shown in Figure (4.2a). Dirichlet boundary conditions are used to compute the equilibrium. The numerical solution obtained of Grad-Shafranov equation is shown in Figure (4.2b).

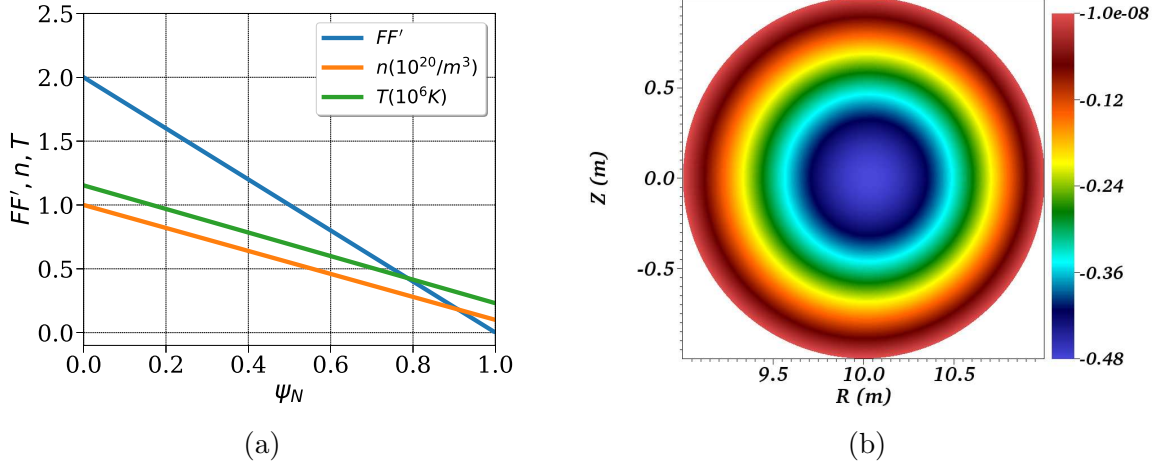


Figure 4.2: For a circular equilibrium 1: (a) The density, temperature and FF' profiles plotted vs ψ_N . (b) Numerically computed equilibrium ψ .

Equilibrium 2

This equilibrium is similar to the equilibrium 1. The coefficients used for the density profile are:

$$\rho_0 = 1, \rho_1 = 0.1, C(1) = -1, C(2) = 0, C(3) = 0, C(4) = 1, C(5) = 5$$

The coefficients used for the temperature profile are:

$$T_0 = 4.335 \times 10^{-4}, T_1 = 10^{-8}, C(1) = -0.8, C(2) = 0, C(3) = 0, C(4) = 1, C(5) = 5$$

The coefficients used for the FF' profile are:

$$FF_0 = 2, FF_1 = 0, C(1) = -7, C(2) = 0, C(3) = 0, \\ C(4) = 0.01, C(5) = 5, C(6) = 1, C(7) = 10, C(8) = 1$$

With $F_0 = 19.45$, resulting profiles are shown in Figure (4.3a). Dirichlet boundary conditions are used to compute the equilibrium. The numerical solution obtained for Grad-Shafranov equation is shown in Figure (4.3b).

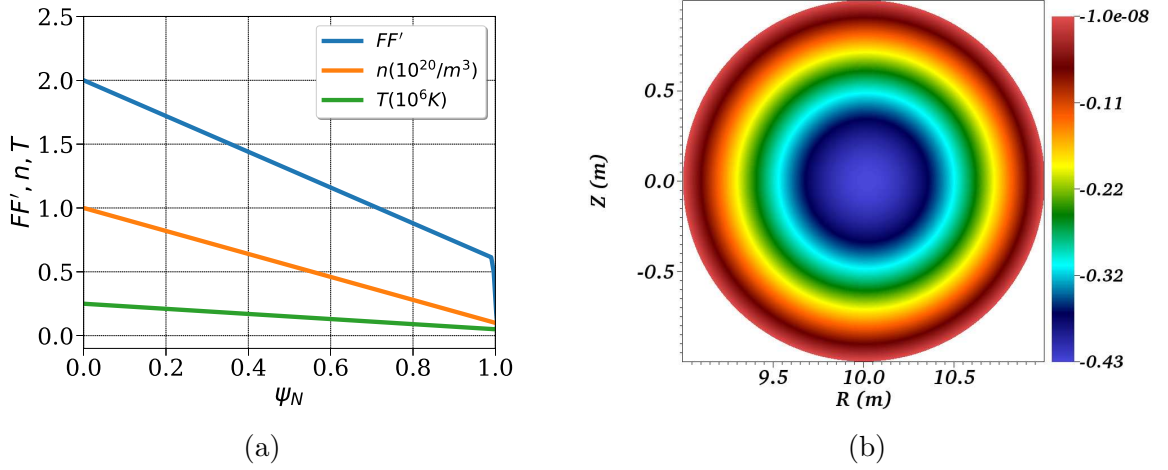


Figure 4.3: For a circular equilibrium 2: (a) The density, temperature and FF' profiles plotted vs ψ_N . (b) Numerically computed equilibrium $\psi..$

Equilibrium 3

Here, we use the `cbm18.dens18` equilibrium used for bench marking NIMROD [19], M3D-C 1 [29], and BOUT++ [99]. The coefficients used for the density profile are:

$$\rho_0 = 1, \rho_1 = 0.99, C(1) = -1, C(2) = 0, C(3) = 0, C(4) = 99, C(5) = 99$$

The coefficients used for the temperature profile are:

$$T_0 = 0.038727, T_1 = 10^{-6}, C(1) = -0.2191, C(2) = -0.1901, \\ C(3) = 0.0503, C(4) = 0.0398, C(5) = 0.5893$$

The coefficients used for the FF' profile are:

$$FF_0 = 3.28, FF_1 = 0, C(1) = -0.2, C(2) = -5.2, C(3) = 4.97, \\ C(4) = 0.00001, C(5) = 0.7, C(6) = -0.36, C(7) = 0.59, C(8) = 0.0424$$

With $F_0 = 6$, resulting profiles are shown in Figure (4.4a). Dirichlet boundary conditions are used to compute the equilibrium. The numerical solution obtained for Grad-Shafranov equation is shown in Figure (4.4b).

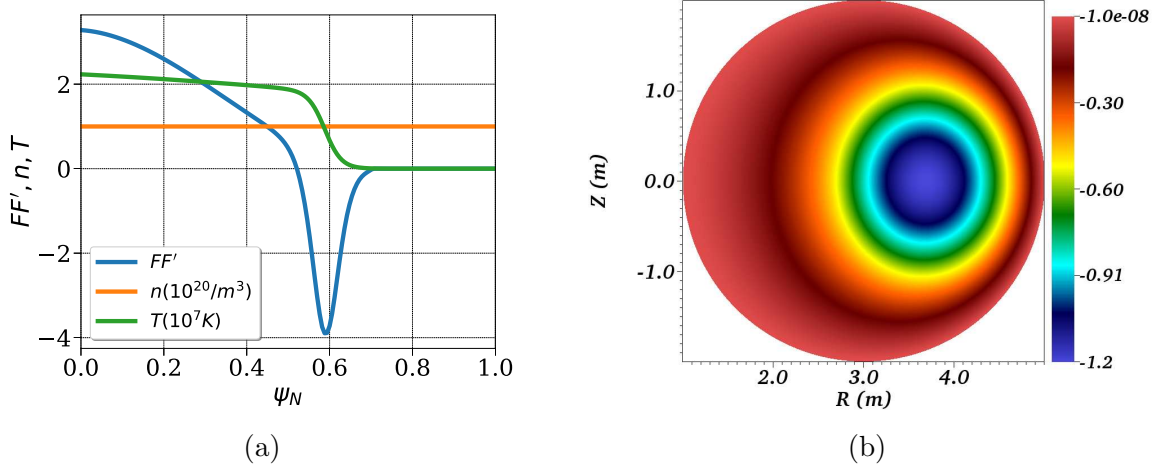


Figure 4.4: For a circular equilibrium 3 (cbm18): (a) The density, temperature and FF' profiles plotted vs ψ_N . (b) Numerically computed equilibrium ψ .

Equilibrium 4

This is an artificial equilibrium similar to a JET plasma and uses the divertor configuration. The coefficients used for the density profile are:

$$\rho_0 = 1, \rho_1 = 0.01, C(1) = -1, C(2) = 0, C(3) = 0, C(4) = 0.08, C(5) = 0.94$$

The coefficients used for the temperature profile are:

$$T_0 = 0.03, T_1 = 0.0003, C(1) = -0.66, C(2) = 0, \\ C(3) = 0, C(4) = 0.08, C(5) = 0.94$$

The coefficients used for the FF' profile are:

$$FF_0 = 1.6, FF_1 = 0, C(1) = -1, C(2) = 0, C(3) = 0.0857, \\ C(4) = 0.00001, C(5) = 1, C(6) = -0.254, C(7) = 0.88, C(8) = 0.058$$

With $F_0 = 3$, resulting profiles are shown in Figure (4.5a). The equilibrium is first solved on the polar grid with 100 and 150 points in radial and poloidal direction respectively with major radius $R_0 = 3$ m and minor radius $a = 1$ m. The polar grid is non-circular and based on Soloviev equilibrium where ellipticity E is set to 1.7, triangularities and upper quadrangularties set to 0 while lower quadrangularity is set to -0.4 (see subsection (3.4) on polar grid generation). The boundary condition

specified on the ψ is plotted vs θ in Figure (4.5b) and is based on Soloviev equilibrium. Grad-Shafranov equation is solved on this polar grid first and the polar grid along with the contours of ψ are shown in Figure (4.5c). It can be seen that ψ field has one saddle point. As described in section (3.4), the new grid aligned to flux surfaces is generated and is shown by red color in Figure (4.5d). Finally, Grad-Shafranov equilibrium is solved again on the new grid using the same profiles for ρ , T and FF' and the numerical equilibrium is shown in Figure (4.5e).

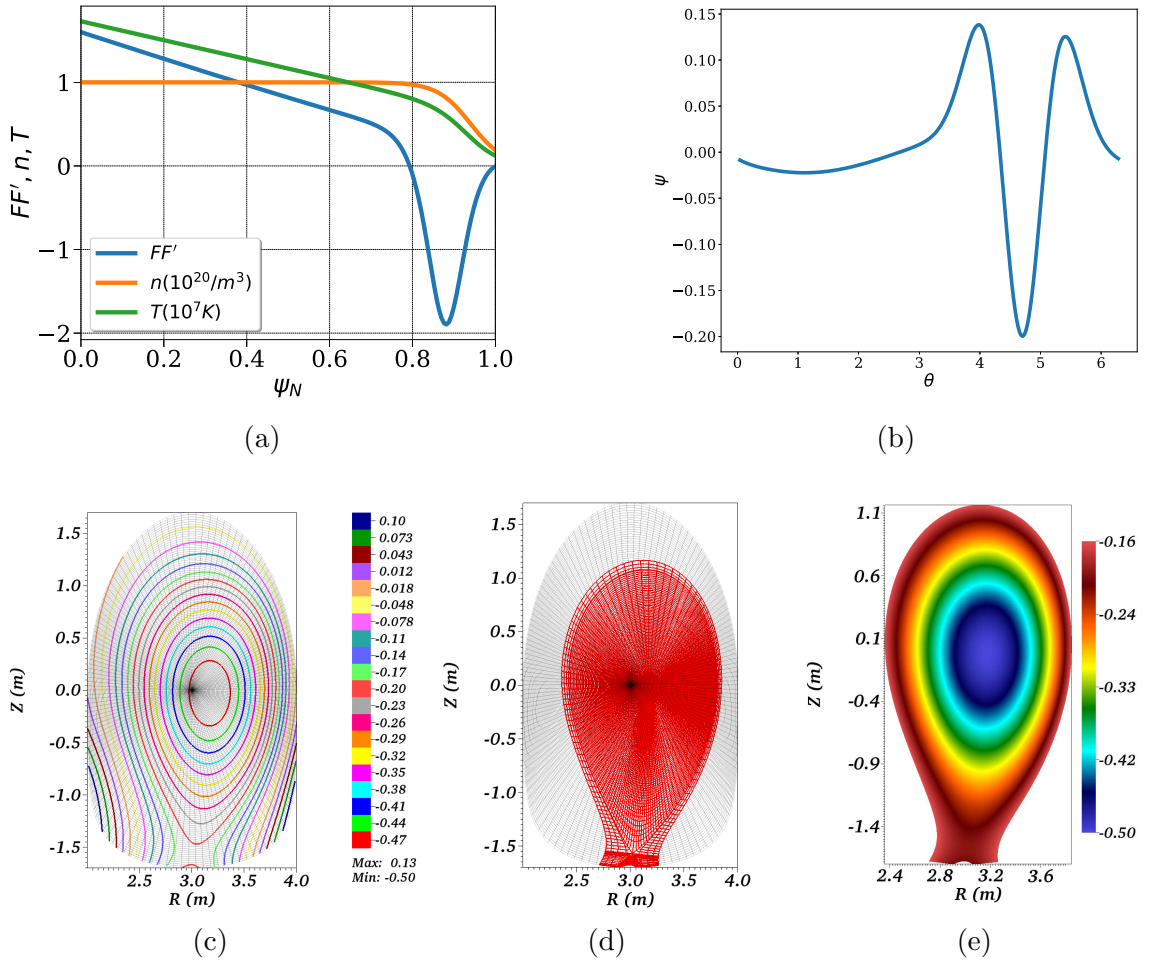


Figure 4.5: For a JET like equilibrium: (a) The density, temperature and FF' profiles plotted vs ψ_N . (b) Boundary conditions specified for ψ on the polar grid. (c) Polar grid on which Grad-Shafranov equation is solved and contours for numerical solution ψ . (d) Grid aligned to numerical solution ψ shown in red color. (e) Pseudocolor plot of ψ on the flux aligned grid.

4.2 Implementation of full MHD model

In previous section we demonstrated the application of FEM to Grad-Shafranov equation. The next step is to apply FEM to the full MHD model given by equations (2.43). The vector variables of the full MHD model are written in the cylindrical (toroidal) coordinate system (R, Z, ϕ) , for example, the velocity vector is represented as: $\mathbf{v} = v_R \mathbf{e}_R + v_Z \mathbf{e}_Z + v_\phi \mathbf{e}_\phi$. Whereas the magnetic potential vector is represented as: $\mathbf{A} = A_R \mathbf{e}_R + A_Z \mathbf{e}_Z + A_3 \nabla \phi$, where $A_3 = R A_\phi$ and $\nabla \phi = \mathbf{e}_\phi / R$ is the contravariant basis vector. In an axisymmetric equilibrium, A_3 is equivalent to the magnetic poloidal flux ψ . For a system of PDEs detailed steps to apply FEM have been described in (3.2). In this section we focus upon the FEM applied to full MHD model and the choice of test functions. The weak form of the density equation is written by multiplying it with a test function ρ^* and integrating over entire domain as:

$$\begin{aligned} \int_{\Omega} \rho^* \frac{\partial \rho}{\partial t} d\Omega &= \int_{\Omega} \rho^* \left(-\nabla \cdot (\rho \mathbf{v}) + \nabla \cdot (\underline{\mathbf{D}} \nabla \rho) + S_\rho \right) d\Omega \\ &= -\int_{\Omega} \rho^* \nabla \cdot (\rho \mathbf{v}) d\Omega - \int_{\Omega} \underline{\mathbf{D}} \nabla \rho \cdot \nabla \rho^* d\Omega + \int_{\partial\Omega} \rho^* (\underline{\mathbf{D}} \nabla \rho) \cdot \hat{\mathbf{n}} dS \\ &\quad + \int_{\Omega} \rho^* S_\rho d\Omega \end{aligned}$$

The particle diffusion term is integrated by parts and $\hat{\mathbf{n}}$ is the outward unit normal to the surface element dS .

The weak form of the pressure equation is obtained in the similar way by multiplying it with a test function p^* and integrating over entire domain:

$$\begin{aligned} \int_{\Omega} p^* \frac{\partial p}{\partial t} d\Omega &= \int_{\Omega} p^* \left(-\mathbf{v} \cdot \nabla p - \gamma p \nabla \cdot \mathbf{v} + \nabla \cdot (\underline{\boldsymbol{\kappa}} \nabla T) + (\gamma - 1) \underline{\boldsymbol{\pi}} : \nabla \mathbf{v} + S_T \right) d\Omega \\ &= -\int_{\Omega} p^* \mathbf{v} \cdot \nabla p d\Omega - \int_{\Omega} p^* \gamma p \nabla \cdot \mathbf{v} d\Omega - \int_{\Omega} \underline{\boldsymbol{\kappa}} \nabla T \cdot \nabla p^* d\Omega \\ &\quad + \int_{\partial\Omega} T^* (\underline{\boldsymbol{\kappa}} \nabla T) \cdot \hat{\mathbf{n}} dS + \int_{\Omega} (\gamma - 1) p^* \underline{\boldsymbol{\pi}} : \nabla \mathbf{v} d\Omega + \int_{\Omega} p^* S_T d\Omega \end{aligned}$$

where heat conduction term is integrated by parts.

The weak form of the velocity equation is written by multiplying it with the vector

test function \mathbf{v}^* and integrating over entire domain:

$$\begin{aligned} \int_{\Omega} \mathbf{v}^* \cdot \rho \frac{\partial \mathbf{v}}{\partial t} d\Omega &= \int_{\Omega} \mathbf{v}^* \cdot \left(-\rho \mathbf{v} \cdot \nabla \mathbf{v} - \nabla p + \mathbf{J} \times \mathbf{B} + \nabla \cdot \underline{\boldsymbol{\pi}} + \mathbf{S}_v \right) d\Omega \\ &= - \int_{\Omega} \mathbf{v}^* \cdot (\rho \mathbf{v} \cdot \nabla \mathbf{v}) d\Omega - \int_{\Omega} \mathbf{v}^* \cdot \nabla p d\Omega + \int_{\Omega} \mathbf{v}^* \cdot (\mathbf{J} \times \mathbf{B}) d\Omega \\ &\quad + \int_{\Omega} \mathbf{v}^* \cdot (\nabla \cdot \underline{\boldsymbol{\pi}}) d\Omega + \int_{\Omega} \mathbf{v}^* \cdot \mathbf{S}_v d\Omega \end{aligned}$$

Since in the normalized units $\mathbf{J} = \nabla \times \mathbf{B}$, the identity $\mathbf{J} \times \mathbf{B} = \mathbf{B} \cdot \nabla \mathbf{B} - \nabla \left(\frac{\mathbf{B} \cdot \mathbf{B}}{2} \right)$ can be used to further simplify the weak form. Furthermore, a simplified viscosity tensor $\underline{\boldsymbol{\pi}} = \mu \nabla \mathbf{v}$ is used where μ is the coefficient of the viscosity. Therefore, the viscous term becomes:

$$\nabla \cdot \underline{\boldsymbol{\pi}} = \mu \nabla \mathbf{v} = \mu \nabla (\nabla \cdot \mathbf{v}) - \mu (\nabla \times \nabla \times \mathbf{v})$$

Using above identity, the viscous term in the weak form becomes:

$$\int_{\Omega} \mathbf{v}^* \cdot (\nabla \cdot \underline{\boldsymbol{\pi}}) d\Omega = \int_{\Omega} \mathbf{v}^* \cdot \mu \nabla (\nabla \cdot \mathbf{v}) d\Omega - \int_{\Omega} \mathbf{v}^* \cdot \mu (\nabla \times \nabla \times \mathbf{v}) d\Omega$$

Putting these terms in the weak form of the velocity equation and using the integration by parts:

$$\begin{aligned} \int_{\Omega} \mathbf{v}^* \cdot \rho \frac{\partial \mathbf{v}}{\partial t} d\Omega &= \int_{\Omega} \mathbf{v}^* \cdot \left(-\rho \mathbf{v} \cdot \nabla \mathbf{v} + \mathbf{B} \cdot \nabla \mathbf{B} \right) d\Omega + \int_{\Omega} \left(p + \frac{\mathbf{B} \cdot \mathbf{B}}{2} \right) (\nabla \cdot \mathbf{v}^*) d\Omega \\ &\quad - \int_{\Omega} \mu (\nabla \cdot \mathbf{v}) (\nabla \cdot \mathbf{v}^*) d\Omega - \int_{\Omega} \mu (\nabla \times \mathbf{v}) \cdot (\nabla \times \mathbf{v}^*) d\Omega + \int_{\Omega} \mathbf{v}^* \cdot \mathbf{S}_v d\Omega \\ &\quad - \int_{\partial\Omega} \left(p + \frac{\mathbf{B} \cdot \mathbf{B}}{2} \right) \mathbf{v}^* \cdot \hat{\mathbf{n}} dS + \int_{\partial\Omega} \mu (\nabla \cdot \mathbf{v}) \mathbf{v}^* \cdot \hat{\mathbf{n}} dS \\ &\quad + \int_{\partial\Omega} \mu (\mathbf{v}^* \times \nabla \times \mathbf{v}) \cdot \hat{\mathbf{n}} dS \end{aligned}$$

where, μ is assumed constant. In practice, μ can be a function of temperature T .

Finally, the weak form of the induction equation is written by multiplying it with the vector test function \mathbf{A}^* and integrating over entire domain:

$$\begin{aligned} \int_{\Omega} \mathbf{A}^* \cdot \frac{\partial \mathbf{A}}{\partial t} d\Omega &= \int_{\Omega} \mathbf{A}^* \cdot \left(\mathbf{v} \times \mathbf{B} + \eta (\mathbf{J} - \mathbf{S}_J) \right) d\Omega \\ &= \int_{\Omega} \mathbf{A}^* \cdot (\mathbf{v} \times \mathbf{B}) d\Omega + \int_{\Omega} \mathbf{A}^* \cdot \eta \nabla \times \mathbf{B} d\Omega - \int_{\Omega} \mathbf{A}^* \cdot \mathbf{S}_J d\Omega \\ &= \int_{\Omega} \mathbf{A}^* \cdot (\mathbf{v} \times \mathbf{B}) d\Omega + \int_{\Omega} \nabla \times (\eta \mathbf{A}^*) \cdot \mathbf{B} d\Omega \\ &\quad - \int_{\partial\Omega} (\eta \mathbf{A}^* \times \mathbf{B}) \cdot \hat{\mathbf{n}} dS - \int_{\Omega} \mathbf{A}^* \cdot \mathbf{S}_J d\Omega \end{aligned}$$

where the definition of current $\mathbf{J} = \nabla \times \mathbf{B}$ is used and then integration by parts is performed.

The next step is to construct a finite dimensional space in which the trial functions are sought for. The domain Ω is subdivided into curved quadrangular elements Ω_e via grid generation (see section (3.4)) such that $\Omega_h = \bigcup \Omega_e$. The global basis functions V_j are constructed on the discretized domain Ω_h such that any variable w can be represented in terms of basis functions as: $w = \sum_j w_j V_j$, where w_j are the DoFs. For scalar equations, the test functions are chosen from the space of basis functions of Galerkin FEM. Hence, the discrete weak form of the density equation becomes:

$$\begin{aligned} \int_{\Omega_h} V_i \frac{\partial \rho}{\partial t} d\Omega_h &= - \int_{\Omega_h} V_i \nabla \cdot (\rho \mathbf{v}_h) d\Omega_h - \int_{\Omega_h} \underline{\mathbf{D}} \nabla \rho \cdot \nabla V_i d\Omega_h + \int_{\partial\Omega_h} \underline{\mathbf{D}} \nabla \rho \cdot \hat{\mathbf{n}} dS \\ &+ \int_{\Omega_h} V_i S_\rho d\Omega_h \end{aligned}$$

and similarly, the discrete weak form of the pressure equation can be written as:

$$\begin{aligned} \int_{\Omega_h} V_i \frac{\partial p}{\partial t} d\Omega_h &= - \int_{\Omega_h} V_i \mathbf{v} \cdot \nabla p d\Omega_h - \int_{\Omega_h} V_i \gamma p \nabla \cdot \mathbf{v} d\Omega_h - \int_{\Omega_h} \underline{\boldsymbol{\kappa}} \nabla T \cdot \nabla V_i d\Omega_h \\ &+ \int_{\partial\Omega_h} \underline{\boldsymbol{\kappa}} \nabla T \cdot \hat{\mathbf{n}} dS + \int_{\Omega_h} V_i (\gamma - 1) \underline{\boldsymbol{\pi}} : \nabla \mathbf{v} d\Omega_h + \int_{\Omega_h} V_i S_T d\Omega_h \end{aligned}$$

The vector test functions may also be used as projections to obtain individual equations for each of the vector field components. In principle, the vector test functions \mathbf{A}^* to get equations for the components \mathbf{A} can be: $V_i \mathbf{e}_R$, $V_i \mathbf{e}_Z$ and $V_i \mathbf{e}_\phi$. However a convenient choice of a covariant basis vector is made such that the vector test function for A_3 equation is written as: $V_i R \mathbf{e}_\phi$. This choice helps to get rid of the factor $1/R$. Using these test functions, the equations for A_R , A_Z and A_3 can be written as:

$$\begin{aligned} \int_{\Omega_h} V_i \frac{\partial A_R}{\partial t} d\Omega &= \int_{\Omega_h} V_i \mathbf{e}_R \cdot (\mathbf{v} \times \mathbf{B}) d\Omega + \int_{\Omega_h} \nabla \times (\eta V_i \mathbf{e}_R) \cdot \mathbf{B} d\Omega_h \\ &- \oint ((\eta V_i \mathbf{e}_R) \times \mathbf{B}) dS - \int_{\Omega_h} V_i \mathbf{e}_R \cdot \eta \mathbf{S}_J d\Omega_h \\ \int_{\Omega_h} V_i \frac{\partial A_Z}{\partial t} d\Omega &= \int_{\Omega_h} V_i \mathbf{e}_Z \cdot (\mathbf{v} \times \mathbf{B}) d\Omega + \int_{\Omega_h} \nabla \times (\eta V_i \mathbf{e}_Z) \cdot \mathbf{B} d\Omega_h \\ &- \oint ((\eta V_i \mathbf{e}_Z) \times \mathbf{B}) dS - \int_{\Omega_h} V_i \mathbf{e}_Z \cdot \eta \mathbf{S}_J d\Omega_h \\ \int_{\Omega_h} V_i \frac{\partial A_3}{\partial t} d\Omega &= \int_{\Omega_h} V_i R \mathbf{e}_\phi \cdot (\mathbf{v} \times \mathbf{B}) d\Omega + \int_{\Omega_h} \nabla \times (\eta V_i R \mathbf{e}_\phi) \cdot \mathbf{B} d\Omega_h \\ &- \oint ((\eta V_i R \mathbf{e}_\phi) \times \mathbf{B}) dS - \int_{\Omega_h} V_i R \mathbf{e}_\phi \cdot \eta \mathbf{S}_J d\Omega_h \end{aligned}$$

Again, in principle, the vector test functions \mathbf{v}^* to get equations of the velocity components can be used respectively as: $V_i \mathbf{e}_R$, $V_i \mathbf{e}_Z$ and $V_i \mathbf{e}_\phi$. However this is not the numerically stable choice, as noted in [44, 74]. Even simple simulations with this projections are seen to be polluted by numerical noise. To remove this issue, a choice of ‘parallel projection’ [43] is used where the vector test functions are chosen respectively as: $V_i \mathbf{e}_R$, $V_i \mathbf{e}_Z$ and $V_i \mathbf{B}$. With the first test function, the weak form of the equations of v_R can be written as:

$$\begin{aligned} \int_{\Omega} V_i \rho \frac{\partial v_R}{\partial t} d\Omega &= \int_{\Omega} V_i \mathbf{e}_R \cdot (-\rho \mathbf{v} \cdot \nabla \mathbf{v} + \mathbf{B} \cdot \nabla \mathbf{B}) d\Omega + \int_{\Omega} \left(p + \frac{B^2}{2} \right) (\nabla \cdot (V_i \mathbf{e}_R)) d\Omega \\ &\quad - \int_{\Omega} \mu (\nabla \cdot \mathbf{v}) (\nabla \cdot (V_i \mathbf{e}_R)) d\Omega - \int_{\Omega} \mu (\nabla \times \mathbf{v}) \cdot (\nabla \times (V_i \mathbf{e}_R)) d\Omega \\ &\quad + \int_{\Omega} V_i \mathbf{e}_R \cdot \mathbf{S}_v d\Omega - \int_{\partial\Omega} \left(p + \frac{\mathbf{B} \cdot \mathbf{B}}{2} \right) V_i \mathbf{e}_R \cdot \hat{\mathbf{n}} dS \\ &\quad + \int_{\partial\Omega} \mu (\nabla \cdot \mathbf{v}) V_i \mathbf{e}_R \cdot \hat{\mathbf{n}} dS + \int_{\partial\Omega} \mu V_i (\mathbf{e}_R \times \nabla \times \mathbf{v}) \cdot \hat{\mathbf{n}} dS \end{aligned}$$

Similarly the weak form for v_Z equation is written as:

$$\begin{aligned} \int_{\Omega} V_i \rho \frac{\partial v_Z}{\partial t} d\Omega &= \int_{\Omega} V_i \mathbf{e}_Z \cdot (-\rho \mathbf{v} \cdot \nabla \mathbf{v} + \mathbf{B} \cdot \nabla \mathbf{B}) d\Omega + \int_{\Omega} \left(p + \frac{B^2}{2} \right) (\nabla \cdot (V_i \mathbf{e}_Z)) d\Omega \\ &\quad - \int_{\Omega} \mu (\nabla \cdot \mathbf{v}) (\nabla \cdot (V_i \mathbf{e}_Z)) d\Omega - \int_{\Omega} \mu (\nabla \times \mathbf{v}) \cdot (\nabla \times (V_i \mathbf{e}_Z)) d\Omega \\ &\quad + \int_{\Omega} V_i \mathbf{e}_Z \cdot \mathbf{S}_v d\Omega - \int_{\partial\Omega} \left(p + \frac{\mathbf{B} \cdot \mathbf{B}}{2} \right) V_i \mathbf{e}_Z \cdot \hat{\mathbf{n}} dS \\ &\quad + \int_{\partial\Omega} \mu (\nabla \cdot \mathbf{v}) V_i \mathbf{e}_Z \cdot \hat{\mathbf{n}} dS + \int_{\partial\Omega} \mu V_i (\mathbf{e}_Z \times \nabla \times \mathbf{v}) \cdot \hat{\mathbf{n}} dS \end{aligned}$$

Finally the weak form of the velocity equation obtained by parallel projection $V_i \mathbf{B}$ is used to evolve v_ϕ :

$$\begin{aligned} \int_{\Omega} V_i \mathbf{B} \cdot \rho \frac{\partial \mathbf{v}}{\partial t} d\Omega &= - \int_{\Omega} V_i \mathbf{B} \cdot (\rho \mathbf{v} \cdot \nabla \mathbf{v}) d\Omega + \int_{\Omega} V_i \mathbf{B} \cdot \nabla p d\Omega \\ &\quad + \int_{\Omega} V_i \mathbf{B} \cdot (\nabla \cdot \underline{\boldsymbol{\pi}}) d\Omega + \int_{\Omega} V_i \mathbf{B} \cdot \mathbf{S}_v d\Omega \end{aligned}$$

It can be seen that the Lorentz force term $\mathbf{J} \times \mathbf{B}$ is eliminated as it is dotted with \mathbf{B} . This removes fast magnetosonic waves from the v_ϕ equations that pollute the numerical solution. The advantage of using parallel projection is demonstrated in [44, 43] with the help of the numerical tests for standard MHD instabilities. It is indeed observed that v_ϕ contains numerical noise with test function $V_i \mathbf{e}_\phi$.

The weak form of equations above can be written as a system of semi-discrete equations:

$$\int \mathbf{w}^* \cdot \mathbb{P}(\mathbf{w}) \frac{d\mathbf{w}}{dt} d\Omega = \int \mathbf{w}^* \cdot \mathbf{Q}(\mathbf{w}, t) d\Omega$$

where, the vector of primitive variables \mathbf{w} is:

$$\mathbf{w} = \{\rho, v_R, v_Z, v_\phi, T, A_R, A_Z, A_3\}^T$$

and $\mathbf{Q}(\mathbf{w}, t)$ is the right hand side of each equation. The matrix \mathbb{P} and the jacobians $\partial_{\mathbf{w}}\mathbf{Q}$ required for the implementation of the implicit method are given in Appendix A along with the boundary integral terms. The variable time step Gears method described in section (3.3) is the implicit method used here. It is shown in [43] that even with so called ‘parallel projection’ a second order convergence is obtained for the implicit time integration method considered.

Initial and boundary conditions:

The numerical solution (ψ) of Grad-Shafranov equation (2.35) is used to specify initial conditions for MHD simulations. The magnetic vector potential is initiated from ψ . Since we are interested in the evolution of perturbation about ideal MHD equilibrium (ψ), the initial equilibrium is perturbed by small numbers $\epsilon(\boldsymbol{\xi})$. Initial density and temperature field are specified from the profiles $\rho(\psi_N)$ and $T(\psi_N)$ and plasma velocity is initialized to zero.

$$\begin{aligned} A_R(\boldsymbol{\xi}, \phi, t = 0) &= A_Z(\boldsymbol{\xi}, \phi, t = 0) = 0 \\ A_3(\boldsymbol{\xi}, \phi, t = 0) &= \psi(\boldsymbol{\xi}) + \epsilon(\boldsymbol{\xi}) \\ \mathbf{v}(\boldsymbol{\xi}, \phi, t = 0) &= 0 \\ \rho(\boldsymbol{\xi}, \phi, t = 0) &= \rho(\psi(\boldsymbol{\xi})) \\ T(\boldsymbol{\xi}, \phi, t = 0) &= T(\psi(\boldsymbol{\xi})) \end{aligned}$$

The form of the perturbation added in ψ is given by:

$$\begin{aligned} \psi'(\boldsymbol{\xi}) &= \epsilon \psi_N (1 - \psi_N) \\ \psi_N &= \frac{\psi - \psi_a}{\psi_e - \psi_a} \end{aligned}$$

where ψ_N , ψ_a and ψ_e is the normalized poloidal flux, value of ψ the magnetic axis and at the boundaries. ψ_N takes value 0 at the magnetic axis and 1 at the boundaries and ϵ is a small real number which denotes the amplitude of perturbations.

Depending upon the simulation set-up, a boundary of a grid can either be aligned to flux surfaces or not. If a boundary is aligned to ψ , then all variables are kept fixed in time (Dirichlet boundary condition). If a boundary intersects magnetic field lines, then a mixture of Dirichlet and Neumann boundary conditions is applied. In such a case, Dirichlet condition is enforced for the magnetic vector potential \mathbf{A} , free outflow of density is allowed as Neumann boundary condition, while Mach-1 and Sheath boundary conditions are applied to velocity and temperature respectively, such that

$$\begin{aligned} \mathbf{v} \cdot \mathbf{b} &= \pm c_s = \sqrt{\gamma T} \\ nT\mathbf{v} \cdot \mathbf{b} + \kappa_{\parallel} \nabla_{\parallel} T &= \gamma_{sh} nT\mathbf{v} \cdot \mathbf{b} \end{aligned}$$

where \mathbf{b} is the unit vector along the magnetic field, γ_{sh} is the ion sheath transmission factor, which is typically taken between 4.5 and 10, depending on the ion or electron temperature, and on transient energy fluxes [86].

4.3 Linear simulations

In this section, we present the numerical results to validate the full model and benchmark it with the reduced MHD model that has already been implemented and used for a wide range of physical phenomena [47]. The standard MHD instabilities that are relevant to tokamaks are chosen such as internal kink modes, tearing modes and ballooning modes for validation.

4.3.1 Resistive internal kink modes

Kink modes are current driven modes in which the dominant driving source of instability is proportional to the parallel current. Depending upon the location of a ‘resonant surface’ (rational q surface), kink modes can be categorized into internal and external modes. In case of the internal modes, a resonant surface lies inside the core of a plasma.

To simulate the internal kink modes ‘equilibrium 1’ from section (4.1) is used. The $\rho(\psi_N)$, $T(\psi_N)$ and $FF'(\psi_N)$ profiles along with the numerical solution of Grad-Shafranov equation is shown in Figure (4.2). For this equilibrium configuration, $q = 1$ surface lies inside the core at $\psi_N \approx 0.5$ as shown in Figure (4.6a). When such equilibrium is perturbed, the instability with the structure of mode $m = n = 1$ grows around $q = 1$ surface. The simulations are run for $n = 0$ and 1, by keeping $n = 0$

mode fixed. This is done to investigate a growth rate of $n = 1$ mode. Simulations in which $n = 0$ mode is not evolved are called as linear runs. Flux aligned polar grids are used to run the internal kink simulations as shown in Figure (3.7c). Since it is expected that instabilities will occur around $q = 1$ surface, the grids are radially accumulated around $\psi_N \approx 0.5$ to ensure that the solution structures are well resolved. The plasma beta for this case is $\beta_N = 0.425\%$. Gears method is used for the time integration.

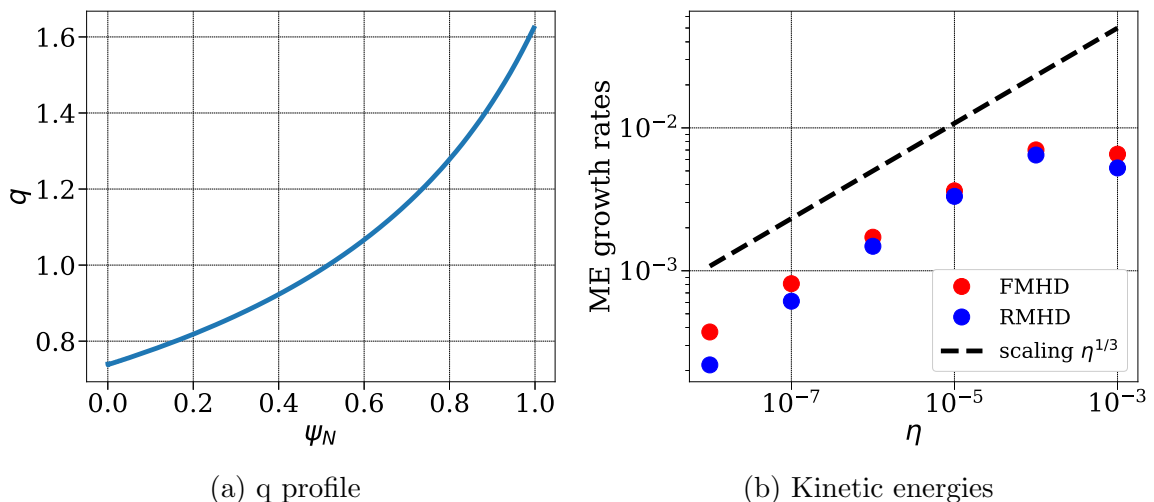


Figure 4.6: Linear runs for internal kink mode: (a) q profile showing the location of $q = 1$ surface roughly at $\psi_N = 0.5$ (b) magnetic energies (ME) vs resistivity for full MHD (FMHD) and reduced MHD (RMHD) models.

The internal kink mode simulations are run with resistivity alone and hence the term ‘resistive kink modes’. All other diffusivities such as viscosity, thermal and particle diffusivities are set to zero. The resistivity is set to a constant value (independent of T) and a scan in resistivity is performed. For each value of the resistivity, growth rates in kinetic and magnetic energies are computed. Figure (4.6b) shows magnetic energies obtained using full and reduced MHD models plotted vs resistivity. It can be seen that growth rates obtained using both models agree with each other as well as the theoretical scaling $\eta^{1/3}$. The kinetic energies also show the similar behavior. Each value of the growth rate is determined by running the simulations on the series of grids with increasing resolution until a convergence of growth rate is obtained. Table (4.1) shows the numerical values of the growth rates of the magnetic energies obtained on a series of grids for some values of η .

In Figure (4.7), visualizations of internal kink mode instabilities plotted on $\phi = 0$ poloidal plane are shown. These visualizations show perturbations in the variables

Grid	$\eta = 10^{-7}$	$\eta = 10^{-6}$	$\eta = 10^{-5}$
50×50	8.089653614E-04	1.715721384E-03	3.627257497E-03
60×60	8.103627001E-04	1.716151821E-03	3.627635158E-03
70×70	8.111041129E-04	1.716608095E-03	3.627832391E-03
80×80	8.111041129E-04	1.716823911E-03	3.627928350E-03
90×90	8.111041129E-04	1.716981313E-03	3.627993444E-03

Table 4.1: Growth rates (in normalized units) of magnetic energies for internal kink mode obtained by full MHD model on a series of grids. The grid is denoted by $N_\psi \times N_\theta$ where N_ψ and N_θ are the number of points in radial and poloidal direction.

A_3 , T and v_R for three different values of η . The instabilities are seen to develop a structure of $m = n = 1$ mode and linearly grow in time. It can be seen that the structures become finer as resistivity decreases. For a resistivity $\eta = 10^{-8}$, more resolution is needed to capture kink modes correctly, as the structures are very thin. On the other hand, for resistivities $\eta \geq 10^{-4}$ the instability structures are comparable in size to the plasma domain and hence scaling is lost. It can be seen in Figure (4.6b) that the growth rates for such resistivities do not follow $\eta^{1/3}$ curve.

4.3.2 Tearing Modes

Tearing modes are essentially resistive and current driven modes that can become unstable around a rational surface. The tearing mode instability in a tokamak is driven by radial gradients of the equilibrium toroidal current density [96]. Tearing of the magnetic field lines occur during such instability because of finite resistivity. The theoretical scaling of the growth rate is proportional to $\eta^{3/5}$.

To simulate the tearing modes ‘equilibrium 2’ from the section (4.1) is used. The $\rho(\psi_N)$, $T(\psi_N)$ and $FF'(\psi_N)$ profiles along with the numerical solution of Grad-Shafranov equation is shown in Figure (4.3). For this equilibrium configuration, $q = 2$ surface lies inside the core at $\psi_N \approx 0.28$ as shown in Figure (4.8a). When such equilibrium is perturbed, the instability with the structure of mode $m = 2, n = 1$ grows around $q = 2$ surface. The simulations are run for $n = 1$ by keeping $n = 0$ toroidal harmonic fixed. Flux aligned polar grids are used to run tearing mode simulations as shown in Figure (3.7c). Since it is expected that instabilities will occur around

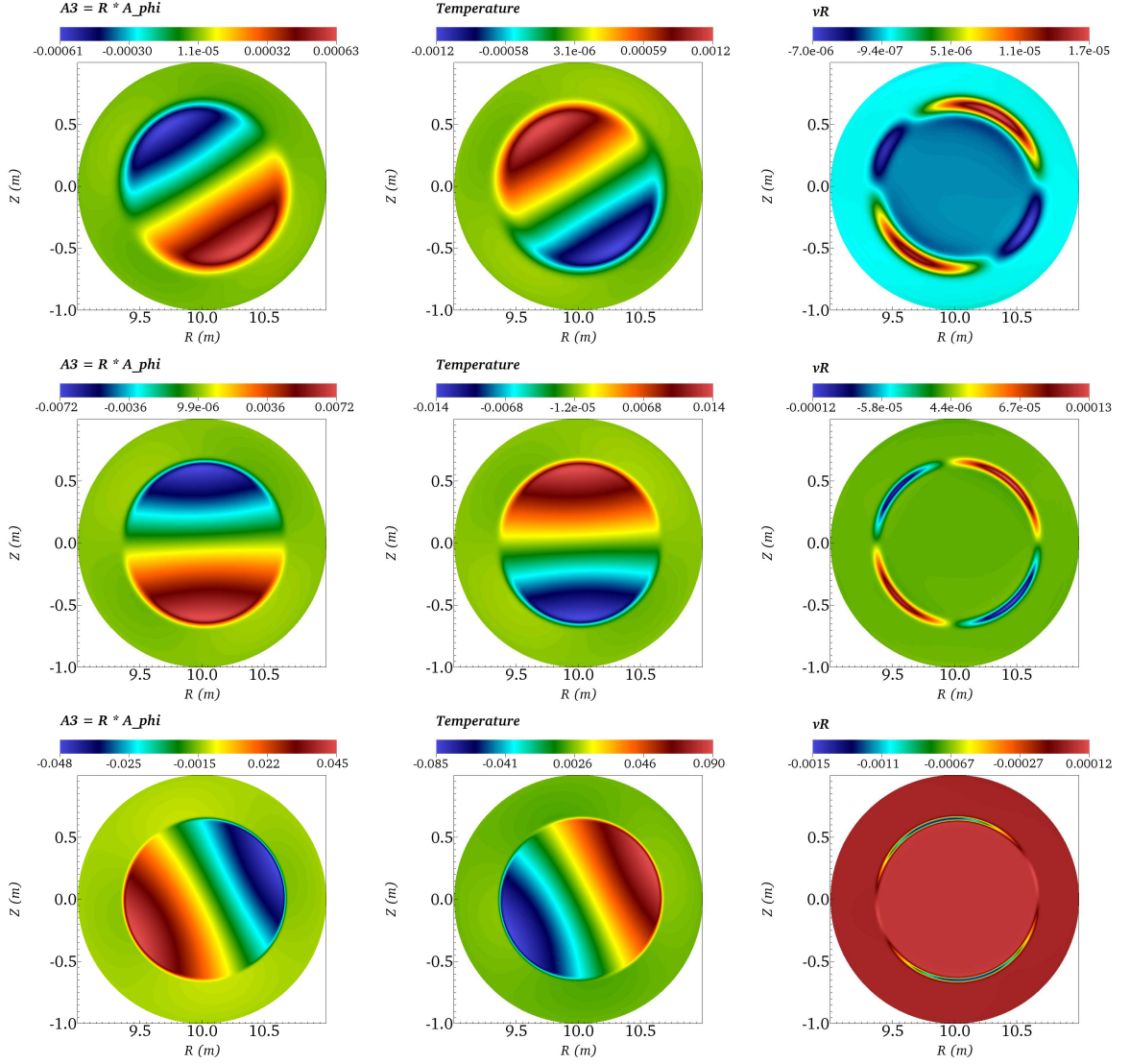


Figure 4.7: Visualizations for the perturbations in internal kink simulations plotted on the poloidal plane $\phi = 0$. The first, second and third row show results for $\eta = 10^{-5}$, 10^{-6} and 10^{-7} (in normalized) units respectively. The first, second and third columns show the perturbations in A_3 , T and v_R respectively.

$q = 2$ surface, the grids are radially accumulated around $\psi_N \approx 0.28$ to ensure that the solution structures are well resolved. The plasma beta for this case is $\beta_N = 0.046\%$. Gears method is used for the time integration.

Tearing simulations are run by specifying all diffusivity coefficients and the resistivity. The coefficient of viscosity μ , D_{\perp} , and κ_{\perp} are fixed as 10^{-8} while κ_{\parallel} is set to 1 (in normalized units). The resistivity is set to a constant value (independent of T) and a scan in resistivity is performed, like the internal kink simulations in above subsection. For each value of the resistivity, growth rates in kinetic and magnetic

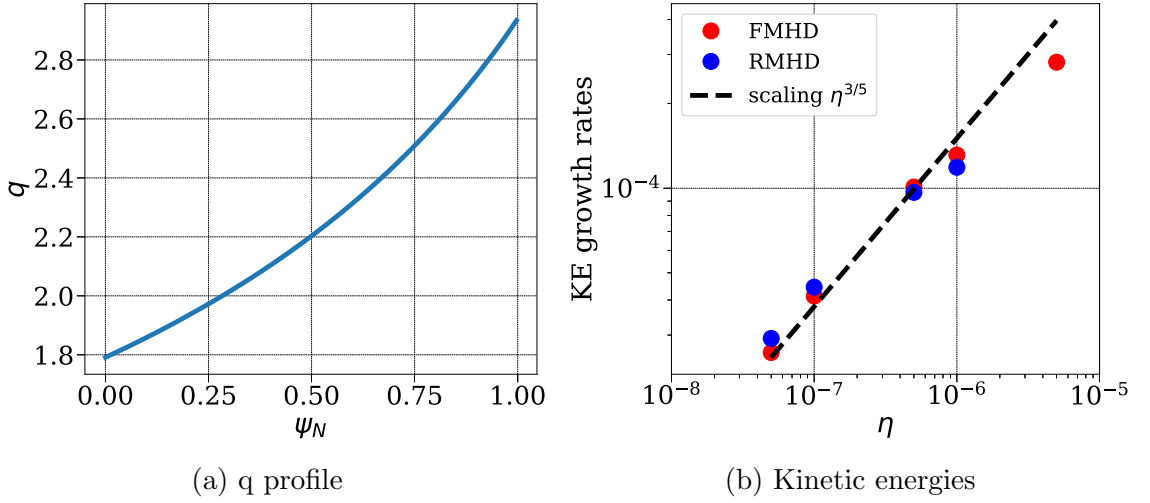


Figure 4.8: Linear runs for tearing mode: (a) q profile showing the location of $q = 1$ surface roughly at $\psi_N \approx 0.28$ (this corresponds to $R \approx 10.5$) (b) magnetic energies (ME) vs resistivities for full MHD (FMHD) and reduced MHD (RMHD) models.

energies are computed. Figure (4.8b) shows magnetic energies obtained using full and reduced MHD models plotted vs resistivity. It can be seen that growth rates obtained using both models agree with each other. The theoretical scaling is also well represented by the scaling $\eta^{3/5}$ for lower resistivities. The kinetic energies also show the similar behavior. Each value of the growth rate is determined by running the simulations on the series of grids with increasing resolution until a convergence in the growth rate is obtained. Table (4.2) shows the numerical values of the growth rates of the magnetic energies obtained on a series of grids for some values of η .

Grid	$\eta = 5 \times 10^{-8}$	$\eta = 10^{-7}$	$\eta = 5 \times 10^{-7}$
50×51	2.455923655E-05	4.022210311E-05	1.005353787E-04
60×71	2.578588617E-05	4.115275969E-05	1.009738128E-04
70×91	2.590501466E-05	4.125351362E-05	1.010148643E-04
80×111	2.594115382E-05	4.127952158E-05	1.010224675E-04
90×131	2.596923153E-05	4.128825390E-05	1.010259615E-04

Table 4.2: Growth rates (in normalized units) of magnetic energies for tearing modes obtained by full MHD model on a series of grids. The grid is denoted by $N_\psi \times N_\theta$ where N_ψ and N_θ are the number of points in radial and poloidal direction.

In Figure (4.9), visualizations of tearing mode instabilities plotted on the poloidal

plane $\phi = 0$ are shown. These visualizations are for perturbations in the variables A_3 , T and v_ϕ for two different values of η . The instabilities are seen with structures $m = 2$ which linearly grow in time. It can be seen in Figure (4.8b) that the growth rates for such resistivities do not follow $\eta^{3/5}$ curve.

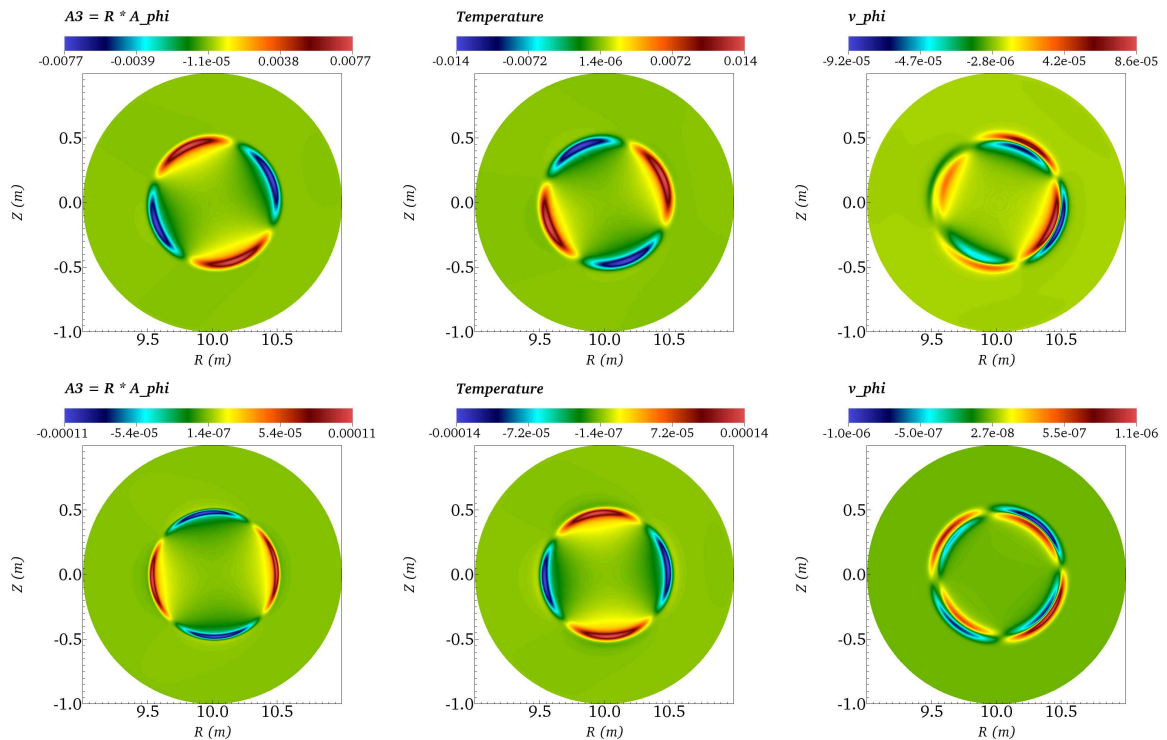


Figure 4.9: Visualizations for the perturbations in tearing mode simulations plotted on the poloidal plane $\phi = 0$. The first and second row show results for $\eta = 10^{-6}$ and 10^{-7} (in normalized) units respectively. The first, second and third columns show the perturbations in A_3 , T and v_ϕ respectively.

4.3.3 Ballooning modes

This is the test case for ballooning modes in a circular plasma with the radius of device is 3 m and radius of a plasma 2 m. Ballooning mode instability is driven by pressure gradients. If the pressure gradient is high, perturbations can concentrate in the region of destabilizing curvature resulting in the ballooning modes.

The initial condition is set such that ρ is kept almost constant and a sharp gradient in the T profile is set that make initial T field as shown in Figure (4.10). The flux aligned grid is constructed which is locally refined in the region of the sharp gradient. Note that, the grid center of polar grid is at the location of magnetic axis of the

plasma where $\nabla\psi = 0$. The location of the center is very much shifted from the actual geometric center of the circular domain. This shift is known as Shafranov shift [96, 36] which is a consequence of a plasma equilibrium.

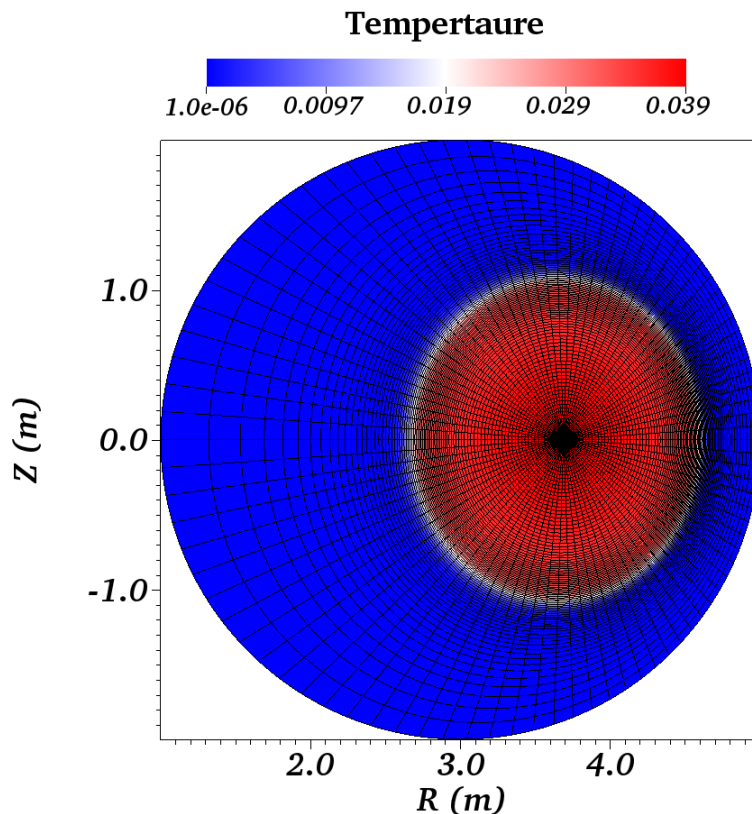


Figure 4.10: Flux aligned grid used for circular ballooning mode where magnetic axis is shifted to $R \approx 3.68\text{m}$. Pseudocolor shows the temperature field at the $t = 0$. The grid is clustered around the sharp gradient in the temperature to capture ballooning modes.

This case is run for individual toroidal mode numbers between $n = 4$ and $n = 16$. To simulate circular ballooning modes ‘equilibrium 3’ from section (4.1) is used. The $\rho(\psi_N)$, $T(\psi_N)$ and $FF'(\psi_N)$ profiles along with the numerical solution of Grad-Shafranov equation is shown in Figure (4.4). The q profile is shown in Figure (4.11a) that shows q profile increases rapidly near the boundary $\psi_N = 1$. The plasma beta for this case is $\beta_N = 1.5\%$. Flux aligned polar grids are used to run ballooning mode simulations as shown in Figure (3.7c). Gears method is used for the time integration.

The resistivity and other diffusive coefficients μ , D_{\perp} , and κ_{\perp} are set to 10^{-6} while κ_{\parallel} is set to 1 (in normalized units). Growth rates in kinetic and magnetic energies are computed for the simulations with each n and magnetic energies are

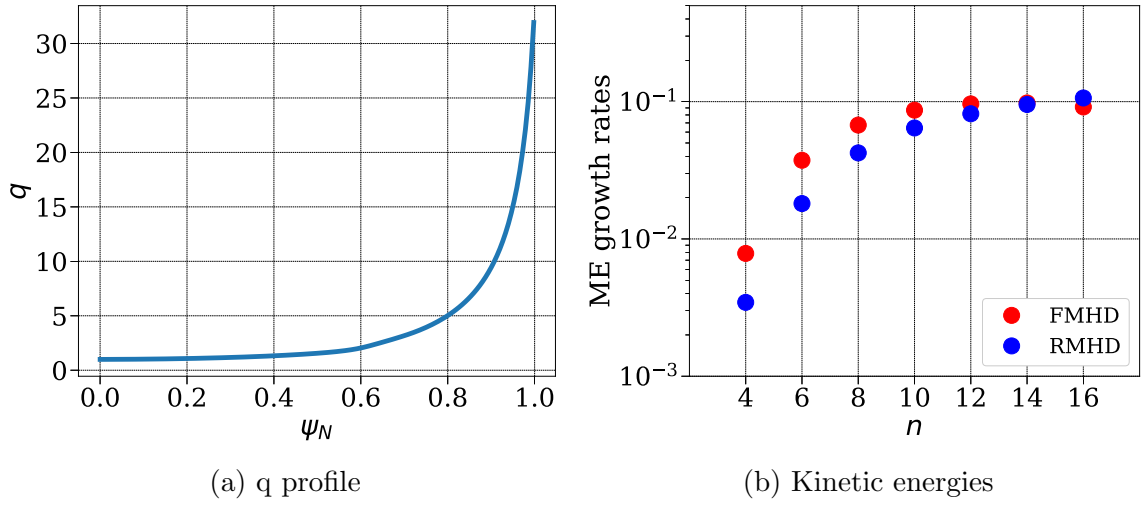


Figure 4.11: Linear runs for circular ballooning mode: (a) q profile (b) magnetic energies (ME) vs resistivities for full MHD (FMHD) and reduced MHD (RMHD) models.

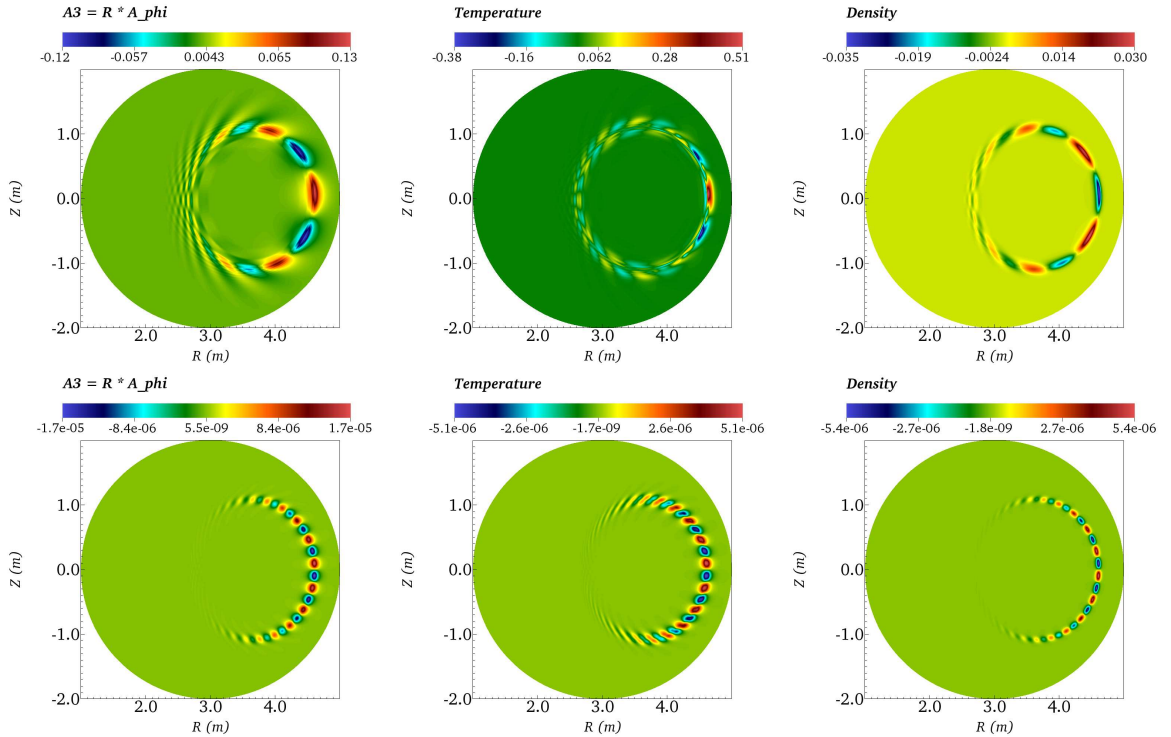


Figure 4.12: Visualizations for the perturbations in circular ballooning mode simulations plotted on the poloidal plane $\phi = 0$. The first and second row show results for $n = 4$ and 16 respectively. The first, second and third columns show the perturbations in A_3 , T and ρ respectively.

plotted in Figure (4.11b). Growth rates obtained using both full and reduced MHD model agree reasonably with each other. The kinetic energies also show the similar behavior. In Figure (4.12), visualizations of ballooning mode instabilities are shown. These visualizations are for perturbations in the variables A_3 , T and ρ for $n = 4$ and 16 respectively. The ballooning structures are observed across the temperature (or pressure) gradient (Figure (4.10)).

4.3.4 Ballooning modes in X-point plasma

Next, an X-point plasma is run for ballooning instabilities. This is an artificial equilibrium similar to JET plasma. To simulate ballooning modes in X-point plasma ‘equilibrium 4’ from section (4.1) on the flux aligned grid shown in Figure (4.5d) is used. The $\rho(\psi_N)$, $T(\psi_N)$ and $FF'(\psi_N)$ profiles along with the numerical solution of Grad-Shafranov equation is shown in Figure (4.5). The q profile is plotted in Figure (4.13a) shows that the near boundaries q increases rapidly. The plasma beta for this case is $\beta_N = 3.36\%$. Gears method is used for the time integration.

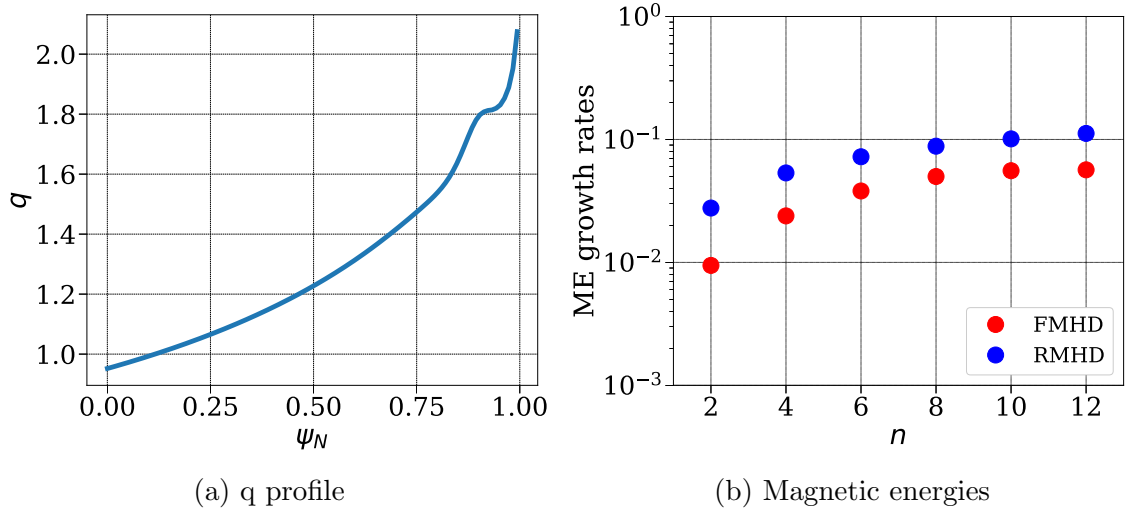


Figure 4.13: Linear runs for ballooning modes in JET like X-point plasma (a) q profile (b) magnetic energies (ME) vs number of harmonics n for full and reduced MHD models.

The linear simulations are run for $n = 2, 4, 6, 8, 10$ and 12. The resistivity and diffusivities used for the simulations are set in normalized units as:

$$\eta = 10^{-5}, \quad \mu = 3 \times 10^{-6}, \quad D_{\perp} = \kappa_{\perp} = 10^{-6}, \quad \kappa_{\parallel} = 10$$

The plasma corresponds to $\beta_N = 3.36 \%$. Growth rates in kinetic and magnetic energies are computed for the simulations with each n and plotted in Figure (4.13b). Although the growth rates obtained using both full and reduced MHD model do not match the trend of growth rates as n increases is alike. The mismatch in the growth rates is primarily because grid convergence is not performed for these simulations. Nevertheless, visualizations of the numerical results show ballooning mode structures as expected. In Figure (4.14), visualizations of ballooning mode instabilities are shown for $n = 10$. The ballooning mode structures are observed across the pressure gradient. It has been shown in the [74] that the growth rates match well for both models with $\beta_N = 2.5 \%$ and different set of diffusivities.

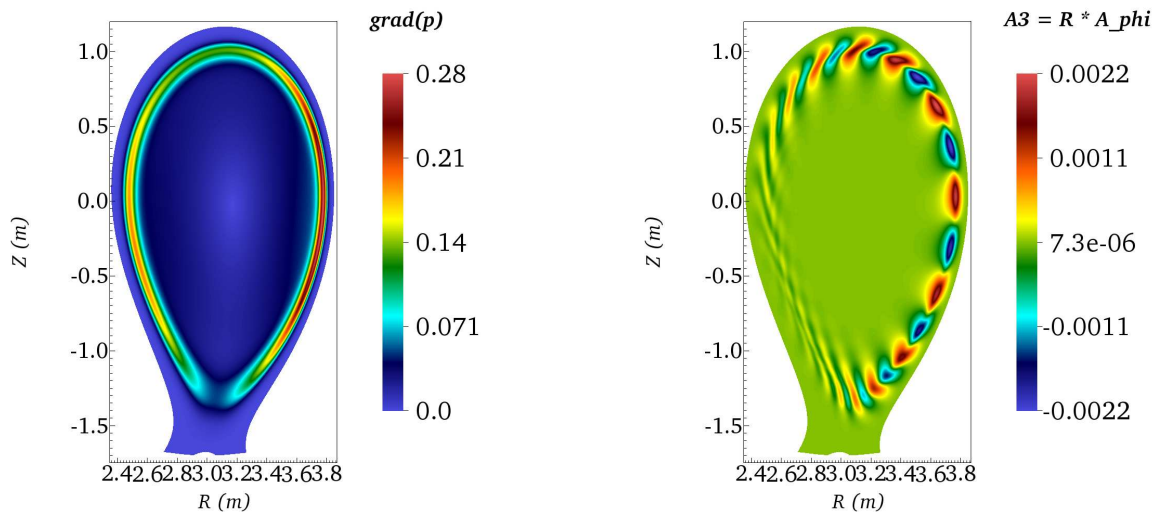


Figure 4.14: Visualizations for the perturbations in X-point plasma for ballooning mode simulations for $n = 10$. The left and right window shows $|\nabla p|$ and perturbations in A_3 respectively plotted on a poloidal plane $\phi = 0$.

4.4 Nonlinear Simulations

In previous section, validation of the full MHD model is shown by computing MHD instabilities. The comparison of results obtained with reduced MHD models shows a good agreement. The simulations presented in the previous section are linear runs, where a single harmonic is evolved with the stationary $n = 0$ harmonic in the background. However, the goal is to simulate nonlinear MHD phenomena with many toroidal harmonics all evolving in time. The reduced MHD models have already been used extensively to perform nonlinear MHD simulations [47]. Next, we demonstrate

that the full MHD model can also be used for nonlinear simulations. In this section, we present the nonlinear simulations for internal kink modes.

Before we present nonlinear MHD simulations, some numerical aspects are discussed. The numerical properties of a numerical tool depend upon a grid as well as numerical method used. The desirable quality for any numerical tool is that there should not be sudden variations in the numerical properties across grid nodes. Therefore, grids should be constructed in a way that grid shocks are avoided.

During nonlinear simulations, when MHD activities increase, it is often the case that the time step needs to be decreased. Across a jump in the time step classical Gears method for constant time stepping is not strictly valid and it loses second order accuracy. Therefore, the time integration method adapted to variable time stepping is used to avoid effects of jumps in the time steps and is discussed in subsection (4.4.1).

Similarly, numerical properties of the polar grid center are likely to be different than surrounding grid vertices. In general, any vertex of a grid is shared by 4 quadrangular elements and in this situation a choice of FEM gives continuous representation of functions and their gradients. At the polar grid center however, a single vertex is shared by many elements, one edge of each element reduces to a point and as a consequence mapping of such elements to the unit reference element is singular. This vertex can be a source of spurious waves in the numerical solution. The treatment proposed in subsection (3.4.5) is implemented on the elements sharing polar grid center and the results are discussed in subsection (4.4.2).

Finally, nonlinear simulations for internal kink modes are discussed in the subsection (4.4.3) where both strategies are implemented.

4.4.1 Effect of variable time step Gears method

Although the linear simulations presented in previous section are performed using variable time step Gears method, constant time steps have been used in all simulations. This means that the method effectively reduces to a classical Gears method. However, in practice, the time steps may be required to decrease during nonlinear simulations, for example when MHD dynamics occur over smaller time scales, the time step needs to be decreased. Across such a jump in the time step, a classical Gears method is not strictly valid. Therefore a consistent method for variable time step that will preserve second order representation is derived in the section (3.3) and is implemented here. In order to demonstrate its advantages, internal kink and

ballooning mode simulations are performed with variable time steps with full and reduced MHD models. As an example we present here numerical results for internal kink simulations with full MHD model alone, as the results with the reduced MHD show similar trend.

The set up for internal kink simulation is described in section (4.3). In order to demonstrate the effectiveness of the variable time step Gears method we design following tests with jumps in the time steps:

- Test1 : Δt alternates between 200 and 50 after each 20 time steps.
- Test2 : Δt alternates between 100 and 10 after each 20 time steps.
- Test3 : Δt alternates between 200 and 10 after each 10 time steps.

Hence the ratio of successive time steps encountered in these 3 tests respectively are 4, 10 and 20 (and their inverse). In Figure (4.15) it can be seen that across a jump in the time steps, with classical Gears method, the growth rates show spikes. As the ratio of successive time steps become extreme, spikes in growth rates also becomes larger. However, the use of variable time step method removes these spikes. This demonstrates the correction that the variable time step method brings across a jump in the time step.

If the time step is determined via a criterion like Courant conditions, in general, each time step can be different than its successive time step. For such simulations, the use of variable time step Gears method is desirable, provided the ratio of time steps follow certain restrictions for stability.

4.4.2 Effect of polar grid center treatment

The treatment that enforces $C1$ continuity in (R, Z) plane at the polar grid center is described in section (3.4.5) and is implemented here. This treatment uses the new basis functions and DoFs for the elements on the polar grid center. The effect of these new basis functions is shown below in linear and nonlinear tearing modes and linear circular ballooning mode simulations below.

The set up and the equilibrium for tearing modes is described in the section above. Here, only resistivity $\eta = 10^{-6}$ (in normalized units) is specified and all other diffusivities, i.e., particle, heat diffusivities are set to zero. A series of grids is used with the number of points in the radial direction $N_\psi = 101$ and in the azimuthal

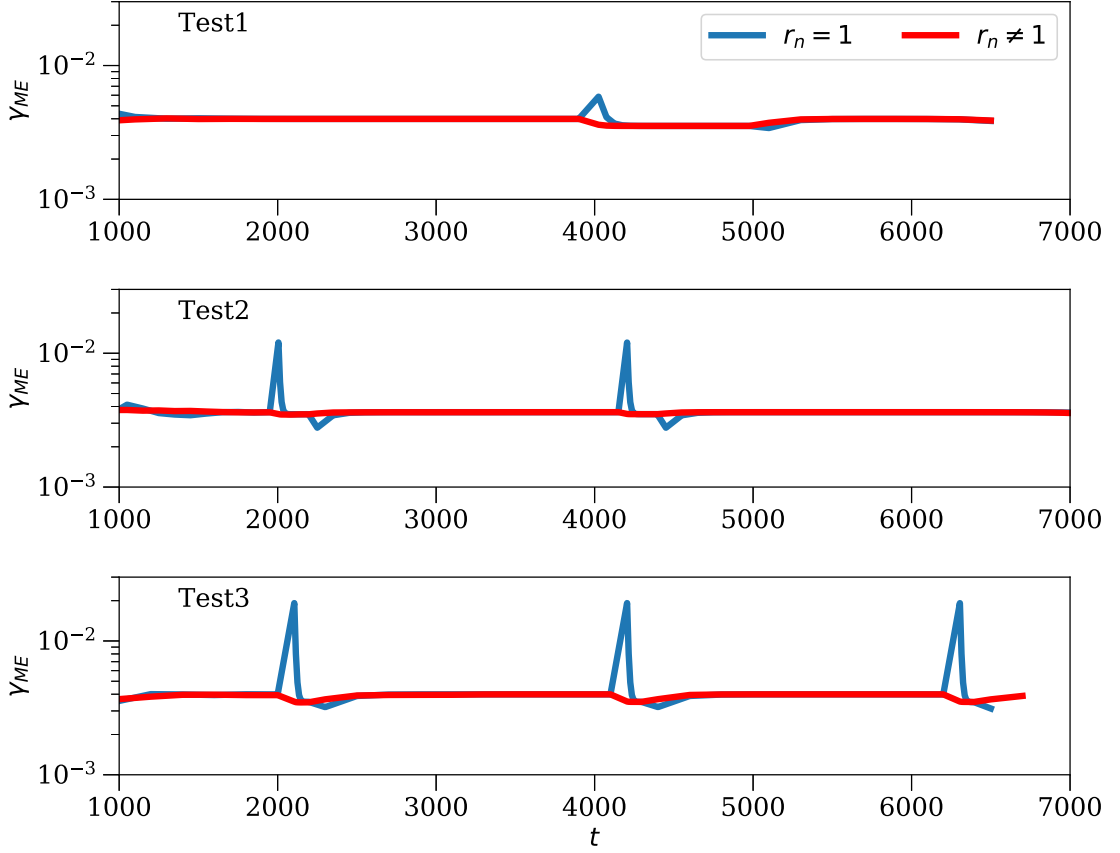


Figure 4.15: Comparison of growth rates of magnetic energies γ_{ME} plotted vs t for internal kink modes obtained using Gears method with $r_n = 1$ and $r_n \neq 1$ for the 3 tests described.

direction $N_\theta = 70$ with different amount of clustering of the vertices near the polar grid center. The factor a controls the grid accumulation in radial direction near the polar grid center whose effect is shown in Figure 4.16. Smaller the a , higher is the accumulation of points near the center while $a = 99$ denotes a random large value that denotes no accumulation of points. Hence, this series of grids creates a sense of local refinement near the grid center.

Both linear and nonlinear simulations are run with $n = 0, 1$ on the series of grids with old and new basis functions at the grid center and magnetic energies (ME) are plotted vs time in Figure (4.17). It can be seen that as the grid is refined near the center, growth rate of ME decreases. In fact simulations with old basis show numerical noise near the grid center as can be seen in Figure (4.18a) and (4.18c) for linear and nonlinear runs respectively. This noise grows faster than the instabilities of the tearing

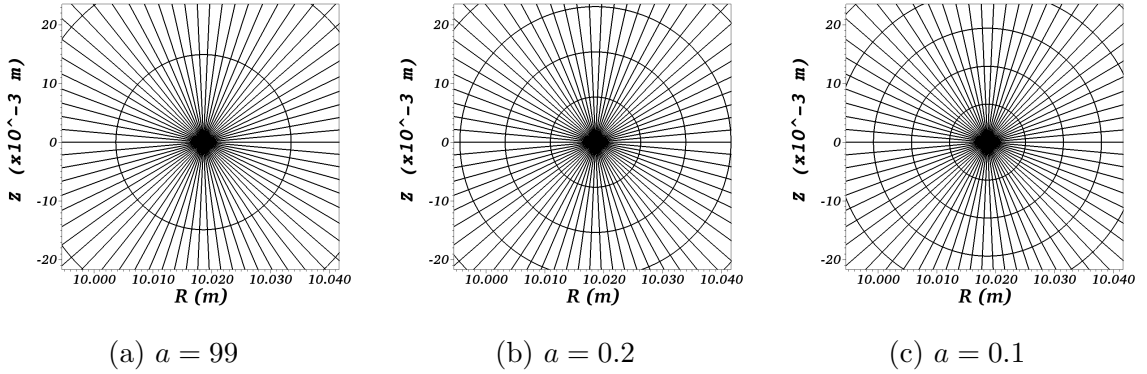


Figure 4.16: Grids used for tearing mode simulations with new basis for the elements of the polar grid center. These grids are zoomed near grid center to show the effect of parameter a on grid accumulation. As a reduces, grid is accumulated near the center, while $a = 99$ denotes no accumulation.

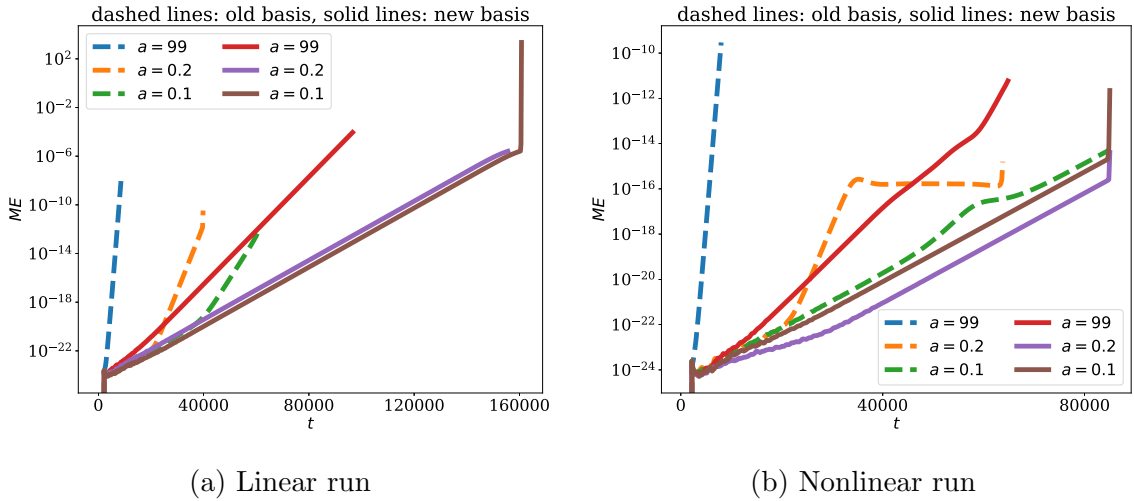


Figure 4.17: Magnetic energies for (a) linear and (b) nonlinear tearing mode run with $n = 0, 1$. The factor a in the legends denote amount grid accumulation near the polar grid center. With old basis functions at the grid center numerical noise is seen. With new basis functions at the grid center the noise is removed.

modes and hence growth rates for simulations with old basis are higher. As the grid is refined near the grid center the numerical noise reduces. With new basis functions, a level of noise at the grid center is very small as compared to the tearing modes perturbations. On the grids with $a = 0.1$, clean solutions are obtained at the grid center as can be seen in the figure (4.18b) and (4.18d) for linear and nonlinear runs respectively. As a result, the growth rates obtained are only due to the instabilities of the tearing modes.

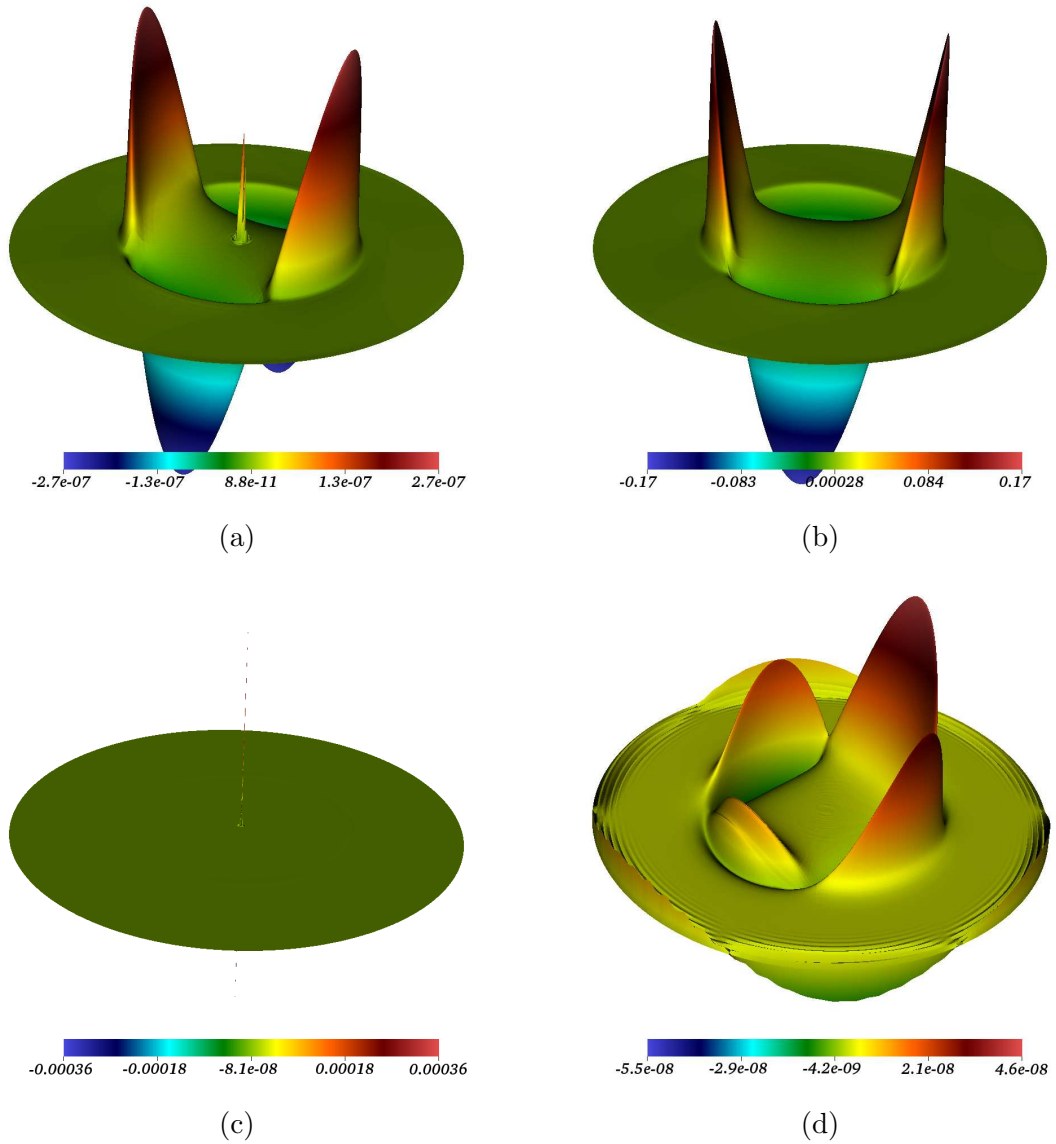


Figure 4.18: Effect of polar grid center treatment: First and second row show visualizations for linear and nonlinear runs for tearing modes respectively. First and second column show visualizations without and with polar grid center treatment respectively. (a) and (b) show perturbations in A_3 for linear tearing mode runs. (c) and (d) show perturbations in v_ϕ for nonlinear tearing mode runs.

The similar effect of the new basis functions is seen in linear simulation of the circular ballooning modes with $n = 0$ and 6. Once again, the equilibrium 3 is used and simulations are run without any diffusivities but with $\eta = 10^{-6}$. Figure (4.19) shows the visualization of perturbation in v_ϕ , where it can be seen that the noise at the grid center disappears and a clean solution is obtained with the new basis functions. Note that the grid center is Shafranov shifted from the geometrical center

as shown in the Figure (4.10) and hence the location of noise at the grid center is skewed.

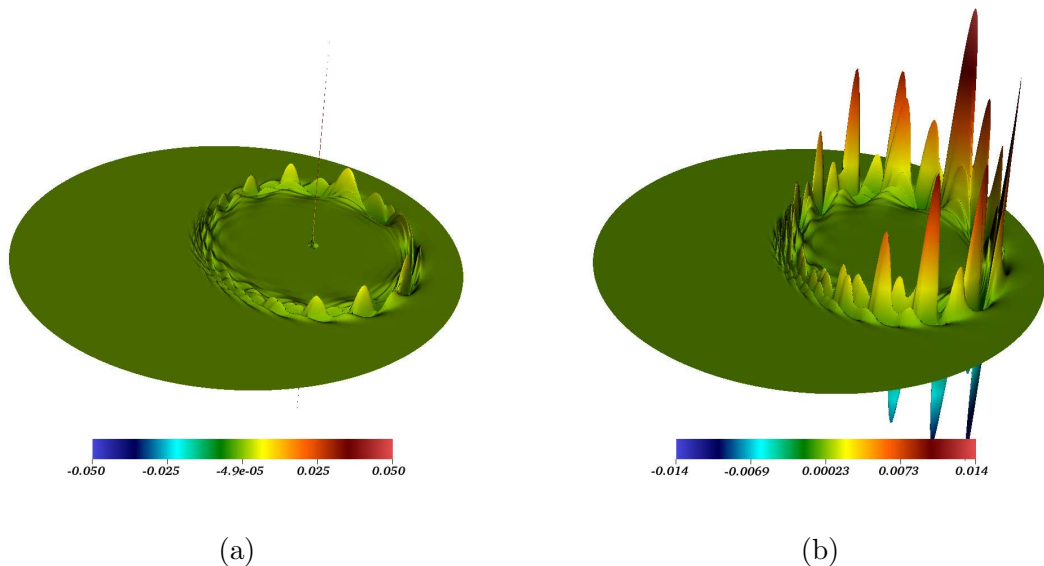


Figure 4.19: Perturbations in v_ϕ with (a) old and (b) new basis functions at the polar grid center. With the new basis functions the noise at the grid center disappears.

The exercises shown in this subsection highlight the advantage of the treatment of the grid center proposed in the section (3.4.5). This treatment is used in the nonlinear simulations presented below and in next Chapter.

4.4.3 Nonlinear runs for internal kink modes

In a typical nonlinear simulation of the internal kink mode, instabilities grow linearly in the first stage. At the end of linear growth, follows a ‘saturation’ phase in which the modes may interact nonlinearly with each other and undergo a cyclic dynamics. Such cyclic dynamics or oscillations are investigated numerically in [41, 42] in the context of the internal kink modes, where sawtooth oscillations are observed for realistic plasma parameters. Sawtooth oscillations consists of repeated ramps and crashes in the nonlinear phase of the internal kink dynamics, a phenomenon often observed in experiments. To simulate the physically realistic sawtooth oscillations, the full MHD model may need inclusion of diamagnetic terms and Ohmic heating term, former are not used in this work and latter is currently ignored from the full MHD model for the numerical reasons.

Remark: Excluding Ohmic heating terms

The Ohmic heating term is ignored from the full MHD model. To compute the current, second derivative of \mathbf{A} is required: $\mathbf{J} = \nabla_h \times \nabla_h \times \mathbf{A}$. Moreover, the current is a divergence free quantity $\nabla \cdot \mathbf{J} = \nabla \cdot (\nabla \times \mathbf{B}) = 0$. Since the FEM used here promises continuity of \mathbf{A} only upto the gradients, the computed current is not continuous across elements and the numerically obtained current is not divergence free. FEM with higher order continuity is needed to cleanly incorporate the Ohmic heating term, the work which is currently under development [76].

Excluding Ohmic heating and diamagnetic terms, an attempt is made to push a nonlinear internal kink simulation in a saturation phase with large values of resistivities and numerical stabilization rather than computing realistic sawtooth oscillations, which is one of the future perspective of this work.

The resistivity is set to $\eta = 10^{-5}$ and all other physical diffusivities are set to zero. The time stepping is fixed by the Courant criterion (CFL number) given by:

$$\text{CFL} = \Delta t \min_e \left(\frac{h_e}{\lambda_{\max}^e} \right)$$

where h_e is the characteristic element size, λ_{\max}^e is the maximum characteristic speed over an element and index e runs over total number of element. The element size is evaluated as minimum of the lengths of the lines joining midpoints of opposite edges (assuming a linear quadrangular element). The characteristic speed is chosen as the speed of fast magnetosonic waves from the characteristic analysis of ideal MHD system and is specified as:

$$\lambda_{\max}^e = \max_e \left(\sqrt{\frac{\gamma p + \mathbf{B} \cdot \mathbf{B}}{\rho}} \right)$$

The time integration method used is Crank Nicholson method and time steps are determined by setting $\text{CFL} = 500$. The numerical stabilization is added via shock capturing terms in the equations of the velocity, density and pressure. Instead of shock detecting stabilization matrix terms, the stabilization coefficient is used everywhere by setting:

$$\underline{\mathbf{T}}_{\text{SC}} = 10^{-2} \frac{h_e}{\lambda_{\max}} \mathbf{I}$$

This essentially means that diffusivities in the velocity, density and pressure equations are set numerically and have coefficients that are grid dependent.

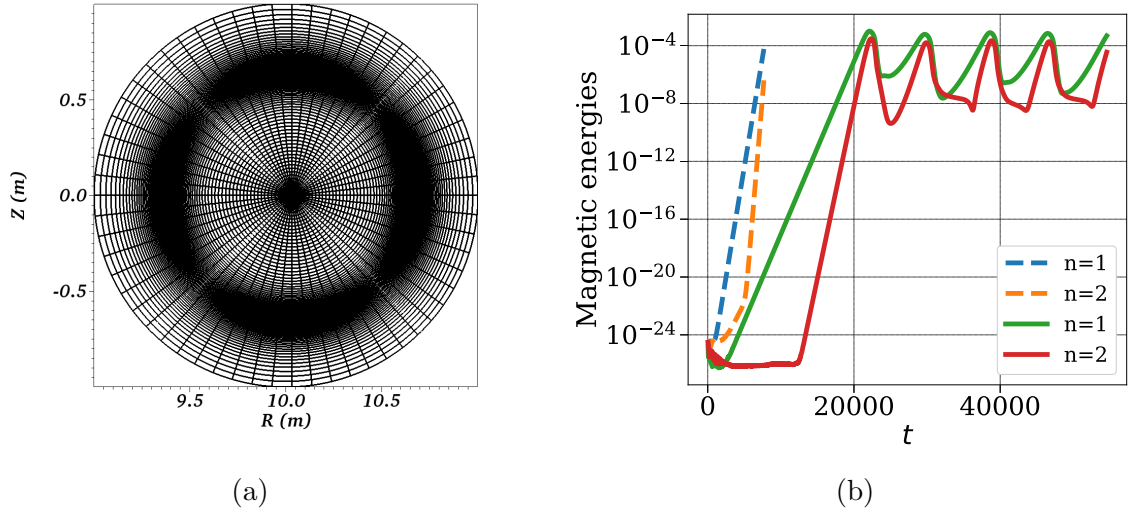


Figure 4.20: (a) Flux surface aligned polar grid used for nonlinear simulation of internal kink mode (b) Evolution of energies with (solid lines) and without (dotted lines) numerical stabilization.

Nonlinear internal kink simulations are run with $n = 0, 1, 2, 3, 4$ on flux aligned polar grid as shown Figure (4.20a). The ‘equilibrium 1’ from the section (4.1) is used and the grid is refined at the location of $q = 1$ surface. Figure shows comparison of energies for $n = 1$ mode with and without numerical stabilization. It can be seen in Figure (4.20b) that the growth of energies obtained using numerical stabilization are clearly lower than the actual rates. Note that the numerical stabilization used in this case is very high and plasma beta β_N drops from 0.38 to 0.025 % during the simulation.

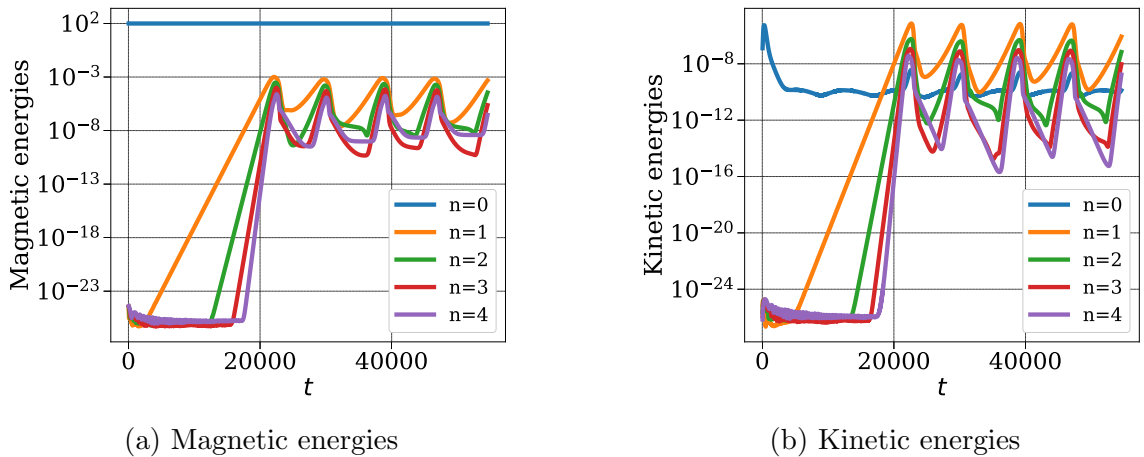


Figure 4.21: Evolution of energies showing nonlinear saturation phase after linear growth of internal kink modes.

In Figure (4.21) the evolution of the magnetic and kinetic energies are shown for all $n > 0$ harmonics obtained with the numerical stabilization and it can be seen that kink modes are saturated and undergo kink cycles. The similar behavior of kink cycles is also observed with high values of $D_{\perp} \approx 10^{-6}$ to 10^{-5} and $\kappa_{\perp} \approx 10^{-4}$ and 10^{-3} using Gears method.

4.5 Conclusion

In this chapter, implementation of FEM is described for Grad-Shafranov and the full MHD equations. The full MHD model is validated by performing standard instability problems like internal kink, tearing and ballooning modes. The numerical results obtained with full and reduced MHD are seen to be in agreement. In [74] the benchmark is performed for the full MHD model with reduced MHD model as well as other codes such as CASTOR and MISHKA. With the help of the numerical stabilization, the nonlinear simulations of internal kink modes enter into a nonlinear saturation phase.

A first implementation of the full MHD model was demonstrated in [44] which was restricted to the simple geometries and standard MHD instabilities. It was shown in [74] that the full model is ready for production by demonstrating several nonlinear simulations like a model disruptions problem, ELMs etc. The linear tests presented in this Chapter are similar to that in [74]. They are kept here for the sake of the discussion and used further to demonstrate the advantages due to the added numerical features such as the numerical stabilization, variable time step method and the polar grid center treatment. The numerical results for massive material injection (MMI) simulations using all the developed tools are presented in next Chapter.

Chapter 5

Nonlinear simulations with Massive Material Injection

Basic experimental process of Massive Material Injection (MMI) is described in Chapter 1 and equations to govern MMI in tokamak plasma are described in Chapter 2. The equations form a system of nonlinear hyperbolic PDEs with sources. Massive gas injection (MGI) involves a stationary source through which a massive amount of neutral gas is injected inside a tokamak plasma. Shattered pellet injection (SPI) involves a moving source that models multiple fragments of a shattered pellet in the plasma which generate impurity particles via interactions with plasma electrons. Both processes can be modeled either with single or two temperature models discussed in Chapter 2. The numerical tools to discretize these equations are described in Chapter 3 while the details of their implementation and numerical validations are shown in Chapter 4. In this Chapter we present the proof of concept and the numerical results for MMI obtained using full MHD model.

In both kinds of injections, MHD instabilities are triggered at rational q surfaces. As injection is usually done at the edge of a plasma, a cooling front develops in the outer layer of a plasma that may cause the magnetic field to become stochastic (to be visualized via Poincaré plots) in the outer layer of a plasma. Later the cooling front propagates radially inwards in the plasma core. The core modes may grow and interact nonlinearly with each other causing plasma core to become stochastic. In presence of both mechanisms, that means MHD instabilities in outer layer and core modes, a complete loss of plasma confinement (stochatization) may be seen which is associated with the sudden drop in the plasma thermal energy. Such plasma dynamics have already been seen in JOREK simulations with reduced MHD for MGI [30, 68, 69]

and for SPI [49, 70, 46, 50].

The main focus of this Chapter is on the SPI simulations with the full MHD. The SPI set up used here is similar to [49] where the simulations are performed using reduced MHD model on JET like equilibrium with Ar injection. Some physical characteristics of the results in [49] include the stochastization of the outer layer of plasma, the current and temperature profile contractions, excitation of core modes and a distinct TQ phase. The full MHD simulations performed here use Ne SPI instead of Ar.

5.1 Preliminary validations: MGI and SPI

JET like equilibrium that resembles JET pulse No. 85943 at time 62.4 s is used to simulate MGI and SPI. Some parameter for this pulse are as follows:

- toroidal magnetic field $B_\phi \approx 3$ T
- total plasma current $I_p \approx 2$ MA
- core electron temperature $T_e(\psi_N = 0) \approx 3.28$ keV
- core electron density $n_e(\psi_N = 0) \approx 2.1 \times 10^{19} \text{ m}^{-3}$.

A polar grid is used to solve Grad-Shafranov equation with boundary condition on ψ shown in Figure (5.1b). The coefficients used to construct the density profile (in normalized units) are:

$$\rho_0 = 1, \rho_1 = 0.01, C(1) = -1.1946, C(2) = 0.9443, C(3) = -0.4874, \\ C(4) = 0.03, C(5) = 0.98$$

The coefficients used for the temperature profile (in normalized units) are:

$$T_0 = 0.0279, T_1 = 10^{-4}, C(1) = -1.9810, C(2) = 1.6734, \\ C(3) = -0.6742, C(4) = 0.03, C(5) = 0.98$$

The value T_0 corresponds to the core electron temperature 3.28 keV. The coefficients used for the FF' profile are:

$$FF_0 = 5.6089, FF_1 = 0, C(1) = -1.4947, C(2) = 0.0949, C(3) = 0.4078, \\ C(4) = 0.01, C(5) = 0.9800, C(6) = 0, C(7) = 0.9750, C(8) = 0.022$$

With $F_0 = -8.7829$, the resulting profiles for ρ , T and FF' are shown in Figure (5.1a). The poloidal magnetic flux ψ obtained by numerical solution of Grad-Shafranov equation whose contours are shown in Figure (5.1c) along with the polar grid. A new flux aligned grid is generated with one X-point and Grad-Shafranov equation is solved again on this new grid which are shown Figures (5.1d) and (5.1e), respectively. Finally, profile for q is plotted vs ψ_N in Figure (5.1f) and it can be seen that $q = 2, 3, 4, 5$ surfaces are present at $\psi_N \approx 0.58, 0.79, 0.89, 0.95$ respectively. On the flux aligned grid, the contours of ψ_N are plotted for the values those correspond to rational q surfaces and is shown in Figure (5.1d) by red contour lines. It can be seen that $q = 1$ surface lies close to the magnetic axis, while $q = 6, 7$ surfaces are close to separatrix at $\psi_N \approx 0.99$.

Massive Gas Injection

We present a MGI simulation performed using the two temperature full MHD model in which D gas is injected into a plasma with JET like equilibrium described above. The governing equations based on the two temperature model (2.69) are written below:

$$\begin{aligned}
\frac{\partial \rho_n}{\partial t} &= \nabla \cdot (\underline{\mathbf{D}}_n \nabla \rho_n) - \rho \rho_n S_{ion}(T_e) + \rho^2 \alpha_{rec}(T_e) + \dot{\rho}_n \\
\frac{\partial \rho}{\partial t} + \nabla \cdot (\rho \mathbf{v}) &= \nabla \cdot (\underline{\mathbf{D}} \nabla \rho) + \rho \rho_n S_{ion}(T_e) - \rho^2 \alpha_{rec}(T_e) + \dot{\rho} \\
\rho \frac{\partial \mathbf{v}}{\partial t} + \rho \mathbf{v} \cdot \nabla \mathbf{v} + \nabla p - \mathbf{J} \times \mathbf{B} &= \mu \nabla^2 \mathbf{v} + \dot{\mathbf{m}} - \mathbf{v} (\rho \rho_n S_{ion}(T_e) - \rho^2 \alpha_{rec}(T_e) + \dot{\rho}_n) \\
\frac{1}{(\gamma - 1)} \left(\frac{\partial p_e}{\partial t} + \mathbf{v} \cdot \nabla p_e + \gamma p_e \nabla \cdot \mathbf{v} \right) &= \mu \nabla \mathbf{v} : \nabla \mathbf{v} + \nabla \cdot (\underline{\boldsymbol{\kappa}}_e \nabla T_e) + S_{T_e} - \rho \nu (T_i - T_e) \\
\frac{1}{(\gamma - 1)} \left(\frac{\partial p_i}{\partial t} + \mathbf{v} \cdot \nabla p_i + \gamma p_i \nabla \cdot \mathbf{v} \right) &= \mu \nabla \mathbf{v} : \nabla \mathbf{v} + \nabla \cdot (\underline{\boldsymbol{\kappa}}_i \nabla T_i) + \rho \nu (T_i - T_e) \\
\frac{\partial \mathbf{A}}{\partial t} - \mathbf{v} \times \mathbf{B} &= -\eta \mathbf{J}
\end{aligned} \tag{5.1}$$

with,

$$S_{T_e} = -\xi^* \rho \rho_n S_{ion}(T_e) - \rho \rho_n L_{line}(T_e) - \rho^2 L_{brem}(T_e)$$

This is the system of equations for neutral (in this case D) density (ρ_n), total density (ρ), velocity (\mathbf{v}), electron temperature (T_e), ion temperature (T_i) and magnetic vector potential (\mathbf{A}) along with Gauss law $\nabla \cdot \mathbf{B} = 0$ and Ampère's law $\nabla \times \mathbf{B} = \mathbf{J}$. The

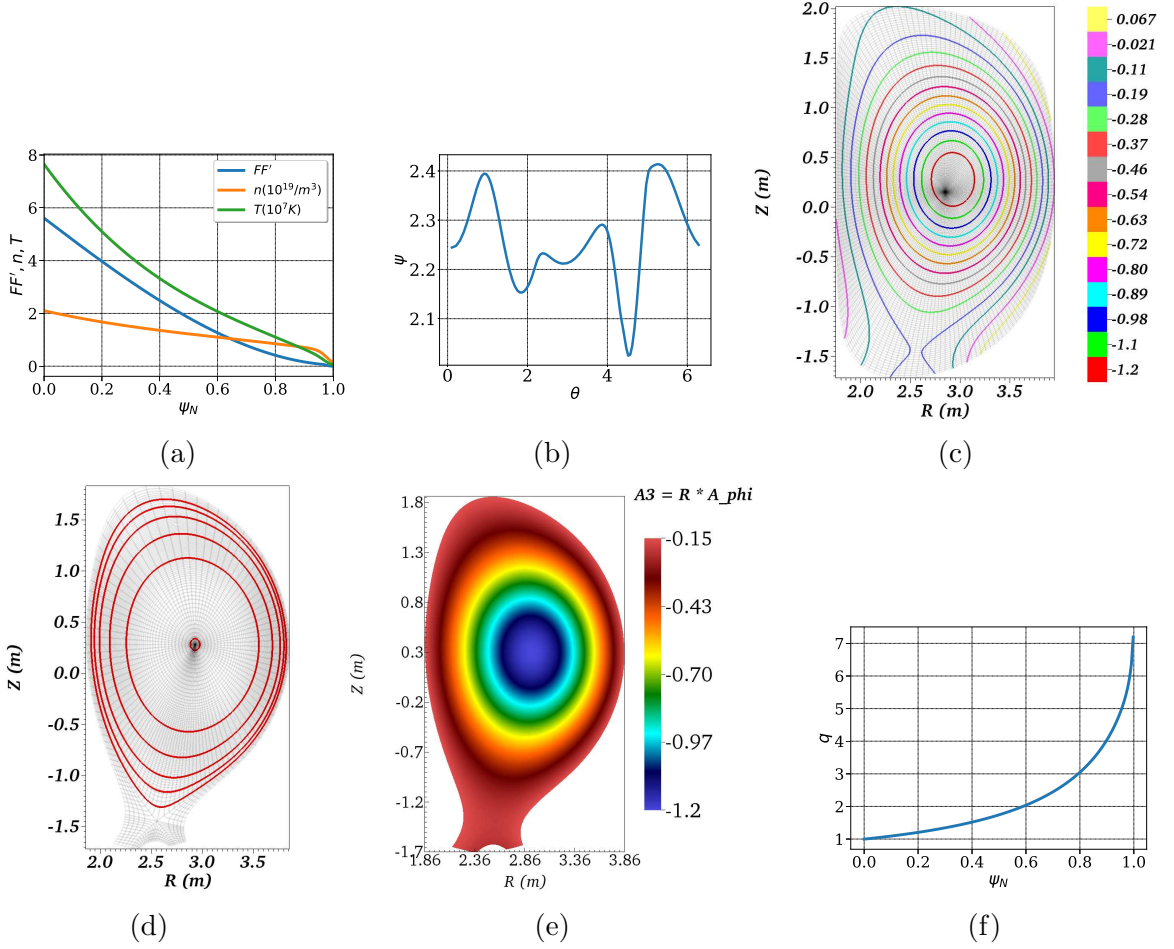


Figure 5.1: JET like equilibrium used for MMI simulations: (a) ρ , T and FF' profiles plotted vs ψ_N . (b) Boundary conditions specified to solve Grad-Shafranov equation on the polar grid. (c) Contours showing the numerical solution of the Grad-Shafranov equation ψ plotted upon polar grid. (d) Flux aligned grid with the contours of ψ_N highlighting $q = 1, 2, \dots, 6$ surfaces (drawn radially outwards) (e) Numerical solution ψ plotted on the flux aligned grid. (f) q profile plotted vs ψ_N .

forms used for the viscosity coefficient, particle and heat diffusivities are described in Chapter 3. The neutrals transport equation is modeled in [30] and contains only particle diffusion term. Since the neutrals are not affected by presence of the magnetic field, the diagonal diffusion tensor used is written as follows:

$$\underline{D}_n = \begin{bmatrix} D_{n_R} & 0 & 0 \\ 0 & D_{n_Z} & 0 \\ 0 & 0 & D_{n_\phi} \end{bmatrix}$$

The ionization rate S_{ion} and recombination rate α_{rec} coefficients for D2 are parameterized [94, 30] as:

$$S_{ion}(T_e) = 0.2917 \times 10^{-13} \left(\frac{13.6}{T_e} \right)^{0.39} \frac{1}{0.232 + \frac{13.6}{T_e}} \exp\left(- \frac{13.6}{T_e} \right)$$

$$\alpha_{rec}(T_e) = 0.7 \times 10^{-19} \left(\frac{13.6}{T_e} \right)^{1/2}$$

where S_{ion} and α_{rec} are in m^3/s and eV respectively. The normalized ionization energy of a D2 atom is denoted by ξ^* and is equal to 13.6 eV. The term $\dot{\rho}_n$ denotes the neutral source term and is specified as:

$$\dot{\rho}_n = \frac{dN_n f(R, Z, \phi)}{dt \int f dV}$$

where

$$f = \exp\left(- \frac{(R - R_{mgi})^2 + (Z - Z_{mgi})^2}{\Delta R_{mgi}^2} \right) \exp\left(- \frac{(\phi - \phi_{mgi})^2}{\Delta \phi_{mgi}^2} \right)$$

where, $(R_{mgi}, Z_{mgi}, \phi_{mgi})$ is the position where neutrals are delivered into plasma. The poloidal and toroidal extents of the neutral source are denoted by ΔR_{mgi} and $\Delta \phi_{mgi}$ respectively. The form of dN_n/dt , based on experimental set-up, can be found in [13, 30]. The symbols L_{line} and L_{brem} denote the line and bremsstrahlung radiation rate coefficients and the open ADAS [1] database is used to compute these coefficients. The last terms in the both temperature equations denote the ion-electron collisional energy exchange terms where ν is the electron-ion collision rate for the background species.

All the variables and physical quantities are written in normalized units, unless specified otherwise. The same temperature profile is used for ions and electrons. The temperature independent values of resistivity and viscosity coefficient are specified as: $\eta = 10^{-5}$ and $\mu = 10^{-5}$. The parallel and perpendicular components for heat conductive coefficients for both the electron and ion temperature equations are specified as $\kappa_{\parallel} = 10^4$ and $\kappa_{\perp} = 10^{-6}$. The perpendicular particle diffusion coefficient is specified as $D_{\perp} = 10^{-6}$. The neutrals diffusion coefficients are specified as $D_{n_R} = D_{n_Z} = D_{n_{\phi}} = 10^{-5}$. The thermal equilibration terms are not used in this simulation. Boundary conditions used are described in section (4.2).

Flux aligned grid is built with the number of points in radial and poloidal directions in the core $n_{\psi} = 51$ and $n_{\theta} = 64$ respectively. To resolve private and SOL regions respectively 5 and 2 points are used. D2 gas is injected at $(R_{mgi}, Z_{mgi}, \phi_{mgi}) = (3.65, 0.25, 5.89)$ with 1 bar pressure (which is very much lower than the experimental

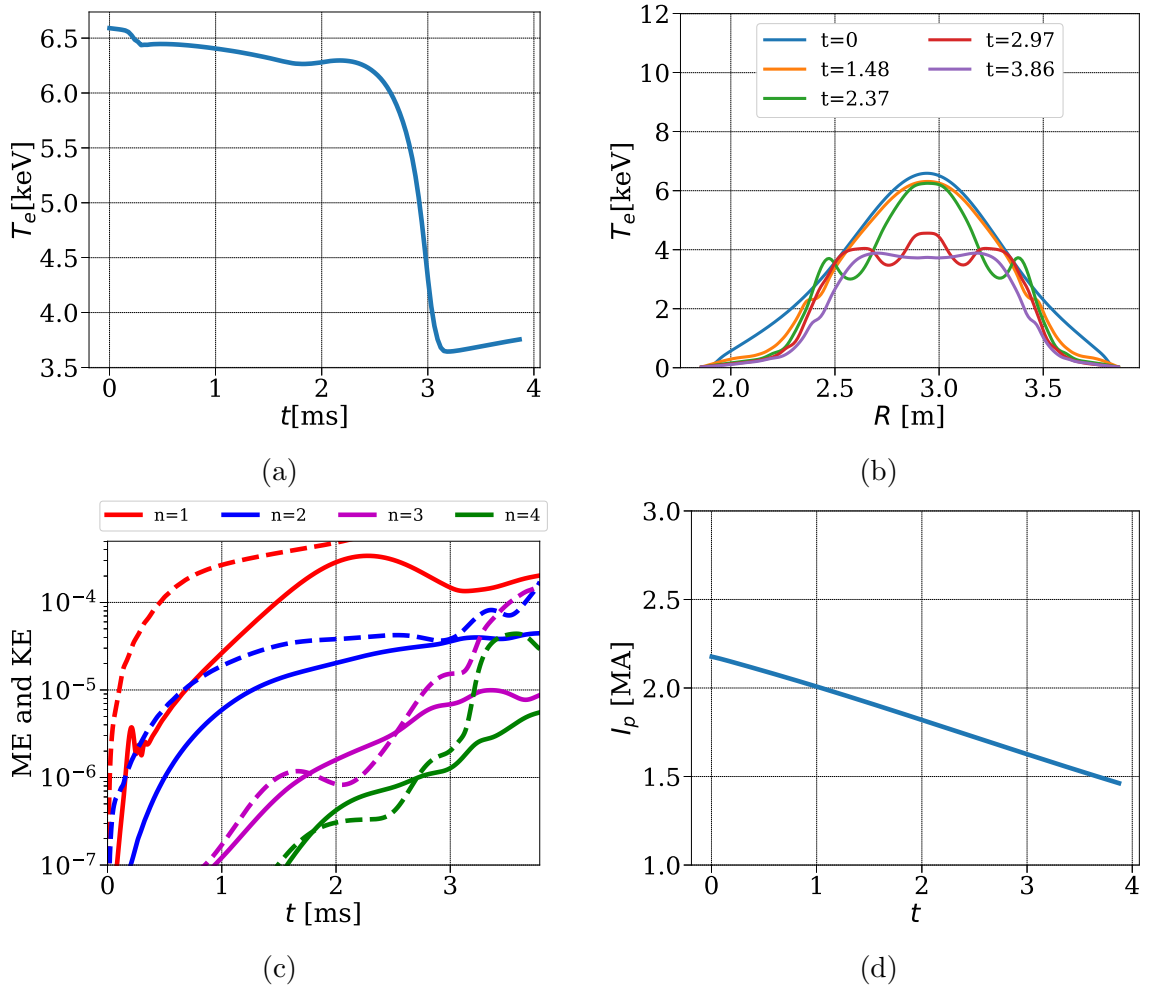


Figure 5.2: MGI with full MHD: (a) T_e at the magnetic axis. (b) T_e profiles at midplane plotted vs R . Evolution of : (c) magnetic energies (solid lines) and kinetic energies (dotted lines) for $n = 1, 2, 3, 4$ (d) plasma current I_p .

value of 33 bar) at $t = 0$ (in practice, the code is run without injection for some time before the injection, as it is done in SPI simulations). The shape of source is specified with $\Delta R_{mgi} = 0.08$ and $\Delta \phi_{mgi} = 1.2$. Toroidal harmonics used in the simulations are $n = 0, 1, 2, 3, 4$ and number of equidistant planes used in the toroidal direction are 16.

The evolution of the temperature at the magnetic axis as shown in Figure (5.2a) and it shows the sign of thermal quench (TQ) around 3 ms. Sudden drop in T_e starts roughly at 2.5 ms and last until 3.1 ms. In Figure (5.2b) T_e profiles at midplane are shown, where a sudden drop in T_e profile is seen, for example, T_e profile at $t = 2.97$ ms is much lower than that at $t = 2.37$ ms. The drop in T_e is associated with the increase in energies as shown in Figure (5.2c). Figure (5.2d) shows evolution of plasma current

I_p which decreases steadily due to the fact that the resistivity used is higher for this simulation. (Here, I_p is an integrated quantity over plasma volume. The expression for I_p and other relevant integrated quantities are shown in Appendix (B)).

In Figure (5.3), visualizations of T_e (in keV) and ρ (particle density in 10^{20}) are shown at time instants $t = 1.48, 2.37, 2.97$ and 3.86 ms along with Poincaré plots of magnetic fields. As more and more particles are injected in plasma, a cooling front is developed in the outer layer which is seen in the T_e field at $t = 1.48$. This can also be seen in Figure (5.2b) where gradient in T_e is developed in the outer region. This cooling is associated with the growth of 3/1 mode seen in the outer layer of the Poincaré plot in Figure (5.3) at $t = 1.48$ ms. Beyond this time, the energies associated with $n = 3$ and 4 grow which is seen in Figure (5.2c) and $m/n = 3/1$ mode grows as can be seen at the further time instants in Figure (5.2c). At $t = 2.97$ ms presence of 2/1 mode is seen which grows for some time and then stabilizes. At $t = 3.86$ ms T_e at the magnetic axis drops to almost half of the initial value and in the significant portion, plasma becomes stochastic as seen from the last Poincaré plot in Figure (5.3).

With the time step of 10, the simulation stops converging after $t = 3.86$ ms as modes starts to interact with each other and MHD activities increase. In practice, a typical simulation is restarted by reducing the time step at such a stage, as it is done in SPI simulation. Although this simulation is performed on a coarse grid with the parameters selected mostly for the ease of numerical treatment (which cause I_p to drop unrealistically faster rate), it shows overall physical characteristics similar to TQ, growth of core modes and stochastization of plasma.

Shattered pellet injection

The single temperature full MHD model used for SPI simulations is rewritten below:

$$\begin{aligned}
\frac{\partial \rho_{\text{imp}}}{\partial t} + \nabla \cdot (\rho_{\text{imp}} \mathbf{v}) &= \nabla \cdot (\underline{\mathbf{D}}_{\text{imp}} \nabla \rho_{\text{imp}}) + \dot{\rho}_{\text{imp}} \\
\frac{\partial \rho}{\partial t} + \nabla \cdot (\rho \mathbf{v}) &= \nabla \cdot (\underline{\mathbf{D}} \nabla \rho) + \dot{\rho}_i + \dot{\rho}_{\text{imp}} \\
\rho \frac{\partial \mathbf{v}}{\partial t} + \rho \mathbf{v} \cdot \nabla \mathbf{v} + \nabla p - \mathbf{J} \times \mathbf{B} &= \mu \nabla^2 \mathbf{v} + \dot{\mathbf{m}} - \mathbf{v}(\dot{\rho}_i + \dot{\rho}_{\text{imp}}) \\
\frac{1}{(\gamma - 1)} \left(\frac{\partial p}{\partial t} + \mathbf{v} \cdot \nabla p + \gamma p \nabla \cdot \mathbf{v} \right) &= \mu \nabla \mathbf{v} : \nabla \mathbf{v} + \nabla \cdot (\underline{\boldsymbol{\kappa}} \nabla T) + S_T - C_{\text{ion}} \\
\frac{\partial \mathbf{A}}{\partial t} - \mathbf{v} \times \mathbf{B} &= -\eta \mathbf{J}
\end{aligned} \tag{5.2}$$

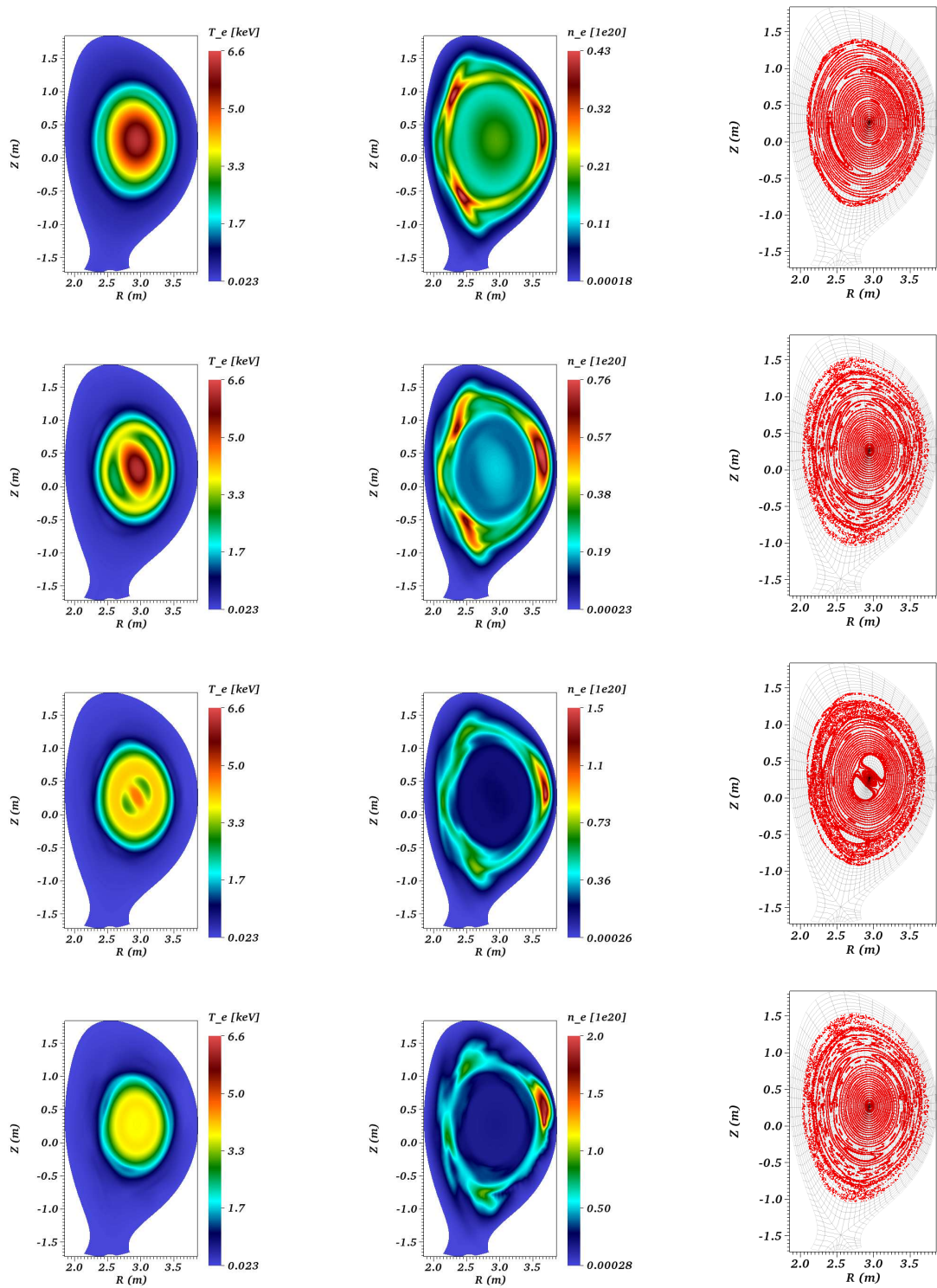


Figure 5.3: MGI with full MHD: First, second and third column shows T_e [keV], n_e (10^{20}) and Poincaré plots respectively. First, second, third and fourth row corresponds to $t = 1.48, 2.37, 2.97, 3.86$ in ms respectively.

with Gauss law $\nabla \cdot \mathbf{B} = 0$ and Ampères law $\nabla \times \mathbf{B} = \mathbf{J}$. The source term S_T is given by equations (2.64) and (2.65) while C_{ion} is given by equations (2.66) and (2.51). In SPI a frozen pellet of D2 or Ar or Ne or mixture of them is shattered before the injection into tokamak plasma. The number of atoms in the pellet and the number of shattered fragments can be specified as inputs to the code. Each fragment generates neutrals through ablation process. In JET-like equilibrium described at the beginning of this section, we simulate the injection of 100 Ne fragments.

The physical parameters used for the simulation are as follows:

- The temperature dependent resistivity with the value at the magnetic axis $\eta_0 = 10^{-8}$ is specified only in A_3 equation and not in A_R and A_Z equation. The temperature and effective charge (Z_{eff}) dependence of the resistivity is specified in the equation (2.67).
- The coefficient of viscosity is set with the value at the magnetic axis as $\mu_0 = 10^{-6}$ with the Spitzer like temperature dependence. The viscous heating terms are ignored in this simulation.
- The total density diffusion coefficients are set as $D_{\perp} = D_{\parallel} = 5 \times 10^{-5}$. The same coefficients are used for impurity density diffusion. For the total density equation, D_{\parallel} has no physical origin and is used only for numerical stability reasons.
- The coefficients of heat conduction at the magnetic axis are set as $\kappa_{\perp 0} = 5 \times 10^{-7}$ and $\kappa_{\parallel 0} = 4 \times 10^4$ where κ_{\parallel} depends upon the temperature as $\kappa_{\parallel} = \kappa_{\parallel 0} (T/T_0)^{5/2}$ while κ_{\perp} is constant.

Flux aligned grid with one X-point is built with the number of points in radial and poloidal directions in the core $n_{\psi} = 51$ and $n_{\theta} = 64$ respectively. To resolve private and SOL regions respectively 4 and 3 points are used, while 10 points are used in each left and right leg region. Toroidal harmonics used in the simulations are $n = 0, 1, \dots, 7$ and the number of planes used in the toroidal direction are 32.

The effective charge Z_{eff} and the charge state distribution functions $\mathcal{P}(z, T_e, n_e)$ are determined using coronal equilibrium (CE) assumption. The openADAS [1] database is used to determine $\mathcal{P}(z)$ and Z_{eff} which are plotted in the figure (5.4a) and (5.4b) respectively, for the electron density $n_e = 10^{20} \text{ m}^{-3}$. For given values of T_e , the charge state distribution functions of all charge states z sums up to 1. These

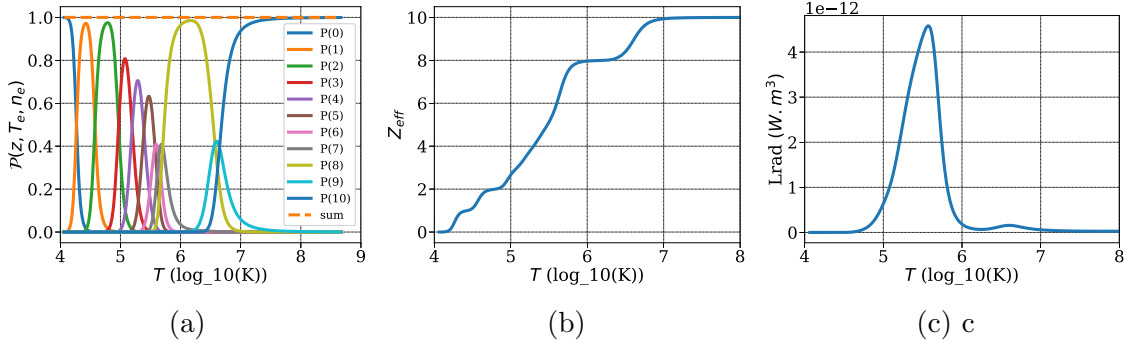


Figure 5.4: The data obtained from CE assumption and openADAS [1] database: (a) the charge state distribution function $\mathcal{P}(z)$ plotted vs electron temperature (in $\log_{10}(K)$) where $z \in 0, 10$ for Neon atom. The legend ‘sum’ denotes summation of $\mathcal{P}(z)$ over all charge states. (b) Z_{eff} plotted vs electron temperature. (c) Radiation function plotted vs electron temperature (in $\log_{10}(K)$).

functions are used to compute the ionization potential energy E_{ion} . The radiation power function ($Lrad$) to determine the radiation power loss, including contribution from line radiation, recombination radiation and bremsstrahlung radiation, is also determined at CE from the open ADAS data [1] and is shown in Figure (5.4c). For simplicity we assume that there is no absorption of the radiated power. For more details on assumptions made and the impact of CE assumption, see [49].

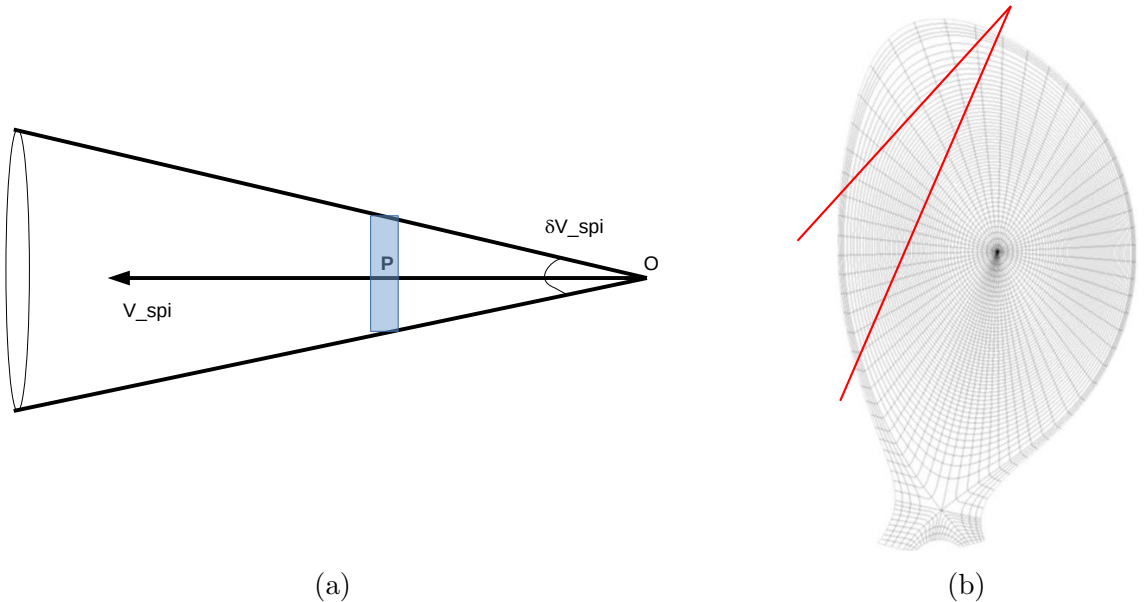


Figure 5.5: Sketch illustrating SPI: (a) Distribution of initial position and velocity of the SPI fragments (b) The direction and the extent of SPI fragments propagation.

All fragments are assumed to come from the same point O and appear suddenly

after a certain time t_{spi} in the simulation so that they travel inside a cone of aperture δV_{spi} with the apex O as shown in Figure (5.5a). The point $P = (R_{spi}, Z_{spi}, \phi_{spi})$ is the location around which fragments arrive in the domain directly. These locations are chosen randomly in the neighborhood of the point P. The velocity of each fragment V_{frag} is chosen around the SPI reference velocity V_{spi} such that the difference between V_{frag} and V_{spi} is picked randomly between 0 and $\delta V_{spi}/2$, where δV_{spi} is shown in Figure (5.5a). Figure (5.5b) shows the sketch of the propagation of the SPI fragments based on the SPI velocity and the initial position of fragments specified here. This configuration mimics the SPI system installed on JET and that in [49].

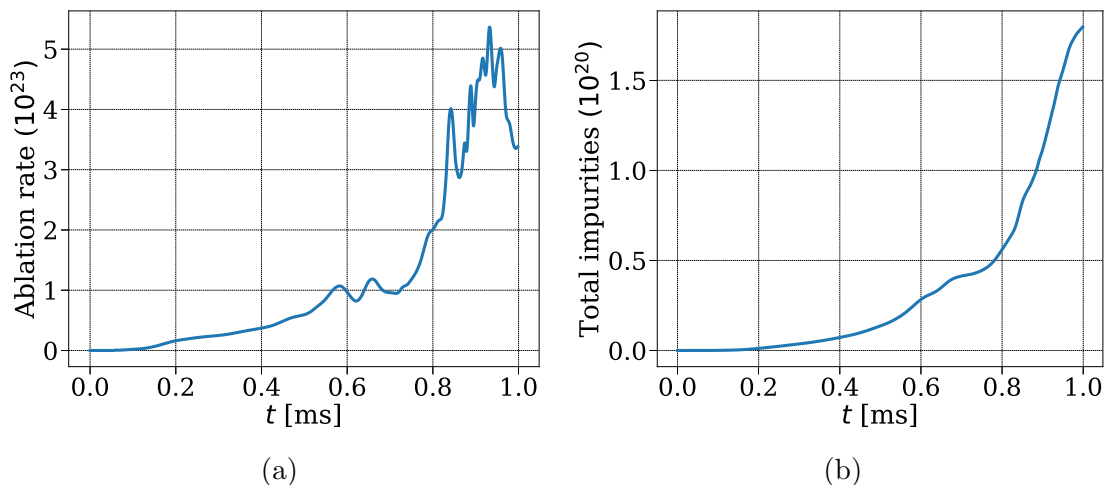


Figure 5.6: (a) Ablation rate plotted vs t (b) Total number of Ne atom in plasma plotted vs t .

Neutral gas shielding (NGS) model is used to determine the ablation rate. The ablated neutral cloud is assumed to have a circular cross-section in poloidal plane, with a radius equal to R_{spi} and a toroidal extent $\Delta\phi_{spi}$. The details of the source term due to SPI are given in section (2.3). The number fragments are assumed to be 100. We assume the fragment size r_p follows the statistical fragmentation model [79] as follows:

$$\mathcal{P}(r_p) = \frac{r_p K_0(\kappa_p r_p)}{I}; \quad I \equiv \int_0^\infty r_p K_0(\kappa_p r_p) dr = \kappa_p^{-2}$$

where K_0 is the modified Bessel function of the second kind, and κ_p is the inverse of the characteristic fragment size. These fragments arrive at the location around $(R_{spi}, Z_{spi}, \phi_{spi}) = (3.05, 1.7, 4.51)$ after the time $t_{spi} = 0.03564$ ms. The shape of a gas cloud formed by the fragments is specified by equation (2.60) with $\Delta R_{spi} = 0.08$ and $\Delta\phi_{spi} = 1.2$. R , Z and ϕ components of the SPI velocity are specified as -89.4427 ,

-178.885 and 0 respectively in m/s with $\delta V_{spi} = 0.349$ m/s. The total number of Ne atoms injected are 1.5×10^{22} . The ablation rate and the total number of Ne atoms ablated in the simulation are shown in Figure (5.6).

A shock capturing stabilization is added where $|\nabla \cdot \mathbf{v}|$ is used as a criterion to detect discontinuities and high gradients. This criterion is chosen based on the observation that near the location of fragments, higher gradients in T , ρ and \mathbf{v} are seen that eventually lead to negative densities. However, a more reasonable stabilization scheme is devised which is presented in next section. Fourth order diffusion terms are also added in all the equations, except those of \mathbf{A} , with a constant coefficient 10^{-12} to remove the high wavenumber spurious oscillations from the numerical solution.

Figure (5.7) shows snapshots of n_{imp} [10^{20}], T [keV], A_3 and Z_{eff} plotted on $\phi = 0$ plane at $t = 0.83, 0.88$ and 1 ms. As opposed to MGI, SPI involves a moving source with SPI velocity v_{spi} and it can be seen from ρ_{imp} snapshots that the impurity source is moving in the plasma core. The moving fragments interact with electrons and create impurities via ablation which can be seen from the high values of ρ_{imp} in Figure (5.7). These high values also approximately show the location of the fragments. As fragments move inside the plasma core, MHD instabilities are triggered along the rational q surfaces and it can also be seen in the evolution of the magnetic and kinetic energies in Figure (5.9a). Along the rational q surfaces, the convective mixing helps impurities to spread in plasma which is seen from Z_{eff} plots in Figure (5.7). As impurities spread, a cooling front is generated around plasma core that propagates inwards which is seen from the snapshots of the temperature.

Snapshots of A_3 are also shown in Figure (5.7) showing MHD instabilities developing along rational q surfaces. This leads to stochasticization of plasma as can be seen from Poincaré plot of the magnetic field in Figure (5.8). The blue dots show location of the fragments at $t = 1$ ms. The growth of the modes in the outer layer of plasma cause magnetic surfaces to break as fragments propagate inside plasma. The breaking of the magnetic surfaces is a sign of loss of confinement. The mode $m/n = 1/1$ grows near the magnetic axis, as $q = 1$ surface is close to the magnetic axis. After $t = 0.75$ ms the growth in $1/1$ mode causes the core temperature to collapse. The growth of $2/1$ can also be seen in Poincaré plot at the radial location where the fragments are located at $t = 1$ ms.

Figure (5.9a) shows that until 0.7 ms energies increase during which the temperature profile also increases as can be seen in Figure (5.9b) and (5.9c). After $t = 0.75$ ms, because of the growth of $1/1$ mode, the temperature profile cools rapidly and

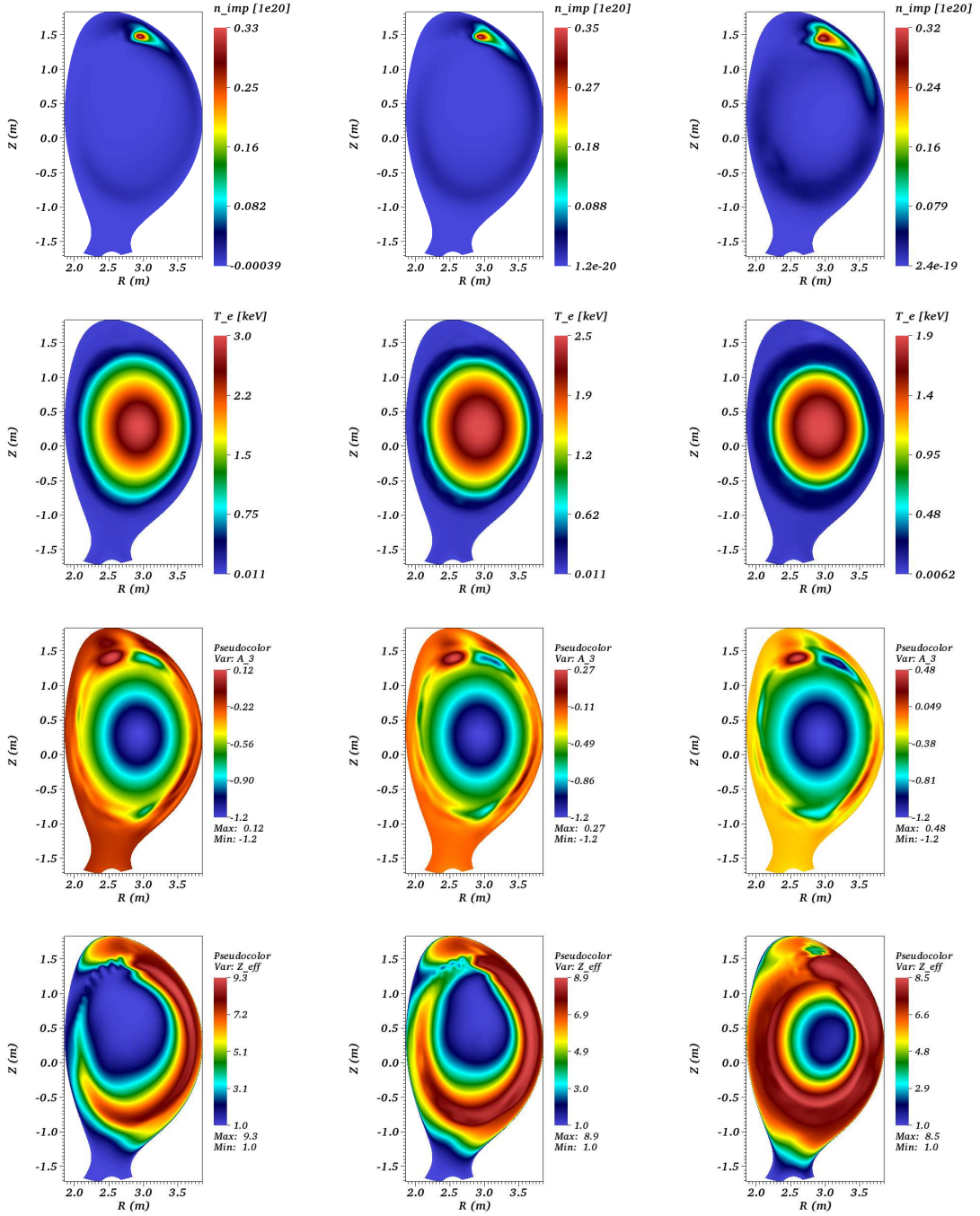


Figure 5.7: First, second, third and fourth row show visualization of $n_{\text{imp}} [10^{20}]$, T [keV], A_3 and Z_{eff} while first, second and third columns shows the quantities plotted at $t = 0.83, 0.88$ and 1 ms. All the figures are plotted at $\phi = 0$ plane.

energies increase more rapidly. In Figure (5.10), a sign of a thermal quench is seen via rapid decrease in the thermal energy (TE) and increase in the radiation energy.

Figure (5.10c) shows the evolution of the plasma current I_p which is the integrated

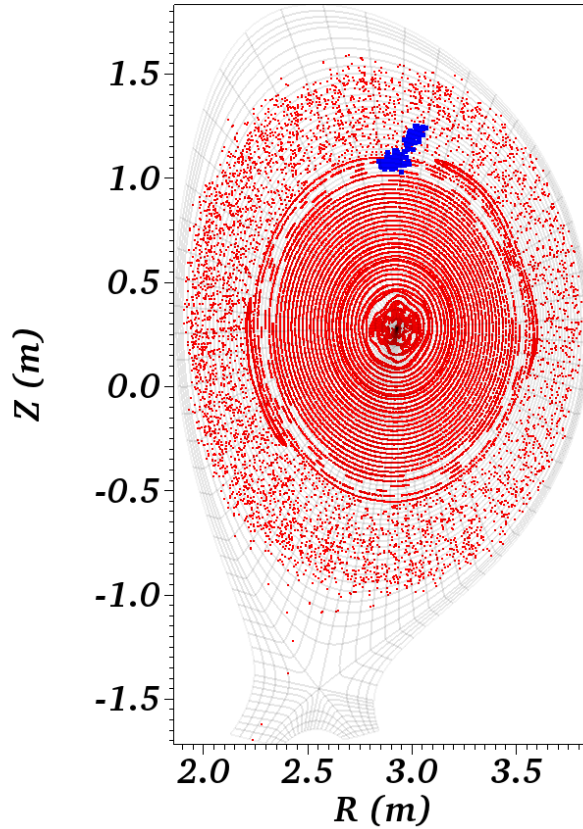


Figure 5.8: Poicaré plot of magnetic field plotted at $t = 1$ ms along with the position of SPI fragments marked by blue dots.

quantity over the plasma volume. At the beginning of the injection I_p shows dramatic decrease which is a consequence of not using η in A_R and A_Z equations. This drawback is eliminated when we use the resistivity in all components of the magnetic potential (shown in next subsection). Figure (5.9d) shows $j = -R j_\phi$ profiles (where j is a variable of the reduced MHD model) at the midplane plotted vs R . A smoothing operation is performed on these profile as the continuous description of the current vector is not available and j profile obtained is non smooth. The current profile contraction is seen approximately at $R = 3.6$ m where gradients in T profiles are also seen. Both T and j profiles' contractions follow the cooling front.

Despite the use of a coarse grid, removal of η from A_R and A_Z equations and absence of Ohmic heating term, physical aspects of SPI are captured in these simulations which look similar to JET SPI simulations in [49] and a MGI simulation in [74]. MHD instabilities are triggered by two mechanisms, first a convective mixing

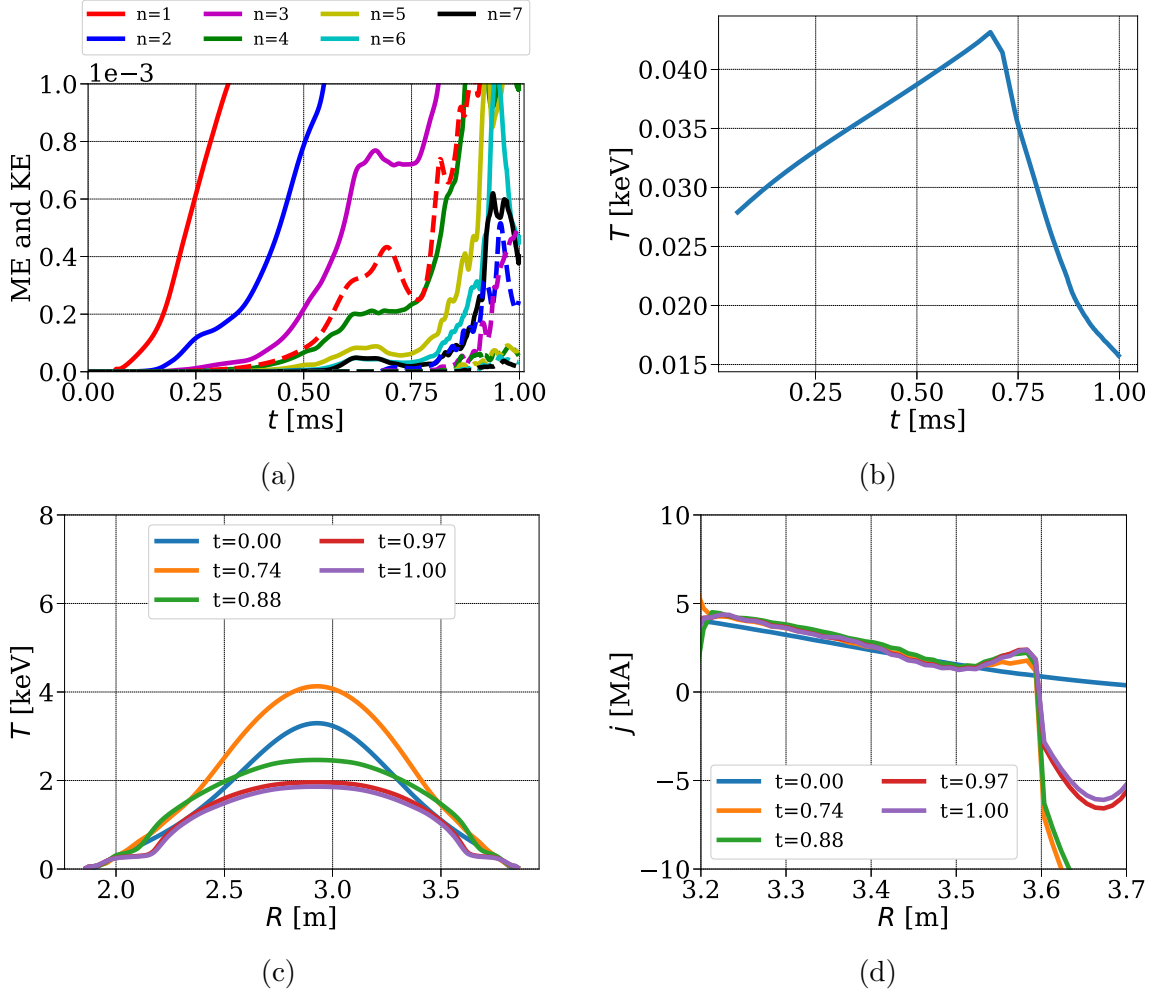


Figure 5.9: SPI with full MHD: Evolution of (a) magnetic energies (solid lines) and kinetic energies (dotted lines) for $n = 1, 2, 3, 4, 5, 6, 7$ (b) T at the magnetic axis. (c) T profiles at midplane plotted vs R . (d) $j = -Rj_\phi$ profiles at midplane plotted vs R . Smoothing operation is performed on this profile.

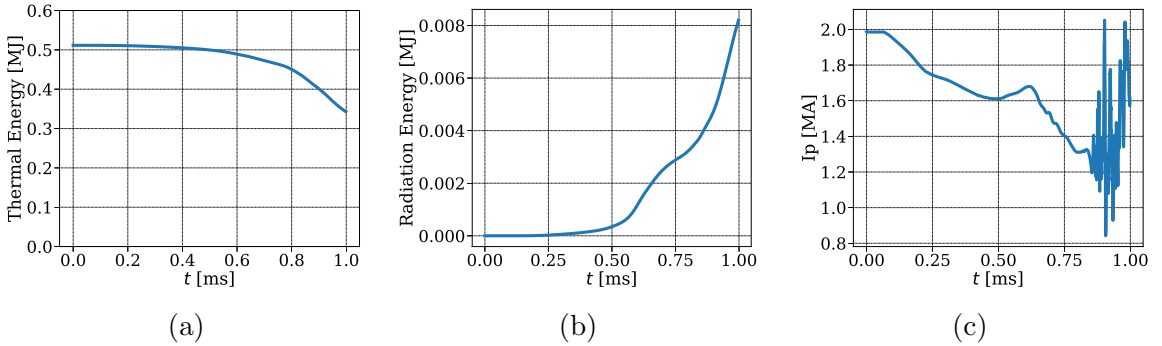


Figure 5.10: SPI with full MHD: Evolution of (a) thermal energy (b) radiation energy (c) plasma current I_p . These are integrated quantities over plasma volume.

in the outer layer of plasma triggered by SPI fragments and then the growth of core 1/1 mode. A TQ like phase is seen after which the linear solver fails to converge as negative values of ρ_{imp} are seen, which denotes the need of higher resolution and/or numerical stabilization. Summarizing, physical characteristics of TQ like phase is seen in the simulation which is associated with the increase in MHD activities and growth of core modes leading to plasma stochastization in the outer layer.

5.2 SPI triggered MHD dynamics

The SPI parameters used in following simulations are the same as the SPI simulation described in the above section. Nonlinear simulations are performed in a range of parameters to study plasma response to SPI.

Stabilization based on acoustic waves

It is observed in the preliminary simulations that high values of $\nabla \cdot \mathbf{v}$ follow the SPI fragments and may lead to numerical problems such as the negative densities near the location of the fragments. Indeed, the presence of impurities alters the equation of pressure and the speed of sound. Let us look at the pressure equation:

$$\frac{\partial p}{\partial t} + \mathbf{v} \cdot \nabla p + \gamma p \nabla \cdot \mathbf{v} + (\gamma - 1) \rho_{\text{imp}} \left(\frac{\partial E_{\text{ion}}}{\partial t} + \mathbf{v} \cdot \nabla E_{\text{ion}} \right) = R_p$$

where, R_p denotes all other terms in the pressure equation and the pressure is given as $p = (\rho + \alpha_{\text{imp}} \rho_{\text{imp}}) T$. Recalling the assumption that E_{ion} is a (strong) function of electron temperature (and a weak function of n_e , so that the variation with respect to n_e is ignored):

$$\frac{\partial p}{\partial t} + \mathbf{v} \cdot \nabla p + \gamma p \nabla \cdot \mathbf{v} + (\gamma - 1) \rho_{\text{imp}} \frac{\partial E_{\text{ion}}}{\partial T} \left(\frac{\partial T}{\partial t} + \mathbf{v} \cdot \nabla T \right) = R_p \quad (5.3)$$

Using the definition of the total pressure $p = (\rho + \alpha_{\text{imp}} \rho_{\text{imp}}) T$,

$$\begin{aligned} \frac{\partial p}{\partial t} &= \tilde{\rho} \frac{\partial T}{\partial t} + T \frac{\partial \rho}{\partial t} + \alpha_{\text{imp}} T \frac{\partial \rho_{\text{imp}}}{\partial t} \\ \nabla p &= \tilde{\rho} \nabla T + T \nabla \rho + \alpha_{\text{imp}} T \nabla \rho_{\text{imp}} \end{aligned} \quad (5.4)$$

where,

$$\tilde{\rho} = \left(\rho + \alpha_{\text{imp}} \rho_{\text{imp}} + \rho_{\text{imp}} T \frac{\partial \alpha_{\text{imp}}}{\partial T} \right)$$

Using Eq. (5.4) into (5.3),

$$\begin{aligned} & \frac{\partial p}{\partial t} + \mathbf{v} \cdot \nabla p + \gamma p \nabla \cdot \mathbf{v} + (\gamma - 1) \frac{\rho_{\text{imp}}}{\tilde{\rho}} \frac{\partial E_{\text{ion}}}{\partial T} \left(\frac{\partial p}{\partial t} + \mathbf{v} \cdot \nabla p \right) \\ & - (\gamma - 1) \frac{\rho_{\text{imp}}}{\tilde{\rho}} T \frac{\partial E_{\text{ion}}}{\partial T} \left(\frac{\partial \rho}{\partial t} + \mathbf{v} \cdot \nabla \rho \right) \\ & - (\gamma - 1) \frac{\rho_{\text{imp}}}{\tilde{\rho}} \alpha_{\text{imp}} T \frac{\partial E_{\text{ion}}}{\partial T} \left(\frac{\partial \rho_{\text{imp}}}{\partial t} + \mathbf{v} \cdot \nabla \rho_{\text{imp}} \right) = R_p \end{aligned}$$

and further using equations of ρ and ρ_{imp} in the pressure equation:

$$\begin{aligned} & \left(1 + (\gamma - 1) \frac{\rho_{\text{imp}}}{\tilde{\rho}} \frac{\partial E_{\text{ion}}}{\partial T} \right) \left(\frac{\partial p}{\partial t} + \mathbf{v} \cdot \nabla p \right) \\ & + \left[\gamma + (\gamma - 1) \frac{\rho_{\text{imp}}}{p} \left(\frac{T \rho}{\tilde{\rho}} \frac{\partial E_{\text{ion}}}{\partial T} + \frac{T \alpha_{\text{imp}} \rho_{\text{imp}}}{\tilde{\rho}} \frac{\partial E_{\text{ion}}}{\partial T} \right) \right] p \nabla \cdot \mathbf{v} = R_p \end{aligned}$$

where, rest of the terms in ρ and ρ_{imp} equations are absorbed into R_p . Therefore, the pressure equation is written in compact notation as:

$$\frac{\partial p}{\partial t} + \mathbf{v} \cdot \nabla p + \tilde{\gamma} p \nabla \cdot \mathbf{v} = R_p$$

where

$$\tilde{\gamma} = \frac{\gamma + (\gamma - 1) \frac{\rho_{\text{imp}}}{p} \left(\frac{T \rho}{\tilde{\rho}} \frac{\partial E_{\text{ion}}}{\partial T} + \frac{T \alpha_{\text{imp}} \rho_{\text{imp}}}{\tilde{\rho}} \frac{\partial E_{\text{ion}}}{\partial T} \right)}{1 + (\gamma - 1) \frac{\rho_{\text{imp}}}{\tilde{\rho}} \frac{\partial E_{\text{ion}}}{\partial T}}$$

This analysis suggests that the sound speed in the plasma changes due to the presence of impurities and becomes:

$$c_s^2 = \frac{\tilde{\gamma} p}{\rho}$$

Therefore, a simplified VMS stabilization (Eq. (3.16)) that focuses only on the acoustic waves should take into account the contribution in the pressure due to impurities as well. The stabilization terms added in the velocity equation then takes the form:

$$\mathbf{d}_v = k_c \frac{\gamma p}{\rho} (\nabla \cdot \mathbf{v}^*) (\nabla \cdot \mathbf{v})$$

where, p is the total pressure. The constant stabilization coefficient is specified as $k_c = 10^{-6}$. Since the stabilization term will be effective only when the divergence of \mathbf{v} is high, the grid (h_e) dependence of the stabilization coefficient is ignored.

Boundary conditions

Boundary conditions at the divertor enforces the Mach 1 flow of the plasma as described in Section (4.2) . Rewriting the total pressure as:

$$p = \left(1 + \alpha_{\text{imp}} \frac{\rho_{\text{imp}}}{\rho} \right) \rho T \quad (5.5)$$

The term in the bracket is a factor that arises due to the presence of impurities and needs to be accounted for in the boundary conditions at the divertor. The ratio of atomic mass of an ion and Ne atom is roughly $1/20$ and Z_{imp} for Ne ranges in between 1 to 10. An approximate estimate can be made for α_{imp} based on

$$\alpha_{\text{imp}} = \frac{1}{2} \frac{m_i}{m_{\text{imp}}} (Z_{\text{imp}} + 1) - 1$$

and it can be seen that α_{imp} takes values in between $-19/20$ and $-29/40$. For simplicity, the average value of these two limits $-67/80$ is used to update the boundary conditions for the presence of the impurities such that the pressure at the divertor is written as:

$$p = \left(1 - \frac{67}{80} \frac{\rho_{\text{imp}}}{\rho} \right) \rho T$$

Ideally, the definition (5.5) needs to be implemented in the boundary conditions which, in practice, will require computation of α_{imp} and therefore calling CE and openADAS routines in the subroutine of boundary conditions. This implementation will be beneficial if one uses high values of D_{\parallel} which transports impurities fast up to the divertors causing high values of ρ_{imp} at the divertors. When D_{\parallel} is not used, the simplification of using average value is reasonable since low ρ_{imp} values are observed at the divertors.

Effect of resistivity in poloidal equations

The SPI simulation shown in previous section uses resistivity only in A_3 equation which resulted in large variations in I_p . The rationale behind using the resistivity only in A_3 equation was that the MHD dynamics is assumed to be dominated by this equation. In this subsection the effect of suppressing η from A_R and A_Z equations is discussed. The coarse grid used for the simulation presented in the previous section is used again to run the two cases with the temperature dependent resistivity with the values at the magnetic axis as:

- $\eta_0 = 10^{-8}$ in all A_R , A_Z and A_3 equations.
- $\eta_0 = 10^{-10}$ in A_R and A_Z equations while $\eta_0 = 10^{-8}$ in A_3 equation.

The other physical parameters used are as follows:

- The temperature dependent viscosity coefficient with the value at the magnetic axis $\mu = 10^{-6}$.
- The particle diffusion coefficients $D_{\parallel} = D_{\perp} = 5 \times 10^{-5}$ in both density equations.
- The perpendicular heat conductivity is specified as $\kappa_{\perp} = 2 \times 10^{-5}$ while the temperature dependent parallel conductivity is specified with the value at the magnetic axis as $\kappa_{\parallel 0} = 4000$.

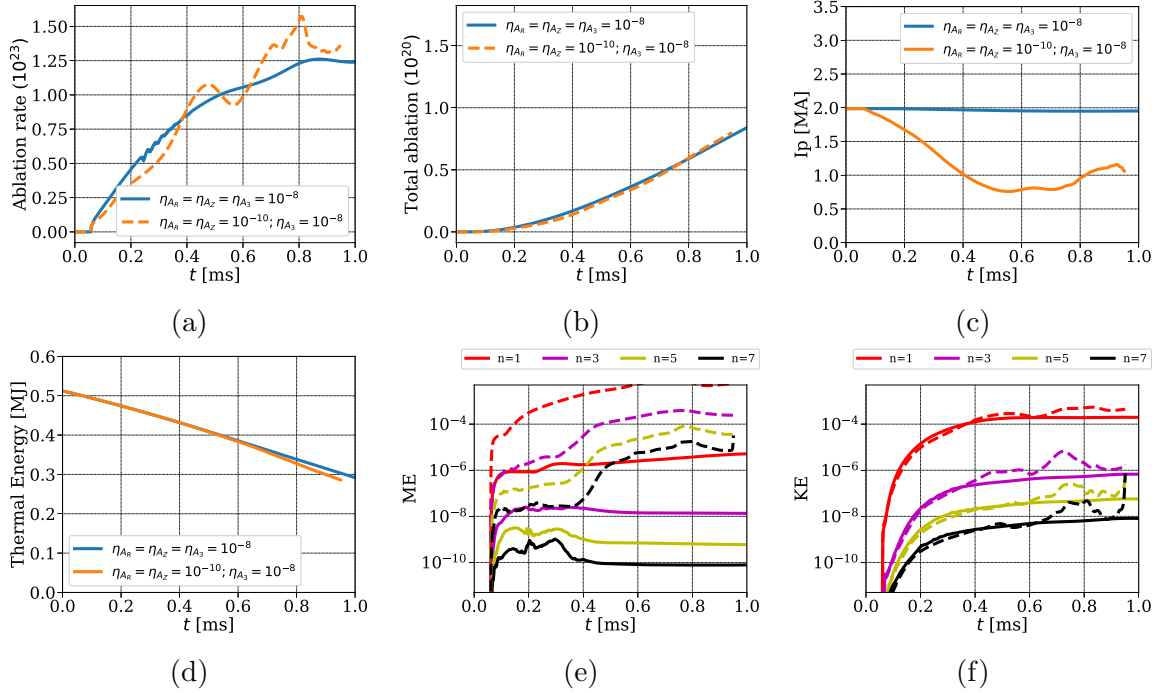


Figure 5.11: Effect of η in A_R and A_Z equations: (a) ablation rates (b) Total impurities injected (c) plasma current I_p (d) plasma thermal energy (e) magnetic energies (ME) (f) kinetic energies (KE). For ME and KE solid lines denote the energies obtained using the same value of η in all equations A_R , A_Z and A_3 . While, dashed lines denote the energies obtained by the use of smaller value of η in A_R and A_Z equation.

Figure (5.11) shows the comparison of ablation rates, total impurities injected, I_p , plasma thermal energy, magnetic and kinetic energies for the two cases. Removing or suppressing η in A_R and A_Z affects the numerical solution greatly. The use of the

smaller value of η in A_R and A_Z makes the dynamics faster which causes I_p to change significantly. It also causes A_3 to change dramatically as can be seen Figure (5.7).

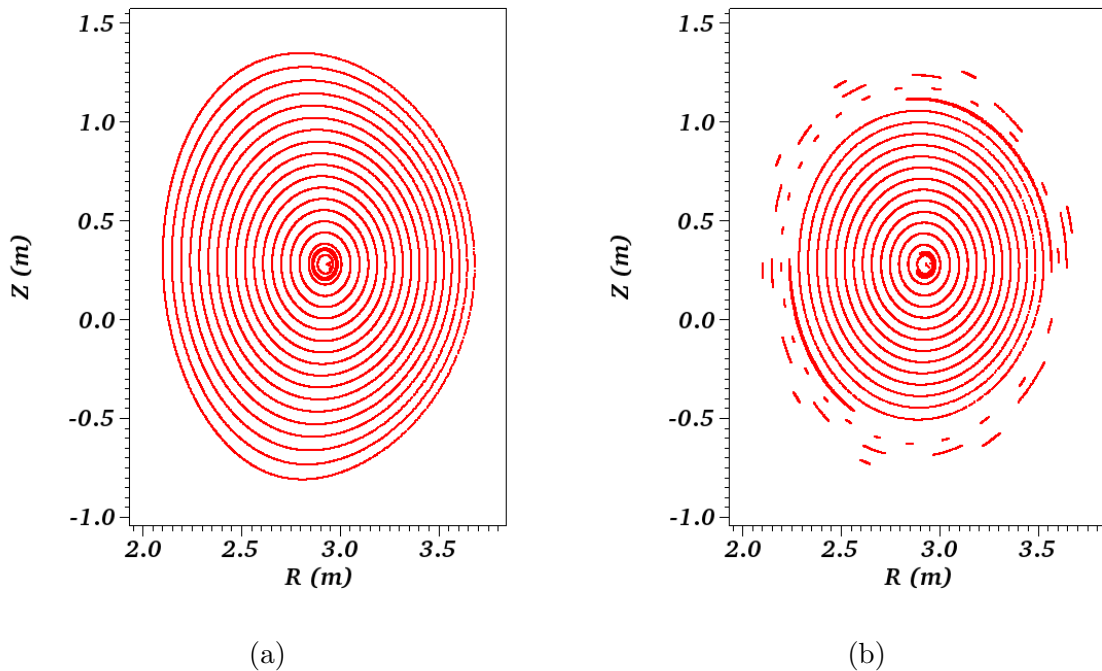


Figure 5.12: Poicaré plots of the magnetic field at $t = 0.94$ ms showing effect of η in A_R and A_Z equations.

The use of the smaller value of η in A_R and A_Z equations triggers the MHD instabilities which can be seen from the evolution of the magnetic and kinetic energies in Figure (5.11). The magnitude of magnetic energies are much lower for the simulation with the same value of η used in all three equations. The effect is also seen in the kinetic energies at later times. Suppression of η from A_R and A_Z destabilizes the MHD modes and may trigger disruptions. For this case, the plasma thermal energy plotted in (5.11d) starts to decrease from $t \approx 0.8$ ms. This is the result of the stochasticization of the magnetic field in the outer layer of plasma as seen in Figure (5.12b), where the magnetic island associated with 2/1 mode is also seen. MHD instabilities and stochasticization of the magnetic field are not seen in the simulation where $\eta = 10^{-8}$ in all three equations (Figure (5.12a)).

Therefore, the assumption that MHD dynamics is dominated by the A_3 equation seems not valid, at least for the resistivities of the order 10^{-8} which are practically relevant. Henceforth, the same value of the resistivity is added in all three equations for A_R , A_Z and A_3 . In contrast, the poloidal resistivities (those in A_R and A_Z equations) should be higher than the toroidal resistivity [15] which may be a step

towards more realistic simulations in future.

Scan in resistivity

In this subsection the scan over η is performed. The grid used is as described above with $n_\psi = 51$ and $n_\theta = 64$. The SPI parameters used are described in previous section and the numerical results are shown for $\eta = 10^{-6}, 10^{-7}$ and 10^{-9} . The other physical parameters used are as follows:

- The coefficient of viscosity: $\mu = 10^{-6}$.
- The particle diffusion coefficients $D_{\parallel} = 0$ and $D_{\perp} = 10^{-5}$ in both total and impurity density equations.
- The coefficients of heat conductivities are specified as $\kappa_{\perp} = 5 \times 10^{-6}$ and $\kappa_{\parallel} = 4000$.

The use of the temperature dependence in the resistivity leads to the high values and sharp gradients in η field near the edge. Such regions are found to be numerically unstable for the resistivities specified by $\eta_0 \geq 10^{-7}$. Hence, the temperature dependence on η is removed from the simulations with $\eta_0 \geq 10^{-7}$. Similarly, the viscosity coefficient is also kept independent of the temperature. The reason being, at the divertors low temperatures results in high viscosity coefficients that destabilize the viscous heating term.

These simulations with different values of η are run until approximately 1 ms. The ablation rates and the number of impurity particles ablated do not depend significantly upon the resistivity as can be seen in Figure (5.13). The similar observation is made for plasma current I_p and the plasma thermal energy. The simulation with $\eta = 10^{-9}$ uses temperature as well as Z_{eff} dependent resistivity (in all three A_R , A_Z and A_3 equations). Therefore, as Z_{eff} in plasma domain increases the resistivity also increases which may explain the drop in I_p . Figure (5.14) shows the ratio of the resistivity at $t \approx 0.72$ and $t \approx 0.057$ ms and it can be seen that the resistivity becomes almost twice in the layer where Z_{eff} values are higher than 1. The sharp peak in the ratio is seen at the location of SPI injection where T drops down significantly. Magnetic energies increase with the decrease in η (Figure (5.13e)), while no significant effect of the resistivity is seen on the kinetic energies, until $t = 1$ ms.

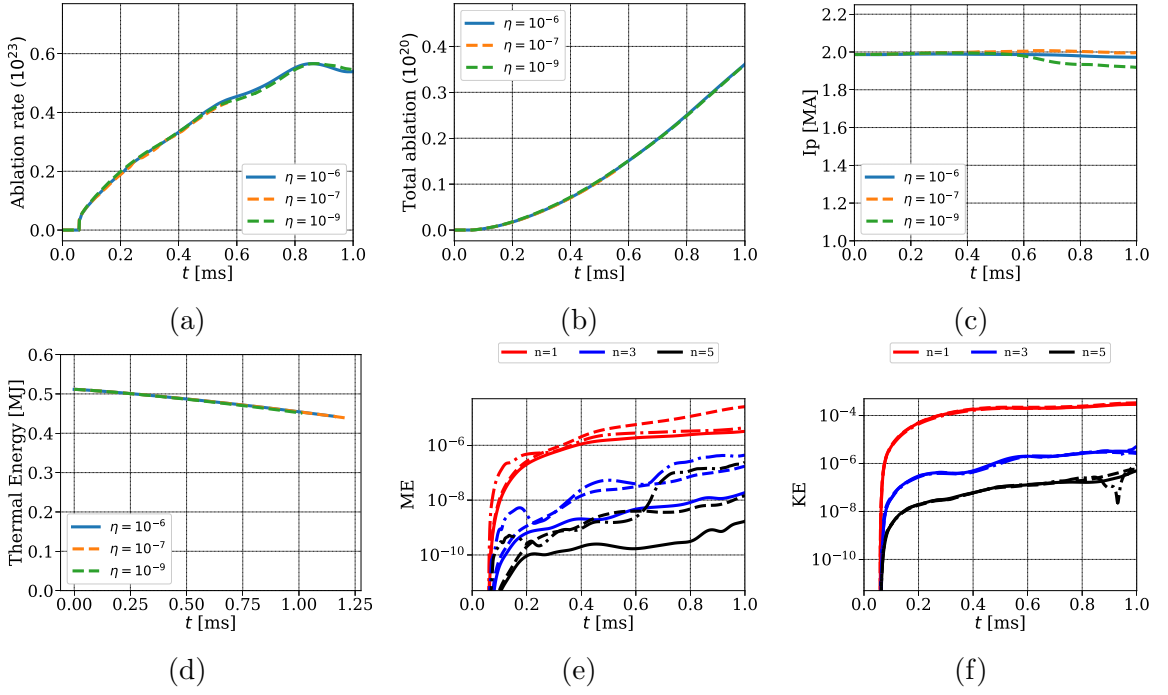


Figure 5.13: Effect of η on SPI simulations: (a) ablation rates (b) Total impurities injected (c) plasma current I_p (d) plasma thermal energy (e) magnetic energies (ME) (f) kinetic energies (KE). For ME and KE solid lines, dashed lines and dotted-dashed lines denote the energies obtained using $\eta = 10^{-6}, 10^{-7}$ and 10^{-9} .

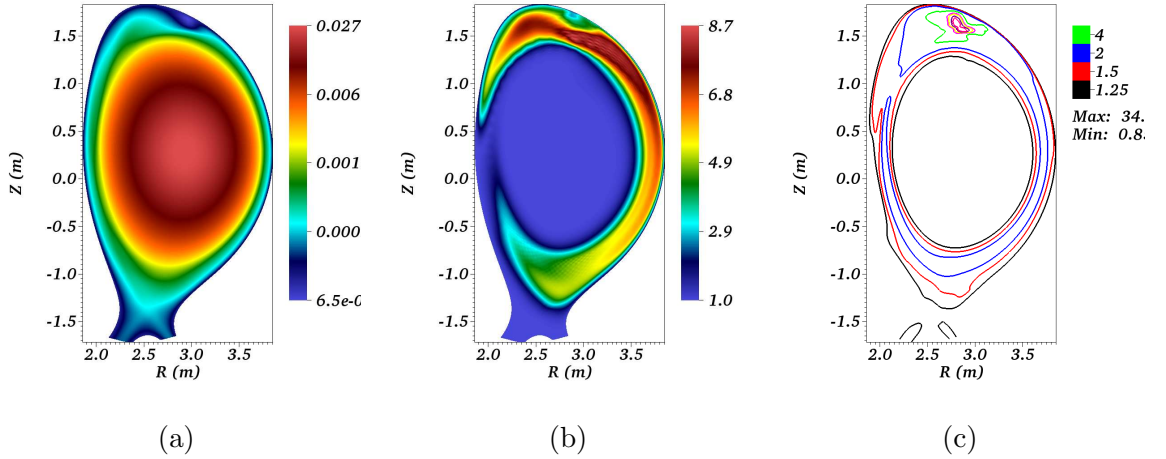


Figure 5.14: Effect of T and Z_{eff} dependence on the resistivity (a) T (in normalized units) plotted in log scale at $t \approx 0.72$ ms (b) Z_{eff} plotted at $t \approx 0.72$ ms (c) ratio of resistivities (in normalized units) $\eta(t \approx 0.72)/\eta(t \approx 0.057)$

Summarizing, in the early stages of SPI simulations physics is not effected by the resistivities significantly. In order to incorporate the dynamics due to the temperature and Z_{eff} dependent resistivity, smaller values of the resistivities (than 10^{-7} in

normalized units) should be considered which are also practically relevant values of η .

Grid convergence

SPI simulations are run with the constant resistivity $\eta = 10^{-7}$ on the series of 5 grids described in Table (5.1). The simulation on the last grid uses the number of toroidal harmonics $n = 0, 1, \dots, 12$ as opposed to first four that use $n = 0, 1, \dots, 7$. The emphasis is given to the refinement in the azimuthal (θ) direction since the convection in azimuthal direction is observed as SPI fragments penetrates in plasma.

Grid #	n_ψ	n_θ	n	N_p
Grid 1	51	64	7	32
Grid 2	71	100	7	32
Grid 3	71	128	7	32
Grid 4	71	151	7	32
Grid 5	71	151	12	64

Table 5.1: A series of grids used for SPI simulation with constant $\eta = 10^{-7}$. Here, n_ψ and n_θ denotes the number of points in radial and azimuthal direction respectively. n denotes the number of toroidal harmonics added in the simulations and N_p denotes the number of equidistant planes in the toroidal direction which needs to be chosen for FFT implementation.

The other physical parameters used are as follows:

- The constant viscosity coefficient is set to $\mu = 10^{-6}$.
- The particle diffusion coefficients are specified as $D_{\parallel} = 0$ and $D_{\perp} = 10^{-5}$ for both the total and impurity densities.
- The perpendicular heat conductivity is specified as $\kappa_{\perp 0} = 5 \times 10^{-6}$ and temperature dependent parallel heat conductivity with $\kappa_{\parallel 0} = 4000$.

Figure (5.15a) shows physical times until which the simulations are run. A typical simulation is started with the time step of $\Delta t = 5$ normalized units from the beginning of the injection. As fragments move inside the plasma core and reach the rational

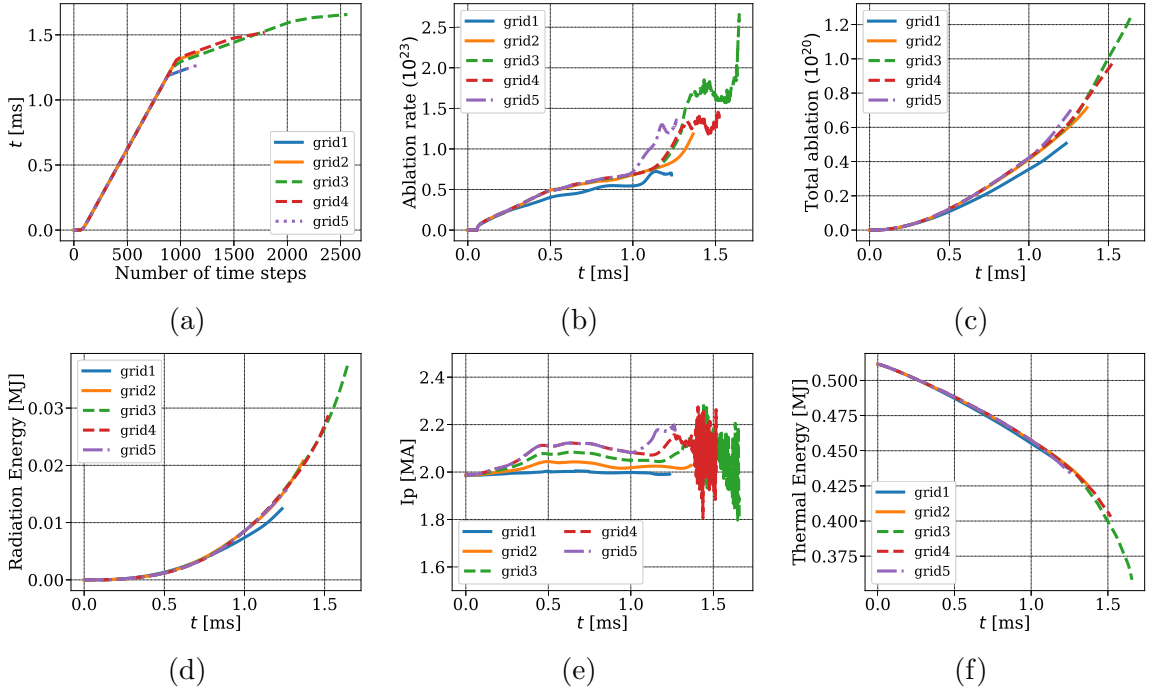


Figure 5.15: SPI simulations run on a series of grids for $\eta = 10^{-7}$ (a) physical time for which simulation is run (b) ablation rates (c) total impurities injected (d) radiation energy (e) plasma current I_p (f) plasma thermal energy.

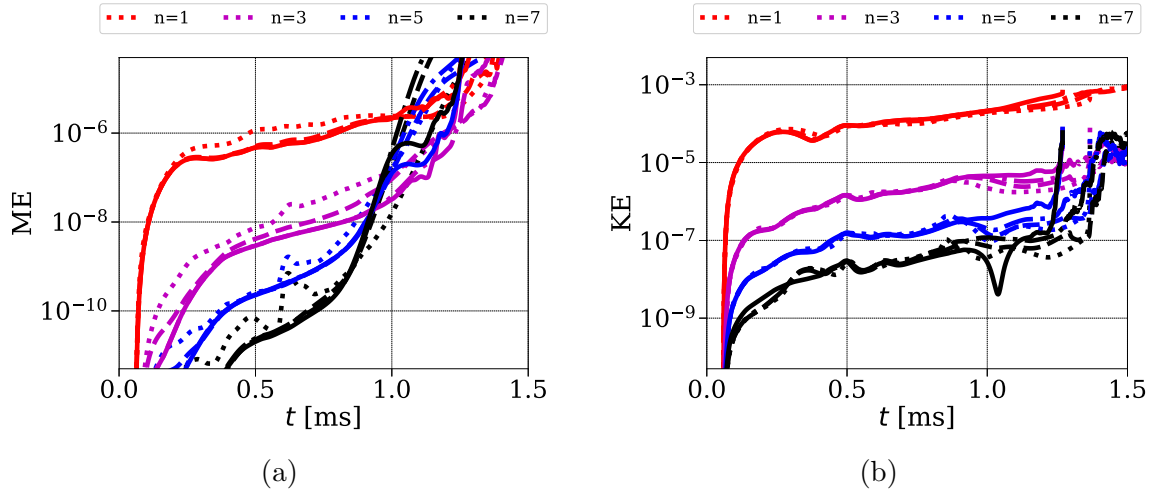


Figure 5.16: SPI simulations run on a series of grids for $\eta = 10^{-7}$ (a) magnetic energies (b) kinetic energies. Dotted, dashed, dashed-dotted and solid lines represents energies plotted for grid 2, 3, 4 and 5 respectively.

q surfaces, the convection of impurities in the azimuthal direction is observed. This plasma dynamics occurs on smaller time scales and hence the time steps need to be reduced otherwise a linear solver fails to converge. This can be seen in the Figure

(5.15a) that in each simulation the time step has been reduced before the onset of the convection in θ direction. Although initially the ablation rates are almost the same in each simulation, it is found to be highly dependent on the grid in later stages as can be seen in Figure (5.15b). The coarse grid (Grid1) underestimates the ablation rate. This may be due to the extra stabilization effect produced by the physical diffusivities (resistivity, particles diffusion and heat conductivity) on the coarser grids that underestimates the temperatures and densities in the region of fragments, which further underestimates the ablation rates. Later in the simulations, the ablation rates obtained are higher for the finer grids and consequently the larger number of impurity particles are deposited in the plasma which is seen Figure (5.15c).

No significant effect of the grid refinement is seen on the radiation and thermal energies which can be seen in Figure (5.15d) and (5.15f). Figure (5.15e) shows the plasma current evolution obtained with all grids for which a convergence behavior is seen at initial times. A correlation between ablation rate and plasma current is seen such that, the ablation rate and I_p both increase with the grid refinement. On the most refined grid, I_p begins to deviate from $t \approx 1$ ms and at the same time increase in the ablation rate is also observed. Such increase in the ablation rates occur earlier with the grid refinement and is associated with the growth of magnetic energies. The magnetic energies on the finer grids grow rapidly as seen in Figure (5.16a). After certain time, the magnetic energies of the higher toroidal harmonics dominates the energies of the lower harmonics and oscillations are seen in the I_p and the ablation rates. This behavior indicates the need of the numerical stabilization of the magnetic field. Figure (5.16b) shows the evolution of the kinetic energies on the series of grids which do not show significant difference, indicating that the hydrodynamic part of the model is well resolved.

Finally the comparison of Poincaré plots is shown in Figure (5.30) for Grid 2, 3, 4 and 5, approximately at the same physical times. On Grid 5 the formation of a stochastic layer near the edge of the plasma is seen at $t = 1.262$ ms whereas with all other grids there is no sign of stochastization even at later physical time instants. As ablation rate begins rise later with the first four grids, the outer layer of the plasma also becomes stochastic later in time (not shown here).

The grid convergence is seen in SPI simulation however, a rapid growth in the magnetic energies highlight the of stabilization of the magnetic field. The lack of temperature and Z_{eff} dependence of the resistivity cannot take into account the the increase in the resistivity due to plasma cooling and increase in Z_{eff} due to SPI.

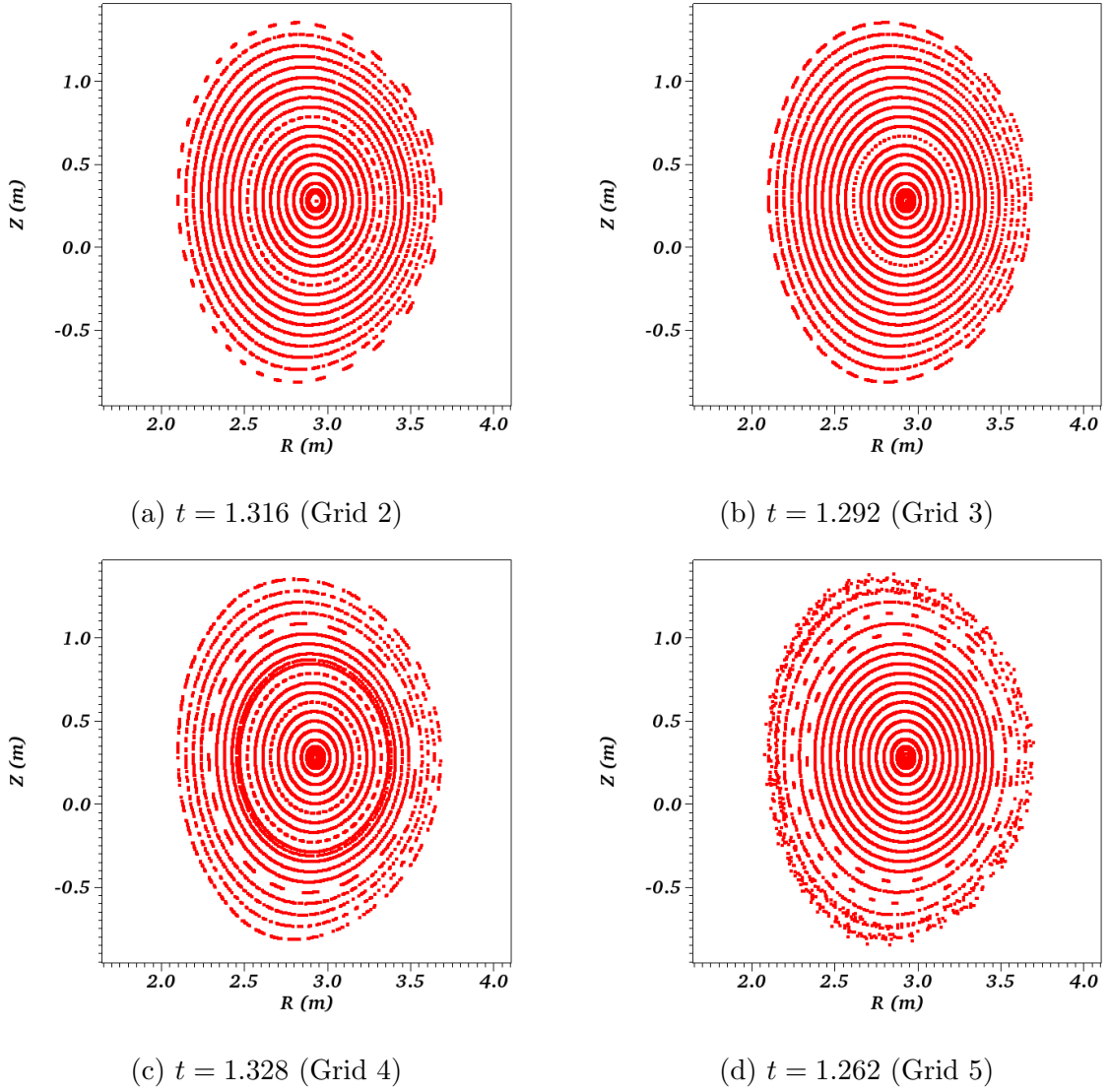


Figure 5.17: Poincaré plots of the magnetic field plotted for the simulation with $\eta = 10^{-7}$ at the mentioned time instants and grids.

Effect of the particle diffusion

On the grid with $n_\psi = 71$ and $n_\theta = 100$ and with the toroidal harmonics included from $n = 0$ to 7, following simulations are run to see the effect of D_\perp :

- $D_\perp = 10^{-5}$ with the time step $\Delta t = 5$
- $D_\perp = 2 \times 10^{-5}$ with $\Delta t = 5$
- $D_\perp = 2 \times 10^{-5}$ with $\Delta t = 2$

A constant reactivity with $\eta_0 = 10^{-7}$ is specified along with the constant viscosity coefficient $\mu = 10^{-6}$. The heat conductivities are specified as $\kappa_{\perp 0} = 5 \times 10^{-6}$ and temperature dependent κ_{\parallel} with $\kappa_{\parallel 0} = 4000$.

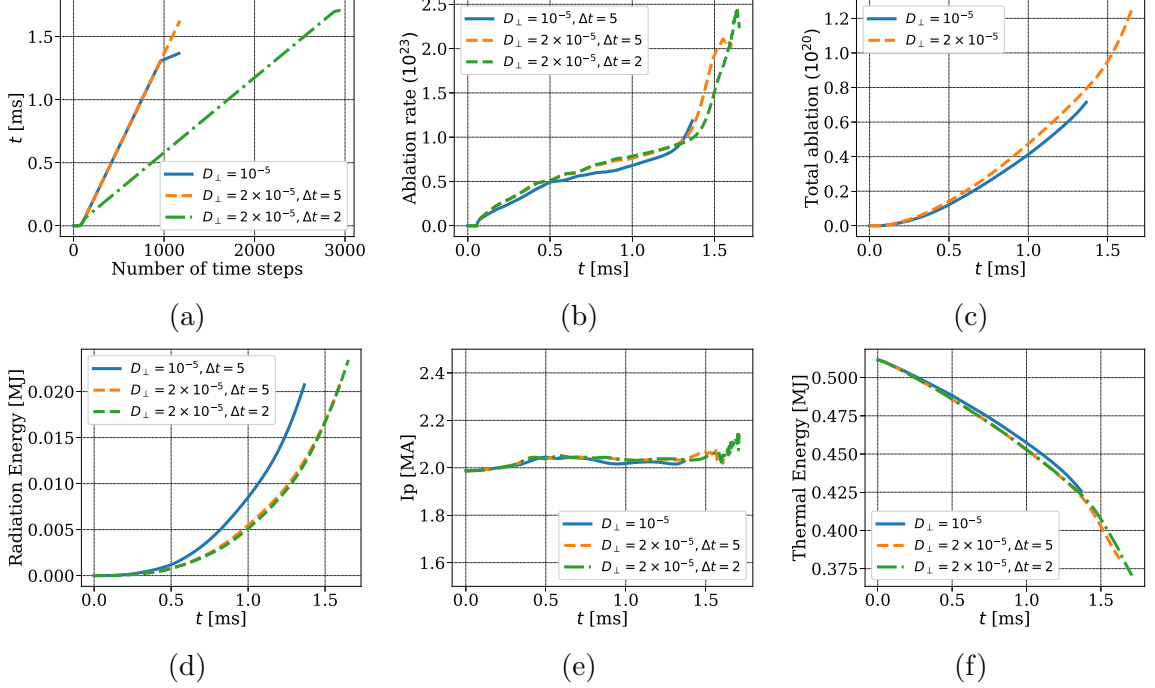


Figure 5.18: SPI simulations to show effect of D_{\perp} with $\eta = 10^{-7}$ (a) physical time for which simulation is run (b) ablation rates (c) total impurities injected (d) radiation energy (e) plasma current I_p (f) plasma thermal energy.

Figure (5.18a) shows the physical time for which simulations are run vs number of time steps. The simulation with $D_{\perp} = 2 \times 10^{-5}$ runs for longer physical times than that with $D_{\perp} = 10^{-5}$. Although higher ablation rates are obtained with $D_{\perp} = 2 \times 10^{-5}$, the number of impurities deposited and the radiation energy obtained are lower than that with $D_{\perp} = 10^{-5}$ as can be seen in Figure (5.18). The evolution of plasma current I_p obtained is almost the same in all cases (Figure (5.18e)). As expected the thermal energies are higher with $D_{\perp} = 10^{-5}$. Since the simulations with $D_{\perp} = 2 \times 10^{-5}$ run for longer physical times, the SPI fragments penetrate further into plasma and starts cooling effect. This can be seen via faster decrease in thermal energies near $t = 1.5$ ms.

With the large time step the ablation rate is higher and hence the amount of impurities deposited. A higher ablation rate results into slightly faster decrease in thermal energies as seen in Figure (5.18). The comparison of the magnetic and kinetic energies for the toroidal harmonics $n = 1, 3, 5$ and 7 is shown in Figure (5.19).

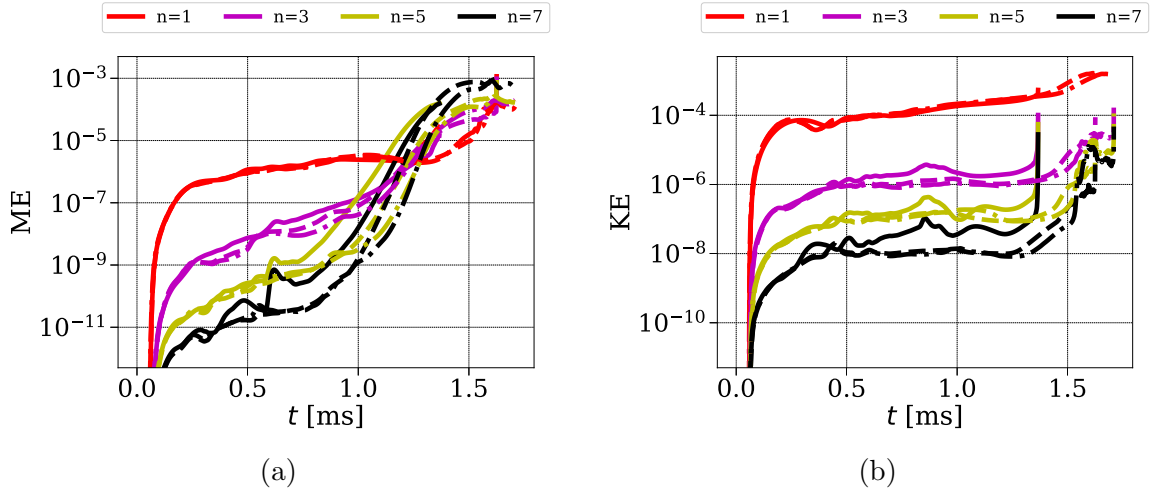


Figure 5.19: SPI simulations to show effect of D_{\perp} with $\eta = 10^{-7}$ (a) magnetic energies (b) kinetic energies. Solid, dashed and dashed-dotted lines represents energies plotted for the simulations ($D_{\perp} = 10^{-5}, \Delta t = 5$), ($D_{\perp} = 2 \times 10^{-5}, \Delta t = 5$) and ($D_{\perp} = 2 \times 10^{-5}, \Delta t = 2$) respectively.

The rise in ablation rate is associated with the rise in magnetic energies as seen in Figure (5.19a) which again highlights the need of stabilization of the magnetic field. The kinetic energies are smaller for $D_{\perp} = 2 \times 10^{-5}$ which is expected due to the stabilization provided by larger particle diffusion. With the smaller time step no significant difference is seen in the kinetic energies.

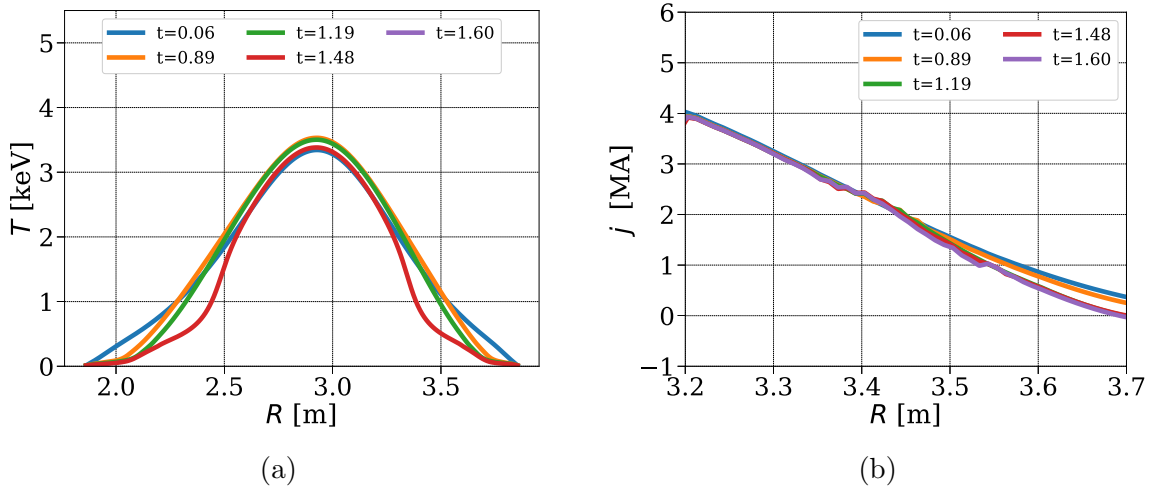


Figure 5.20: SPI simulations to show effect of D_{\perp} with $\eta = 10^{-7}$ (a) T (b) $j = -R j_{\phi}$ plotted at midplane vs R for ($D_{\perp} = 2 \times 10^{-5}, \Delta t = 2$).

In Figure (5.20), T and $j = -R j_{\phi}$ profiles are plotted at the midplane at different time instants for the simulation with $\Delta t = 2$. The cooling of plasma is seen

in the outer layer of plasma. The current profiles do not change significantly and current contraction is not prominently seen. As temperature profiles go down in the outer layer, the current profiles also go down. Ideally, these simulations may be pushed forward in physical time by further reducing time steps and/or by the use of stabilization. The purpose of this exercise was to show effect of D_{\perp} .

It is found that use of the smaller values of D_{\perp} than 10^{-5} needs restrictive time steps and higher grid resolution. For the grids used in this work 10^{-5} seems the lower limit of the D_{\perp} that can be used.

Effect of numerical stabilization

Although the numerical stabilization based on the acoustic waves is added in all the simulations, we now present the effect of the simplified VMS stabilization based on convective terms. The VMS stabilization is supposed to account the effect of the unresolved scales and hence the comparison performed between the simulation with the stabilization and the simulation without stabilization but on the finer grid in the θ direction. The details of the two simulations are as follows:

- sim1 : Simplified VMS stabilization based on the convective terms (equation (3.16)) is used in the simulation on the grid with $n_{\psi} = 71$ and $n_{\theta} = 100$ along with the acoustic wave stabilization. The stabilization matrix is specified as:

$$\underline{\mathbf{T}} = 10^{-2} \frac{h_e}{\lambda_{\max}} \mathbb{I}$$

- sim2 : Only simplified stabilization based on the acoustic wave is added on the finer grid in the poloidal plane with $n_{\psi} = 71$ and $n_{\theta} = 128$. In this case, the stabilization is added in the velocity equation with the stabilization coefficient specified as 10^{-6} .

Both simulation are run with the toroidal harmonics $n = 0, 1, \dots, 7$. The physical parameters used for these simulations are as follows:

- The temperature and Z_{eff} dependent resistivity is used with $\eta_0 = 10^{-8}$ (in all three A_R , A_Z and A_3 equations).
- The constant viscosity coefficient $\mu = 10^{-6}$ is used.

- The coefficient of the density diffusion $D_{\perp} = 2 \times 10^{-5}$ is used while the D_{\parallel} is set to 0 in both the density equations.
- The perpendicular heat conductivity are specified as $\kappa_{\perp} = 5 \times 10^{-6}$ and the temperature dependent parallel conductivity with $\kappa_{\parallel 0} = 4000$.

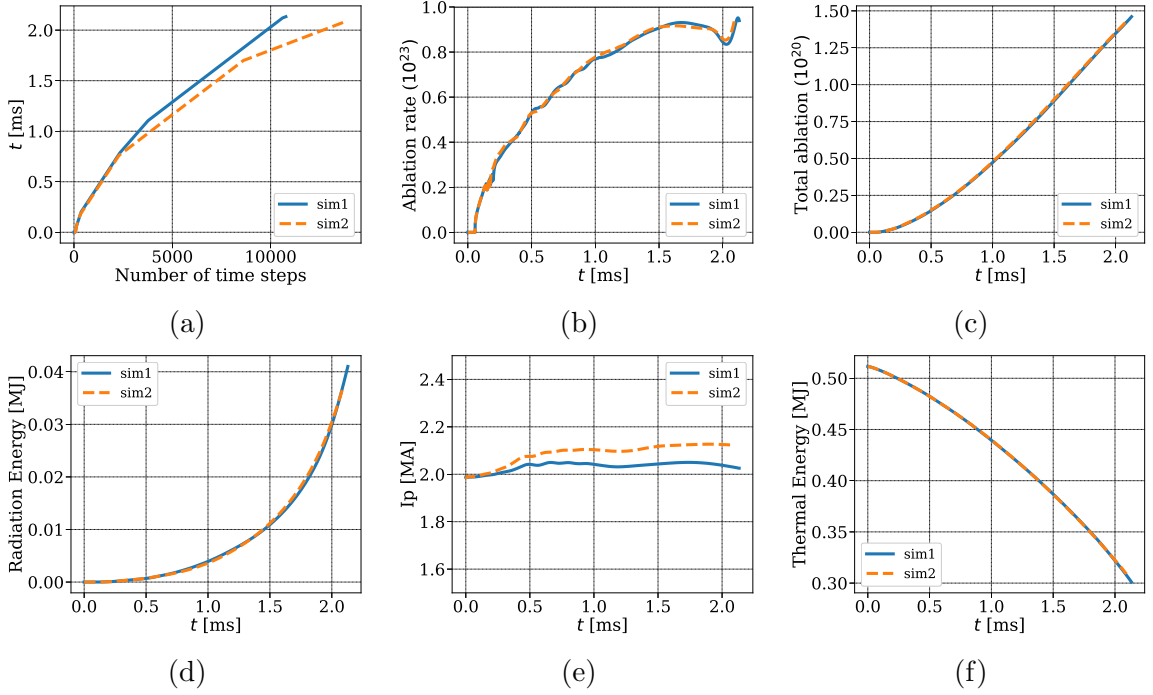


Figure 5.21: SPI simulations to show effect of the numerical stabilization : (a) physical time for which simulation is run (b) ablation rates (c) total impurities injected (d) radiation energy (e) plasma current I_p (f) plasma thermal energy.

Figure (5.21a) show that both simulations have been run approximately until same physical time. The finer grid demands smaller time steps and hence needs more number of time steps to reach the same physical time. Change in slopes in Figure (5.21a) denote the reduction in the time steps. The ablation rate, number of impurities injected, radiation energy and thermal energy obtained are almost the same in the two simulations (Figure (5.21)). The evolution of the kinetic energy is also comparable for the two simulations as can be seen in Figure (5.22b), except that the kinetic energy of $n = 7$ is lower because of the use of the numerical stabilization.

The evolution of the plasma current I_p obtained with ‘sim1’ is different than that with ‘sim2’ (Figure (5.21e)). This is the effect of the different grid resolutions as discussed in the subsection on grid refinement. The magnetic energies of lower harmonics are comparable while the distinct effect of the stabilization is seen in the

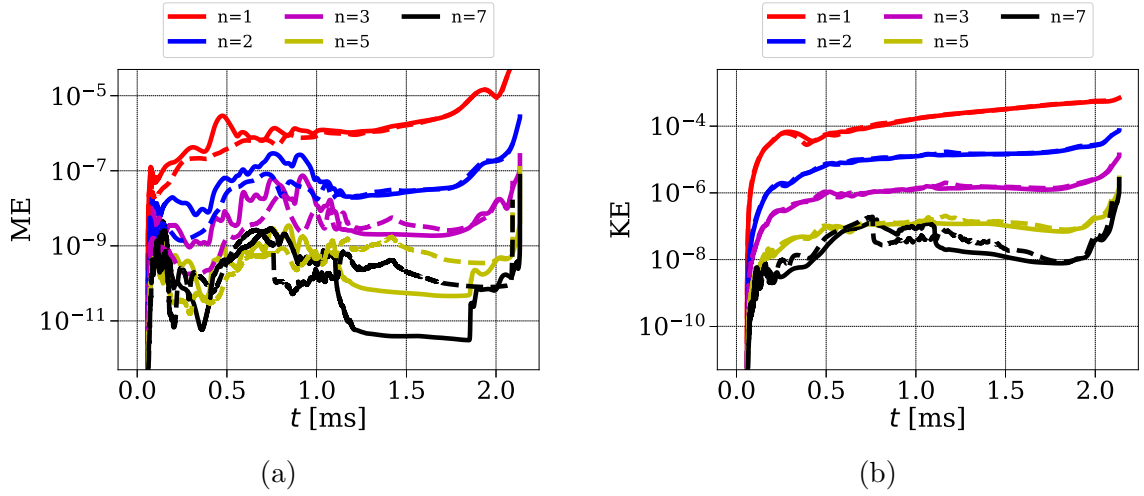


Figure 5.22: SPI simulations to show effect of the numerical stabilization (a) magnetic energies (b) kinetic energies. Solid and dashed represents energies plotted for the sim1 and sim2 respectively.

energies of the higher harmonics (5.22a). For example the magnetic energy of $n = 7$ is lowered by the order of 10 due to the stabilization.

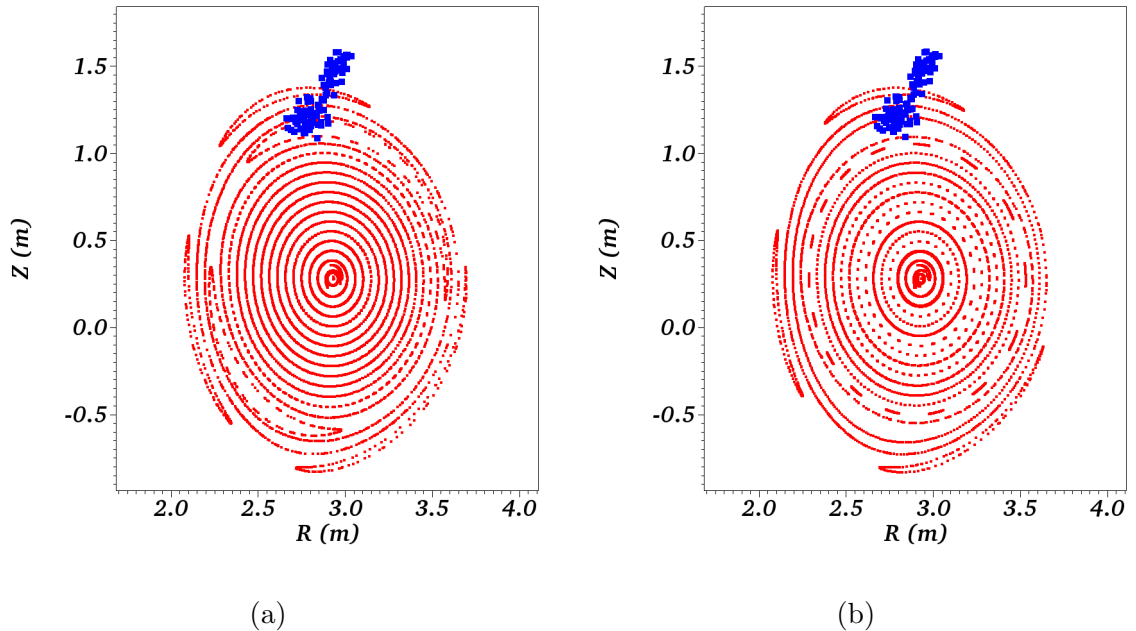


Figure 5.23: SPI simulations to show effect of the numerical stabilization. Poincaré plots shown for (a) sim1 at $t = 2.118$ ms and for (b) sim2 at $t = 2.088$ ms.

Figure (5.23) shows Poincaré plots obtained using two simulations where the similarity of the MHD dynamics obtained is seen. The blue dots show the position of SPI fragments in the plasma. Poincaré plot for 'sim1' is shown at $t = 2.118$ ms (Figure

(5.23)) where the magnetic island associated with 3/1 and 2/1 modes can be seen. Poincaré plot for ‘sim2’ also shows the growth of 3/1 mode and the onset of 2/1 mode as it is slightly behind in the physical time. The signature of 1/1 mode is also seen near the magnetic axis however, the mode does not grow significantly until the simulations have been run.

This exercise shows that the use of the numerical stabilization formulated here does not alter the physics. The stabilization terms used in the induction equation are not however adequate to stabilize the magnetic energies. This is because the terms containing the current in VMS stabilization are ignored as the second derivatives with respect to ϕ are not yet implemented in JOREK via DFT. Use of the stabilization of the magnetic fields is the scope for the future work and may help push simulations until thermal quench as observed in [49]. Following we present the simulation with high value of the particle diffusion in order to simulate SPI for longer physical times that helps to capture a pre-TQ physics.

Pre-thermal quench

This simulation is run for longer physical time than the previous runs and the physical parameters specified are:

- To be able to use the temperature dependent resistivity, the resistivity is chosen with $\eta_0 = 10^{-8}$ (in all three A_R , A_Z and A_3 equations).
- The constant viscosity coefficient $\mu = 10^{-6}$ is used.
- The perpendicular density diffusivity is specified as $D_{\perp} = 5 \times 10^{-5}$ while the parallel diffusivity D_{\parallel} is set to 0 in both the density equations. This value of D_{\perp} is higher than the previous runs and adds the stabilization effect allowing larger time steps.
- The perpendicular heat conductivity are specified as $\kappa_{\perp} = 10^{-6}$ and the temperature dependent parallel conductivity with $\kappa_{\parallel 0} = 4000$.
- The grid is built with $n_{\psi} = 71$ and $n_{\theta} = 100$ points and the number of toroidal harmonics used are $n = 0, 1, \dots, 7$.

The simulation runs until $t \approx 2.4$ ms and at the beginning of SPI the time step used is $\Delta t = 2$ (in normalized units) which is reduced by the factor of 2 in 4 steps whenever

the linear solver fails to converge. The ablation rate, total impurities ablated and radiation energy obtained are shown in Figure (5.24). The ablation rate rises rapidly at the end of the simulation where magnetic and kinetic energies also rise rapidly (Figure (5.29)). The plasma current I_p do not vary significantly over the time but starts to decrease after 2 ms (Figure (5.24d)). The thermal energy decreases steadily but does not show any sign of TQ (Figure (5.24e)). The temperature at the magnetic axis rises until almost $t \approx 1.75$ and then decreases (Figure (5.24f)).

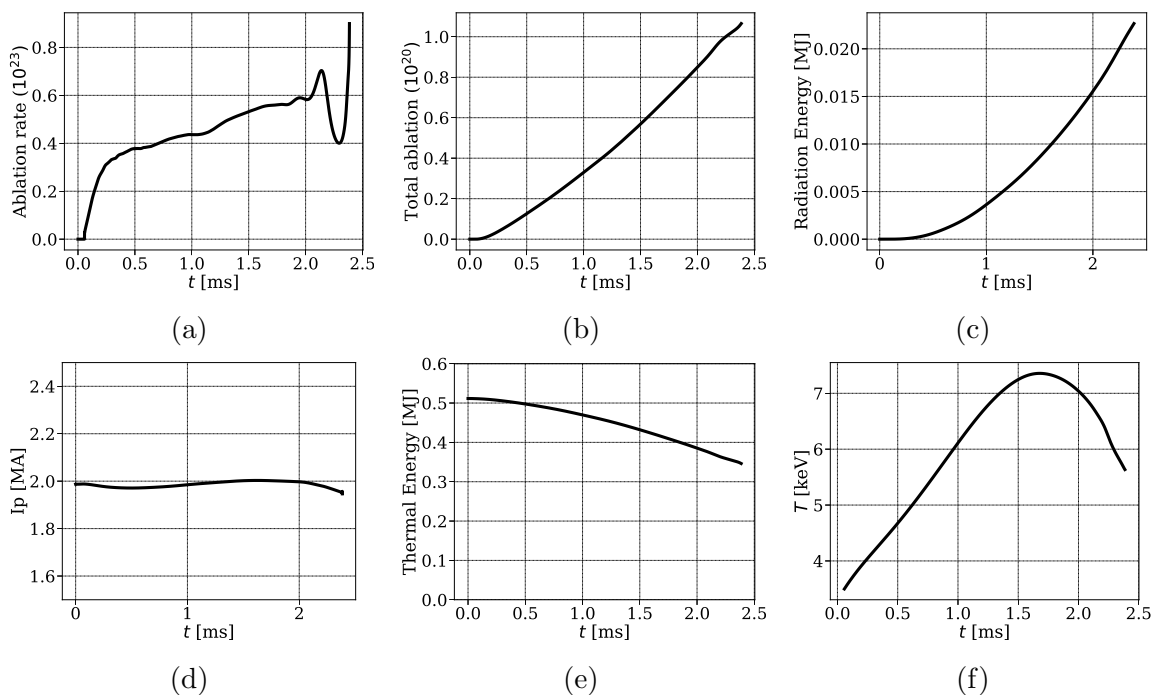


Figure 5.24: SPI simulation with $\eta = 10^{-8}$: (a) The ablation rates (b) total impurities injected (c) radiation energy (d) plasma current I_p (e) plasma thermal energy (f) T at the magnetic axis.

Figure (5.25) shows the temperature and current profiles plotted at midplane vs R . The temperature profile rises in the core initially until $t \approx 1.75$ ms as can also be seen in Figure (5.9b). However, during this time the plasma cools in the outer layer due to the effect of impurities from SPI. After $t \approx 1.75$ ms, the entire temperature profile starts to drop. The distinct current contraction is not obtained as opposed to [49]. However, the current profile drops in the outer layer (5.25b) following the behavior of the temperature profile.

Figure (5.26 - 5.28) show snapshots of the mentioned variables at the time instants $t = 0.651, 1.207, 1.95$ and 2.381 ms. All the snapshots are plotted at $\phi = 0$ plane and in normalized units. The rational surfaces are marked by the dotted lines in the

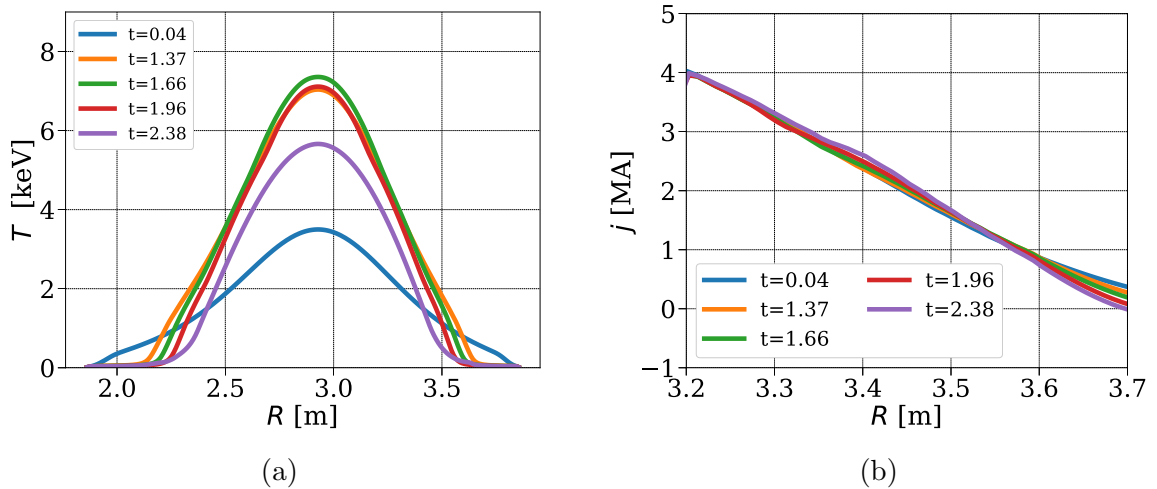


Figure 5.25: The temperature and current profiles plotted at midplane at the mentioned time instants for the SPI simulation with $\eta = 10^{-8}$: (a) T vs R (b) $j(= -R J_\phi)$ vs R .

visualizations which correspond to $q = 5, 4, 3, 2$ surfaces identified radially inwards. The presence of SPI fragments in the plasma starts the ablation process, i.e., interaction of the fragments with the electrons and it results the release of neutral atoms into plasma. These neutral atoms then interact with plasma ions and electron via ionization, recombination and charge exchange processes forming charged impurities. The formation of the charged impurities along with the neutral impurities is realized by the local rise in ρ_{imp} field. Ionization process involve the liberation of the ionization energy. The charged species with different level of charge states gives rise to Z_{eff} field in plasma. Effects of the atomic processes along with the radiation energy losses are shown in the visualizations.

The time instant $t = 0.651, 1.207$ and 1.95 approximately corresponds to arrival of the SPI fragments at $q = 4, 3$ and 2 surfaces respectively. Arrival of the fragments on the rational q surface triggers the convection of the impurities in θ direction as can be seen from the snapshots of ρ_{imp} . The spread of impurities in θ direction is seen in the snapshots via the mass ratio ρ/ρ_{imp} (Figure 5.26), Z_{eff} and ionization potential energy field (Figure 5.27). Impurities in the outer layer of plasma results into the cooling front around the plasma core and causes T and j profiles to decrease in the outer layer. Further in time the cooling front propagates radially inwards to cross $q = 3$ and 2 surfaces, which causes entire temperature profile to drop down. The need of the reduction in the time step is associated with the fragments reaching $q = 3$ and 2 surfaces as MHD dynamics occur on faster time scales. From the snapshot of ρ_{imp}

at $t = 2.381$ ms shown in Figure (5.26), a strong convection in the θ direction is seen and at the same location plasma temperature drops. The A_3 field is also affected by the cooling of the core as shown in Figure (5.28).

Along with A_3 , Figure (5.28) also shows the quantities $\mathbf{B} \cdot \nabla T$ and $\mathbf{v} \cdot \nabla \rho_{\text{imp}}$ plotted at the same time instants. The localized peak of high values in $\mathbf{v} \cdot \nabla \rho_{\text{imp}}$ field denotes the approximate location of the SPI fragments at respective time instants. Snapshots also show that the convection of impurities in the poloidal plane is enhanced particularly at $q = 2$ surface. The quantity $\mathbf{B} \cdot \nabla T$ denotes the change in the temperature in the direction of the magnetic field. This quantity shows high values along the rational q surfaces and the structures in the visualizations highlight the growth of the respective MHD modes. As cooling front propagates inwards, the modes inside the plasma core are highlighted. In the last snapshot, the rapid increase in the magnitude of the $\mathbf{B} \cdot \nabla T$ is seen which is also associated with the distortion of A_3 field at the same time.

Figure (5.29) shows the evolution of the magnetic and kinetic energies which begin to increase rapidly after $t = 2$ ms as SPI fragments cross $q = 2$ surface. The smooth behavior of the energies is the result of the stabilization provided by large value of D_{\perp} . After $t = 2$ ms, despite a rapid increase in the energies, the growth is lead by the lower harmonics. The rapid growth is associated with the SPI fragments crossing $q = 2$ surface.

Finally Poincaré plots of the magnetic field is shown in Figure (5.30) at the mentioned time instants along with the locations of SPI fragments marked by blue dots. At $t = 1.653$ ms fragments have crossed $q = 4$ surface while at $t = 1.95$ fragments are at $q = 3$ surface. The growth of 3/1 mode is seen by the magnetic island in Poincaré plot at $t = 1.95$. As fragments penetrate further in the plasma core 2/1 mode is excited as can be seen at $t = 2.247$ ms along with the other core modes. The plasma dynamics occur over faster time scales further and the modes 3/1 and 2/1 grows rapidly. This is associated with the formation of the stochastic layer in the outer region of the plasma core. The crossing of $q = 2$ surface is associated with strong convection currents which further cause stochastization in the plasma core. However, the simulation does not lead to the TQ and current profile contraction.

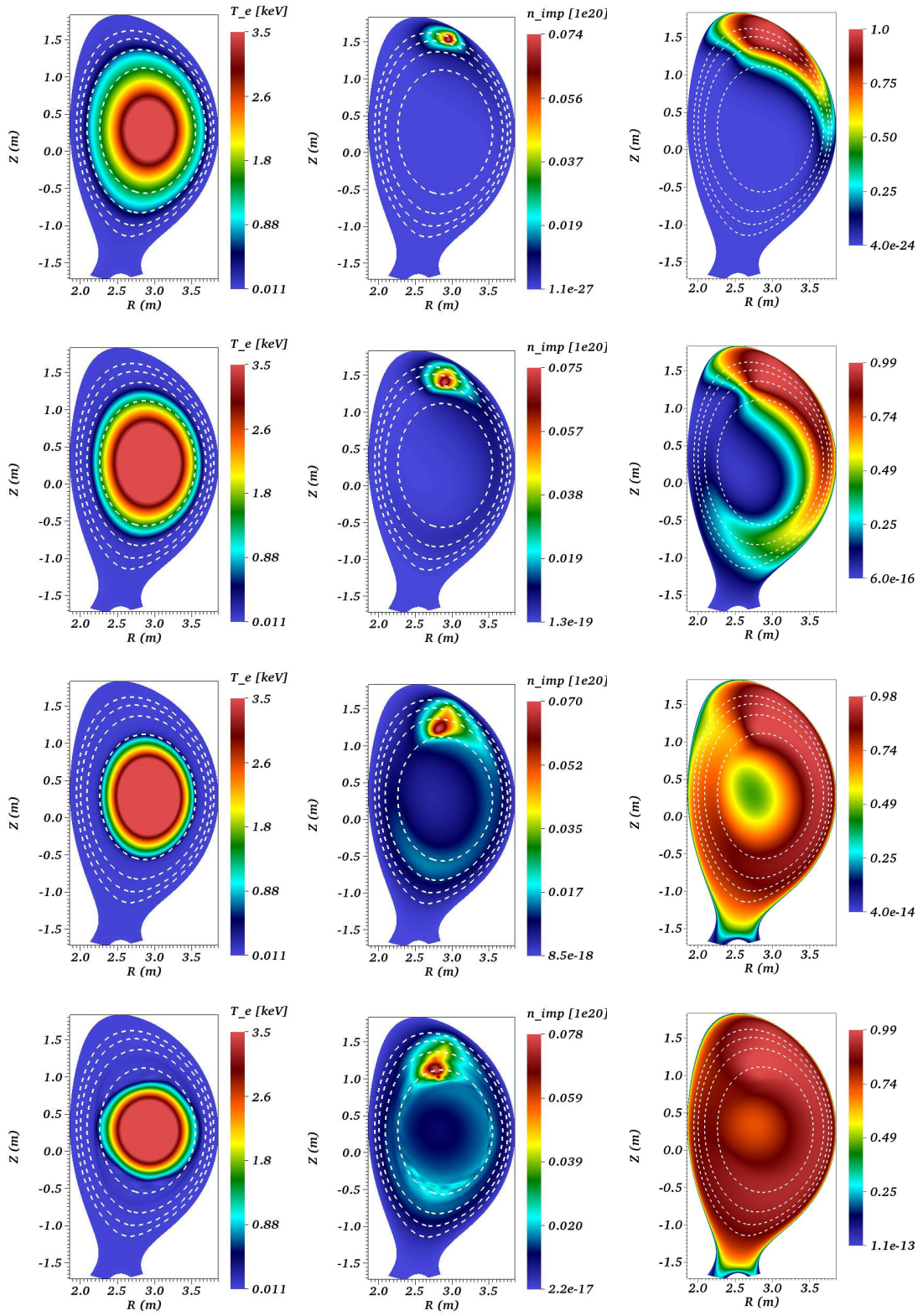


Figure 5.26: Visualizations of SPI simulation with $\eta = 10^{-8}$. 1st, 2nd and 3rd columns show T [keV], $n_{\text{imp}} [10^{20}]$ and ρ_{imp}/ρ while 1st, 2nd, 3rd and 4th row show snapshots at $t = 0.651, 1.207, 1.95$ and 2.381 ms respectively.

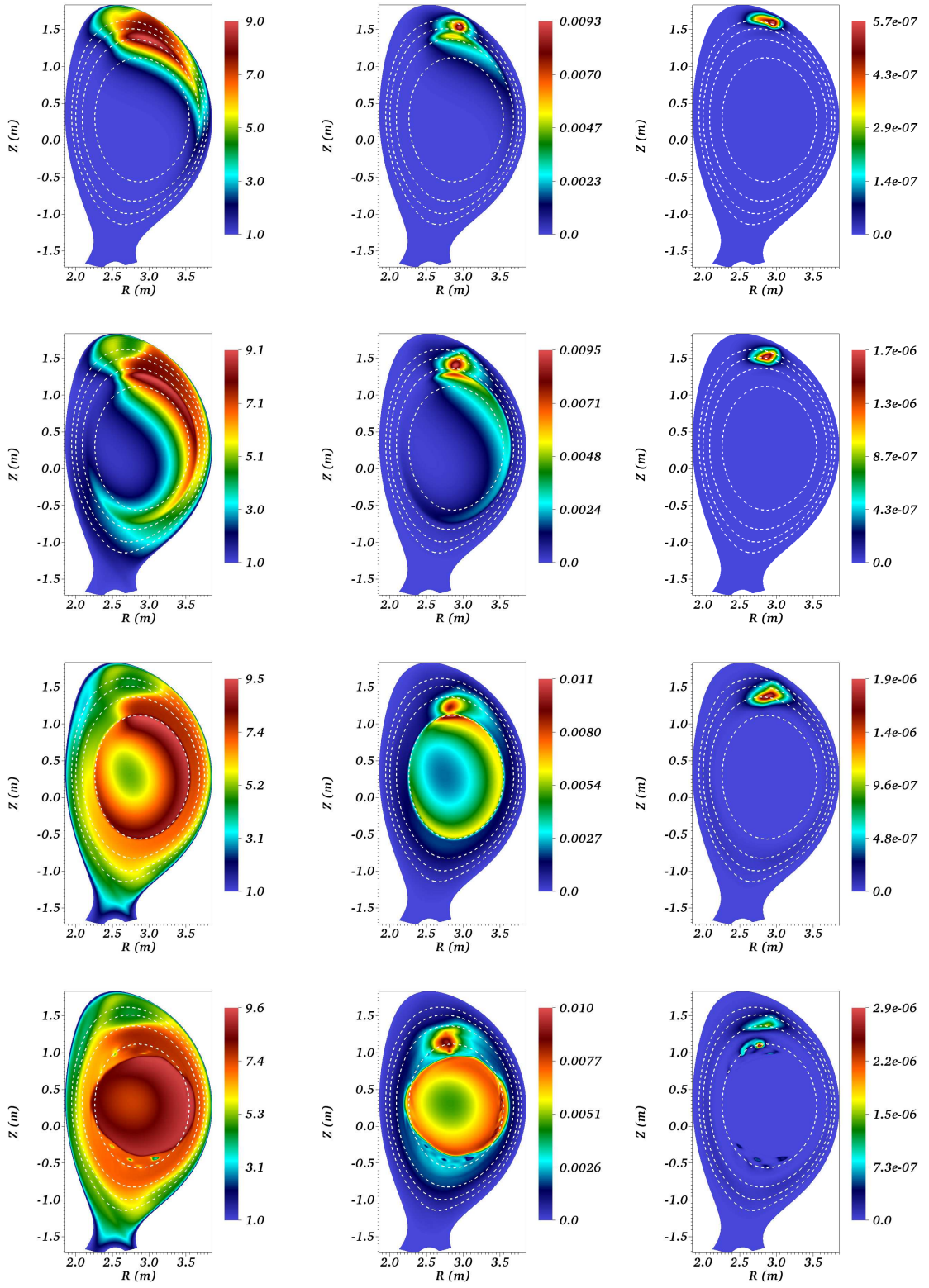


Figure 5.27: Visualizations of SPI simulation with $\eta = 10^{-8}$. 1st, 2nd and 3rd columns show Z_{eff} , $(\gamma - 1) \rho_{imp} E_{ion}$ and P_{rad} while 1st, 2nd, 3rd and 4th row show snapshots at $t = 0.651, 1.207, 1.95$ and 2.381 ms respectively.

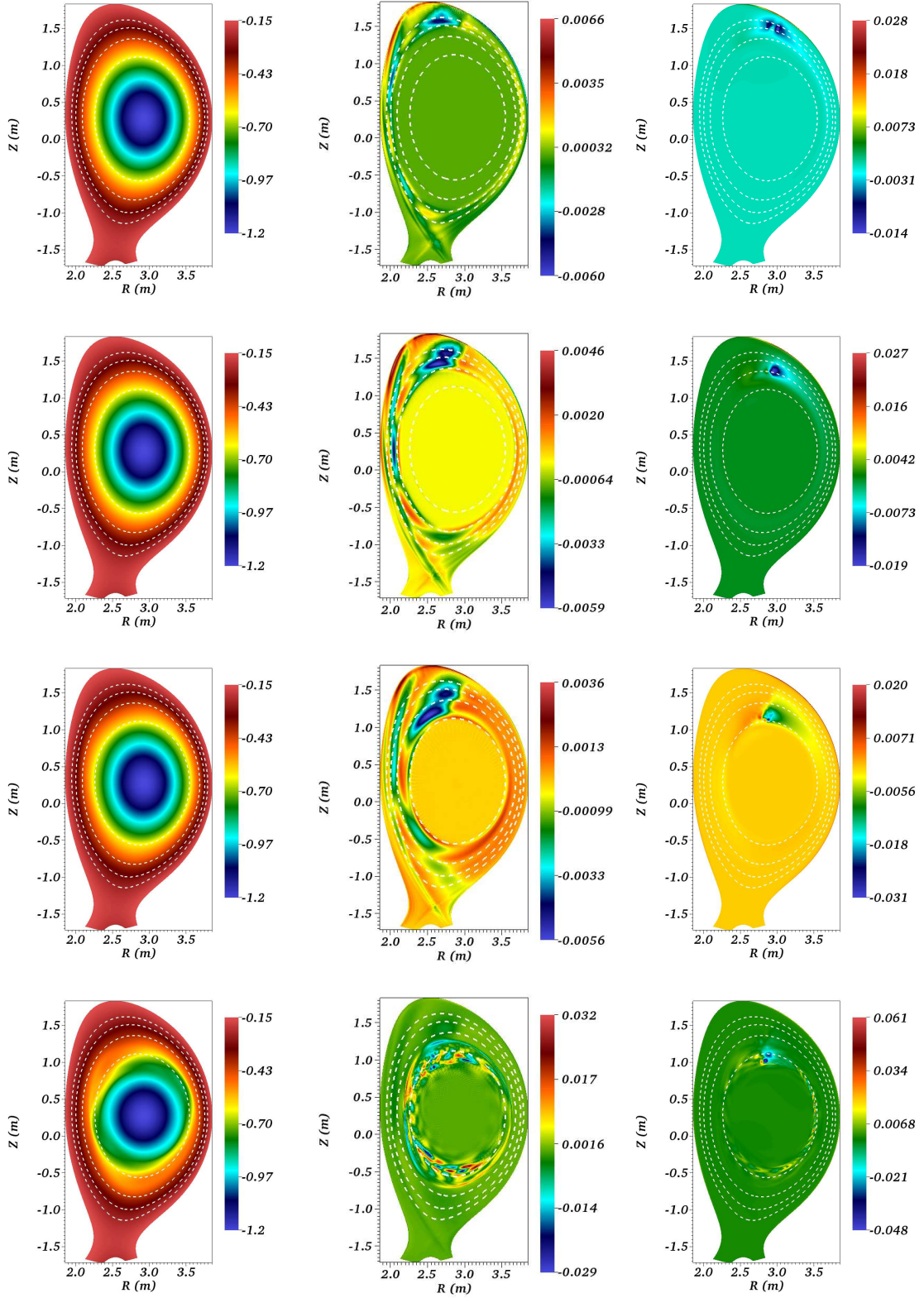


Figure 5.28: Visualizations of SPI simulation with $\eta = 10^{-8}$. 1st, 2nd and 3rd columns show A_3 , $\mathbf{B} \cdot \nabla T$ and $\mathbf{v} \cdot \nabla \rho_{\text{imp}}$ while 1st, 2nd, 3rd and 4th row show snapshots at $t = 0.651, 1.207, 1.95$ and 2.381 ms respectively.

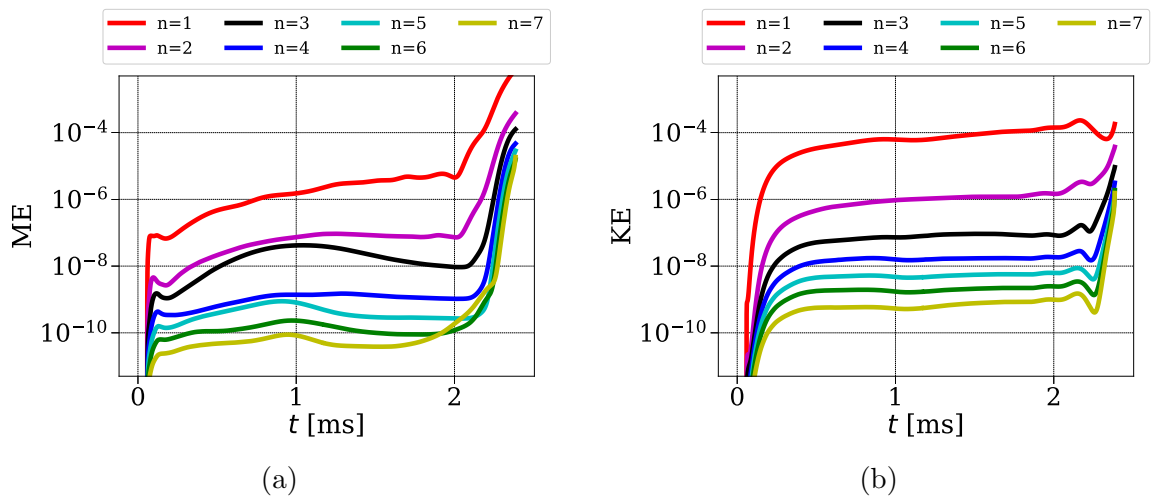


Figure 5.29: SPI simulation with $\eta = 10^{-8}$: (a) magnetic energies (b) kinetic energies.

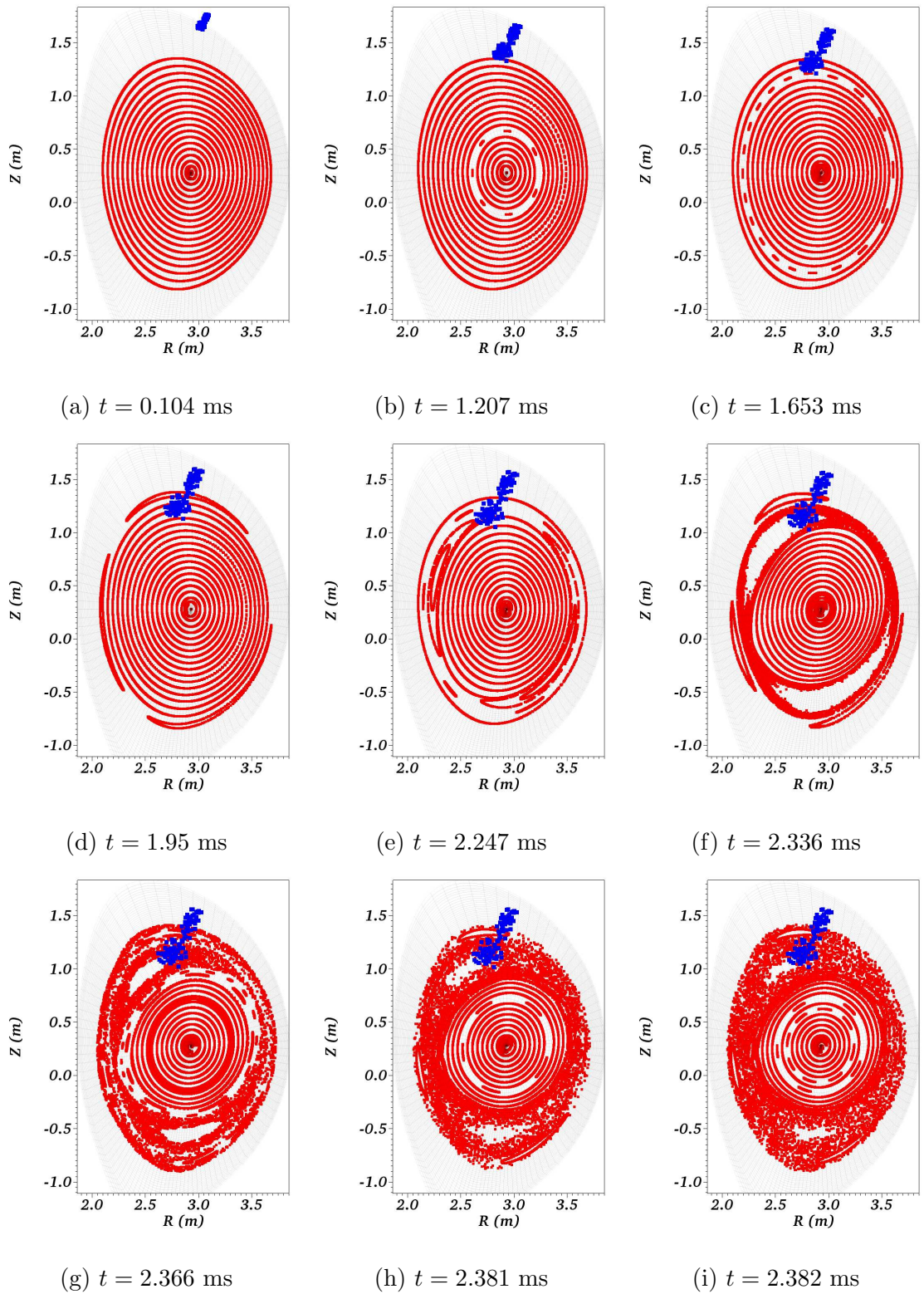


Figure 5.30: Poincaré plots of the magnetic field at mentioned time instants along with the projected position of SPI fragments shown by blue dots.

Effect of SPI parameters

The initial position and velocity of SPI fragments specified in the previous simulations mimics the actual SPI experiments in JET. For the simulation presented below, a hypothetical SPI set up is used and compared with the previous set up in the sketches shown in Figure (5.31a) and (5.31b). With the second set up the fragments travel primarily in the negative R direction.

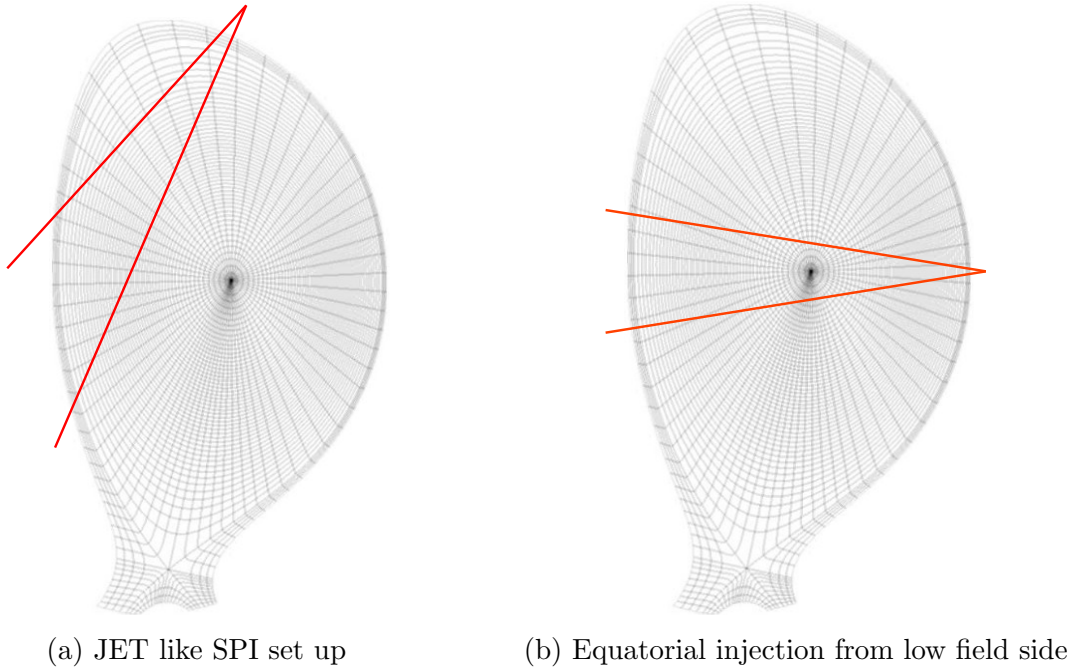


Figure 5.31: Two SPI configurations used each using different initial position and SPI velocity.

The initial position of SPI fragments is chosen around the location $(R_{spi}, Z_{spi}, \phi_{spi}) = (3.86, 0.28, 4.51)$ m while the SPI velocity of the fragments is chosen around the velocity vector $(V_{R_{spi}}, V_{Z_{spi}}, V_{\phi_{spi}}) = (-91.1, 0, 0)$ m/s. This velocity corresponds to the magnitude of almost 10 times smaller than the previous configuration. All other SPI parameters are kept same as the JET like SPI set up 1. The physical parameters chosen are as follows:

- The temperature and Z_{eff} dependent resistivity is specified with the value $\eta_0 = 10^{-9}$ (in all three A_R , A_Z and A_3 equations).
- The constant viscosity coefficient $\mu = 10^{-6}$ is used.
- The perpendicular density diffusivity is specified as $D_{\perp} = 2 \times 10^{-5}$ while the

parallel diffusivity D_{\parallel} is set to 0 in both the total and impurity density equations.

- The perpendicular heat conductivity is specified as $\kappa_{\perp} = 5 \times 10^{-6}$ and the temperature dependent parallel conductivity is specified with $\kappa_{\parallel 0} = 4000$.
- The grid is built with $n_{\psi} = 71$ and $n_{\theta} = 100$ points and the number of toroidal harmonics used are $n = 0, 1, \dots, 7$.

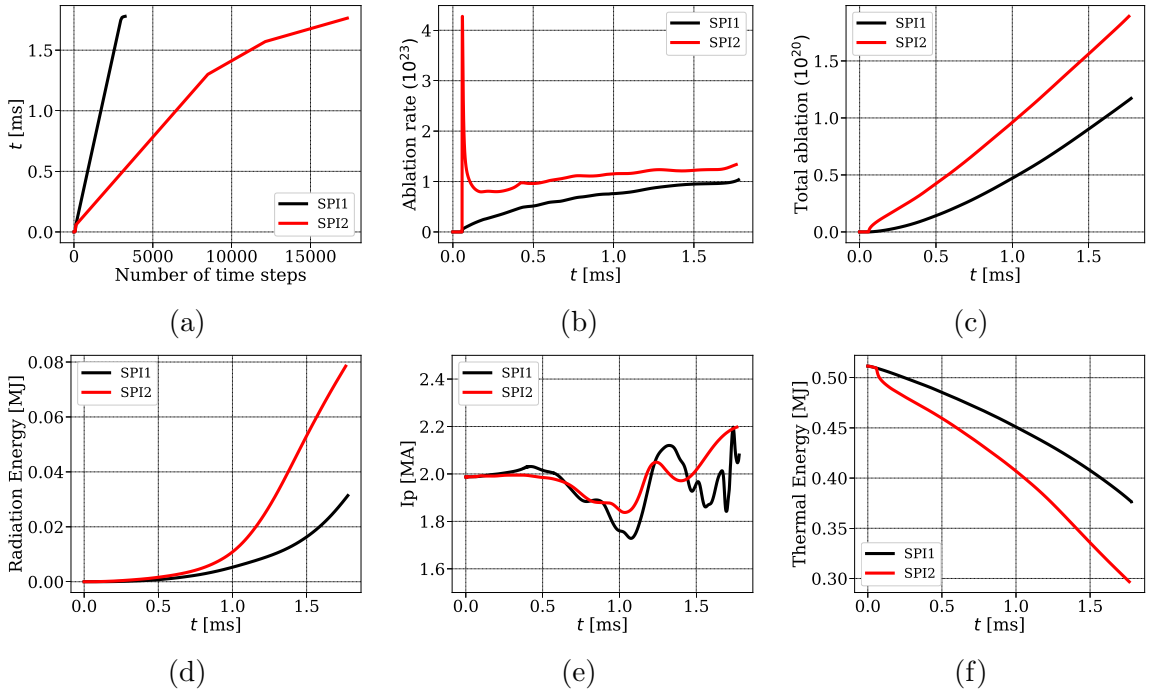


Figure 5.32: SPI simulations compared with two different injection set ups: (a) physical time for which simulations are run (b) ablation rates (c) total impurities injected (d) radiation energy (e) plasma current I_p (f) plasma thermal energy.

The simulations with the two set ups are compared and some quantities are shown in Figure (5.32). From the beginning, the simulation with the new set up demands a low time step of $\Delta t = 0.5$. Figure (5.32a) shows the comparison of the number of time steps required for the two simulations to reach almost the same physical time. With the new SPI set up, a huge spike is observed at the beginning of the simulation in the ablation rate, which cause higher deposition of impurities in plasma (5.32b). The spike in the ablation rate may be due to higher gradients in T and n_e at the new initial position. Since the ψ_N contours are densely packed near the new initial location, a small distance that fragment travel must encounter rapid increase in the

temperature and density. Indeed, a sharp rise in the density profile near $\psi_N = 1$ can be seen in Figure (5.1a). Overall, the ablation rate, the number of impurity atoms deposited and the radiation energy vs time is higher for the new SPI set up as shown in Figure (5.32). The decrease in the thermal energy at the beginning of the simulations is associated with the higher deposition of impurities. Throughout the simulation thermal energy decreases faster than that in the old set up (Figure (5.32f)). The overall behavior of plasma current I_p obtained with the both set ups shows a similar trend (Figure (5.32e)).

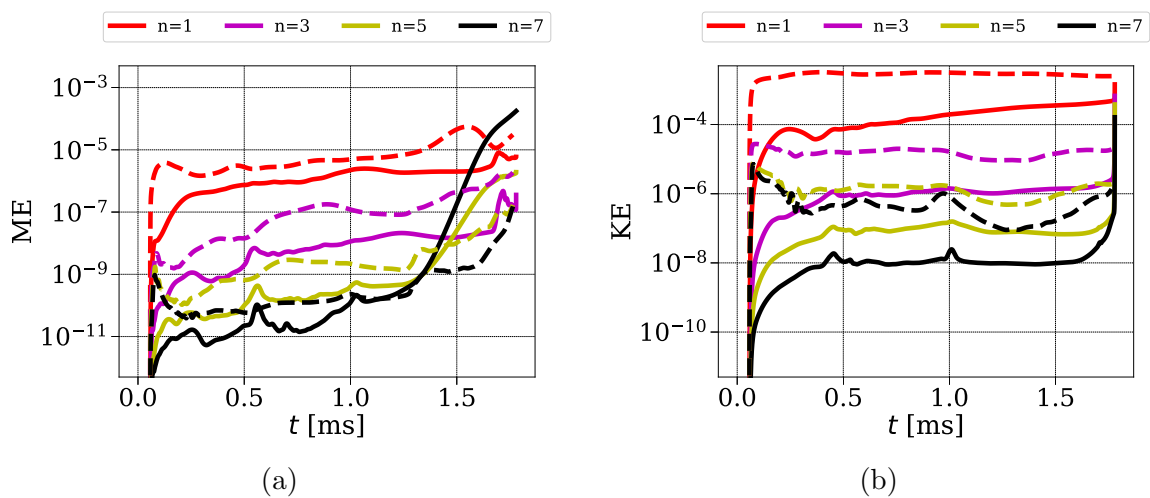


Figure 5.33: The comparison of the evolution of the energies with SPI simulations with two different injection set ups: (a) magnetic energies (b) kinetic energies. Solid and dashed represents energies plotted for the old and new SPI set up respectively.

Note that since the comparison involves two different SPI set ups, the focus is only on the qualitative comparison. Figure (5.33) shows the evolution of the magnetic and kinetic energies with the both SPI set ups. Overall, it can be seen that both magnetic and kinetic energies with the new set up are higher. Energies with the new set up show rapid growth at the beginning of the injection which is associated with the spike in the ablation rate. With the old set up the magnetic energies grow rapidly after $t = 1$ ms similar to the simulations presented before. However, the magnetic energies with the new set up are well behaved in the sense that the rapid growth of the energies are not seen and the growth is always lead by the lower harmonics. The effect is also seen in I_p evolution which is smoother than the old set up.

Figure (5.34 - 5.36) show snapshots of the mentioned variables at the time instants $t = 0.336, 0.93, 1.638$ and 1.762 ms. All the snapshots are plotted at $\phi = 0$ plane and in normalized units. The rational q surfaces are marked by the dotted lines in the

visualizations which corresponds to $q = 5, 4, 3, 2$ surfaces identified radially inwards. The time instant $t = 0.336$ and 0.93 ms approximately corresponds to arrival of the SPI fragments at $q = 3$ and 2 surfaces respectively. Arrival of the fragments on the rational q surface triggers the convection of impurities in θ direction as can be seen from the snapshots of ρ_{imp} , ρ/ρ_{imp} , Z_{eff} and ionization potential energy field (Figure 5.35). The spread of impurities in the outer layer of plasma forms the cooling front around the plasma core and causes T and j profiles to decrease in the outer layer. Further in time, the cooling front propagates radially inwards to cross $q = 3$ and 2 surfaces, which causes entire temperature profile to drop down. A_3 field is seen to develop fine scale structures in the outer layer of plasma in Figure (5.36) where the contours to denote rational q surfaces have been removed for clarity.

Figure (5.36) shows the snapshots of A_3 , $\mathbf{B} \cdot \nabla T$ and v_ϕ plotted at the same time instants. The quantity $\mathbf{B} \cdot \nabla T$ shows the effect of cooling front that propagates radially inwards and highlights the structures of MHD modes. As opposed to the previous simulation with $\eta = 10^{-8}$, rapid increase in the values of $\mathbf{B} \cdot \nabla T$ at the end of the simulation is not observed which is related to the fact that magnetic energies do not grow violently in this simulation. The distortion of A_3 field is also milder as compared to the simulation with $\eta = 10^{-8}$. The snapshots of v_ϕ show that the transport of the impurities drives parallel flows. The parallel flows driven by the SPI fragments convect the impurities around the torus, the observation which is similar to SPI simulations with NIMROD [59]. It is also observed in [59] that the mixed D2/Ne SPI fragments drives stronger flows than the pure Ne SPI resulting in greater parallel transport of the impurities, greater mixing and less radiation asymmetry.

Figure (5.37) shows the temperature and current profiles plotted at midplane vs R . As opposed to the previous simulation with $\eta_0 = 10^{-8}$ where the temperature profile initially rises, in this simulation the temperature profile decreases from the beginning of the simulation (Figure (5.37a)). Initially the plasma cools in the outer layer due to SPI fragments and later it cools in the core region as core modes grow. The distinct current contraction is not observed as opposed to [49]. However, the current profile drops down slightly in the outer layer (5.37b) following the trend of the temperature profile.

Finally Poicaré plots of the magnetic field are shown in Figure (5.38) at the mentioned time instants along with the locations of SPI fragments marked by blue dots. At $t = 1.638$ ms the fragments have already crossed $q = 2$ surface and the magnetic islands associated with $3/1$ and $2/1$ modes are visible in Figure (5.38a). As fragments

further travel in the plasma core, the outer layer become stochastic (Figure 5.38b). At $t = 1.761$ ms, the 2/1 islands are still visible. However, TQ is not observed in this simulation.

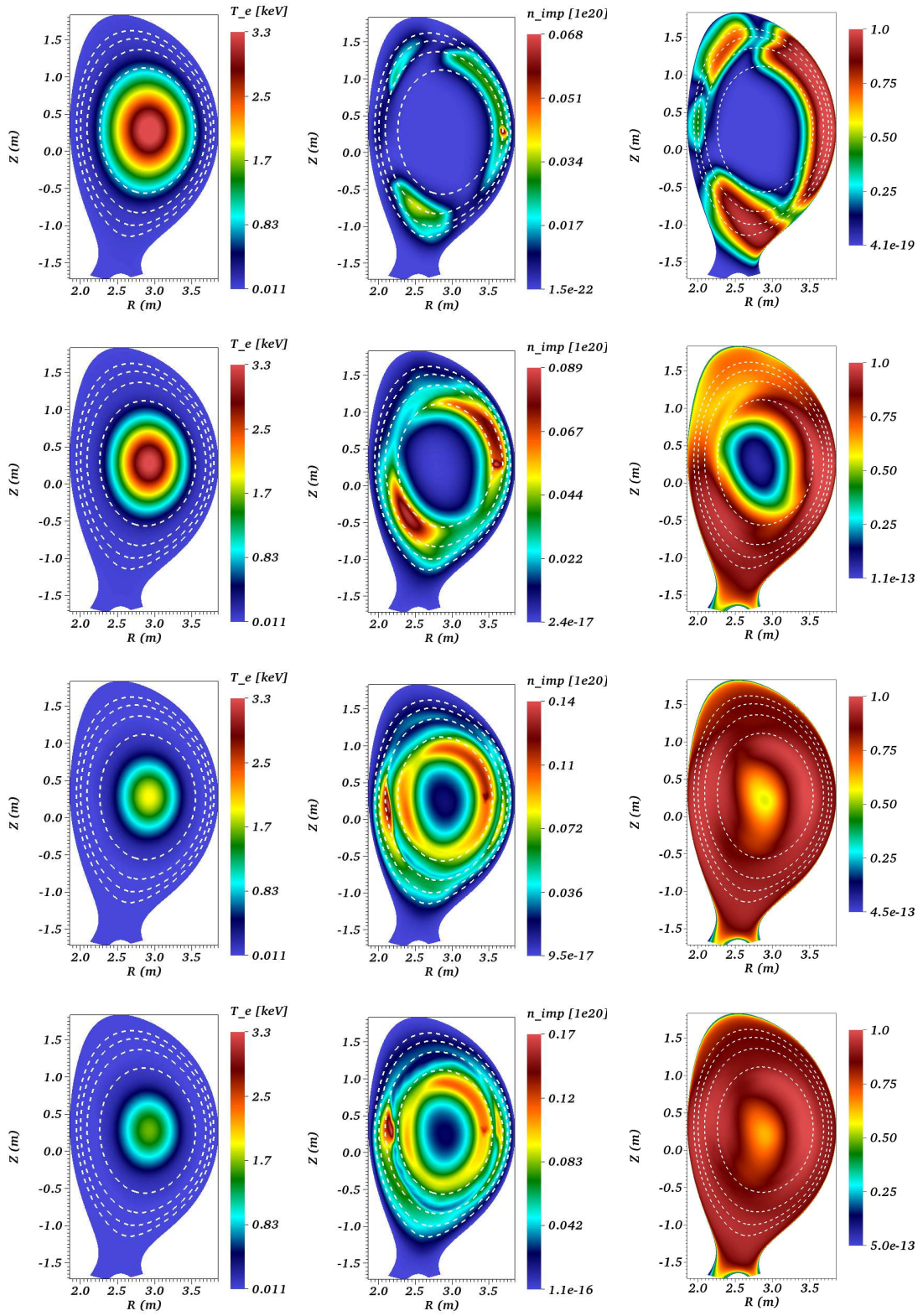


Figure 5.34: Visualizations of SPI simulation with $\eta = 10^{-9}$ and different configuration. 1st, 2nd and 3rd columns show T [keV], $n_{\text{imp}} [10^{20}]$ and $\rho_{\text{imp}}/\rho_{\text{ho}}$ while 1st, 2nd, 3rd and 4th row show snapshots at $t = 0.336, 0.93, 1.638$ and 1.762 ms respectively.

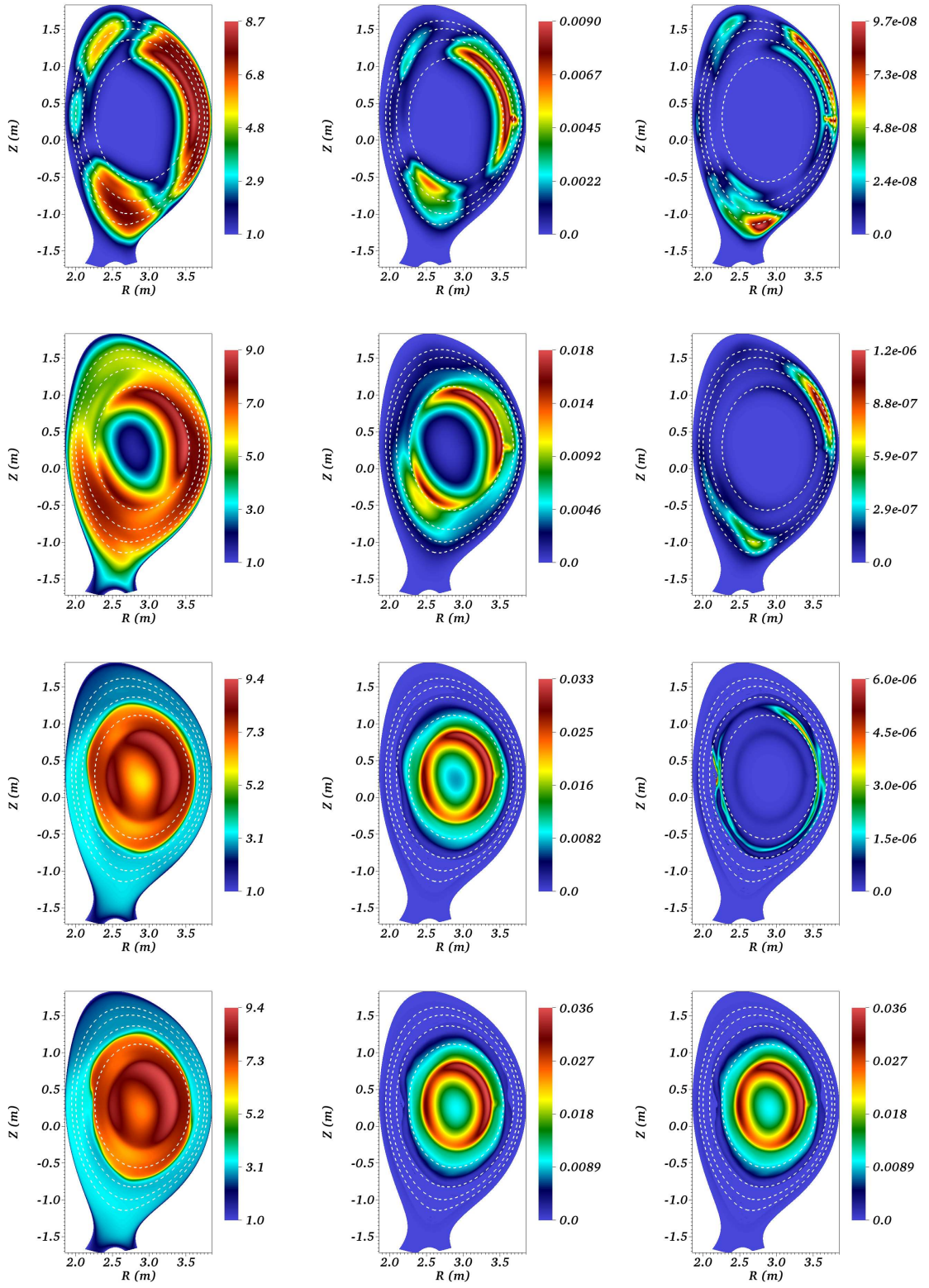


Figure 5.35: Visualizations of SPI simulation with $\eta = 10^{-9}$ and different configuration. 1st, 2nd and 3rd columns show Z_{eff} , $(\gamma - 1) \rho_{imp} E_{ion}$ and P_{rad} while 1st, 2nd, 3rd and 4th row show snapshots at $t = 0.336, 0.93, 1.638$ and 1.762 ms respectively.

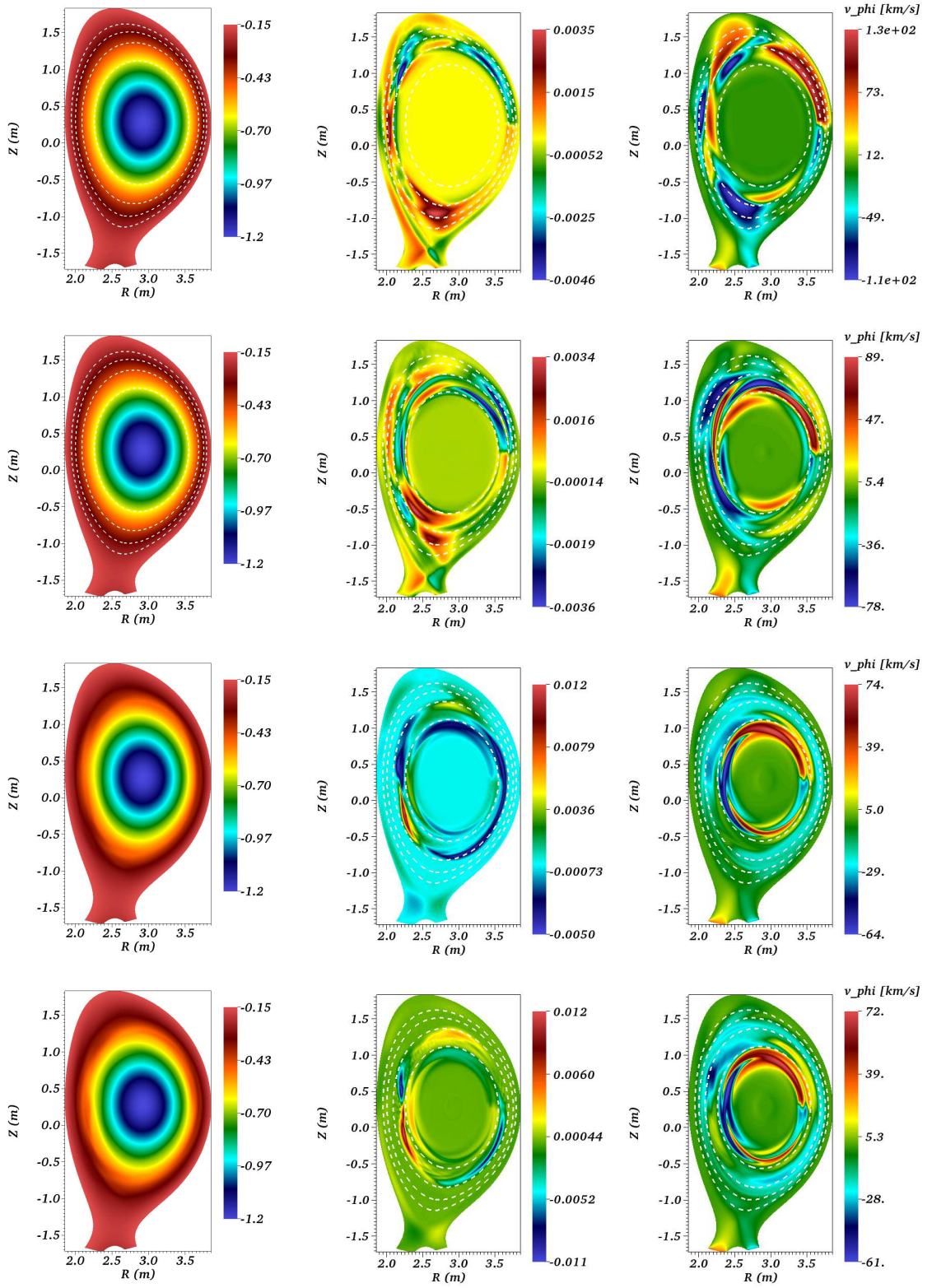


Figure 5.36: Visualizations of SPI simulation with $\eta = 10^{-9}$ and different configuration. 1st, 2nd and 3rd columns show A_3 , $\mathbf{B} \cdot \nabla T$ and v_ϕ [km/s] while 1st, 2nd, 3rd and 4th row show snapshots at $t = 0.336, 0.93, 1.638$ and 1.762 ms respectively.

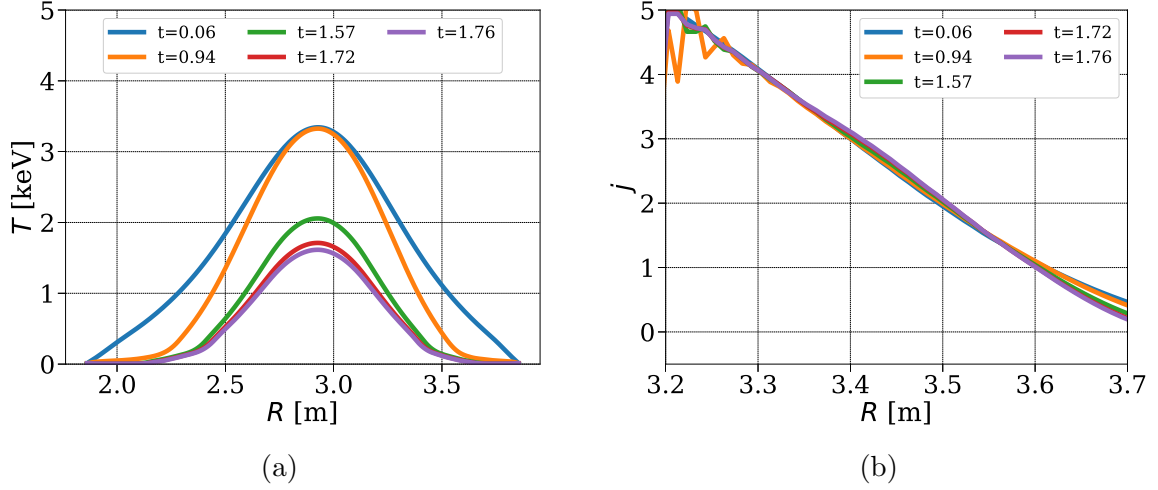


Figure 5.37: The temperature and current profiles plotted at midplane at the mentioned time instants for the SPI simulation with $\eta = 10^{-9}$ and a new SPI set up: (a) T vs R (b) $j(= -R J_\phi)$ vs R .

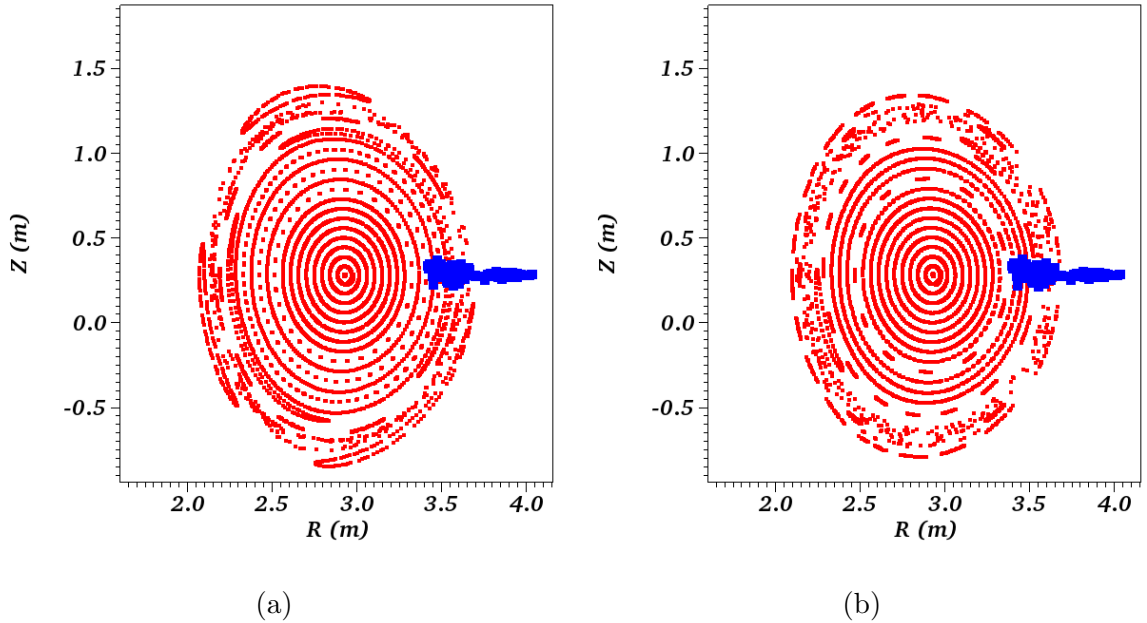


Figure 5.38: Poincaré plots of the magnetic field for the simulation with a new SPI set up: (a) $t = 1.638$ ms and (b) at $t = 1.761$ ms.

5.3 Conclusion

Nonlinear MHD simulations have been performed to simulate MMI in tokamak plasma using full MHD model. MGI simulation with the two temperature MHD model show TQ like physics even on a coarse grid. However, the main focus was SPI simulations. In the first step, nonlinear SPI simulations are performed by removing the resistivity from A_R and A_Z equations, which gave deceptively stable results. It is noted that the removal or suppression of the resistivity from the A_R and A_Z equations seems to yield numerical solutions showing TQ, however A_3 field and the plasma current I_p in such a case show unphysical behavior. Hence the same value of the resistivity is added in all three equation of the components of the magnetic vector potential. The effect of the resistivity, grid refinement, particle diffusivity and numerical stabilization is discussed. Based on the observation of these simulations, the parameters are identified that will allow long run simulations. These simulations capture pre-TQ physics well. The key physical phenomena that show onset of TQ such as parallel convection driven by impurities, cooling of plasma, growth of core modes and stochastization of the magnetic field in the outer layer of plasma are seen.

All SPI simulations presented here crash after certain point when fragments arrives at $q = 2$ surface and magnetic energies grow violently. The removal of the resistivity from A_R and A_Z gives a seemingly stable model but yields unrealistic results where plasma current I_p drops at unrealistically faster rates. Retaining the resistivity in A_R and A_Z -equations however requires the use of the numerical stabilization. The numerical stabilization scheme developed here suffers from two drawbacks:

- The stabilization terms containing current are not taken into account. This is because the second derivatives with respect to ϕ direction, to be obtained via DFT, have not yet been implemented in JOREK.
- Shock/discontinuity detecting criterion that will make the shock capturing stabilization terms effective needs to be formulated.

Despite absence of the Ohmic heating term and a complete numerical stabilization scheme, MHD dynamics of pre-TQ is captured well by the full MHD model.

Chapter 6

MHD destabilization and thermal quench

VMS stabilization provides L^2 stability which is useful when solutions are smooth. When shocks and discontinuities are present in the numerical solution, spurious oscillations may be generated around discontinuities which can cause severe accuracy and stability problems. The rationale behind a shock or discontinuity capturing stabilization is that the stabilization should act only in neighborhood of a sharp discontinuities to mitigate the spurious oscillations. The idea has been used to develop stabilization schemes for finite volume methods [56] and discontinuous Galerkin methods [7, 92]. The similar approach has also been used successfully for continuous Galerkin methods [34, 90, 88].

SPI source terms gives rise to sharp discontinuities in the solution field. In the previous Chapter, VMS based stabilized FEM is used for SPI simulations to capture pre-TQ physics. However, simulations fail to enter into TQ stage. At onset of TQ, MHD activities increase where the matrix solver demands very small time steps to converge which indicates stability problems. The stabilized FEM presented in Chapter 3, in principle, contains shock-capturing stabilization terms. Shock/discontinuity detection criterion is the important part of the shock-capturing stabilization scheme. In this chapter, we demonstrate the use of a proper discontinuity detection criterion that enables simulations to capture MHD destabilization and TQ stage during SPI simulations. The numerical results obtained here uncover similar dynamics captured using the reduced MHD model [49].

6.1 Discontinuity capturing criterion

In order to discuss the discontinuity detection criterion, we first rewrite the shock-capturing stabilization terms from section (3.2.3) as:

$$\mathbf{d} = \sum_e \int_{\Omega_e} \nabla \mathbf{w}^* : (\underline{\mathbf{T}}_{SC} \nabla \mathbf{w}_h) d\Omega_e$$

where the stabilization coefficient matrix is simplified to

$$\underline{\mathbf{T}}_{SC} = k_{SC} \mathbb{I}$$

Here, we adapt the discontinuity detection criterion based on that given in [7, 34] and is written as:

$$k_{SC} = C h_e^2 \frac{d_p}{p} f_p \quad (6.1)$$

where, h_e is the characteristic element size, C is a user defined parameter,

$$d_p = \left| \sum_{i=1}^{n_v} \frac{\partial p}{\partial \mathbf{w}_i} \tilde{\mathcal{R}}(\mathbf{w}_i) \right| \quad \text{and} \quad f_p = \frac{\|\nabla p\|}{p} h_e$$

The quantity f_p is the shock-sensor based on the pressure p . The quantity d_p denotes the nonlinear weights for f_p and depends upon the approximated residual $\tilde{\mathcal{R}}(\mathbf{w}_i)$ of the equations in the variables \mathbf{w}_i where n_v denotes the number of variables. For the full MHD model pressure (p) depends upon the density and temperature and hence d_p becomes the sum of two terms. For extended full MHD model for SPI, d_p is the sum of three terms because the total pressure depends upon the impurity density as well. Similarly, the term f_p needs to be accounted for the pressure due to impurities in case of SPI. Here, the approximated residuals are chosen as:

$$\begin{aligned} \tilde{\mathcal{R}}(\rho) &= \nabla \cdot (\rho \mathbf{v}) \\ \tilde{\mathcal{R}}(T) &= (\gamma - 1) T (\nabla \cdot \mathbf{v}) + \mathbf{v} \cdot \nabla T \\ \tilde{\mathcal{R}}(\rho_{\text{imp}}) &= \nabla \cdot (\rho_{\text{imp}} \mathbf{v}) \end{aligned}$$

The term k_{SC} takes high values in the vicinity of discontinuities and very small values everywhere else making a good criterion to be utilized in the shock-capturing method. The term k_{SC} is used as the coefficient of shock capturing stabilization and hence stabilization acts near discontinuities only. The parameter C in k_{SC} is to be

controlled by user to tune the sufficient amount of stabilization and in general C depends on the grid resolution. In the following Section we demonstrate the use of shock-capturing stabilization in SPI simulations and effect of the parameter C .

Although, a general stabilization scheme written in Chapter 3 includes isotropic as well as anisotropic stabilization terms, only isotropic stabilization is used here. Furthermore, the criterion (6.1) may be updated by adding the effect of source terms [7], however the approximate residuals written above are found to be sufficient to push simulations into TQ. The addition of source terms may be needed if the sources are stronger, for example, larger amount of material being injected in plasma.

6.2 Thermal quench

The JET like equilibrium and SPI configuration from Chapter 5 is used here to run SPI simulations with shock-capturing stabilization. SPI simulations with constant and temperature dependent resistivities are presented below. As mentioned in Chapter 5, when $\eta_0 \geq 10^{-7}$ the temperature dependence in the resistivity is removed for the numerical reasons. The simulations with $\eta_0 < 10^{-8}$ however use the Spitzer like temperature dependence. Such dependence is physically more relevant and yields more realistic physical modeling of plasma.

6.2.1 SPI with constant resistivity

SPI simulations presented in this subsection use the constant resistivity with $\eta_0 = 10^{-6}$. The simulations are run on two different grids (denoted by g) and with different values of C . The resulting cases are shown in Table (6.1).

The other physical parameters used are as follows: The constant viscosity coefficient is set to $\mu = 10^{-6}$. The particle diffusion coefficients are specified as $D_{\parallel} = 0$ and $D_{\perp} = 10^{-5}$ for both the total and impurity densities. The perpendicular heat conductivity is specified as $\kappa_{\perp 0} = 5 \times 10^{-6}$ and temperature dependent parallel heat conductivity with $\kappa_{\parallel 0} = 4000$.

All the cases listed in Table (6.1) are started with $\Delta t = 5$ from the point of the injection. Figure (6.1a), (6.1b) and (6.1c) show comparisons of ablation rates, total ablation and radiation energy respectively, for the cases in Table (6.1). The matrix solver for ‘case 1.0’ fails to converge shortly after 1 ms even if time step is reduced

case g.C	n_ψ	n_θ	n	C
case 1.0	51	64	7	0
case 1.1	51	64	7	1
case 2.1	71	100	7	1
case 2.5	71	100	7	5
case 2.10	71	100	12	10

Table 6.1: SPI simulations with constant $\eta = 10^{-6}$ identified by grid (g) and the shock-capturing stabilization parameter (C) as ‘case g.C’

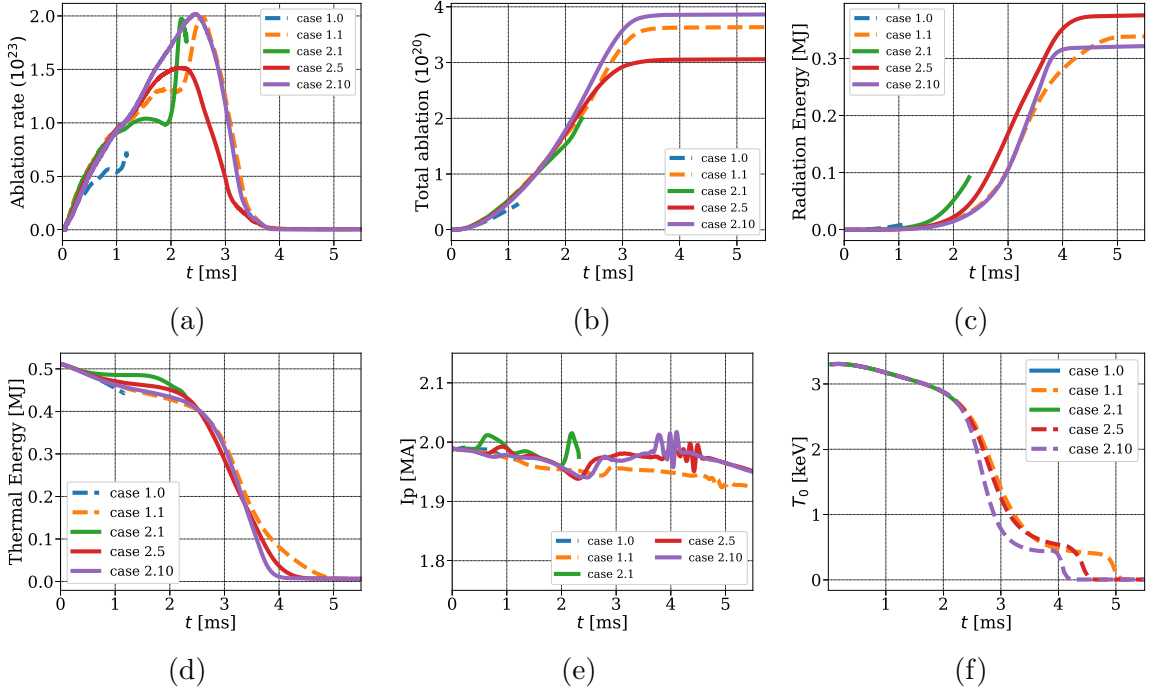


Figure 6.1: Evolution of (a) ablation rates (b) total impurities injected (c) radiation energy (d) plasma thermal energy (e) plasma current I_p (f) temperature at the magnetic axis for the cases shown in Table (6.1).

to $\Delta t = 1$. In ‘case 1.1’, shock-capturing stabilization with $C = 1$ is used where the solver converge with $\Delta t = 5$ and ‘case 1.1’ runs for a long physical time. With more resolved grid and $C = 1$, shock-capturing stabilization appears insufficient and the matrix solver for ‘case 2.1’ fails to converge shortly after 2 ms. Increasing C to 5 and 10 allows the matrix solver to converge with $\Delta t = 5$ where ‘case 2.5’ and ‘case 2.10’ run for long physical time. Between ‘case 2.5’ and ‘case 2.10’, ablation rates and total

ablation is higher in ‘case 2.10’ while radiation energy is lower. The ablation rates and radiation energy is influenced by the parameter C and therefore it is important to find the optimum value for C .

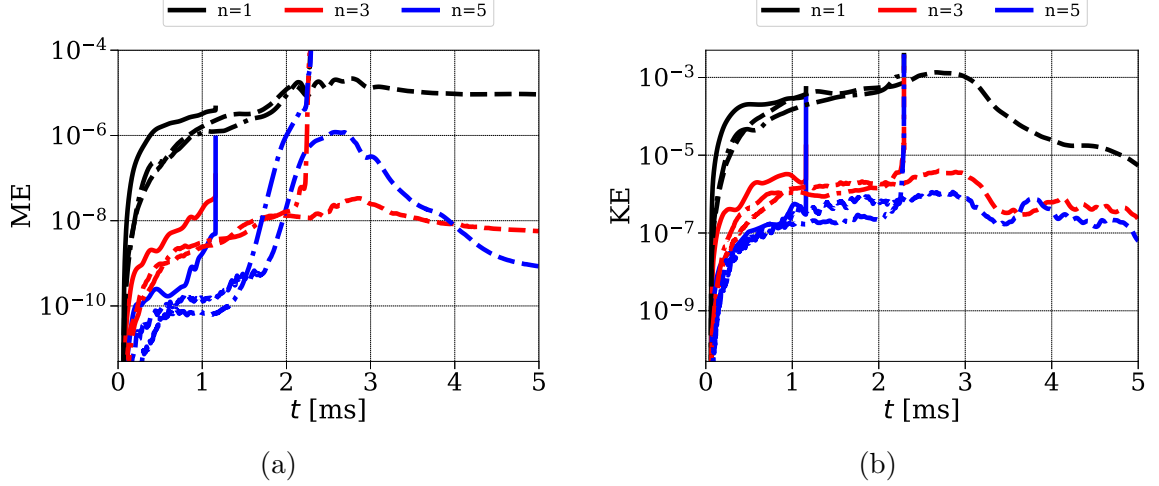


Figure 6.2: Comparison of the evolution (a) magnetic energies (b) kinetic energies for SPI simulations with $\eta_0 = 10^{-6}$. Solid, dashed and dashed dotted lines denote ‘case 1.0’, ‘case 1.1’ and ‘case 2.1’ respectively.

Figure (6.1d) shows comparison of plasma thermal energy obtained for the five simulations under discussion. In ‘case 1.1’, ‘case 2.5’ and ‘case 2.10’ plasma loses thermal energy rapidly after 2 ms and this phase is identified as TQ. In ‘case 2.5’ and ‘case 2.10’, the grid is more resolved where the decrease of thermal energy is more rapid than that with ‘case 1.1’. Since ‘case 2.10’ yields higher ablation (total impurities deposited) the TQ obtained in more rapid than ‘case 2.5’. Figure (6.1e) shows comparison of plasma current obtained in different simulations showing the effect of grid and C . The notable feature is a signature of I_p spike which is usually observed in experiments at the end of TQ. When thermal energy becomes minimum, I_p shows a spike followed by oscillatory behavior in ‘case 1.1’, ‘case 2.5’ and ‘case 2.10’. Figure (6.1f) shows evolution of the temperature at the magnetic axis where two stages of rapid decrease of the temperature are seen and second stage corresponds to occurrence of I_p spike.

Figure (6.2) shows comparison among the evolution of the magnetic and kinetic energies for ‘case 1.0’, ‘case 1.1’ and ‘case 2.1’. It can be seen that energies for ‘case 1.0’ increase rapidly before simulation fails to converge. Strong discontinuities develop in ‘case 1.0’ which can be seen in the top row of Figure (6.3) where discontinuity capturing criterion k_{SC} is evaluated and plotted at the mentioned time instants. Very

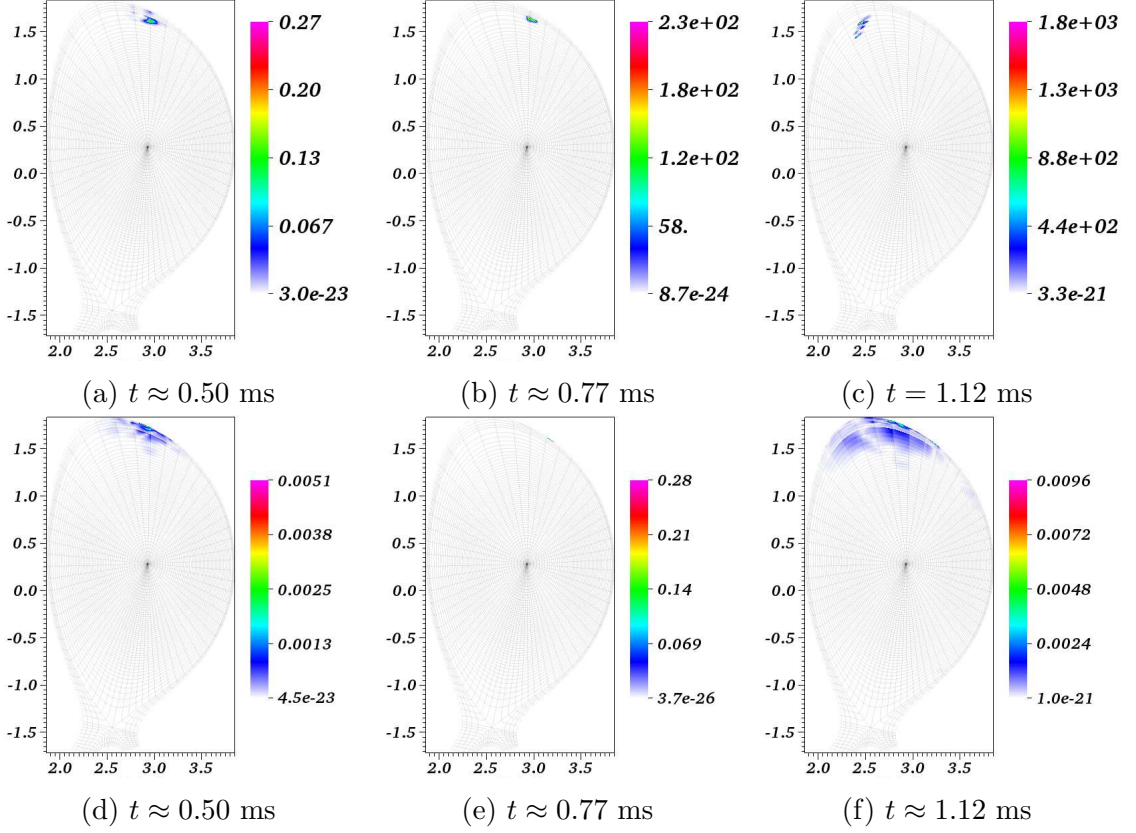


Figure 6.3: Discontinuity detecting criterion k_{SC} plotted to show the local nature of the shock-capturing stabilization scheme. Top row shows the estimate of k_{SC} with $C = 1$ for ‘case 1.0’ while the bottom row shows the same for ‘case 1.1’.

high values of k_{SC} are seen near the location of the injection at $t \approx 0.5$ and $t \approx 0.77$ ms highlighting the location of discontinuities while everywhere else k_{SC} takes very low values. At $t = 1.12$ in ‘case 1.0’, k_{SC} highlights the location of oscillations developed due to the presence of discontinuities. In the bottom row of Figure (6.3), k_{SC} evaluated for ‘case 1.1’ at the same time instants shows much smaller values. Indeed, ‘case 1.1’ runs for very long physical time with $\Delta t = 5$ and the evolution of energies for ‘case 1.1’ is seen in Figure (6.2). The ‘case 2.1’ uses refined grid with $C = 1$ and fails shortly after 2 ms, however the magnetic and kinetic energies of the ‘case 1.1’ and ‘case 2.1’ are comparable before the ‘case 2.1’ fails.

Figure (6.4) shows comparison among the evolution of the magnetic and kinetic energies for ‘case 2.1’, ‘case 2.5’ and ‘case 2.10’ which use the same refined grid but different values of C . As discussed before, $C = 1$ does not provide sufficient amount of stabilization, however ‘case 2.5’ and ‘case 2.10’ run for long physical times with the comparable evolution of the magnetic and kinetic energies. Long time simulations

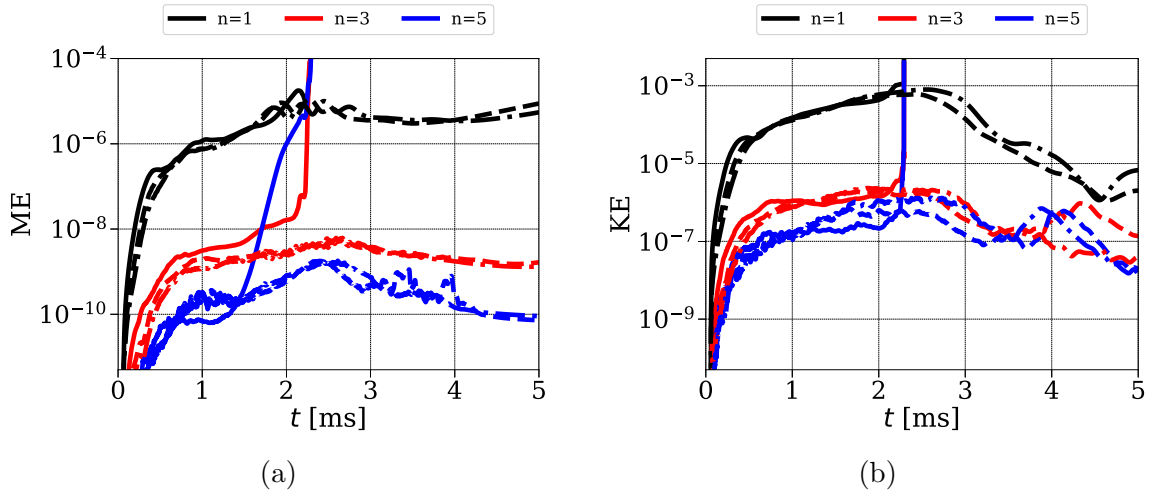


Figure 6.4: Comparison of the evolution (a) magnetic energies (b) kinetic energies for SPI simulations with $\eta_0 = 10^{-6}$. Solid, dashed and dashed dotted lines denote ‘case 2.1’, ‘case 2.5’ and ‘case 2.10’ respectively.

show that the growth in the magnetic energies after $t = 2$ ms which is associated with the SPI fragments crossing $q = 2$ surface and the growth of 2/1 mode in the plasma core. The MHD dynamics beyond this stage was not obtained in the simulations with VMS stabilization presented in Chapter 5. It is the shock-capturing stabilization terms that allow simulations beyond this stage.

Figure (6.5) shows visualizations of T [keV], $n_{\text{imp}} [10^{20}]$ and v_ϕ [km/s] at $\phi = 0$ plane and at the mentioned time instants for ‘case 2.5’. In the first column, temperature field is plotted to show cooling of plasma due to TQ as time progresses. During the simulation, impurities are transported due to parallel convection in the plasma forming a cooling front. It can be seen from the second and third column in Figure (6.5) that as time progresses parallel convection is seen via v_ϕ which drives transport of impurities first in the poloidal (helical) direction to form the cooling front surrounding the plasma core. Then as SPI fragments travel radially inwards, cooling front also propagates inwards that leads to destabilization of core modes and TQ.

Figure (6.6) shows the temperature and current plotted at midplane vs R at the mentioned time instants for ‘case 2.5’. The effect of formation of a cooling front in the outer layer of plasma is seen in T profiles at $t = 1.37$ and 2.08 ms where plasma starts to cool in the outer layer. The effect of radially inward propagation of the cooling front is seen at the further time instants where plasma cools in the core region. Evolution of the current profile shows the signature of current sheet formation at the location of the cooling front, the observation which is similar to

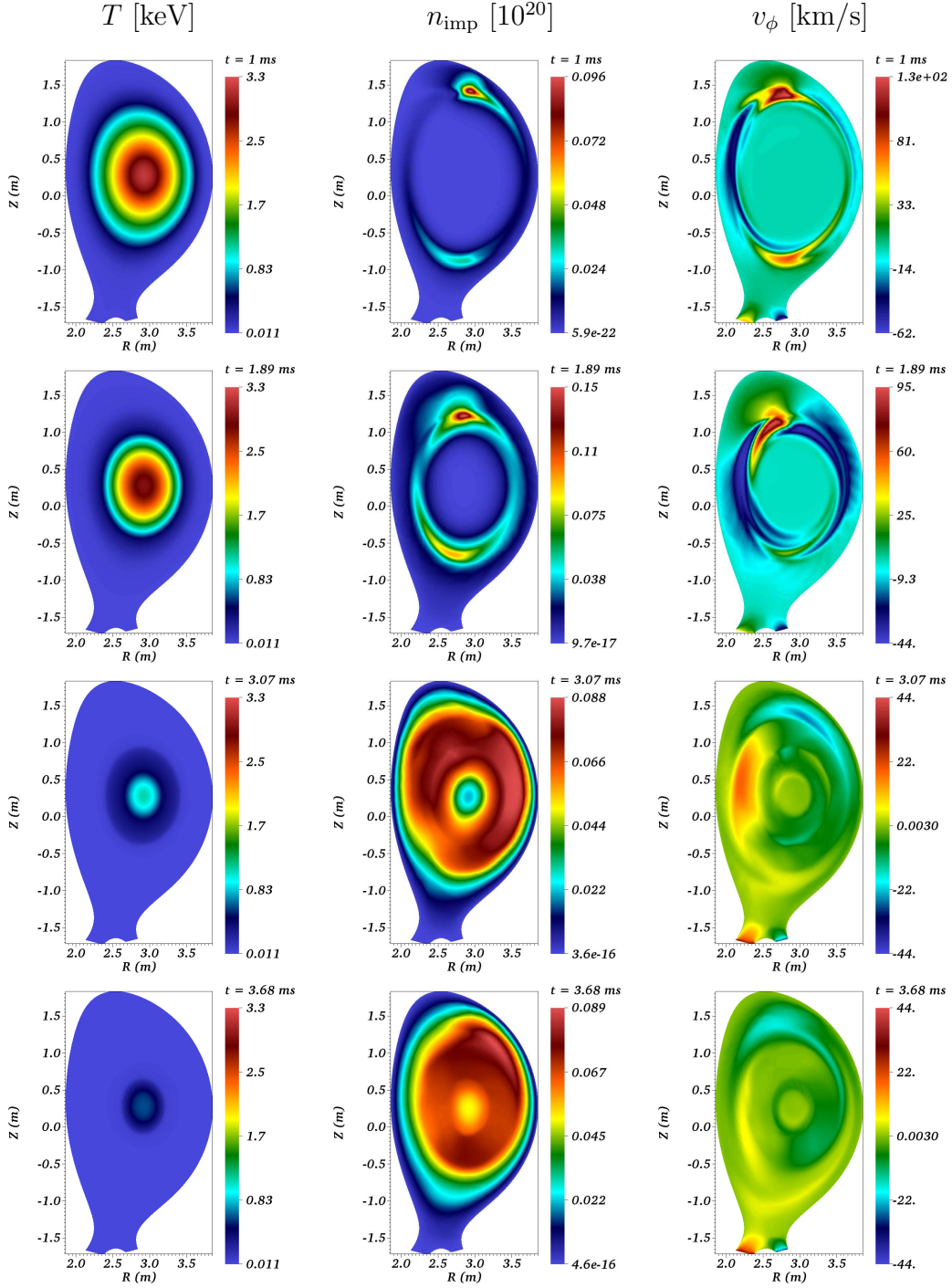
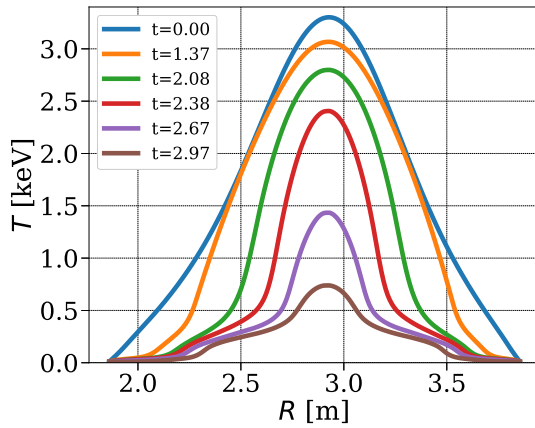
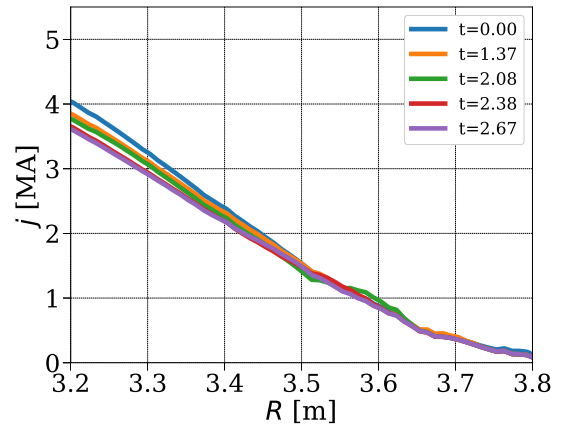


Figure 6.5: Visualizations of SPI simulation with $\eta = 10^{-6}$ for ‘case 2.5’. 1st, 2nd and 3rd columns show T [keV], n_{imp} [10^{20}] and v_ϕ [km/s] at the mentioned time instants.

[49]. Note that a smoothing operation is performed on the current profile during post-processing as the computed current profile, being the second derivative of the magnetic vector potential, is discontinuous.



(a) T at midplane vs R



(b) j at midplane vs R

Figure 6.6: Profiles of temperature and current plotted at midplane at the mentioned time steps for SPI simulations with $\eta = 10^{-6}$ for ‘case 2.5’.

Figure (6.7) shows Poincaré plots of the magnetic field for ‘case 2.5’ at the mentioned time instants. At $t = 1.9579$ ms growth of 3/1 mode is seen which is associated with the cooling of outer layer of plasma. As SPI fragments move inwards, 2/1 mode grows further cooling plasma in the outer layer which is seen at $t = 2.5519$ ms and plasma stochastization is seen near the separatrix. At further time instants, core modes are seen to nonlinearly interact with each other and cause plasma core to cool rapidly. At $t = 5.8189$ ms plasma is completely cooled where 2/1 island is still seen. Complete stochastization of plasma is not seen in these simulations.

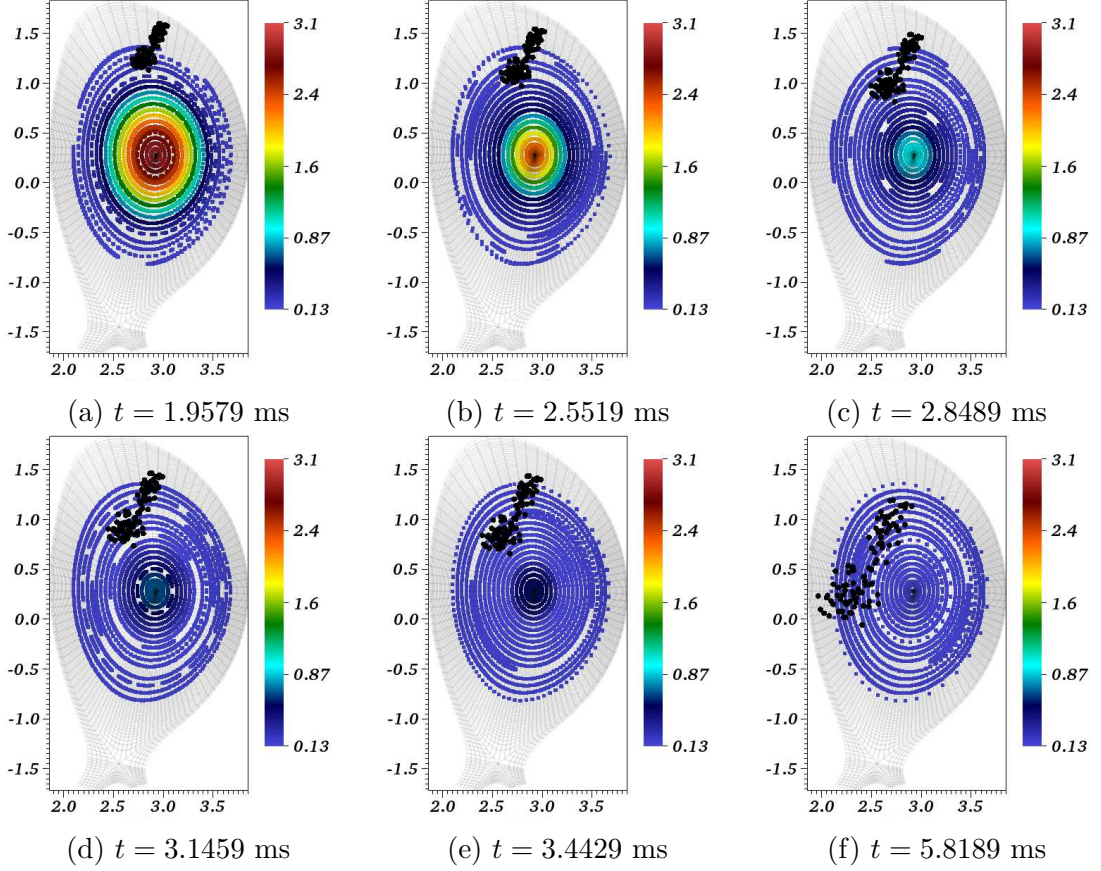


Figure 6.7: Poicaré plots of the magnetic field for the SPI simulation with constant resistivity specified by $\eta_0 = 10^{-6}$ for ‘case 2.5’. The color maps denote the plasma temperature (in keV) and solid black circles denote the projection of the position of SPI fragments in $\phi = 0$ plane.

6.2.2 SPI with realistic resistivity

SPI simulations presented in this subsection use T as well as Z_{eff} dependent resistivity with $\eta_0 = 10^{-8}$ and therefore more realistic model. The simulations are run on two different grids without and with shock-capturing stabilization. The resulting cases are shown in Table (6.2).

The other physical parameters used are as follows: The constant viscosity coefficient is set to $\mu = 10^{-6}$. The particle diffusion coefficients are specified as $D_{\parallel} = 0$ and $D_{\perp} = 2 \times 10^{-5}$ for both the total and impurity densities. The perpendicular heat conductivity is specified as $\kappa_{\perp 0} = 5 \times 10^{-6}$ and temperature dependent parallel heat conductivity with $\kappa_{\parallel 0} = 4000$.

Figure (6.8a) compares the number of time steps for the simulations listed in Table (6.2) where the effect of shock capturing stabilization is immediately seen.

case g.C	n_ψ	n_θ	n	C
case 1.0	71	100	7	0
case 1.1	71	100	7	1
case 2.0	71	128	7	0
case 2.1	71	128	7	1

Table 6.2: SPI simulations with temperature dependent resistivity with $\eta_0 = 10^{-8}$ identified by by grid (g) and the shock-capturing stabilization parameter (C) as ‘case g.C’.

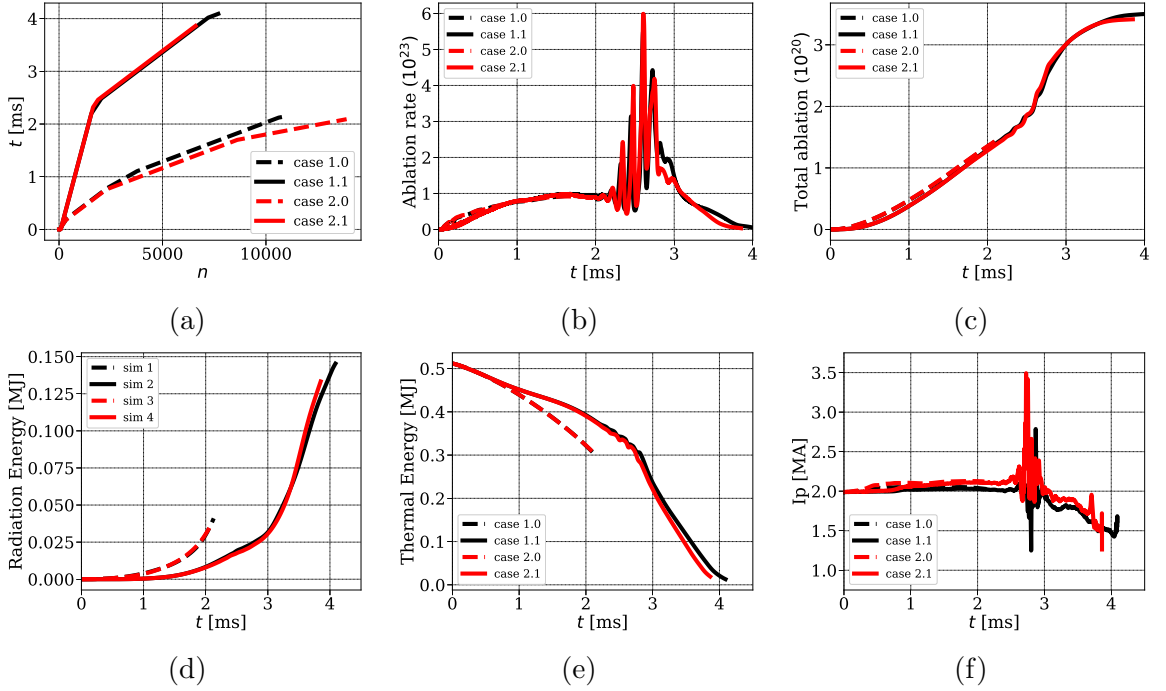


Figure 6.8: SPI simulations to show effect of shock-capturing stabilization with temperature dependent resistivity specified by $\eta_0 = 10^{-8}$: (a) physical time for which simulation is run (b) ablation rates (c) total impurities injected (d) radiation energy (e) plasma thermal energy (f) plasma current I_p .

The shock capturing stabilization allows the use of larger time steps for the matrix solver to converge enabling simulations for longer physical times in lesser number of time steps. Figure (6.8b) and (6.8c) show that the ablation rate and the total ablation for the cases under discussion has no significant effect due to the use of the shock-capturing stabilization. Figure (6.8d) shows the radiation energy with shock capturing stabilization is lower but rises sharply after 3 ms. During this interval TQ

is obtained as can be seen from Figure (6.8e) where plasma thermal energy drops rapidly over the time scale of 1 ms. At the beginning of TQ, oscillations are seen in the plasma thermal energy, ablation rate and I_p . No significant effect of the grid and shock-capturing stabilization is seen on I_p .

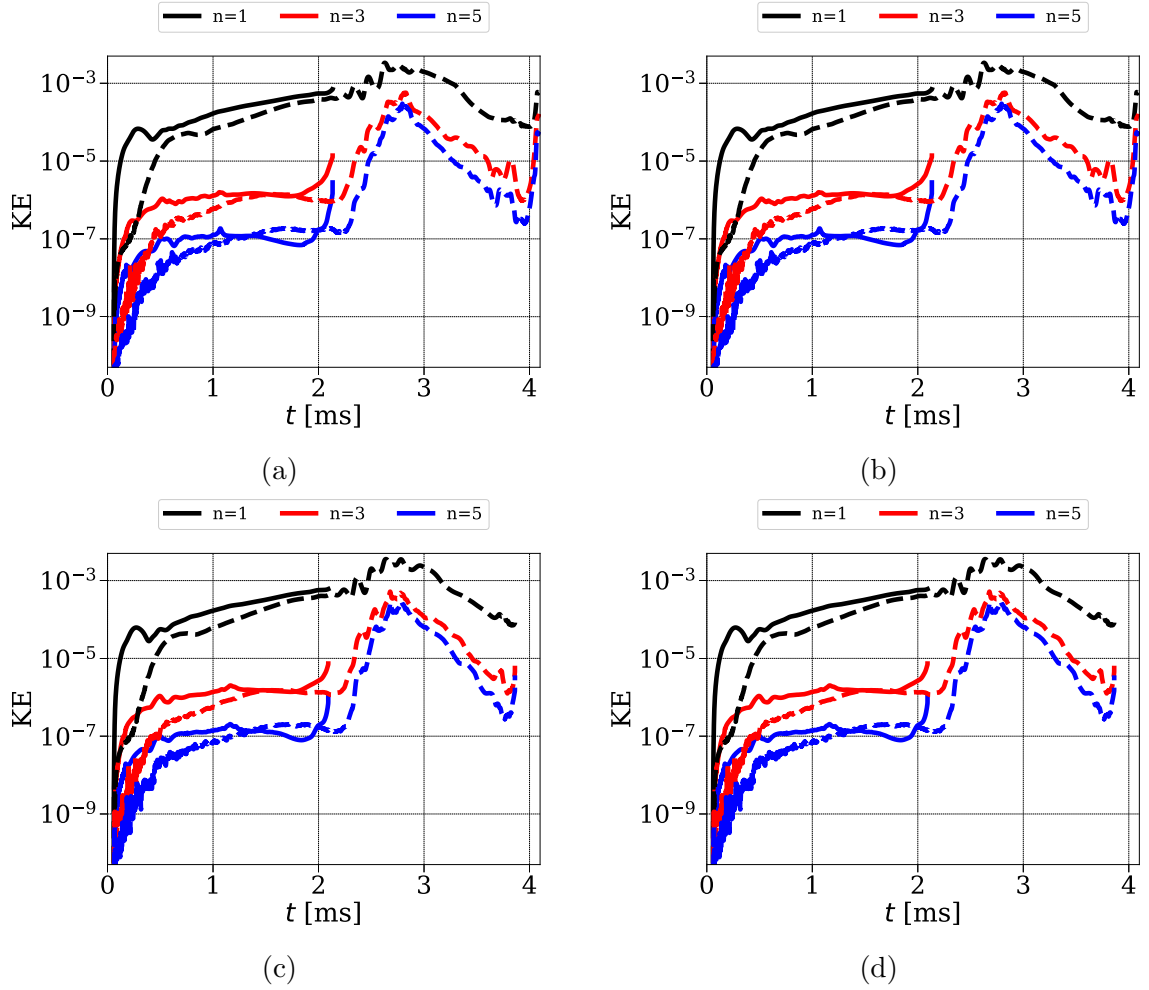


Figure 6.9: Effect of shock-capturing stabilization on SPI simulation with temperature dependent resistivity specified by $\eta_0 = 10^{-8}$. For ‘case 1.0’ and ‘case 1.1’, comparison of the evolution of (a) magnetic and (b) kinetic energies. For ‘case 2.0’ and ‘case 2.1’, comparison of the evolution of (c) magnetic and (e) kinetic energies. Solid lines corresponds to $C = 0$ while dashed lines corresponds to $C = 1$.

Figure (6.9a) and (6.9b) show comparison of the evolution of the magnetic and kinetic energies respectively for ‘case 1.0’ and ‘case 1.1’. Similarly, Figure (6.9c) and (6.9d) show comparison of the evolution of the magnetic and kinetic energies respectively for ‘case 2.0’ and ‘case 2.1’. The simulations without shock-capturing stabilization do not converge shortly after 2 ms where 2/1 mode grows and fails to

capture increased MHD activities. Shock-capturing stabilization helps to simulate increased MHD activities which are seen as rise in the energies. Since the magnetic, kinetic and plasma energies along with I_p are comparable for all 4 simulations, the $C = 1$ seems a good criterion to allow simulation to run for long physical time without affecting physics.

Figure (6.10) and (6.11) show visualizations for ‘case 1.1’ at the mentioned time instants. In the first column of Figure (6.10), evolution of T field is seen at $\phi = 0$ showing plasma cooling and the effect of TQ. The second and third columns contain snapshots of ρ_{imp} and v_ϕ to show parallel convection, transport of impurities in plasma and evolution of the cooling front. First column of (6.11) shows the evolution of A_3 field which changes significantly showing the signature of magnetic reconnection and loss of magnetic confinement. Second column of (6.11) shows the evolution of Z_{eff} which again highlights the transport of impurities and cooling front propagation in plasma. Third column of (6.11) shows the evolution of η as a function of T and Z_{eff} which shows that as plasma cools the resistivity increases. At the end of the simulation, the resistivity takes the values of order 10^{-6} in the core region.

Figure (6.12a) shows the evolution of the temperature at the magnetic axis for ‘case 1.1’ and ‘case 2.1’ showing rapid cooling of plasma core after 2 ms. Figures (6.12b) and (6.12c) show the temperature and current plotted at midplane vs R at the mentioned time instants for ‘case 1.1’. Initially plasma cools from the outer region as can be seen from T and current profiles at $t = 2.48$ ms. T profiles show sudden gradient in the profile indicating the location of the cooling front. As the cooling front propagates further in the plasma the current sheet is seen in the smoothed current profile.

Finally, Poincaré plots of the magnetic field for ‘case 1.1’ are shown in (6.13) at the mentioned time instants where color maps denote values of the temperature and solid black circles denote projected positions of SPI fragments. When SPI fragments enter the plasma, no immediate magnetic stochasticity is observed. As SPI fragments begin to propagate inwards, 3/1 mode grows (not shown here) as a consequence the plasma begins to cool in the outer layer of plasma, which is seen in (6.12). This pre-TQ dynamics is seen in the previous Chapter as well. Further propagation of fragments excites 2/1 as can be seen at $t = 2.1292$ ms in (6.13). The 3/1 and 2/1 modes continue to grow and the outer layer of plasma becomes stochastic as seen at $t = 2.5281$ ms whose effect can also be seen in the midplane profiles in Figure (6.12).

As SPI fragments move further inwards, the core modes are excited and they

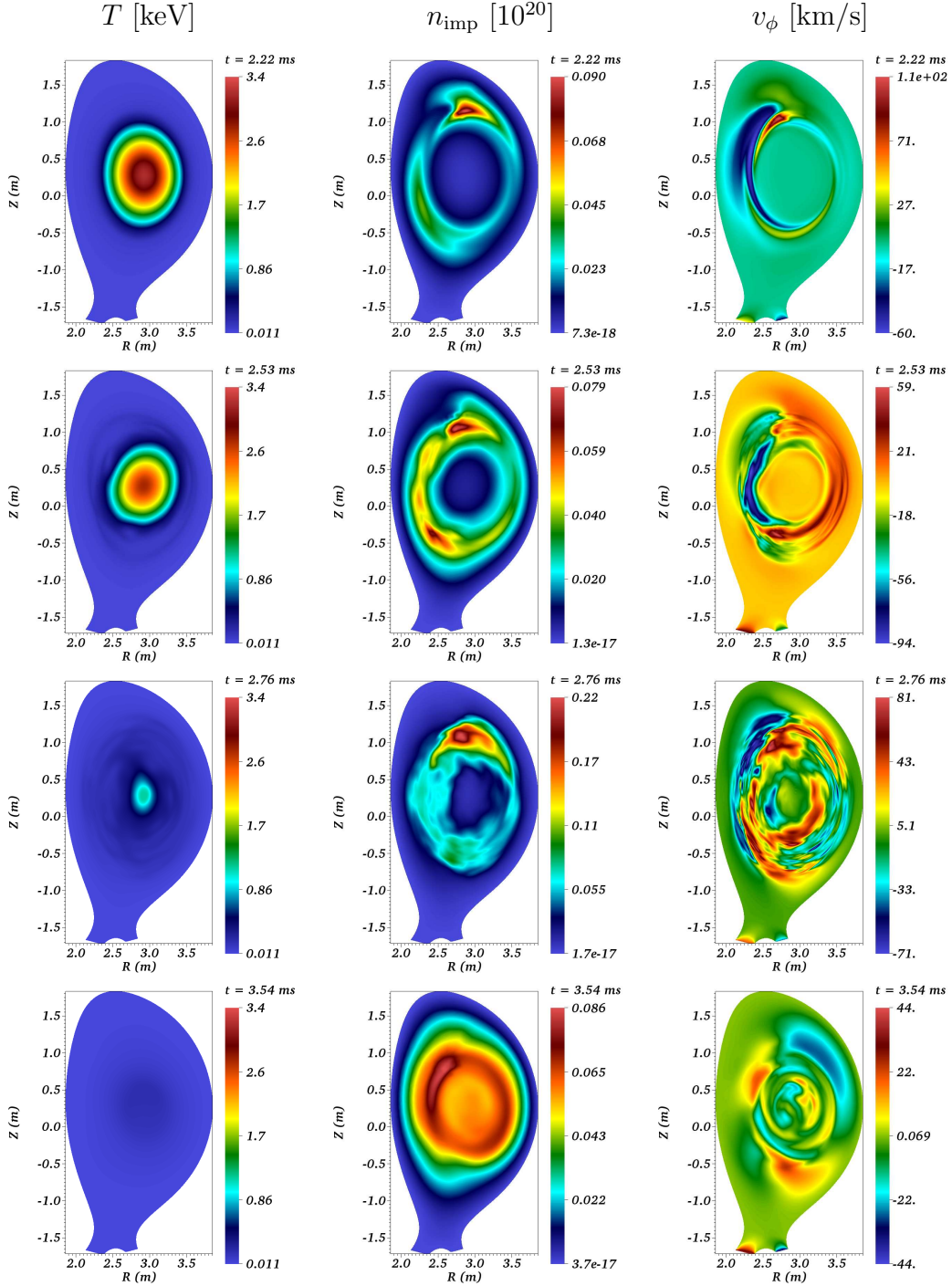


Figure 6.10: Visualizations of SPI simulation with $\eta = 10^{-8}$ for the ‘case 1.1’. 1st, 2nd and 3rd columns show T [keV], n_{imp} [10^{20}] and v_{ϕ} [km/s] at the mentioned time instants.

nonlinearly couple with the outer growing modes to cause stochasticization of plasma as seen at $t = 2.7063$ ms which leads cooling of plasma core. Growth of 1/1 mode is seen at $t = 3.0003$ ms before which cyclic dynamics is seen in energies and ablation

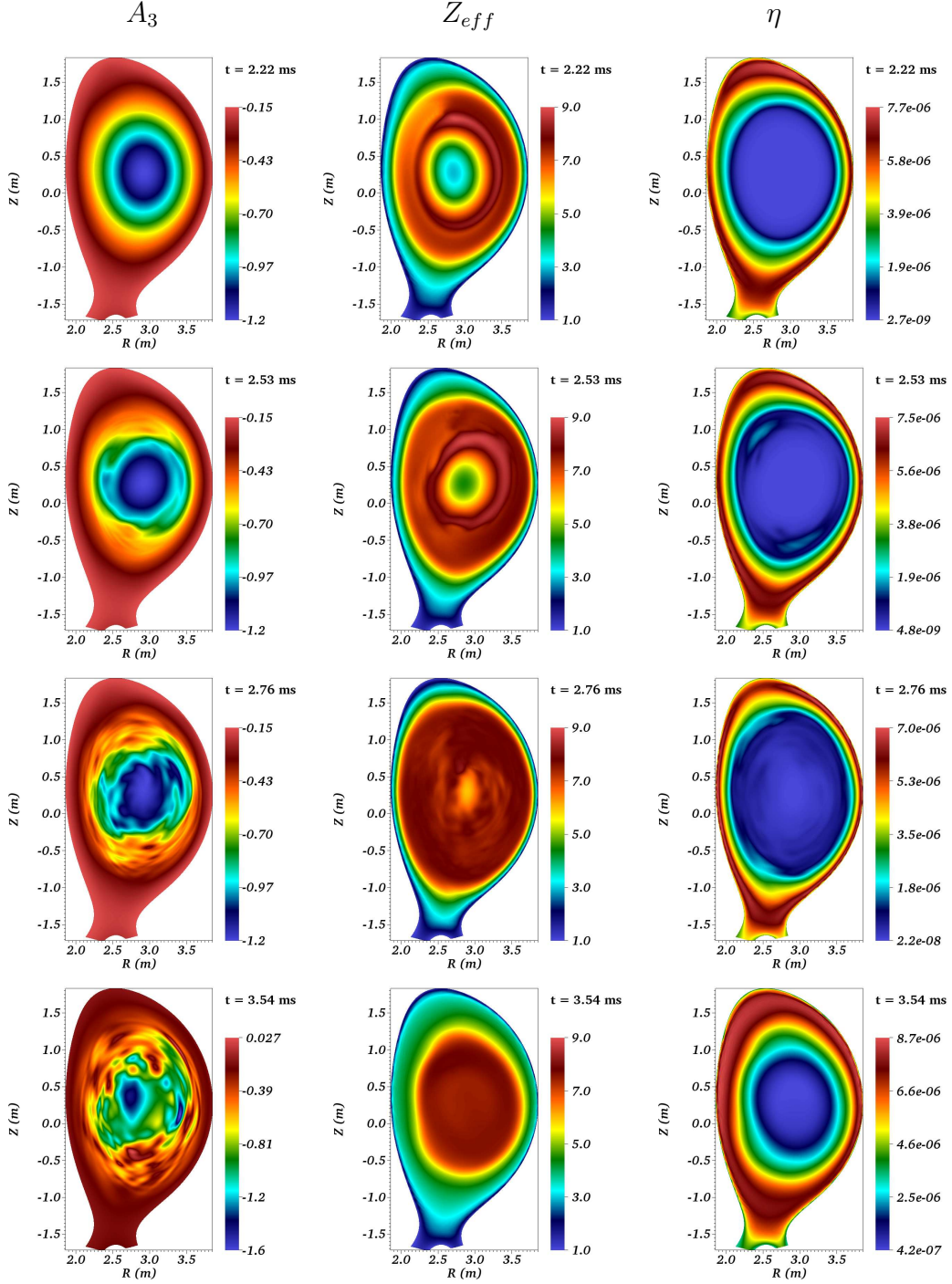


Figure 6.11: Visualizations of SPI simulation with $\eta = 10^{-8}$ for the ‘case 1.1’. 1st, 2nd and 3rd columns show A_3 , Z_{eff} and η (in normalized units) at the mentioned time instants.

rates. This dynamics seems to be related to internal kink modes and triggers the TQ. At further time instants, the core modes look stabilized until the end of TQ. At $t = 4.0487$ ms a complete plasma stochasticization is seen.

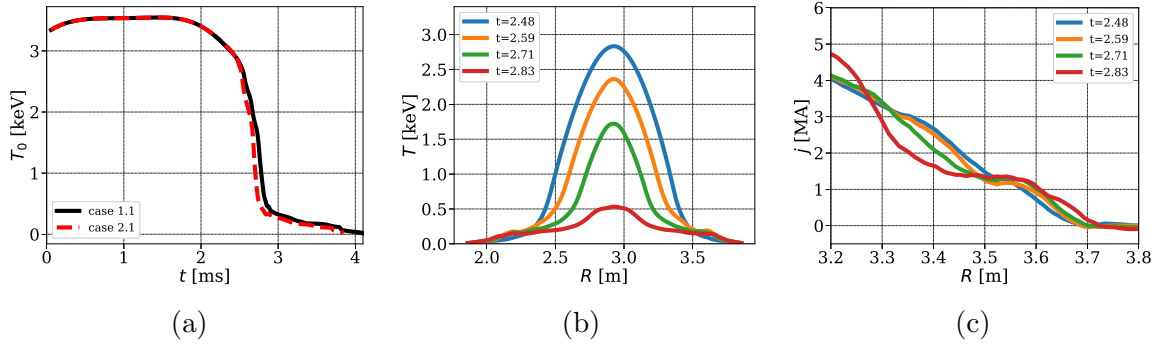


Figure 6.12: SPI simulations with temperature dependent resistivity specified by $\eta_0 = 10^{-8}$: (a) Evolution of T at magnetic axis for ‘case 1.1’ and ‘case 2.1’. (b) temperature and (c) current profile plotted at midplane at the mentioned time instants for ‘case 1.1’.

Summarizing, two phases of MHD destabilization and TQ are seen in SPI process. First, the plasma temperature drops down in the outer layer of the plasma temperature through parallel conduction in a stochastic field region and then through helical convective mixing in the core plasma during the second phase. Some key features of the non-linear dynamics of the MHD destabilization are seen in the simulations such as the formation of magnetic islands and stochastic regions.

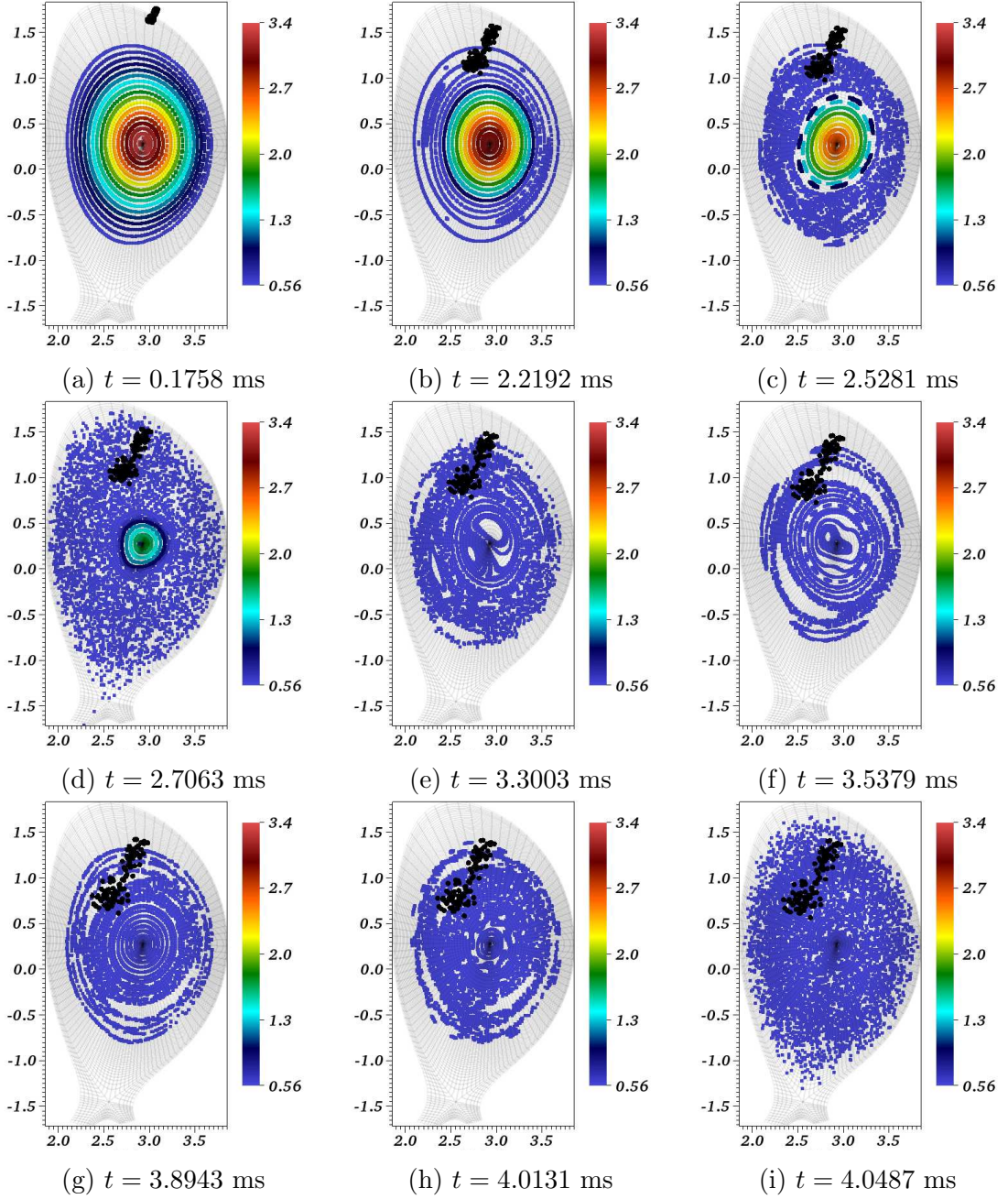


Figure 6.13: Poicaré plots of the magnetic field for the SPI simulation with temperature dependent resistivity specified by $\eta_0 = 10^{-8}$ for ‘case 1.1’. The color maps denote the plasma temperature (in keV) and solid black circles denote the projection of the position of SPI fragments in $\phi = 0$ plane.

6.3 Conclusion

Shock capturing stabilization with a proper discontinuity detection criterion is used to stabilize FEM that helps push SPI simulations into TQ. The discontinuity detection

criterion is the important part of the scheme and it may be further improved by taking into account the effects of source terms [7]. However, the criterion used here works quite well. Further, shock-capturing stabilization terms are included only in the hydrodynamic equations and are found to be sufficient to simulate SPI.

Shock capturing stabilization seems to improve the conditioning of the matrix and thereby allow the solver to converge for larger time steps and hence improves the computational efficiency. It helps capture MHD destabilization dynamics, particularly the dynamics which is followed by growth of 2/1 modes and coupling of core modes. The physical details similar to the TQ over time scale of 1 ms, MHD destabilization during TQ, signature of I_p spike, current profile contraction and complete plasma stochastization are seen in the simulations. These physical details qualitatively look similar to Ar SPI simulated using the reduced MHD model [49].

Chapter 7

Conclusions and perspectives

The work presented in this thesis deals with the development and implementation of stabilized finite element method (FEM) for nonlinear simulations of full MHD equations with applications to tokamak plasma. The application focused is Massive Material Injection (MMI) with the particular emphasis on Shattered Pellet Injection (SPI). SPI is a primary candidate for ITER's Disruption Mitigation System (DMS) and will play a role in deciding lifetime and budget of the Plasma Facing Components (PFC) and wall [59]. Experimental measurements of SPI provide a limited overview while simulations are expected to provide deeper insight with the spatio-temporal details of physics and accurate prediction of the loads. Therefore, accurate modeling of disruption physics and implementation of robust numerical methods is essential. With the robust numerical tool at hand, scans in several parameters can be simulated for which a lot of experiments may be costly to perform.

Physics of SPI phenomenon involves moving sources, convection dominated flows, complex dynamics of thermal quench (TQ) and current quench (CQ). In SPI, shattered pellets of frozen gases are injected at velocities of order hundreds of m/s in tokamak plasma. SPI fragments act as localized sources of impurities which drive a strong parallel flow transporting impurities across the torus. The transported impurities are believed to govern TQ. The time scales of the physical processes involved are diverse, such as resistive (associated with current profile contraction and helical cooling), transport of impurities, flight of SPI fragments in plasma and TQ. The physical model should accommodate all these scales along with impurity transport and sources for SPI.

High resolution numerical methods are required to discretize the physical model

encompassing diverse length and time scales. Galerkin FEM is an attractive choice of high resolution numerical methods with the ability to handle complex geometries. However, they give centered approximation of differential operators and do not provide a mechanism for numerical stabilization. For hyperbolic partial differential equations (PDEs), when the flow is convection dominated, centered approximations can lead to dispersion errors and unphysical behaviors in the numerical solution. The numerical stabilization is needed to suppress the dispersion errors in such a way that the accuracy of the method is not compromised. Variable Multi-Scale (VMS) decomposition offers a general framework to devise the numerical stabilization to be added in the weak form as additional terms. While VMS-stabilization provides L^2 stability which is effective in dealing with smooth solutions, shock/discontinuity capturing stabilization is required to enforce BV stability where the numerical solution contains high gradients. Localized SPI fragments create a region of high gradients of the density, impurity density and temperature in their neighborhood and can lead to Gibbs phenomena generating spurious oscillations in the numerical solution. Therefore, both VMS and shock capturing stabilization terms are required for SPI simulations.

Computational framework of JOREK is used to implement physical models and stabilized FEM. JOREK is a fully implicit a nonlinear MHD code with extended physics that uses mixed bi-cubic Bézier-Spectral FEM. It has proven a useful numerical tool to simulate a wide range of nonlinear MHD physics relevant to tokamak plasma including disruptions, ELMs, vertical displacement events etc using reduced MHD models. The present work involves implementation of a more complete full MHD model in the sense that it contains fast magnetosonic waves which are removed from the reduced modeling. It has been shown in [74] that full MHD model captures the growth of internal kink mode accurately at high plasma beta where reduced model fails. In this light, it will be an interesting study to compare the full and reduced MHD simulations and gain understanding on the region of validity of the reduced MHD model. SPI simulations with reduced MHD have already been performed using JOREK [50, 46, 49]. In this work, we incorporate SPI modeling into full MHD model and use stabilized FEM for nonlinear simulations.

Single and two temperature full MHD models are derived in Chapter 2 while Chapter 3 discusses details of the stabilized FEM. Further numerical improvements implemented involve treatment of the polar grid singularities and use of the consistent BDF2 method adapted to variable time stepping. The grids used in JOREK simulations are essentially polar grids with the grid center being a point of singularity. At

this point continuous representation of functions and their gradients is not guaranteed. Presence of such points in the grid can act as a source of spurious waves that can pollute the numerical solution. A strategy is proposed to enforce \mathcal{C}^1 continuity of variables at the grid center that helps reduce the noise at the grid center.

Chapter 4 presents the details of the implementation the full MHD model and its validation. Single temperature full MHD model was first implemented in JOREK in [44, 43] and was validated for standard MHD test cases on simple geometries. In this work, we extend the capabilities of full MHD models to perform simulations on the production level with the realistic geometries. The linear growth rates for standard MHD instabilities such as internal kink, tearing and ballooning modes obtained using full MHD models are compared with those obtained using the reduced MHD model. The numerical results obtained with the two models are found to be in agreement. The full MHD model is also benchmarked with other codes such as CASTOR3D in [74]. Nonlinear simulations of a disruption and ELMs are shown in [74] which capture the MHD dynamics that is comparable to the dynamics obtained using reduced MHD models. At the end of Chapter 4, a nonlinear simulation of internal kink mode is presented showing the capability of model to simulate nonlinear MHD instabilities.

In Chapter 5 we present nonlinear simulations for MMI performed using stabilized FEM. The governing equations and source modeling for MMI are described in Chapter 2. First, a nonlinear MGI simulation performed using the two temperature full MHD is presented. The numerical results obtained highlight the capability of the model to capture TQ like phase even on a coarse grid. Then, a range of nonlinear SPI simulations are presented with the single temperature full MHD. The numerical simulations uncovered that the neglecting or suppressing resistivity from A_R and A_Z equations give numerically stable but a deceptive model. Henceforth, the same value of the resistivity is added in A_R , A_Z and A_3 equations. Grid convergence, scan in resistivity and particle diffusion is performed to identify the reasonable simulation parameters that will allow simulations to run for long physical times.

In Chapter 6 long run simulations presented using shock-capturing stabilization show the key features such TQ dynamics including transport of impurities by parallel flows; MHD destabilization in the outer layer of plasma; helical mixing of impurities with plasma; growth and interaction of core modes; formation magnetic islands associated with these modes; stochastization of plasma; sudden loss of thermal energy and a signature of I_p spike.

Perspectives

The stabilized FEM designed and implemented in this work makes JOEREK an excellent tool to study a range of MMI physics using the full MHD model. In this light, the possible future perspectives of this work can be identified as follows:

First, the Ohmic heating term, which is ignored in the present implementation of the full MHD model, needs to be included to guarantee the energy conservation. The Ohmic heating term requires computation of second derivatives of the magnetic potential vector and the present implementation of DFT does not include the computation of the second derivatives of the variables and the basis functions with respect to ϕ direction. Further, the full MHD model can be extended to include the SPI modeling for mixed impurities such as Ne/D2, Ar/D2; two temperature equations and multiple SPIs. After intensive validation and comparison of the numerical results with the disruptions experiments, the model to be used for production may be identified.

Appendix A

Jacobians required for the implicit method

The weak form of the full MHD model is written in compact form as:

$$\int \mathbf{w}^* \cdot \mathbb{P}(\mathbf{w}) \frac{\partial \mathbf{w}}{\partial t} d\Omega = \int \mathbf{w}^* \cdot \tilde{\mathbf{Q}}(\mathbf{w}, t) d\Omega$$

where, \mathbf{w} is the vector of primitive variables:

$$\mathbf{w} = \{\rho, v_R, v_Z, v_\phi, T, A_R, A_Z, A_3\}^T$$

$\tilde{\mathbf{Q}}(\mathbf{w}, t)$ is the vector of right hand sides of the each equation and the matrix \mathbb{P} is given by

$$\mathbb{P} = \begin{bmatrix} 1 & 0 & 0 & 0 & 0 & 0 & 0 & 0 \\ 0 & \rho & 0 & 0 & 0 & 0 & 0 & 0 \\ 0 & 0 & \rho & 0 & 0 & 0 & 0 & 0 \\ 0 & 0 & 0 & \rho & 0 & 0 & 0 & 0 \\ T & 0 & 0 & 0 & \rho & 0 & 0 & 0 \\ 0 & 0 & 0 & 0 & 0 & 1 & 0 & 0 \\ 0 & 0 & 0 & 0 & 0 & 0 & 1 & 0 \\ 0 & 0 & 0 & 0 & 0 & 0 & 0 & 1 \end{bmatrix}$$

The test functions with projections to get the components of the vector equations are written as:

$$\begin{aligned}
\mathbf{w}_\rho^* &= \{V_i, 0, 0, 0, 0, 0, 0, 0\}^T \\
\mathbf{w}_{v_R}^* &= \{0, V_i, 0, 0, 0, 0, 0, 0\}^T \\
\mathbf{w}_{v_Z}^* &= \{0, 0, V_i, 0, 0, 0, 0, 0\}^T \\
\mathbf{w}_{v_\phi}^* &= \{0, B_R V_i, B_Z V_i, B_\phi V_i, 0, 0, 0, 0\}^T \\
\mathbf{w}_T^* &= \{0, 0, 0, 0, V_i, 0, 0, 0\}^T \\
\mathbf{w}_{A_R}^* &= \{V_i, 0, 0, 0, 0, V_i, 0, 0\}^T \\
\mathbf{w}_{A_Z}^* &= \{V_i, 0, 0, 0, 0, 0, V_i, 0\}^T \\
\mathbf{w}_{A_3}^* &= \{V_i, 0, 0, 0, 0, 0, 0, R V_i\}^T
\end{aligned}$$

where, ‘parallel projection’ is used to get the equation for v_ϕ . Application of the FEM to the weak form involves the representation of function \mathbf{w} by an finite dimensional approximate form:

$$\mathbf{w} = \sum_j \mathbf{W}_j V_j$$

Rewriting the system of the equation as follows:

$$\mathbf{P}(\mathbf{w}, \mathbf{w}^*) \frac{\partial \mathbf{w}}{\partial t} = Q(\mathbf{w}, \mathbf{w}^*, t)$$

where the integration signs are ignored for brevity and the vector $\mathbf{P}(\mathbf{w}, \mathbf{w}^*) = \mathbb{P}^T \mathbf{w}^*$ and the term $Q(\mathbf{w}, \mathbf{w}^*, t) = \mathbf{w}^* \cdot \tilde{\mathbf{Q}}(\mathbf{w}, t)$. The variable time step Gears method then becomes:

$$\left[(1 + r_n \xi) \mathbf{P}^n - \Delta t_n \theta \left(\frac{\partial Q}{\partial \mathbf{w}} \right)^n \right] \delta \mathbf{w}^n = \Delta t_n Q^n + \xi \mathbf{P}^n \delta \mathbf{w}^{n-1} \quad (\text{A.1})$$

where, the ratio of the time steps r_n and ξ are given by

$$r_n = \frac{\Delta t_{n-1}}{\Delta t_n} \quad \xi = \frac{2\theta - 1}{r_n(1 + r_n)}$$

The jacobian matrix of the implicit method contains the contributions from the terms $\mathbf{P}^n = \mathbf{P}(\mathbf{w}^n, \mathbf{w}^*)$ and $\left(\frac{\partial Q}{\partial \mathbf{w}} \right)^n$. These contributions coming from each equation are shown below.

Density equation

Using the test function \mathbf{w}_ρ^* , the contribution of the term $\mathbf{P}(\mathbf{w}^n, \mathbf{w}_\rho^*)$ for the density equation is straight forward and is:

$$\mathbf{P}(\mathbf{w}^n, \mathbf{w}_\rho^*) = \{V_i V_j, 0, 0, 0, 0, 0, 0, 0\}^T$$

The term $Q_\rho = Q(\mathbf{w}, \mathbf{w}_\rho^*, t)$ for the density equation is:

$$Q_\rho = -V_i \nabla \cdot (\rho \mathbf{v}) - D_\perp \nabla \rho \cdot \nabla V_i - \frac{(D_\parallel - D_\perp)}{B^2} (\mathbf{B} \cdot \nabla \rho) (\mathbf{B} \cdot \nabla V_i) + V_i \dot{\rho}$$

where the density diffusion term is integrated by parts and boundary integral part is ignored for the moment. Differentiating above equation with respect to each variable:

$$\frac{\partial Q_\rho}{\partial \mathbf{w}} = \begin{pmatrix} -V_i \nabla \cdot (V_j \mathbf{v}) - D_\perp \nabla V_j \cdot \nabla V_i - \frac{(D_\parallel - D_\perp)}{B^2} (\mathbf{B} \cdot \nabla V_j) (\mathbf{B} \cdot \nabla V_i) + V_i \frac{\partial \dot{\rho}}{\partial \rho} \\ -V_i \nabla \cdot (\rho V_j \mathbf{e}_R) \\ -V_i \nabla \cdot (\rho V_j \mathbf{e}_Z) \\ -V_i \nabla \cdot (\rho V_j \mathbf{e}_\phi) \\ 0 \\ \partial_{A_R} \left[-\frac{(D_\parallel - D_\perp)}{B^2} (\mathbf{B} \cdot \nabla \rho) (\mathbf{B} \cdot \nabla V_i) \right] \\ \partial_{A_A} \left[-\frac{(D_\parallel - D_\perp)}{B^2} (\mathbf{B} \cdot \nabla \rho) (\mathbf{B} \cdot \nabla V_i) \right] \\ \partial_{A_3} \left[-\frac{(D_\parallel - D_\perp)}{B^2} (\mathbf{B} \cdot \nabla \rho) (\mathbf{B} \cdot \nabla V_i) \right] \end{pmatrix}$$

The source term usually is a part of modeling and may depend upon density but on other variables as well.

Velocity equation

Using the test function $\mathbf{w}_{v_k}^* = V_i \mathbf{e}_k$, the contribution of the term $\mathbf{P}(\mathbf{w}^n, \mathbf{w}_{v_k}^*)$ for the equation of each velocity component is straight forward and is:

$$\mathbf{P}(\mathbf{w}^n, \mathbf{w}_{v_R}^*) = \{0, \rho V_i V_j, 0, 0, 0, 0, 0, 0\}^T$$

$$\mathbf{P}(\mathbf{w}^n, \mathbf{w}_{v_Z}^*) = \{0, 0, \rho V_i V_j, 0, 0, 0, 0, 0\}^T$$

$$\mathbf{P}(\mathbf{w}^n, \mathbf{w}_{v_\phi}^*) = \{0, 0, 0, \rho V_i V_j, 0, 0, 0, 0\}^T$$

The term Q_k for the equation of the each velocity component becomes:

$$Q_k = Q(\mathbf{w}, \mathbf{w}_{v_k}^*, t) = -V_i \rho \mathbf{e}_k \cdot (\mathbf{v} \cdot \nabla \mathbf{v}) - (\mathbf{B} \cdot \nabla V_i)(\mathbf{B} \cdot \mathbf{e}_k) + V_i (\mathbf{B} \otimes \mathbf{B}) : \nabla \mathbf{e}_k \\ + \left(p + \frac{1}{2} B^2 \right) \nabla \cdot (V_i \mathbf{e}_k) - \mu \nabla \mathbf{v} : (\nabla V_i \otimes \mathbf{e}_k) - V_i \nabla \mathbf{v} : \nabla \mathbf{e}_k$$

where $\mathbf{J} \times \mathbf{B}$ is integrated by parts and boundary integral part is ignored for the moment. Differentiating above equation with respect to each variable:

$$\frac{\partial Q_k}{\partial \mathbf{w}} = \left(\begin{array}{c} -V_i V_j \mathbf{e}_k \cdot (\mathbf{v} \cdot \nabla \mathbf{v}) + V_j T \nabla \cdot (V_i \mathbf{e}_k) \\ \\ \partial_{v_R} \left[-V_i \rho \mathbf{e}_k \cdot (\mathbf{v} \cdot \nabla \mathbf{v}) - \mu \nabla \mathbf{v} : (\nabla V_i \otimes \mathbf{e}_k) - V_i \nabla \mathbf{v} : \nabla \mathbf{e}_k \right] \\ \\ \partial_{v_Z} \left[-V_i \rho \mathbf{e}_k \cdot (\mathbf{v} \cdot \nabla \mathbf{v}) - \mu \nabla \mathbf{v} : (\nabla V_i \otimes \mathbf{e}_k) - V_i \nabla \mathbf{v} : \nabla \mathbf{e}_k \right] \\ \\ \partial_{v_\phi} \left[-V_i \rho \mathbf{e}_k \cdot (\mathbf{v} \cdot \nabla \mathbf{v}) - \mu \nabla \mathbf{v} : (\nabla V_i \otimes \mathbf{e}_k) - V_i \nabla \mathbf{v} : \nabla \mathbf{e}_k \right] \\ \\ \rho V_j \nabla \cdot (V_i \mathbf{e}_k) \\ \\ \partial_{A_R} \left[-(\mathbf{B} \cdot \nabla V_i)(\mathbf{B} \cdot \mathbf{e}_k) + V_i (\mathbf{B} \otimes \mathbf{B}) : \nabla \mathbf{e}_k + \left(\frac{1}{2} B^2 \right) \nabla \cdot (V_i \mathbf{e}_k) \right] \\ \\ \partial_{A_Z} \left[-(\mathbf{B} \cdot \nabla V_i)(\mathbf{B} \cdot \mathbf{e}_k) + V_i (\mathbf{B} \otimes \mathbf{B}) : \nabla \mathbf{e}_k + \left(\frac{1}{2} B^2 \right) \nabla \cdot (V_i \mathbf{e}_k) \right] \\ \\ \partial_{A_3} \left[-(\mathbf{B} \cdot \nabla V_i)(\mathbf{B} \cdot \mathbf{e}_k) + V_i (\mathbf{B} \otimes \mathbf{B}) : \nabla \mathbf{e}_k + \left(\frac{1}{2} B^2 \right) \nabla \cdot (V_i \mathbf{e}_k) \right] \end{array} \right)$$

where, is assumed that viscosity of coefficient is constant scalar. In practice, it can be a function of T . The viscosity tensor is assumed to have a form $\mu \nabla \mathbf{v}$ in above equations. The contributions of source terms is straight forward and is not shown here.

However, the parallel projection is used in practice to get the evolution of v_ϕ and in that case the test function $\mathbf{w}_B^* = V_i \mathbf{B}$. The contribution of the term $\mathbf{P}(\mathbf{w}^n, \mathbf{w}_B^*)$ then becomes:

$$\mathbf{P}(\mathbf{w}^n, \mathbf{w}_B^*) = \{0, \rho B_R V_i V_j, \rho B_Z V_i V_j, \rho B_\phi V_i V_j, 0, 0, 0, 0, 0\}^T$$

This choice of projection removes $\mathbf{J} \times \mathbf{B}$ term from the velocity equation and then $Q_B = Q(\mathbf{w}, \mathbf{w}_B^*, t)$ is written as:

$$Q_B = -V_i \rho \mathbf{B} \cdot (\mathbf{v} \cdot \nabla \mathbf{v}) - V_i \mathbf{B} \cdot \nabla p - \mu \nabla \mathbf{v} : (\nabla V_i \otimes \mathbf{B}) - V_i \nabla \mathbf{v} : \nabla \mathbf{B}$$

The last term in above equation contains gradients of the magnetic which are not continuous across the elements. Therefore, the approximation is made such that the effects of curvature of the magnetic field due to $\nabla \mathbf{B}$ are ignored and the resulting equation is written as:

$$Q_B = -V_i \rho \mathbf{B} \cdot (\mathbf{v} \cdot \nabla \mathbf{v}) - V_i \mathbf{B} \cdot \nabla p - \sum_k B_k [\mu \nabla \mathbf{v} : (\nabla V_i \otimes \mathbf{e}_k) + V_i \nabla \mathbf{v} : \nabla \mathbf{e}_k]$$

Finally the contribution of the above term to the jacobian is written as:

$$\frac{\partial Q_B}{\partial \mathbf{w}} = \left(\begin{array}{c} -V_i V_j \mathbf{B} \cdot (\mathbf{v} \cdot \nabla \mathbf{v}) - V_i \mathbf{B} \cdot \nabla (V_i T) \\ \\ \partial_{v_R} \left[-V_i \rho \mathbf{B} \cdot (\mathbf{v} \cdot \nabla \mathbf{v}) - \sum_k B_k [\mu \nabla \mathbf{v} : (\nabla V_i \otimes \mathbf{e}_k) + V_i \nabla \mathbf{v} : \nabla \mathbf{e}_k] \right] \\ \\ \partial_{v_Z} \left[-V_i \rho \mathbf{B} \cdot (\mathbf{v} \cdot \nabla \mathbf{v}) - \sum_k B_k [\mu \nabla \mathbf{v} : (\nabla V_i \otimes \mathbf{e}_k) + V_i \nabla \mathbf{v} : \nabla \mathbf{e}_k] \right] \\ \\ \partial_{v_\phi} \left[-V_i \rho \mathbf{B} \cdot (\mathbf{v} \cdot \nabla \mathbf{v}) - \sum_k B_k [\mu \nabla \mathbf{v} : (\nabla V_i \otimes \mathbf{e}_k) + V_i \nabla \mathbf{v} : \nabla \mathbf{e}_k] \right] \\ \\ -V_i \mathbf{B} \cdot \nabla (\rho V_j) \\ \\ \partial_{A_R} \left[-V_i \rho \mathbf{B} \cdot (\mathbf{v} \cdot \nabla \mathbf{v}) - V_i \mathbf{B} \cdot \nabla p - \sum_k B_k [\mu \nabla \mathbf{v} : (\nabla V_i \otimes \mathbf{e}_k) + V_i \nabla \mathbf{v} : \nabla \mathbf{e}_k] \right] \\ \\ \partial_{A_Z} \left[-V_i \rho \mathbf{B} \cdot (\mathbf{v} \cdot \nabla \mathbf{v}) - V_i \mathbf{B} \cdot \nabla p - \sum_k B_k [\mu \nabla \mathbf{v} : (\nabla V_i \otimes \mathbf{e}_k) + V_i \nabla \mathbf{v} : \nabla \mathbf{e}_k] \right] \\ \\ \partial_{A_3} \left[-V_i \rho \mathbf{B} \cdot (\mathbf{v} \cdot \nabla \mathbf{v}) - V_i \mathbf{B} \cdot \nabla p - \sum_k B_k [\mu \nabla \mathbf{v} : (\nabla V_i \otimes \mathbf{e}_k) + V_i \nabla \mathbf{v} : \nabla \mathbf{e}_k] \right] \end{array} \right)$$

Pressure equation

Using the test function \mathbf{w}_T^* , the contribution of the term $\mathbf{P}(\mathbf{w}^n, \mathbf{w}_T^*)$ for the pressure equation is:

$$\mathbf{P}(\mathbf{w}^n, \mathbf{w}_T^*) = \{T V_i V_j, 0, 0, 0, \rho V_i V_j, 0, 0, 0\}^T$$

The term $Q_p Q(\mathbf{w}, \mathbf{w}_T^*, t)$ for the pressure equation is:

$$\begin{aligned} Q_p = & -V_i \mathbf{v} \cdot \nabla p - \gamma p \nabla \cdot \mathbf{v} - \kappa_{\perp} \nabla T \cdot \nabla V_i - \frac{(\kappa_{\parallel} - \kappa_{\perp})}{B^2} (\mathbf{B} \cdot \nabla T) (\mathbf{B} \cdot \nabla V_i) \\ & + V_i (\gamma - 1) \mu \nabla \mathbf{v} : \nabla \mathbf{v} + V_i S_T \end{aligned}$$

where the heat diffusion term is integrated by parts and boundary integral part is ignored for the moment. Differentiating above equation with respect to each variable:

$$\frac{\partial Q_p}{\partial \mathbf{w}} = \left(\begin{array}{c} -V_i \mathbf{v} \cdot \nabla (V_j T) - \gamma V_j T \nabla \cdot \mathbf{v} + V_i \partial_\rho S_T \\ \\ \partial_{v_R} \left[-V_i \mathbf{v} \cdot \nabla p - \gamma p \nabla \cdot \mathbf{v} + V_i (\gamma - 1) \mu \nabla \mathbf{v} : \nabla \mathbf{v} + V_i S_T \right] \\ \\ \partial_{v_Z} \left[-V_i \mathbf{v} \cdot \nabla p - \gamma p \nabla \cdot \mathbf{v} + V_i (\gamma - 1) \mu \nabla \mathbf{v} : \nabla \mathbf{v} + V_i S_T \right] \\ \\ \partial_{v_\phi} \left[-V_i \mathbf{v} \cdot \nabla p - \gamma p \nabla \cdot \mathbf{v} + V_i (\gamma - 1) \mu \nabla \mathbf{v} : \nabla \mathbf{v} + V_i S_T \right] \\ \\ -V_i \mathbf{v} \cdot \nabla (\rho V_j) - \gamma \rho V_j \nabla \cdot \mathbf{v} - \kappa_\perp \nabla V_j \cdot \nabla V_i \\ - \frac{(\kappa_\parallel - \kappa_\perp)}{B^2} (\mathbf{B} \cdot \nabla V_j) (\mathbf{B} \cdot \nabla V_i) + V_i \partial_T S_T \\ \\ \partial_{A_R} \left[- \frac{(\kappa_\parallel - \kappa_\perp)}{B^2} (\mathbf{B} \cdot \nabla T) (\mathbf{B} \cdot \nabla V_i) \right] \\ \\ \partial_{A_Z} \left[- \frac{(\kappa_\parallel - \kappa_\perp)}{B^2} (\mathbf{B} \cdot \nabla T) (\mathbf{B} \cdot \nabla V_i) \right] \\ \\ \partial_{A_3} \left[- \frac{(\kappa_\parallel - \kappa_\perp)}{B^2} (\mathbf{B} \cdot \nabla T) (\mathbf{B} \cdot \nabla V_i) \right] \end{array} \right)$$

Induction equation

Using the test function $\mathbf{w}_{A_k}^* = V_i \mathbf{e}_k$, the contribution of the term $\mathbf{P}(\mathbf{w}^n, \mathbf{w}_{A_k}^*)$ for the induction equation components is:

$$\begin{aligned}\mathbf{P}(\mathbf{w}^n, \mathbf{w}_{A_R}^*) &= \{0, 0, 0, 0, 0, 0, 0, V_i V_j, 0, 0\}^T \\ \mathbf{P}(\mathbf{w}^n, \mathbf{w}_{A_Z}^*) &= \{0, 0, 0, 0, 0, 0, 0, 0, V_i V_j, 0\}^T \\ \mathbf{P}(\mathbf{w}^n, \mathbf{w}_{A_3}^*) &= \{0, 0, 0, 0, 0, 0, 0, 0, 0, R V_i V_j\}^T\end{aligned}$$

The term Q_{A_k} for the induction equation component is written from the weak form as:

$$Q_{A_k} = V_i \mathbf{e}_k \cdot (\mathbf{v} \times \mathbf{B}) + \nabla \times (\eta V_i \mathbf{e}_k) \cdot \mathbf{B} - V_i \mathbf{e}_k \cdot \mathbf{S}_J$$

where, the resistive term is integrated by parts and the boundary integral term is ignored for the moment. Differentiating Q_{A_k} with respect to \mathbf{w} :

$$\frac{\partial Q_{A_k}}{\partial \mathbf{w}} = \begin{pmatrix} 0 \\ \partial_{v_R} \left[V_i \mathbf{e}_k \cdot (\mathbf{v} \times \mathbf{B}) \right] \\ \partial_{v_Z} \left[V_i \mathbf{e}_k \cdot (\mathbf{v} \times \mathbf{B}) \right] \\ \partial_{v_\phi} \left[V_i \mathbf{e}_k \cdot (\mathbf{v} \times \mathbf{B}) \right] \\ 0 \\ \partial_{A_R} \left[V_i \mathbf{e}_k \cdot (\mathbf{v} \times \mathbf{B}) + \nabla \times (\eta V_i \mathbf{e}_k) \cdot \mathbf{B} - V_i \mathbf{e}_k \cdot \mathbf{S}_J \right] \\ \partial_{A_Z} \left[V_i \mathbf{e}_k \cdot (\mathbf{v} \times \mathbf{B}) + \nabla \times (\eta V_i \mathbf{e}_k) \cdot \mathbf{B} - V_i \mathbf{e}_k \cdot \mathbf{S}_J \right] \\ \partial_{A_3} \left[V_i \mathbf{e}_k \cdot (\mathbf{v} \times \mathbf{B}) + \nabla \times (\eta V_i \mathbf{e}_k) \cdot \mathbf{B} - V_i \mathbf{e}_k \cdot \mathbf{S}_J \right] \end{pmatrix}$$

The resistivity is assumed constant in above equation, however in practice it is a function of T and hence will have contribution in the fifth line.

Boundary integral terms

The contribution of the boundary integral terms can be derived in the similar manner.

They are written as follows:

$$B_\rho = \int_{\partial\Omega} V_i (\underline{\mathbf{D}}\nabla\rho \cdot \hat{\mathbf{n}}) dS$$

$$B_{\mathbf{v}} = \int_{\partial\Omega} \left[(\mathbf{B} \cdot \mathbf{v}^*)(\mathbf{B} \cdot \hat{\mathbf{n}}) - (p + 0.5B^2)(\mathbf{v}^* \cdot \hat{\mathbf{n}}) \right] dS$$

$$B_p = \int_{\partial\Omega} V_i (\underline{\boldsymbol{\kappa}}\nabla T \cdot \hat{\mathbf{n}}) dS$$

$$B_{\mathbf{A}} = \int_{\partial\Omega} \mathbf{A}^* \cdot (\eta\mathbf{B} \times \hat{\mathbf{n}}) dS$$

Appendix B

Integrated quantities

A physical quantity of interest is integrated over whole plasma volume as:

$$I = \int f(R, Z, \phi) dV = \int_0^{2\pi} \int_{\Omega_{\xi}} f R dR dZ d\phi$$

where ξ denoted poloidal plane formed by R and Z coordinates. Further, the integral may be split into two parts to compute the integral over the core region and outside of the core region of a plasma. Following are some quantities used in this work:

- Magnetic energy (ME) with $f = 0.5 \mathbf{B} \cdot \mathbf{B}$
- Kinetic energy (ME) with $f = 0.5 \rho \mathbf{v} \cdot \mathbf{v}$
- Plasma thermal (TE) energy with $f = \rho T + E_{\text{ion}} \rho_{\text{imp}} T$
- Plasma current (I_p) with $f = j = -R J_{\phi}$.

Bibliography

- [1] <http://open.adas.ac.uk>.
- [2] <https://www.iter.org/newsline/-/3267>.
- [3] Patrick R. Amestoy, Iain S. Duff, Jean-Yves L'Excellent, and Jacko Koster. A fully asynchronous multifrontal solver using distributed dynamic scheduling. *SIAM Journal on Matrix Analysis and Applications*, 23(1):15–41, 2001.
- [4] Francisco Javier Artola Such. *FREE-BOUNDARY SIMULATIONS OF MHD PLASMA INSTABILITIES IN TOKAMAKS*. Theses, Université Aix Marseille, November 2018.
- [5] Dinshaw S. Balsara. Linearized formulation of the riemann problem for adiabatic and isothermal magnetohydrodynamics. *The Astrophysical Journal Supplement Series*, 116(1):119–131, may 1998.
- [6] S Barabaschi, C Berke, F Fuster Jaume, J Hill, L Ingelstam, F Troyon, H van der Laan, and JP Watteau. Fusion programme evaluation 1996. *European Commission DGXII, EUR*, 17521, 1996.
- [7] F. Bassi, F. Cecchi, N. Franchina, S. Rebay, and M. Savini. High-order discontinuous galerkin computation of axisymmetric transonic flows in safety relief valves. *Computers and Fluids*, 49(1):203–213, 2011.
- [8] L.R. Baylor, S.J. Meitner, T.E. Gebhart, J.B.O. Caughman, J.L. Herfindal, D. Shiraki, and D.L. Youchison. Shattered pellet injection technology design and characterization for disruption mitigation experiments. *Nuclear Fusion*, 59(6):066008, apr 2019.
- [9] Richard M. Beam and R. F. Warming. Alternating direction implicit methods for parabolic equations with a mixed derivative. *SIAM Journal on Scientific and Statistical Computing*, 1(1):131–159, 1980.

- [10] J. Becker. A second order backward difference method with variable steps for a parabolic problem. *BIT Numerical Mathematics*, 38:644–662, 1998.
- [11] Paul M. Bellan. *Fundamentals of Plasma Physics*. Cambridge University Press, 2006.
- [12] Dieter Biskamp. *Nonlinear Magnetohydrodynamics*. Cambridge Monographs on Plasma Physics. Cambridge University Press, 1993.
- [13] S. Bozhenkov, M. Lehnen, K. Finken, G. Bertschinger, H. Koslowski, D. Reiter, R. Wolf, and T. Team. Fuelling efficiency of massive gas injection in textor: mass scaling and importance of gas flow dynamics. *Nuclear Fusion*, 51:083033, 2011.
- [14] J.U Brackbill and D.C Barnes. The effect of nonzero $\nabla \cdot \mathbf{b}$ on the numerical solution of the magnetohydrodynamic equations. *Journal of Computational Physics*, 35(3):426–430, 1980.
- [15] S. I. Braginskii. Transport processes in a plasma. 1965.
- [16] S. Brenner and R. Scott. *The Mathematical Theory of Finite Element Methods*. Texts in Applied Mathematics. Springer New York, 2007.
- [17] M Brio and C.C Wu. An upwind differencing scheme for the equations of ideal magnetohydrodynamics. *Journal of Computational Physics*, 75(2):400–422, 1988.
- [18] Alexander N. Brooks and Thomas J.R. Hughes. Streamline upwind/petrov-galerkin formulations for convection dominated flows with particular emphasis on the incompressible navier-stokes equations. *Computer Methods in Applied Mechanics and Engineering*, 32(1):199–259, 1982.
- [19] B. J. Burke, S. E. Kruger, C. C. Hegna, P. Zhu, P. B. Snyder, C. R. Sovinec, and E. C. Howell. Edge localized linear ideal magnetohydrodynamic instability studies in an extended-magnetohydrodynamic code. *Physics of Plasmas*, 17(3):032103, 2010.
- [20] F.F. Chen and Plenum Publishing. *Introduction to Plasma Physics and Controlled Fusion*. Number v. 1 in Introduction to Plasma Physics and Controlled Fusion. Springer.
- [21] P.G. Ciarlet. *The Finite Element Method for Elliptic Problems*. Classics in Applied Mathematics. Society for Industrial and Applied Mathematics, 2002.

- [22] Stephen Kirk Combs, Steven J. Meitner, Larry R. Baylor, John B. O. Caughman, Nicolas Commaux, Dan T. Fehling, Charles R. Foust, Tom C. Jernigan, James M. McGill, Paul B. Parks, and Dave A. Rasmussen. Alternative techniques for injecting massive quantities of gas for plasma-disruption mitigation. *IEEE Transactions on Plasma Science*, 38(3):400–405, 2010.
- [23] José Tarcisio Costa. *Éléments finis stabilisés VMS appliqués aux modèles magnétohydrodynamiques (MHD) des plasmas de fusion*. PhD thesis, 2016.
- [24] Olivier Czarny and Guido Huysmans. Bézier surfaces and finite elements for mhd simulations. *Journal of Computational Physics*, 227(16):7423–7445, 2008.
- [25] A. Dedner, F. Kemm, D. Kröner, C.-D. Munz, T. Schnitzer, and M. Wesenberg. Hyperbolic divergence cleaning for the mhd equations. *Journal of Computational Physics*, 175(2):645–673, 2002.
- [26] B.D. Dudson, M.V. Umansky, X.Q. Xu, P.B. Snyder, and H.R. Wilson. Bout++: A framework for parallel plasma fluid simulations. *Computer Physics Communications*, 180(9):1467–1480, 2009.
- [27] Etienne Emmrich. Stability and error of the variable two-step bdf for semilinear parabolic problems. *Journal of Applied Mathematics and Computing*, 19:33–55, 03 2005.
- [28] S. K. Combs et al. R and d in support of the shattered pellet technique for disruption mitigation. 2013.
- [29] N. M. Ferraro, S. C. Jardin, and P. B. Snyder. Ideal and resistive edge stability calculations with m3d-c1. *Physics of Plasmas*, 17(10):102508, 2010.
- [30] Alexandre Fil. *Modeling of massive gas injection triggered disruptions in tokamak plasmas*. PhD thesis, 2015. Thèse de doctorat dirigée par Beyer, Peter Physique et sciences de la matière Aix-Marseille 2015.
- [31] V. Frayssé, L. Giraud, and S. Gratton. A set of gmres routines for real and complex arithmetics. 1997.
- [32] Jeffrey P. Freidberg. *Ideal MHD*. Cambridge University Press, 2014.
- [33] K. Gál, E. Belonohy, G. Kocsis, P. Lang, and G. Veres. Role of shielding in modelling cryogenic deuterium pellet ablation. *Nuclear Fusion*, 48:085005, 2008.

- [34] Giorgio Giorgiani, Hervé Guillard, Boniface Nkonga, and Eric Serre. A stabilized powell sabin finite-element method for the 2d euler equations in supersonic regime. *Computer Methods in Applied Mechanics and Engineering*, 340:216–235, 2018.
- [35] A H Glasser, C R Sovinec, R A Nebel, T A Gianakon, S J Plimpton, M S Chu, D D Schnack, and the NIMROD Team. The NIMROD code: a new approach to numerical plasma physics. *Plasma Physics and Controlled Fusion*, 41(3A):A747–A755, jan 1999.
- [36] J. P. Goedbloed, Rony Keppens, and Stefaan Poedts. *Advanced Magnetohydrodynamics: With Applications to Laboratory and Astrophysical Plasmas*. Cambridge University Press, 2010.
- [37] J. P. Hans Goedbloed and Stefaan Poedts. *Principles of Magnetohydrodynamics: With Applications to Laboratory and Astrophysical Plasmas*. Cambridge University Press, 2004.
- [38] H Grad and H Rubin. Hydromagnetic equilibria and force-free fields. 10 1958.
- [39] David J. Griffiths. *Introduction to Electrodynamics*. Cambridge University Press, 4 edition, 2017.
- [40] Hervé Guillard. The mathematical theory of reduced MHD models for fusion plasmas. Research Report RR-8715, INRIA, April 2015.
- [41] F D Halpern, D Leblond, H Lütjens, and J-F Luciani. Oscillation regimes of the internal kink mode in tokamak plasmas. *Plasma Physics and Controlled Fusion*, 53(1):015011, nov 2010.
- [42] Federico D. Halpern, Hinrich Lütjens, and Jean-François Luciani. Diamagnetic thresholds for sawtooth cycling in tokamak plasmas. *Physics of Plasmas*, 18(10):102501, 2011.
- [43] J.W. Haverkort. *Magnetohydrodynamic waves and instabilities in rotating tokamak plasmas*. PhD thesis, Mathematics and Computer Science, Centrum voor Wiskunde en Informatica, 2013.
- [44] J.W. Haverkort, H.J. Blank, Guido Huijsmans, Jane Pratt, and Barry Koren. Implementation of the full viscoresistive magnetohydrodynamic equations in a

- nonlinear finite element code. *Journal of Computational Physics*, pages 281–302, 04 2016.
- [45] T.C Hender, et el., Disruption the ITPA MHD, and Magnet Group. Chapter 3: MHD stability, operational limits and disruptions. *Nuclear Fusion*, 47(6):S128–S202, jun 2007.
- [46] M. Hoelzl, D. Hu, E. Nardon, and G. T. A. Huijsmans. First predictive simulations for deuterium shattered pellet injection in asdex upgrade. *Physics of Plasmas*, 27(2):022510, 2020.
- [47] M. Hoelzl, G.T.A. Huijsmans, S.J.P. Pamela, M. Bécoulet, E. Nardon, F.J. Artola, B. Nkonga, C.V. Atanasiu, V. Bandaru, A. Bhole, D. Bonfiglio, A. Cathey, O. Czarny, A. Dvornova, T. Fehér, A. Fil, E. Franck, S. Futatani, M. Gruca, H. Guillard, J.W. Haverkort, I. Holod, D. Hu, S.K. Kim, S.Q. Korving, L. Kos, I. Krebs, L. Kripner, G. Latu, F. Liu, P. Merkel, D. Meshcheriakov, V. Mitterauer, S. Mochalsky, J.A. Morales, R. Nies, N. Nikulsin, F. Orain, J. Pratt, R. Ramasamy, P. Ramet, C. Reux, K. Särkimäki, N. Schwarz, P. Singh Verma, S.F. Smith, C. Sommariva, E. Strumberger, D.C. van Vugt, M. Verbeek, E. Westerhof, F. Wieschollek, and J. Zielinski. The JOREK non-linear extended MHD code and applications to large-scale instabilities and their control in magnetically confined fusion plasmas. *Nuclear Fusion*, 61(6):065001, may 2021.
- [48] I Holod, M Hoelzl, P S Verma, GTA Huijsmans, R Nies, and JOREK Team. Enhanced preconditioner for jorek mhd solver, 2021.
- [49] D. Hu, E. Nardon, M. Hoelzl, F. Wieschollek, M. Lehnen, G.T.A. Huijsmans, D. C. van Vugt, S.-H. Kim, JET contributors, and JOREK team. Radiation asymmetry and MHD destabilization during the thermal quench after impurity shattered pellet injection. *Nuclear Fusion*, 61(2):026015, jan 2021.
- [50] D. Hu, E. Nardon, M. Lehnen, G.T.A. Huijsmans, and D.C. van Vugt and. 3d non-linear MHD simulation of the MHD response and density increase as a result of shattered pellet injection. *Nuclear Fusion*, 58(12):126025, oct 2018.
- [51] G. Hughes, T. J. R. Scovazzi and T.E. Tezduyar. Stabilized methods for compressible flows. *J Sci Comput*, 43:343–368, 2010.
- [52] Thomas J. R. Hughes, Guglielmo Scovazzi, and Leopoldo P. Franca. *Multiscale and Stabilized Methods*, chapter 2. American Cancer Society, 2007.

- [53] Thomas J.R. Hughes, Leopoldo P. Franca, and Gregory M. Hulbert. A new finite element formulation for computational fluid dynamics: Viii. the galerkin/least-squares method for advective-diffusive equations. *Computer Methods in Applied Mechanics and Engineering*, 73(2):173–189, 1989.
- [54] P. Hénon, P. Ramet, and J. Roman. Pastix: a high-performance parallel direct solver for sparse symmetric positive definite systems. *Parallel Computing*, 28(2):301–321, 2002.
- [55] M. Ivanov, S.K. Godunov, and A. Zabrodine. *Résolution numérique des problèmes multidimensionnels de la dynamique des gaz*. MIR, 1979.
- [56] Antony Jameson. Origins and further development of the jameson–schmidt–turkel scheme. *AIAA Journal*, 55(5):1487–1510, 2017.
- [57] S.C. Jardin, J. Breslau, and N. Ferraro. A high-order implicit finite element method for integrating the two-fluid magnetohydrodynamic equations in two dimensions. *Journal of Computational Physics*, 226:2146–2174, 10 2007.
- [58] M. Kikuchi. *Frontiers in Fusion Research: Physics and Fusion*. Springer London, 2011.
- [59] Charlson C. Kim, Yueqiang Liu, Paul B. Parks, Lang L. Lao, Michael Lehnen, and Alberto Loarte. Shattered pellet injection simulations with nimrod. *Physics of Plasmas*, 26(4):042510, 2019.
- [60] G. Latu, N. Crouseilles, V. Grandgirard, and E. Sonnendrücker. Gyrokinetic semi-lagrangian parallel simulation using a hybrid openmp/mpi programming. In Franck Cappello, Thomas Herault, and Jack Dongarra, editors, *Recent Advances in Parallel Virtual Machine and Message Passing Interface*, pages 356–364, Berlin, Heidelberg, 2007. Springer Berlin Heidelberg.
- [61] Ph. Lauber, S. Günter, A. Könies, and S.D. Pinches. Ligka: A linear gyrokinetic code for the description of background kinetic and fast particle effects on the mhd stability in tokamaks. *Journal of Computational Physics*, 226(1):447–465, 2007.
- [62] M. Lehnen and et al. Disruptions in iter and strategies for their control and mitigation. *Journal of Nuclear Materials*, 463:39–48, 2015. PLASMA-SURFACE INTERACTIONS 21.

- [63] Hong-lin Liao and Zhimin Zhang. Analysis of adaptive bdf2 scheme for diffusion equations. *Mathematics of Computation*, 90:1207–1226, 08 2020.
- [64] H. Lütjens and Jean-François Luciani. Xtor-2f: A fully implicit newton-krylov solver applied to nonlinear 3d extended mhd in tokamaks. *J. Comput. Physics*, 229:8130–8143, 10 2010.
- [65] G. McCracken and P. Stott. *Fusion: The Energy of the Universe*. Elsevier Science, 2013.
- [66] E. T. Meier and U. Shumlak. A general nonlinear fluid model for reacting plasma-neutral mixtures. *Physics of Plasmas*, 19(7):072508, 2012.
- [67] David Mosher. Coronal equilibrium of high—atomic-number plasmas. *Phys. Rev. A*, 10:2330–2335, Dec 1974.
- [68] E. Nardon, A. Fil, M. Hoelzl, and G. Huijsmans. Progress in understanding disruptions triggered by massive gas injection via 3d non-linear mhd modelling with jorek. *Plasma Physics and Controlled Fusion*, 59, 2017.
- [69] E Nardon, D Hu, F J Artola, D Bonfiglio, M Hoelzl, A Boboc, P Carvalho, S Gerasimov, G Huijsmans, V Mitterauer, N Schwarz, and H Sun. Thermal quench and current profile relaxation dynamics in massive-material-injection-triggered tokamak disruptions. *Plasma Physics and Controlled Fusion*, 63(11):115006, sep 2021.
- [70] E. Nardon, D. Hu, M. Hoelzl, and D. Bonfiglio and. Fast plasma dilution in ITER with pure deuterium shattered pellet injection. *Nuclear Fusion*, 60(12):126040, oct 2020.
- [71] Richard Nies and Matthias Hoelzl. Testing performance with and without block low rank compression in mumps and the new pastix 6.0 for jorek nonlinear mhd simulations, 2019.
- [72] Hiroaki Nishikawa. On large start-up error of bdf2. *Journal of Computational Physics*, 392:456–461, 2019.
- [73] Parks P. The ablation rate of light-element pellets with a kinetic treatment for penetration of plasma electrons through the ablation cloud. *Private communication*.

- [74] S. J. P. Pamela, A. Bhole, G. T. A. Huijsmans, B. Nkonga, M. Hoelzl, I. Krebs, and E. Strumberger. Extended full-mhd simulation of non-linear instabilities in tokamak plasmas. *Physics of Plasmas*, 27(10):102510, 2020.
- [75] S J P Pamela, G T A Huysmans, M N A Beurskens, S Devaux, T Eich, and S Benkadda and. Nonlinear MHD simulations of edge-localized-modes in JET. *Plasma Physics and Controlled Fusion*, 53(5):054014, apr 2011.
- [76] S.J.P. Pamela, G.T.A. Huijsmans, M. Hoelzl, and the JOREK Team. A generalised formulation of g-continuous bezier elements applied to non-linear mhd simulations. *submitted*, 2021.
- [77] Stanislas Pamela. *Simulation magnéto-hydro-dynamiques des Edge-Localised-Modes [ELM] dans un tokamak*. PhD thesis, 2010. Thèse de doctorat dirigée par Mohamed-Benkadda, Mohamed Sadruddin Physique des plasmas, Fusion magnétique Aix-Marseille 1 2010.
- [78] P. B. Parks and R. J. Turnbull. Effect of transonic flow in the ablation cloud on the lifetime of a solid hydrogen pellet in a plasma. *The Physics of Fluids*, 21(10):1735–1741, 1978.
- [79] Paul Parks. Modeling dynamic fracture of cryogenic pellets. 6 2016.
- [80] Richard Pitts, Richard Buttery, and Simon Pinches. Fusion: The way ahead. *Physics World*, 19, 03 2006.
- [81] Kenneth G. Powell. *An Approximate Riemann Solver for Magnetohydrodynamics*, pages 570–583. Springer Berlin Heidelberg, Berlin, Heidelberg, 1997.
- [82] O. Sauter and S.Yu. Medvedev. Tokamak coordinate conventions: Cocos. *Computer Physics Communications*, 184(2):293–302, 2013.
- [83] Vladimir Sergeev, OA Bakhareva, B. Kuteev, and Michael Tendler. Studies of the impurity pellet ablation in the high-temperature plasma of magnetic confinement devices. *Plasma Physics Reports*, 32:363–377, 05 2006.
- [84] V. D. Shafranov. Grad-shafranov equation for mhd equilibrium in a torus. *Sov. Phys.-JETP*, 682(26), 1960.
- [85] W.M. Stacey. *Fusion: An Introduction to the Physics and Technology of Magnetic Confinement Fusion*. Wiley, 2010.

- [86] Peter C Stangeby et al. *The plasma boundary of magnetic fusion devices*, volume 224. Institute of Physics Pub. Philadelphia, Pennsylvania, 2000.
- [87] G. Strang and G. Fix. *An Analysis of the Finite Element Method*. Wellesley-Cambridge Press, 2008.
- [88] Tayfun E. Tezduyar and Masayoshi Senga. Stabilization and shock-capturing parameters in supg formulation of compressible flows. *Computer Methods in Applied Mechanics and Engineering*, 195(13):1621–1632, 2006.
- [89] Y. Todo and T. Sato. Linear and nonlinear particle-magnetohydrodynamic simulations of the toroidal alfvén eigenmode. *Physics of Plasmas*, 5(5):1321–1327, 1998.
- [90] Juan Pablo Trelles and S. Mahnaz Modirkhazeni. Variational multiscale method for nonequilibrium plasma flows. *Computer Methods in Applied Mechanics and Engineering*, 282:87–131, 2014.
- [91] Jeaniffer Vides Higueros. *Godunov-type schemes for hydrodynamic and magnetohydrodynamic modeling*. Theses, Université Nice Sophia Antipolis, October 2014.
- [92] Vincent, P. E. and Jameson, A. Facilitating the adoption of unstructured high-order methods amongst a wider community of fluid dynamicists. *Math. Model. Nat. Phenom.*, 6(3):97–140, 2011.
- [93] J. Von Neumann and R. D. Richtmyer. A method for the numerical calculation of hydrodynamic shocks. *Journal of Applied Physics*, 21(3):232–237, 1950.
- [94] G.S. VORONOV. A practical fit formula for ionization rate coefficients of atoms and ions by electron impact: $z=1-28$. *Atomic Data and Nuclear Data Tables*, 65(1):1–35, 1997.
- [95] Christelle Wervaecke. *Simulation d’écoulements turbulents compressibles par une méthode d’éléments finis stabilisée*. PhD thesis, 2010. Thèse de doctorat dirigée par Nkonga, Boniface et Beaugendre, Héloïse Mathématiques appliquées Bordeaux 1 2010.
- [96] J. Wesson and D.J. Campbell. *Tokamaks*. International series of monographs on physics. Clarendon Press, 2004.

- [97] M L Wilkins. Calculation of elastic-plastic flow. 1 1969.
- [98] Mark L. Wilkins. Use of artificial viscosity in multidimensional fluid dynamic calculations. *Journal of Computational Physics*, 36(3):281–303, 1980.
- [99] X. Q. Xu, B. D. Dudson, P. B. Snyder, M. V. Umansky, H. R. Wilson, and T. Casper. Nonlinear elm simulations based on a nonideal peeling–ballooning model using the bout++ code. *Nuclear Fusion*, 51(10), 9 2011.